Canted-Cosine-Theta Superconducting Accelerator Magnets for High Energy Physics and Ion Beam Cancer Therapy

by

Lucas Nathan Brouwer

A dissertation submitted in partial satisfaction of the
requirements for the degree of
Doctor of Philosophy

in

Engineering - Nuclear Engineering

in the

Graduate Division

of the

University of California, Berkeley

Committee in charge:

Professor Karl van Bibber, Chair
Associate Professor Peter Hosemann
Professor-in-Residence Ka-Ngo Leung
Professor Jonathan Wurtele

Spring 2015

Canted-Cosine-Theta Superconducting Accelerator Magnets for High Energy Physics and Ion Beam Cancer Therapy

Abstract

Canted-Cosine-Theta Superconducting Accelerator Magnets for High Energy Physics and Ion Beam Cancer Therapy

by

Lucas Nathan Brouwer

Doctor of Philosophy in Engineering - Nuclear Engineering

University of California, Berkeley

Professor Karl van Bibber, Chair

Advances in superconducting magnet technology have historically enabled the construction of new, higher energy hadron colliders. Looking forward to the needs of a potential future collider, a significant increase in magnet field and performance is required. Such a task requires an open mind to the investigation of new design concepts for high field magnets. Part I of this thesis will present an investigation of the Canted-Cosine-Theta (CCT) design for high field Nb_3Sn magnets. New analytic and finite element methods for analysis of CCT magnets will be given, along with a discussion on optimization of the design for high field. The design, fabrication, and successful test of the 2.5 T NbTi dipole CCT1 will be presented as a proof-of-principle step towards a high field Nb_3Sn magnet. Finally, the design and initial steps in the fabrication of the 16 T Nb_3Sn dipole CCT2 will be described.

Part II of this thesis will investigate the CCT concept extended to a curved magnet for use in an ion beam therapy gantry. The introduction of superconducting technology in this field shows promise to reduce the weight and cost of gantries, as well as open the door to new beam optics solutions with high energy acceptance. An analytic approach developed for modeling curved CCT magnets will be presented, followed by a design study of a superconducting magnet for a proton therapy gantry. Finally, a new magnet concept called the "Alternating Gradient CCT" (AG-CCT) will be introduced. This concept will be shown to be a practical magnet solution for achieving the alternating quadrupole fields desired for an achromatic gantry, allowing for the consideration of treatment with minimal field changes in the superconducting magnets.

The primary motivation of this thesis is to share new developments for Canted-Cosine-Theta superconducting magnets, with the hope this design will improve technology for high energy physics and ion beam cancer therapy.

To my family

Contents

Contents **ii**

List of Figures **v**

List of Tables **xiii**

I CCT Magnets for High Energy Physics **1**

1 Introduction and Motivation **2**
1.1 Motivation for high field accelerator magnets 2
1.2 Introduction to the CCT concept 4
1.3 Motivation for high field Nb_3Sn CCT dipoles 5
1.4 History of the CCT and scope of the thesis 10

2 Analytic Modeling **12**
2.1 Goals and overview 12
2.2 Winding path to field relation for a CCT layer 14
2.3 A vector potential model for a multi-layer CCT: fields, stored energy, and inductance 21
2.4 Correction of cross-talk in 2-in-1 CCT magnets 28
2.5 Fields in a multi-layer thick winding CCT dipole magnet 36
2.6 Lorentz forces and pressures in a multi-layer thick winding CCT dipole magnet 41
2.7 Limitations of the analytic model 46
2.8 The 3D periodic symmetry region of the CCT 47
2.9 Magnetic and structural boundary conditions for the 3D symmetry 49

3 Finite Element Modeling of CCT Dipoles **53**
3.1 Brick element representation of the conductor 53
3.2 Magnetic modeling in Opera3D 53
3.3 Structural modeling in ANSYS 55

4 Design Choices and Optimization for High Field CCT Dipoles **62**

4.1 Goals and overview . . . 62
4.2 Efficiency of a CCT layer: comparison to an ideal cosine-theta . . . 62
4.3 Conductor length . . . 64
4.4 Design parameters . . . 65
4.5 Choice of midplane tilt angle α . . . 67
4.6 Choice of cable height (strand number) for the innermost layer . . . 73
4.7 Current grading by reducing strand number . . . 74
4.8 A cost study of the CCT design for high field . . . 77

5 CCT1: a 2.5T NbTi Proof-of-Principle Dipole 82
5.1 Introduction and goals . . . 82
5.2 Design . . . 83
5.3 Magnetic modeling . . . 86
5.4 Structural modeling . . . 90
5.5 Fabrication . . . 97
5.6 Test results . . . 100
5.7 Perspective on test results . . . 103

6 CCT2: a 16T Nb_3Sn Dipole Design 104
6.1 Introduction and goals . . . 104
6.2 Design . . . 104
6.3 Magnetic modeling . . . 107
6.4 Inclusion of a Bi2212 HTS insert to reach 18 T . . . 112
6.5 Structural modeling . . . 114
6.6 The LBNL fabrication and test plan towards 16 T . . . 119
6.7 A 5 turn Nb_3Sn reaction and impregnation test . . . 119
6.8 A 64 turn model of layers 1 and 2: 5 T NbTi . . . 122

II CCT Magnets for Ion Beam Cancer Therapy Gantries 128

7 Introduction and Motivation 129
7.1 Ion beam cancer therapy . . . 129
7.2 Motivation for a superconducting CCT gantry magnet . . . 134
7.3 History, previous work, and scope of thesis . . . 136

8 Modeling of Curved CCT Magnets 140
8.1 Introduction and goals . . . 140
8.2 Toroidal coordinates . . . 141
8.3 A CCT winding path in toroidal coordinates . . . 141
8.4 Development of toroidal harmonics . . . 146

9 A Curved CCT Design Study for a Proton Therapy Gantry 151

9.1 Design criteria and goals . . . 151
9.2 Magnetic design . . . 152
9.3 Magnet geometry, structure, and weight . . . 158
9.4 Beam tracking . . . 160
9.5 Lorentz forces . . . 161
9.6 Structural modeling in ANSYS . . . 165
9.7 Conclusion . . . 168

10 The AG-CCT: a New Magnet Concept for an Achromatic Gantry 170
10.1 The AG-CCT concept . . . 170
10.2 Desired magnetic fields for an achromatic proton gantry . . . 171
10.3 Preliminary design of an AG-CCT magnet system for the desired fields . . . 173
10.4 Conclusion and alternative applications . . . 179

III Conclusion 180

11 Summary and Future Work 181

Bibliography 183

A Magnetic Field Representation in Accelerator Magnets 191
A.1 Straight-section harmonics . . . 191
A.2 Integrated harmonics . . . 192

B Current Sheet Vector Potentials 195
B.1 The vector potential from integration . . . 195
B.2 Integration for a current sheet with no axial variation . . . 195
B.3 Potential for a solenoidal current sheet . . . 196
B.4 Potential for a cos(nθ) current sheet . . . 197
B.5 Potential for a constant axial current . . . 198

C Cost Study Design Data 199
C.1 A two layer 11.3 T CCT dipole . . . 199
C.2 A four layer 14.3 T CCT dipole . . . 201
C.3 A six layer 15.8 T CCT dipole . . . 203
C.4 A eight layer 16.8 T CCT dipole . . . 205

List of Figures

1.1 Superconducting hadron colliders. 3
1.2 Future pp collider options within the FCC study. (Fig. from [4]) 4
1.3 Two layers of CCT dipole conductor windings are shown powered such that their transverse fields sum and solenoidal fields cancel. 5
1.4 A CCT winding mandrel is shown. Rectangular channels are machined into a metallic cylinder to produce a mandrel with ribs and a spar. These channels position Rutherford cable for field quality, and the spars and ribs provide structural support at the single conductor turn level. 6
1.5 (a) The magnetic field generated by an idealized 2D dipole current density. (b) The direction and magnitude of the resultant Lorentz forces within the winding. (c) The primary effect of the Lorentz forces in a dipole is to compress the coil from the pole down to the midplane, which is illustrated on a traditional cosine-theta dipole magnet cross section. 7
1.6 The azimuthal stress at the pole region of the superconducting magnet is shown as the current (and Lorentz force) increases towards the nominal operating value for each of the superconducting hadron colliders. The initial compression "After cool-down" is the applied pre-stress. The conductor at the pole is seen unloading towards tension as the magnet is energized, but the applied pre-stress is chosen such that the coil never goes into tension and remains in compression at the nominal current. (Fig. from [12]) 8
1.7 (a) A cross section of the LHC main dipole with the location of the collars indicated. (b) A 15 m pneumatic press at CERN capable of applying 21 tons/m of force to the coil assembly. Presses like this were used in combination with the collars to pre-stress the LHC main dipole coils before being assembled into the iron yoke and additional structure. (Fig. from [20]) 9
1.8 A comparison of Lorentz force interception in a CCT vs. accumulation in a traditional cosine-theta design. 10

2.1 The local unit tangent, radial, and binormal vectors ($\hat{t}$, $\hat{r}$, $\hat{b}$) are shown at point $\vec{p}$ of a parametric path constrained to the surface of a cylinder. 14

2.2 A path is shown patterned axially in integer multiples of the pitch length w. This periodic symmetry condition requires the pitch length be constant for all azimuthal angles, and is represented in the figure by the vector $w\hat{z}$ pointing axially between adjacent paths. 15
2.3 Two views of the conductor path for a CCT dipole layer are shown. 18
2.4 Two views of the conductor path for a CCT quadrupole layer are shown. 19
2.5 A schematic showing the configuration for canceling undesired fields using a pair of CCT layers. 20
2.6 A CAD assembly of a pair of CCT layers is shown with angles and current directions as diagrammed in Figure 2.5. The green splice box on the left connects (splices) layer 1 and layer 2 on the return end. 20
2.7 The LHC "2-in-1" dual bore dipole magnet is shown. (Fig. from [2]) 29
2.8 Displaced harmonics are calculated at R_{ref} in the $z = x+iy$ system due to current sheet located at $r' = R$ in the $z' = x' + iy'$ system. 30
2.9 Streamlines for the uncorrected (a) and corrected (b) 2-in-1 CCT dipole are shown. 35
2.10 The 2D streamlines for the transverse field generated by a single CCT dipole layer of radial thickness are shown. 39
2.11 The 2D streamlines for the transverse field generated by a four layer CCT dipole magnet are shown. 41
2.12 Conductor volume element showing the Frenet-Serret frame $(\beta(\theta), \gamma(\theta), r(\theta))$ following the center of the conductor path. 42
2.13 Comparison of Equation 2.76 with finite element results for a single 4.4 T layer: a_1=28 mm, a_2=43 mm, α=20 deg, w=7.34 mm, and I_0=16.1 kA. 44
2.14 Comparison of Equation 2.76 with finite element results for a four layer 18 T dipole: inner radius of 28 mm, 15.35 mm layer radial thickness, 0.55 mm spacing between layers, w=7.34 mm, α=20 deg, and I_0=16.1 kA. 45
2.15 Comparison of Equation 2.82 with finite element results for a single 4.4 T layer: a_1=28 mm, a_2=43 mm, α=20 deg, w=7.34 mm, and I_0=16.1 kA. 46
2.16 Comparison of Equation 2.84 with finite element results for a four layer 18 T dipole: inner radius of 28 mm, 15.35 mm layer radial thickness, 0.55 mm spacing between layers, w=7.34 mm, α=20 deg, and I_0=16.1 kA. 47
2.17 The conductor and mandrel forming the minimum symmetry region for one CCT layer is shown together and then separated. This symmetry can be repeated axially to form a CCT layer in a laminated fashion. 48
2.18 Two adjacent mandrel laminations are shown with a displacement and then mated. These laminations are identical and the conductor channels match perfectly end to end, representing the periodic symmetry in the winding path. . . . 48
2.19 The 2D axial symmetry of a traditional cosine-theta dipole "cross section" (a) is shown compared to the 3D periodic symmetry region of the CCT "lamination" (b). 49
2.20 A periodic symmetry region is shown meshed around the conductor of a CCT dipole. The outer axial faces of this region are used for the specification of the periodic field and current conditions. 50

2.21 A two layer symmetry region of conductor and mandrels is shown. The constraint equations between lamination face nodes are shown graphically for the conductor of layer two. 51

3.1 A single CCT dipole turn discretized into eight node brick elements is shown. . 54
3.2 An example of a .cond file "layer1.cond" is shown for importing the first two 8-node brick element conductors into Opera3D. 55
3.3 The method for generating the 180 degree symmetry region from the brick element path is illustrated for a CCT dipole conductor layer. 56
3.4 An example of two guesses and the interpolated zero force value for δ_z is shown. Each case represents a solution of the ANSYS model with the "single-strain" condition using the respective value for δ_z. 58
3.5 ANSYS stress results for a single conductor layer are shown using the ANSYS viewer in the global cylindrical frame (r, θ, z). The stress results are also shown converted to a local conductor frame (t, r, b) and plotted in the program ParaView as a single continuous conductor turn. 61

4.1 A single CCT layer is shown with the total physical length L_{tot}, end length L_e, and magnetic length L_m indicated. 67
4.2 Normalized behavior of the pitch, number of turns, and end length is shown as a function of tilt angle for a single layer of fixed total length. 68
4.3 The fractional geometric end and straight-section length is shown as a function of tilt angle for a single layer of fixed total length. It is seen that the effect of a smaller tilt angle is to convert straight-section length into end length. 68
4.4 Dipole harmonics along the axis of the magnet (z) are shown for a single layer. The zoomed region shows the location of the max and plateau field. 69
4.5 The normalized behavior of the magnetic length L_m, plateau field B_{plat}, and integrated field B_{int} are shown for a single layer of fixed total length. There exists a single alpha which maximizes the integrated field. For a given conductor and rib thickness, this optimum angle is a function of layer radius r and total length L_{tot} (see Figure 4.6). 70
4.6 The optimial tilt angle that maximizes the integrated dipole field is shown as a function of total physical length and radius. 71
4.7 The factor relating the radius to the length of a single CCT turn C_l is shown for varying tilt angle α. 72
4.8 The normalized conductor use as a function of tilt angle for a 2.2 m CCT layer is shown added to Figure 4.5. 72
4.9 Equation 4.20 is shown plotted given a typical Nb_3Sn short-sample current density curve. 74
4.10 The load lines for the conductor layers of an ungraded (a) and graded (b) eight layer CCT dipole are shown. 75

4.11 The ungraded (a) and graded (b) conductor cross sections are shown for the eight layer Nb_3Sn dipole design CCT2. 76
4.12 A fit [52] of the Nb_3Sn strand current density for HD3 coil-2 is shown. 78
4.13 The conductor cost of one meter of magnetic length for varying dipole fields is shown for a 100 mm bore CCT. 80
4.14 The scaling of conductor cost as function of number of layers for the ungraded case is shown for a selection of clear bore diameters. 81

5.1 An exploded view of CCT1 with an external key, bladder, and shell loading structure is shown. 83
5.2 The two conductor layers of CCT1 are shown. 84
5.3 A cross section of CCT1's mandrels is shown. 85
5.4 A cross section of the key and bladder outer structure considered for variable loading of CCT1 is shown. 86
5.5 The dipole harmonic (B_1) along the length of CCT1 is shown. The equivalent dipole step function at the central field of 2.52 T is shown with the magnetic length L_m indicated. 87
5.6 The sextupole (b_3) and dodecapole (b_5) harmonics are shown along the length of CCT1. The harmonics are calculated in Opera3D at 2/3 of the clear bore. . . . 88
5.7 The solenoidal field (Bz) is shown along the length of CCT1. 89
5.8 The load line for CCT1 is shown for current density in the superconductor. . . . 90
5.9 The Lorentz force density directed towards the mandrel ribs is shown for CCT1. The results displayed were calculated at the center of the conductor using Opera3D. 91
5.10 The Lorentz force density directed in the radial direction is shown for CCT1. The results displayed were calculated at the center of the conductor using Opera3D. 92
5.11 The 3D periodic symmetry region used for structural calculations in ANSYS is shown for layer 1 of CCT1 and for both layers assembled into a key, bladder, and shell structure. 93
5.12 The Lorentz force induced azimuthal stress (difference between cooldown and operation) for the conductor of CCT1 is compared to results from a model with the inner mandrel spar removed (no interception) and to the predicted azimuthal stress within an equivalent sector coil. The stress in the CCT model with interception is seen reduced to near the single turn level. 95
5.13 Operating azimuthal conductor stress in MPa is shown for CCT1 conductor and structure. 96
5.14 Azimuthal stress in MPa is shown for CCT1 without an external structure for cooldown (a) and operation (b). Without an external structure providing rigidity the coil pack is susceptible to bending under the azimuthally asymmetric Lorentz force loads. 97
5.15 The CNC machining of an aluminum winding mandrel for CCT1 is shown. . . . 98
5.16 The anodized mandrels for layer 1 and layer 2 of CCT1 are shown. The mandrels were wound with conductor by hand with no additional applied tension. 98

5.17 Layer 1 and layer 2 of CCT1 are shown assembled one inside the other and then into an outer aluminum shell. The bottom left image shows the continuous transition between layers that was later replaced with a splice outside the magnet. 99
5.18 The straight-section sextupole (b_3) is shown as function of magnet current for the six current ramps of CCT1. 101
5.19 The straight-section b_5 and b_7 harmonics are shown as function of magnet current for the six current ramps of CCT1. 101
5.20 The measured sextupole harmonic (b_3) as a function of axial position through one end of CCT1 is shown. 102
5.21 Training quenches during the test of CCT1 are shown. 103

6.1 The eight graded conductor layers and mandrels of CCT2 are shown. 105
6.2 The eight conductor layers of CCT2 are shown. 106
6.3 The dipole harmonic (B_1) along the length of CCT2 is shown. The equivalent dipole step function at the central field of 15.87 T is shown with the magnetic length L_m indicated. 108
6.4 The axial variation of the on-axis solenoidal field of CCT2 is shown. 109
6.5 The sextupole (b_3) and dodecapole (b_5) harmonics are shown along the length of CCT2. The harmonics are calculated in Opera3D at 2/3 of the clear bore. . . . 110
6.6 The load lines for CCT2 are shown for current density in the superconductor. . 111
6.7 The dipole along the length of CCT2 with the Bi2112 insert is shown. 113
6.8 The coupled load lines for the hybrid configuration of CCT2 are shown for current density in the strand. 114
6.9 The 3D symmetry region of CCT2 is shown in ANSYS without (a) and with (b) the HTS insert. 115
6.10 Local conductor stress is shown plotted around a single turn for the innermost layer of the eight layers of Nb_3Sn. 116
6.11 Local conductor stress is shown plotted around a single turn for the innermost Bi2212 and Nb_3Sn layer. 117
6.12 (a) Radial displacement in mm is shown for the Nb_3Sn outer. (b) The bending of the coil pack to a non-circular, elliptical shape is seen leading to high stress (in MPa) concentrated on the edge of the inner mandrel. 118
6.13 The effect of extending the spar of the innermost layer (reducing the clear bore) on the maximum longitudinal conductor and spar stress is shown for the Nb_3Sn layers. Increasing this spar reduces coilpack bending at the cost of clear bore. . 118
6.14 The 5 turn mandrel is shown wound with Nb_3Sn cable and then put through the heat treatment reaction. 120
6.15 The 5 turn impregnation tooling is shown along with the results using beeswax. 121
6.16 The dipole harmonic (B_1) along the length of the 64 turn model is shown for the short-sample current of 10.6 kA. 123
6.17 The load line for the 64 turn NbTi model is shown for current density in the superconductor. 124

6.18 The 64 turn layer 1 and 2 mandrels for the NbTi test are shown. Layer 1 is wound with insulated NbTi cable. 125
6.19 The assembly of coil pack into the outer aluminum shell is shown. 127

7.1 A comparison is seen between the depth dose profile of photons and the most commonly used ions for cancer therapy. (Fig. from [65]) 129
7.2 The spread-out Bragg peak (SOBP) is shown generated by a single field and by an opposing set of fields. (Fig. from [69]) 130
7.3 Active scanning of the tumor volume. (Fig. from [74]) 131
7.4 The Heidelberg Ion Therapy Center (HIT). (Fig. from [76]) 132
7.5 A schematic of PSI's proton gantry II is shown with the location of the active scanning and final bending magnet indictaed. (Fig. from [76]) 133
7.6 A curved rapid prototype mandrel is shown wound with eight strand superconducting cable. The red section was created from stacked laminations. 135
7.7 Eddy current losses in a proton therapy mandrel. (Figure courtesy of Heng Pan) 136
7.8 An illustration of the MEVION single room proton system. (Fig. from [98]) . . 137
7.9 An illustration of the NIRS superconducting carbon gantry. (Fig. from [100]) . . 138
7.10 An illustration of the ProNova SC360 superconducting proton gantry. (Fig. from [99]) 139

8.1 Bipolar coordinates $0 < \eta < \infty$ and $0 \leq \xi \leq 2\pi$ 141
8.2 The local unit tangent, normal, and binormal vectors ($\hat{t}$, $\hat{\eta}$, $\hat{b}$) are shown at location $\vec{p}$ of a parametric path constrained to the surface of a torus. 142
8.3 A path is shown patterned around the bend in integer multiples of the pitch angle ϕ_0. 143
8.4 The concavity of the CCT winding path as a function of the azimuthal toroidal angle is shown for three different tilt angles. 147
8.5 The quadrupole-like toroidal harmonic (n=2) is shown for a fixed bore radius R and increasing major radius R_0. The Legendre polynomials needed for the fields were evaluated using the DTOR algorithm [108]. As the aspect ratio of the torus $\epsilon = R/R_0$ tends to zero, the fields are seen approaching those of a straight cylindrical quadrupole. 150

9.1 An illustration of point-to-parallel optics in the horizontal plane. 153
9.2 (a) The two conductor layers optimized for the combined dipole and quadrupole fields. (b) The contribution of each layer to the transverse field on the midplane and their sum as function of distance across the bore of the straight-section. . . 154
9.3 The concavity of the CCT winding path as a function of the azimuthal toroidal angle is shown for layer 1 and layer 2 of the design. 155
9.4 Comparison of analytic (blue) and finite element (red) perpendicular rib thickness between channels is shown as a function of toroidal azimuthal angle for the winding of layer 1. 156

9.5 (a) The path of integration through the dipole. (b) The dipole harmonic as a function of distance along the path. 157
9.6 The distribution of the field at the conductor is shown for layer 1. 158
9.7 The load line and short sample is shown for the design. 159
9.8 Results for tracking through the CCT layers are shown. 161
9.9 The coordinate system for the Lorentz force results is shown. 163
9.10 The Lorentz forces of a single straight-section turn are shown as a function of azimuthal angle. 163
9.11 The Lorentz forces along the length of each layer are shown as a function of bend angle. 164
9.12 An illustration of the primary actions of the Lorentz forces along the bend of the magnet is shown. 164
9.13 The ANSYS model and locations of applied boundary conditions are shown. . . 165
9.14 The net displacement (in mm) is shown along the length, and the displacement along ρ (in mm) is shown for a central cross section. 166
9.15 The von Mises stress (in MPa) is shown along the length and for a central cross section. 167
9.16 The net displacement (in mm) is shown along the length, and the displacement along ρ (in mm) is shown for a central cross section. 167
9.17 The von Mises stress (in MPa) is shown along the length and for a central cross section. 168

10.1 A single alternating focusing quadrupole layer is shown with five sections (FDFDF). The transition scheme between sections of opposite axial period is enlarged with the current direction indicated. This scheme allows for the coil to be generated with one continuous winding, where the relative integral strength of the sections can be tuned by adjusting the number and location of transition points. 171
10.2 A diagram of the proton gantry is shown with the three locally achromatic AG-CCT bending sections (B1, B2, and B3) indicated. 172
10.3 Several proton depth ranges covered by the 25% momentum acceptance of the gantry are shown. 173
10.4 The desired SCOFF fields from Table 10.1 are shown for the 75 degree bends B1 and B2 (a) and the 90 degree bend B3 (b). 174
10.5 The four CCT layer approach to the bending sections is shown. 174
10.6 (a) A slice of the coils for the 75 degree bend. The inner two layers were designed to produce a quadrupole field and the outer two a dipole field. (b) The vertical field on the midplane produced by the windings. 176
10.7 The dipole and alternating quadrupole contributions from the CCT dipole and AG-CCT layers are shown as a function of bending angle for the 75 degree bend (a) and 90 degree bend (b). 177
10.8 The short-sample in the superconductor is shown for both the AG-CCT and CCT dipole layers of the 75 degree bend (B1,B2). 178

10.9 The short-sample in the superconductor is shown for both the AG-CCT and CCT dipole layers of the 90 degree bend (B3). 178

A.1 (a) A coil configuration is shown cut through the center of the straight-section (away from the ends). (b) The complex plane used for the harmonic expression of the transverse fields. 192
A.2 The typical form of the dipole harmonic B_1 along the length of a CCT magnet is shown with the location straight-section dipole field B_1^{SS} indicated. 193
A.3 The integrated dipole field is represented as a step function of height B_1^{SS} and magnetic length L_m. 194

C.1 The load lines for each layer of the 2 layer magnet are shown for the ungraded case (a) and the graded case (b). 199
C.2 The load lines for each layer of the 4 layer magnet are shown for the ungraded case (a) and the graded case (b). 201
C.3 The load lines for each layer of the 6 layer magnet are shown for the ungraded case (a) and the graded case (b). 203
C.4 The load lines for each layer of the 8 layer magnet are shown for the ungraded case (a) and the graded case (b). 205

List of Tables

1.1 Superconducting Magnets for Hadron Colliders 2
1.2 High Field Nb_3Sn R&D Accelerator Magnets 9

2.1 Key Analytic Results 13
2.2 Inductance of Fabricated CCT Magnets 28
2.3 Uncorrected 2-in-1 Harmonic Comparison 34
2.4 Corrected 2-in-1 Harmonic Comparison 34

4.1 CCT Layer Parameters 66
4.2 CCT Magnet Parameters 66
4.3 Assumptions for the CCT Designs 77
4.4 Assumption for Nb_3Sn Strand Cost 77
4.5 Short-Sample Summary 79
4.6 Conductor Cost Summary 79

5.1 SSC Outer NbTi Cable Parameters 84
5.2 CCT1 Mandrel Properties 85
5.3 CCT1 Conductor Use 85
5.4 CCT1: Straight-Section Harmonics from Opera3D (in units of B_1) 88
5.5 CCT1: Integrated Harmonics from Opera3D (in units) 89
5.6 CCT1 Inductance 91
5.7 CCT1 Axial Boundary Condition Results 94
5.8 CCT1 Electrical Measurements 100

6.1 60/61 RRP Nb_3Sn Wire (HD3 Coil-2) 105
6.2 Rutherford Cables for CCT2 106
6.3 CCT2 Nb_3Sn Mandrel Properties 107
6.4 CCT2 Conductor Use 107
6.5 CCT2: Straight-Section Harmonics from Opera3D (in units of B_1) 108
6.6 CCT2: Integrated Harmonics from Opera3D (in units) 110
6.7 Grading Savings for CCT2 112
6.8 Bi2212 and Nb_3Sn Mandrel Properties 112
6.9 The Two ANSYS Models 115

6.10 Max/Min Local Stress Without the HTS Insert . . . 116
6.11 Max/Min Local Stress With the HTS Insert . . . 117
6.12 CCT2 5-Turn Reaction . . . 120
6.13 SSC Inner NbTi Strand Parameters . . . 122
6.14 CCT2 64-Turn Inductance . . . 123
6.15 CCT2 64-Turn Electrical Measurements . . . 126

9.1 Proton Gantry Guidelines . . . 151
9.2 CCT Gantry Magnet Design Criteria . . . 152
9.3 Straight-Section Cylindrical Harmonics . . . 154
9.4 Gantry Magnet Rib Thickness . . . 156
9.5 SSC Inner NbTi Strand Parameters . . . 158
9.6 Radial Buildup (in mm) . . . 159
9.7 Conductor Use . . . 159
9.8 Estimated Weight . . . 160

10.1 Desired SCOFF Model Fields for the AG-CCT Bends . . . 173
10.2 Winding Mandrel Geometry (in mm) . . . 175
10.3 Post Particle Tracking: AG-CCT Split . . . 175
10.4 Short Sample at the Maximum Operating Point . . . 179

C.1 Load Line Calculation for Two Layers . . . 199
C.2 Two Layer Conductor Use: Ungraded . . . 200
C.3 Two Layer Conductor Use: Graded . . . 200
C.4 Two Layer Conductor Cost Summary . . . 200
C.5 Two Layer Short-Sample Fields . . . 200
C.6 Load Line Calculation for Four Layers . . . 201
C.7 Four Layer Conductor Use: Ungraded . . . 202
C.8 Four Layer Conductor Use: Graded . . . 202
C.9 Four Layer Conductor Cost Summary . . . 202
C.10 Four Layer Short-Sample Fields . . . 202
C.11 Load Line Calculation for Six Layers . . . 203
C.12 Six Layer Conductor Use: Ungraded . . . 204
C.13 Six Layer Conductor Use: Graded . . . 204
C.14 Six Layer Conductor Cost Summary . . . 204
C.15 Six Layer Short-Sample Fields . . . 204
C.16 Load Line Calculation for Eight Layers . . . 205
C.17 Eight Layer Conductor Use: Ungraded . . . 206
C.18 Eight Layer Conductor Use: Graded . . . 206
C.19 Eight Layer Conductor Cost Summary . . . 206
C.20 Eight Layer Short-Sample Fields . . . 206

Acknowledgments

I would first like to thank Professor Karl van Bibber for serving as an advisor to this project and as the chair of the thesis committee. I am grateful for your enthusiastic support of the research, assistance with departmental requirements, and for your thorough editing of the thesis. I would also like to thank Professors Jonathan Wurtele, Peter Hosemann, and Ka-Ngo Leung for serving on the committee and for their valuable feedback.

The majority of the work for this project was carried out at Lawrence Berkeley National Laboratory (LBNL), the support of which made this thesis possible. I would like to thank Shlomo Caspi and David Robin of LBNL for serving as advisors to the project and having a positive impact on my time as a graduate student both at and away from the lab. I thank Shlomo for inviting me to the superconducting magnet group, for teaching me superconducting magnet design, for sharing your experience building high field magnets, for always being open to the next idea, for being an innovator in the field, for your generosity away from the lab, and for your friendship. I thank Dave for first inviting me up to the lab to join the gantry group, for teaching accelerator physics, for sharing your passion to bring ion beam cancer therapy to those in need, for an endless supply of optimism, and for your friendship.

I would like to thank and acknowledge the many others at the lab who contributed to this work. Thank you to Ray Hafalia, Tom Lipton, and Nick Heys for fabrication of the mandrels and assembly of the magnets. Thank you to Jim Swanson for winding all the CCT coils by hand. Thank you to Dan Dietderich and Ian Pong for all things conductor. Thank you to Helene Felice, Etienne Rochepault, and Diego Arbelaez for help with ANSYS modeling. Thank you to Xiarong Wang, Maxim Marchevsky, and Marcos Turqueti for running the test of CCT1 at the LBNL test facility and performing the magnetic and electrical measurements. Thank you to Paul Bish and John Pucci for cryogenic support during the CCT1 test. Thank you to Arno Godeke for developments in HTS CCT magnets and the aluminum bronze mandrel material. Thank you to Weishi Wan, Changchun Sun, Andy Sessler, and Dave Robin for sharing the accelerator physics side of gantry design. Thank you to our colleagues at PSI, Marco Schippers and Alex Gerbershagen, for their valuable input in gantry design and operation. Finally, thank you to Soren Prestemon and Steve Gourlay for supporting this work during their time as group leaders of the Superconducting Magnet Group.

This work was supported by the National Science Foundation's Graduate Research Fellowship Program (GRFP).

Part I

CCT Magnets for High Energy Physics

Chapter 1

Introduction and Motivation

1.1 Motivation for high field accelerator magnets

Following the first use of superconducting main ring dipoles in the Tevatron in the 1980's, the push for higher field accelerator magnets has been driven by the needs of the next hadron collider. Figure 1.1 and Table 1.1 show the progression of these superconducting colliders [1, 2], culminating in the construction and operation of the Large Hadron Collider (LHC). The 8.3 T magnets of this machine have pushed niobium-titanium (NbTi) superconductor to its performance limit, requiring the change to a new superconducting material if higher fields are desired.

Table 1.1: Superconducting Magnets for Hadron Colliders

	First Beam	Design Field	Aperture (mm)	Conductor	Number
Tevatron	1983	4.3 T	76.2	NbTi	774
HERA	1991	5.0 T	75	NbTi	416
SSC*	N/A	6.6 T	50	NbTi	N/A
RHIC	2000	3.5 T	80	NbTi	264
LHC	2008	8.3 T	56	NbTi	1276
HL-LHC	2025	140 T/m	150	Nb_3Sn	40
		11 T	60	Nb_3Sn	40

The conductor considered for the next generation of high field magnets is niobium-tin (Nb_3Sn). Development of Nb_3Sn accelerator magnets has been largely driven by the needs of a luminosity upgrade of the LHC. This project requires close to eighty 11-12 T Nb_3Sn magnets, which are scheduled for installation in the machine in 2023 [3, 4]. These will be the first Nb_3Sn magnets operating in an accelerator, and the result of over 20 years of Nb_3Sn magnet development within the US LHC Accelerator Research Program (LARP) and the High Luminosity LHC (HL-LHC) project [5, 6].

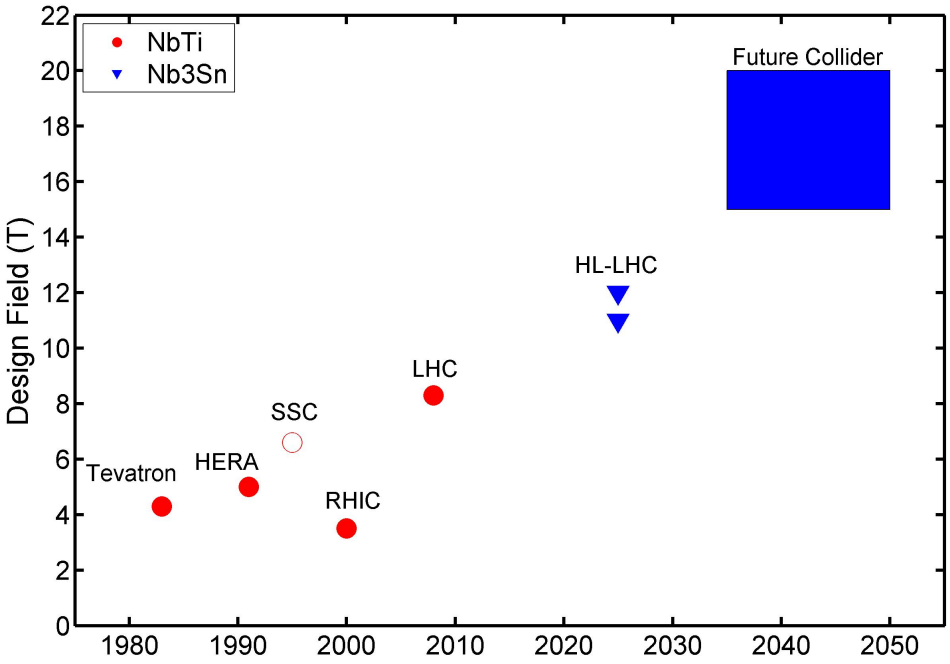

Figure 1.1: Superconducting hadron colliders.

The demand for high field Nb_3Sn accelerator magnets beyond the luminosity upgrade of the LHC is driven by the prospect of a future hadron collider. An investigation of the feasibility and cost of such a machine has begun as part of the Future Circular Collider (FCC) Study [4, 7, 8, 9]. The goal of the FCC study is to produce a conceptual design for a future machine by 2018. One option being considered is a 100 TeV pp collider with either 16 T dipoles in a 100 km ring or 20 T dipoles in a 80 km ring (see Fig 1.2). The approval of such a machine would generate large demand for Nb_3Sn magnets with 4-8 T higher field than those developed for the HL-LHC.

Advancing Nb_3Sn magnet technology to the 16-20 T field level desired for a future collider is an extremely challenging undertaking. One of the most difficult aspects of high field superconducting magnet design is managing the Lorentz forces within the magnet (which scale with the square of the magnetic field). Section 1.3 will describe how the combination of rapidly increasing Lorentz forces and strain-sensitive Nb_3Sn conductor appears to limit the traditional magnet design to a field near 14-15 T. This design is the called the "cosine-theta", and has been used for all superconducting accelerator magnets operating in hadron colliders to date (including the planned HL-LHC upgrade).

Several other high field Nb_3Sn magnet design concepts have been proposed and tested, such as the "common-coil", "block", and "stress-managed block" (see [10] for an overview

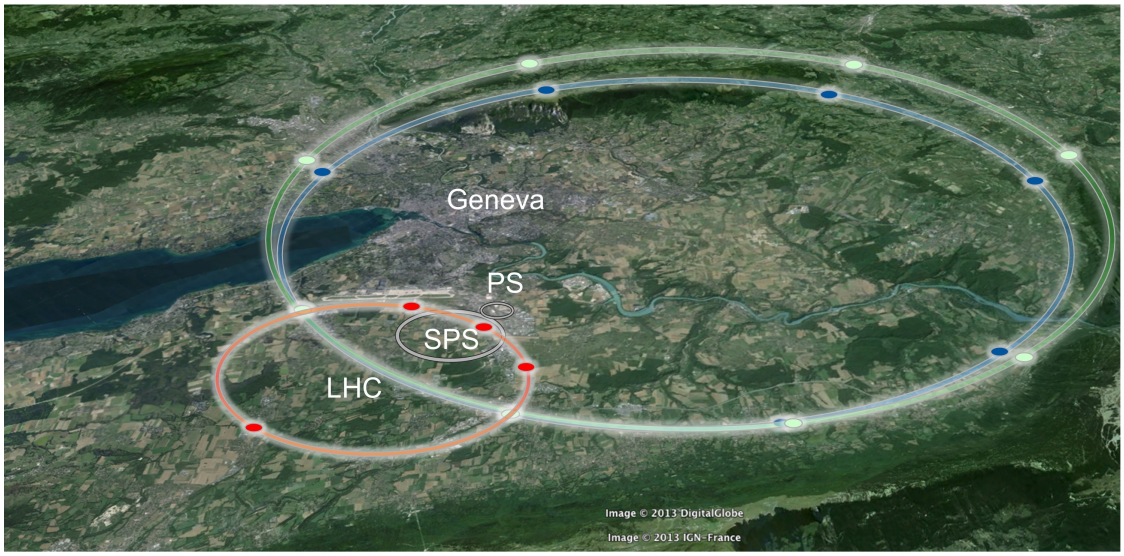

Figure 1.2: Future pp collider options within the FCC study. (Fig. from [4])

of magnet options for the FCC). As of yet, there is no magnet that has shown performance at FCC field levels. Given the long length of time before a potential collider may be built, it is important to keep "all options on the table" and to pursue new ideas showing promise to overcome the challenges of traditional designs. One such idea is the "Canted-Cosine-Theta" (CCT) design, not yet investigated for high field, which shows the potential to overcome the Lorentz force issue. Part I of this thesis will present analysis of the CCT design and a proof-of-principle test, laying the ground work necessary for a test of its performance at very high field. Section 1.2 will present an introduction to the CCT design, followed by an explanation of its perceived advantages for high field in Section 1.3. The history of the CCT concept and scope of the thesis will then be presented in Section 1.4.

1.2 Introduction to the CCT concept

The Canted-Cosine-Theta (CCT) concept is based on pairs of conductor layers wound and powered such that their transverse field components sum and axial (solenoidal) field components cancel. Figure 1.3 shows two layers of conductor windings of opposite tilt for the generation of a dipole field. When powered so the current flows in the direction indicated in the figure, the dipole field contribution from the individual layers sum and the solenoid contributions cancel. As will be described in mathematical detail in Chapter 2, this CCT approach can also be used to produce higher order cylindrical harmonics (quadrupole, sex-

tupole, etc.) or a mix of several harmonics as desired for a combined function magnet.

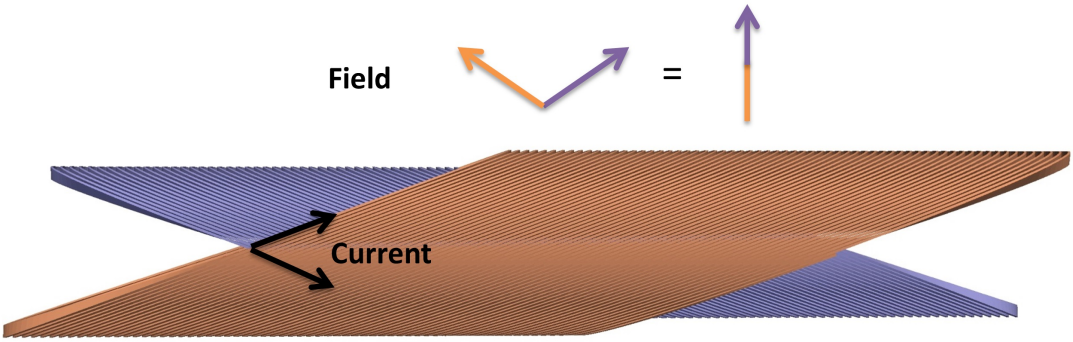

Figure 1.3: Two layers of CCT dipole conductor windings are shown powered such that their transverse fields sum and solenoidal fields cancel.

CCT magnets are constructed using a winding mandrel approach. A mandrel for each conductor layer is created by machining a continuous channel into a thick walled metal cylinder, leaving behind ribs and a spar (Fig. 1.4). The mandrel for each layer is wound with cabled conductor, put through the heat treatment reaction (if Nb_3Sn conductor is used), and then epoxy impregnated. After this, the cylindrical layers can be nested one inside the other to create a multi-layer CCT magnet in a modular process. Aside from positioning the conductor for reaction and impregnation, these mandrels provide structural support against the operating Lorentz forces. The ribs between individual conductor turns prevent the accumulation of forces and the spars provide rigidity to reduce coilpack bending. Section 1.3 will present this structural support as a key advantage for high field dipoles, where traditional magnet designs are challenged by the combination of large Lorentz forces and strain sensitive Nb_3Sn.

1.3 Motivation for high field Nb_3Sn CCT dipoles

Lorentz forces and conductor motion

The conductor of a superconducting magnet carries current in the magnetic field it generates, experiencing a Lorentz force density $\vec{f} = \vec{j} \times \vec{B}$. This force is proportional to the current density and field within the conductor and can be seen plotted for an idealized 2D dipole current distribution in Figure 1.5. It is seen that the primary effect of the Lorentz forces within a dipole magnet is to compress the coil from the pole down towards the midplane.

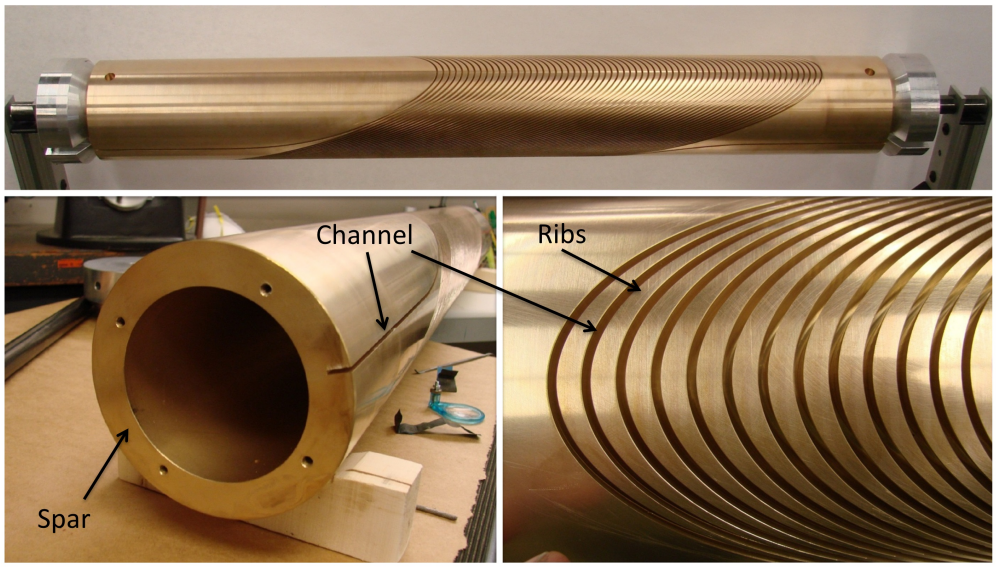

Figure 1.4: A CCT winding mandrel is shown. Rectangular channels are machined into a metallic cylinder to produce a mandrel with ribs and a spar. These channels position Rutherford cable for field quality, and the spars and ribs provide structural support at the single conductor turn level.

These forces can cause movement of the conductor during energization of the magnet which has negative effects. Friction or cracking resulting from movement releases energy which raises the temperature of the superconductor and can cause the magnet to quench.

Because the heat capacity of metals is extremely low at cryogenic temperatures, it takes very little deposited energy (in the millijoule to microjoule range) to raise the temperature to the point where a quench is induced. An in-depth study modeling these friction induced quenches, which is also correlated to data from Nb_3Sn accelerator magnet tests, can be found in [11]. Movement of the conductor is also undesirable due to the generation of magnetic field errors. To achieve accelerator level field quality the location of each conductor has to be controlled to the sub-millimeter level. For these reasons, to limit quenches and field errors, an important aspect of superconducting magnet design is the prevention of conductor motion due to Lorentz forces.

Pre-stress to prevent conductor motion

To prevent conductor movement due to Lorentz forces, traditional superconducting magnet designs use an external structure to compress the conductor before energization of the magnet. This squeezing during assembly is called “pre-stress” and its primary function is to put all the conductor in the magnet into compression before current is applied. Then, as the magnet is energized, the Lorentz forces unload into this compression. If the initial pre-stress

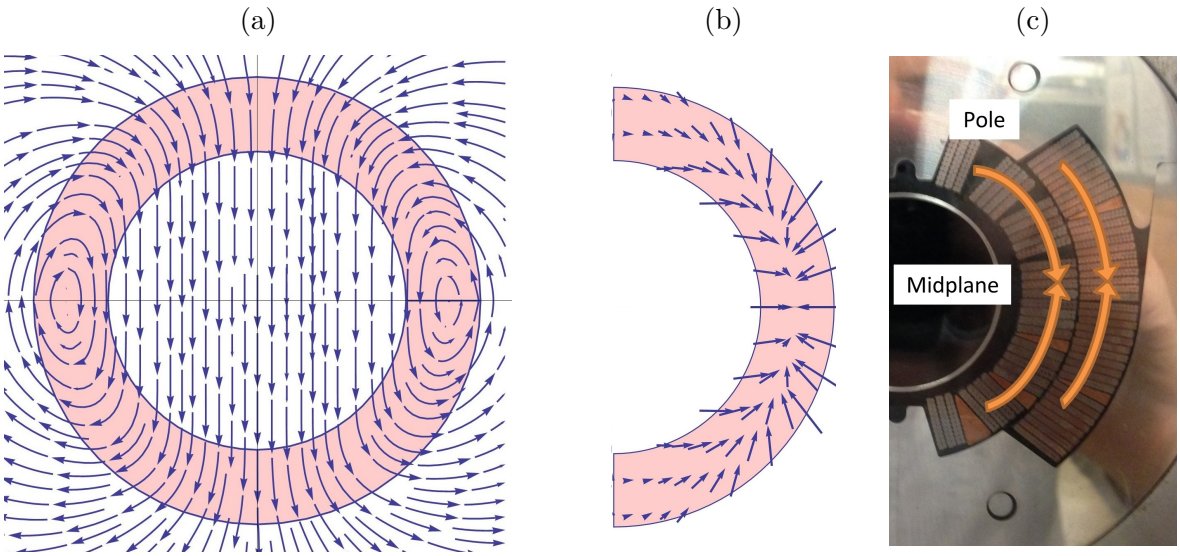

Figure 1.5: (a) The magnetic field generated by an idealized 2D dipole current density. (b) The direction and magnitude of the resultant Lorentz forces within the winding. (c) The primary effect of the Lorentz forces in a dipole is to compress the coil from the pole down to the midplane, which is illustrated on a traditional cosine-theta dipole magnet cross section.

is large enough, the unloading effect of the Lorentz force will be taken up by the pre-stress and prevent any part of the conductor from going into tension. In particular, having enough pre-stress to keep the entire coil in compression prevents the conductor from breaking away from the structure in the pole region (see Fig. 1.5c). Examples of conductor pre-stress and unloading under Lorentz forces can be seen in Figure 1.6, where the stress in the pole region is shown as a function of magnet current for the main dipoles in each of the superconducting hadron collider projects. It is seen that all have been designed with sufficient pre-stress (value at "After-cooldown") such that at the maximum current and Lorentz force (value at "100% Fnom") the conductor does not unload into tension.

Pre-stress is critical to traditional superconducting magnet design, and has been used for the main dipoles in every superconducting hadron collider to date (Tevatron [13], HERA [14], SSC - design only [15, 16], RHIC [17], and the LHC [18]). Pre-stress is traditionally applied using large presses and steel collars, as shown in Figure 1.7, and more recently using an innovative key, bladder, and shell structure developed in the US LARP program [19]. The amount of pre-stress required is dependent on two things: the order of the Lorentz force in individual conductors (scaling with B^2), and how the forces from these individual conductors accumulate within the magnet (unique to the geometry and design of the magnet). In traditional magnet designs there is a tendency for the Lorentz forces to accumulate down from the pole region to midplane, requiring a pre-stress of the order of the sum of the contributions of all conductor turns in that region. As will be discussed, a key advantage of

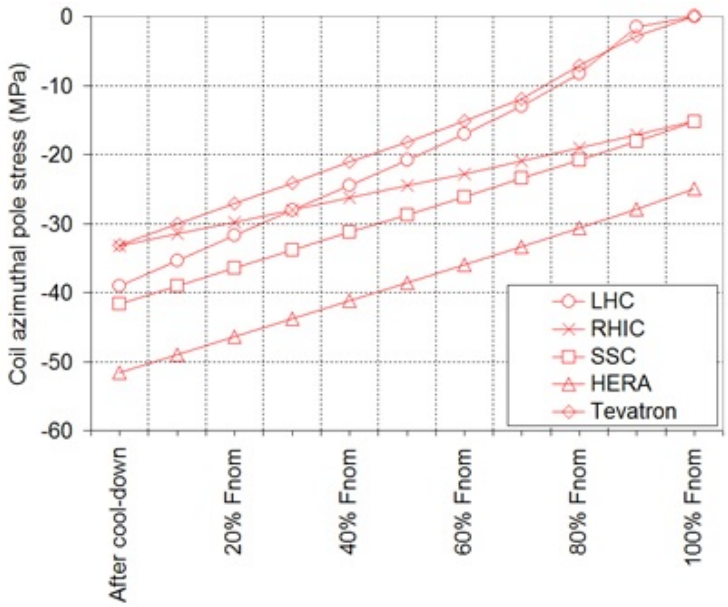

Figure 1.6: The azimuthal stress at the pole region of the superconducting magnet is shown as the current (and Lorentz force) increases towards the nominal operating value for each of the superconducting hadron colliders. The initial compression "After cool-down" is the applied pre-stress. The conductor at the pole is seen unloading towards tension as the magnet is energized, but the applied pre-stress is chosen such that the coil never goes into tension and remains in compression at the nominal current. (Fig. from [12])

the CCT design is the introduction of ribs between individual conductors that prevent the accumulation of Lorentz forces and eliminate the need for a large pre-stress.

Limits of pre-stress for Nb_3Sn

To date, all superconducting magnets in hadron colliders have used NbTi conductor. The capabilities of this material have been pushed to the limit in the 8 T LHC dipole magnets, beyond which requires a change to a conductor that can carry high current densities above 8 T. Currently, the best conductor option for the next generation of high field accelerator magnets is Nb_3Sn. This conductor is inherently more difficult to work with than NbTi due to requiring a heat treatment reaction to be made superconducting. This reaction causes the material to lose its ductility and become brittle. For this reason, most Nb_3Sn accelerator magnet coils are wound (while still ductile) and then put through the heat treatment reaction.

The performance of post reaction Nb_3Sn is strain sensitive due to its brittle nature. Strain causes degradation of the conductor's ability to carry current, which is recoverable up to a limit where the damage becomes permanent. Of critical importance to high field magnet design is the performance of cabled Nb_3Sn conductor under transverse pressure, which is

(a) (b)

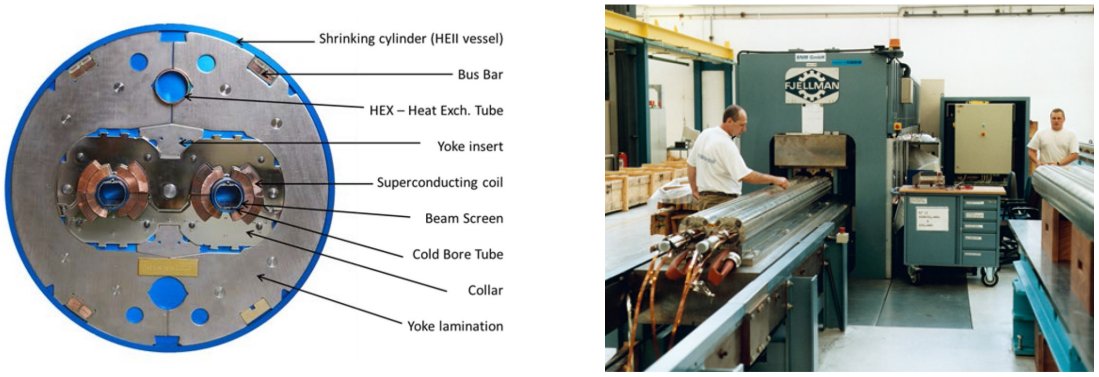

Figure 1.7: (a) A cross section of the LHC main dipole with the location of the collars indicated. (b) A 15 m pneumatic press at CERN capable of applying 21 tons/m of force to the coil assembly. Presses like this were used in combination with the collars to pre-stress the LHC main dipole coils before being assembled into the iron yoke and additional structure. (Fig. from [20])

the direction aligned with azimuthal Lorentz forces (see Fig. 1.5c) and thus also the applied pre-stress. Through a combination of cable measurements [21, 22, 23] and magnet tests, for example the LARP TQSO3 variable pre-stress experiment [24], it is generally accepted that the limit of pre-stress that can be applied to Nb_3Sn without significant degradation is between 150 and 200 MPa. Today's high field Nb_3Sn R&D magnets are designed with a peak conductor stress nearing this limit. Table 1.2 lists this peak conductor stress for several of today's high field R&D accelerator magnets. It is seen that the traditional approaches to high field accelerator magnet design have reached the conductor stress limit, and it would desirable to have a new and fundamentally different magnet concept for Nb_3Sn that is not stress limited.

Table 1.2: High Field Nb_3Sn R&D Accelerator Magnets

	Function	Aperture (mm)	Max Cond. Field (T)	Max Cond. Stress (MPa)
QXF	Quadrupole	150	12.1	180
FNAL 11T	Dipole	60	11+	160
FRESCA2	Dipole	100	13.2	150
HD2	Dipole	36	15.8	180

Peak conductor stress in the design of several of today's high field Nb_3Sn R&D magnets is given [25, 26, 27, 28, 29].

Reduction of conductor stress in the CCT design

The CCT is a new design concept for high field accelerator magnets that shows promise to overcome the stress limitations of the traditional designs. In the CCT, each conductor turn sits in its own channel machined into a metal winding mandrel (Fig. 1.4) such that it is separated from the adjacent turn by a metallic rib. These ribs between turns "intercept" the Lorentz forces and transfer them to the mandrel, preventing accumulation of Lorentz forces across multiple turns. This leads to an order of magnitude reduction in the peak conductor stress, and because the turns are individually supported there is minimal need for pre-stress. Figure 1.8 illustrates stress interception in the CCT compared to accumulation in a traditional cosine-theta design. While the CCT has many other features that will be discussed in further detail, the fundamental motivation for investigating the CCT design for high field Nb_3Sn dipoles is the promise to overcome the conductor stress limitations of today's technology.

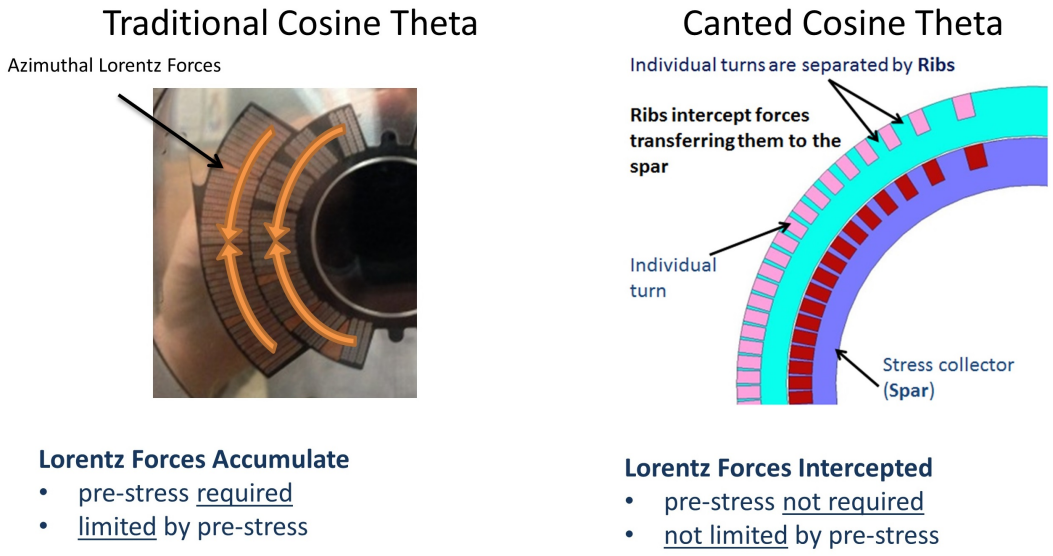

Figure 1.8: A comparison of Lorentz force interception in a CCT vs. accumulation in a traditional cosine-theta design.

1.4 History of the CCT and scope of the thesis

In the first published record of the design in 1970, Donald Meyer proposed the tilted winding concept for a high energy physics dipole magnet [30]. Professor Meyer, from the Physics Department of the University of Michigan, worked in collaboration with high energy physics experiments at Fermilab and suggested this tilted winding approach for the simplicity of its

construction and desirable field quality. Following this lone publication the idea lay dormant for many years until the early 2000's. At this time there was investigation by both industry and national laboratories into the tilted winding concept, likely without knowledge of Meyer's original publication. This research was focused primarily on the magnetic properties of the design, with a key development being the formulation for tilted windings capable of producing higher order harmonics or combined function fields [31, 32, 33, 34, 35, 36, 37, 38, 39, 40].

Previous work was focused on low field applications using NbTi conductor in the single strand form. There are two published superconducting magnet test results, both of which had maximum fields of less than 2 T [35, 37]. The scope of the high energy physics portion of this thesis is to investigate and develop the CCT concept for high field Nb_3Sn magnets. This involves developing the level of understanding, modeling capabilities, and construction methods required for a 16-18 T dipole magnet. Of particular importance for high field CCT design is structural analysis, for which there is no previously published research. A key component of the development is to design, build, and test a superconducting CCT magnet in a configuration that scales to high field. This may use NbTi conductor, but would be the first to test key aspects of a high field CCT. In particular, this prototype would implement Rutherford cables for high current density and machined mandrels for stress interception, serving as a proof-of-principle test before making the investment in a high field Nb_3Sn CCT dipole.

Part I of this thesis presents an investigation of the CCT design for high field accelerator magnets. Chapter 2 begins with the development of an analytic formulation for the design. In Chapter 3 methods for finite element modeling are presented, followed by a discussion of design optimization for high field in Chapter 4. The design, fabrication, and test of CCT1 (a 2.5 T proof-of-principle dipole) is then presented in Chapter 5. Finally, Chapter 6 details the design of the 16 T Nb_3Sn dipole CCT2 and reports on initial steps taken in a program towards the test of a 16 T CCT magnet.

Chapter 2

Analytic Modeling

2.1 Goals and overview

This chapter develops new analytic formulations capable of accurately predicting the relation between CCT windings and the fields they create. Of particular interest is to use these relations to solve the so called "inverse problem", to gain the capability to generate a set of CCT windings based on a desired field. A formulation will be developed that generalizes CCT windings to a parametric path, averages them into a current density, and relates this current density to the magnetic field in the bore. It will be shown that this process can be used in reverse order to generate CCT windings that produce single, or a combination of multiple, field harmonics (e.g. dipole, quadrupole, sextupole, etc.). This allows for excellent field quality to be obtained using simple winding formulas, avoiding numerical optimization of conductor position common to the design of traditional superconducting magnets (see, for example, the program ROXIE [41]).

One benefit of an analytic formulation is the ability to gain insight into the effect of free parameters (design choices), which will be used to develop an approach to CCT design optimization in Chapter 4. The formulation is also useful for the generation of the geometry of the conductor winding. This will be used to pass the conductor geometry to finite element codes for magnetic and structural analysis, to be further discussed in Chapter 3, and to CAD software as needed for the construction of the magnet itself. This chapter will focus on the development of the analytic formulation for the CCT design starting with a single layer and moving on to a multi-layer CCT magnet.

The magnetic field to winding relation will first be developed for a current sheet model general to any desired multipole. Then a magnetic vector potential based on current sheets will be introduced to find expressions for the fields, stored energy, and inductance of a multi-layer CCT magnet. This same approach will then be applied to the cancellation of cross-talk in a dual bore CCT magnet as desired for high energy hadron colliders. After this, the focus will shift to expressions for a multi-layer CCT dipole using a cable of non-zero radial thickness. The Lorentz force induced pressure (approximate stress) within such a dipole will

be derived. Finally, any approximations made will be discussed with a focus on situations where finite element methods should be used for increased accuracy.

Following this development, the straight-section symmetry of the CCT will be introduced. This symmetry is 3D and axially periodic, which is significantly different from the straight-section symmetry of traditional designs. This difference requires the development of new boundary conditions. Magnetic boundary conditions for the symmetry region will be specified. Three different axial boundary conditions for structural modeling using the CCT symmetry will also be presented, with a discussion of test configurations to which they are applicable. Methods for implementing these boundary conditions in finite element modeling will be developed in Chapter 3. A summary of key developments in this chapter and their location can be found in Table 2.1.

Table 2.1: Key Analytic Results

Winding Path	Generalized	Eqn: 2.9, 2.11
	Dipole	Eqn: 2.15
	Quadrupole	Eqn: 2.18
	Combined Function	Eqn: 2.20
Current	Single Sheet	Eqn: 2.6, 2.12
	Multi-Sheet	Eqn: 2.21
Vec. Potential	Multi-Sheet	Eqn: 2.23, 2.24
Magnetic Field	Current Sheet	Eqn: 2.25, 2.26
	Thick Winding	Sec: 2.5
	2-in-1	Sec: 2.4
Force, Pressure	Thick Winding	Sec: 2.6
Stored Energy	Multi-Sheet	Eqn: 2.50, 2.51
Inductance	Multi-Sheet	Eqn: 2.51
3D Symmetry	Magnetic B.C.	Eqn: 2.86
	Mechanical B.C.	Eqn: 2.87, 2.89, 2.89

2.2 Winding path to field relation for a CCT layer

Definition of the parametric path

The starting point for the definition of a CCT layer is a parametric path constrained to the surface of a cylinder as shown in Figure 2.1. This path can be parameterized in terms of the azimuthal angle by position

$$\vec{p}(\theta) = r\hat{r} + p_z(\theta)\hat{z}, \tag{2.1}$$

where r is the radius of the cylinder, θ is the azimuthal angle, and $p_z(\theta)$ is yet undefined function of θ which describes the axial movement of the path. It is useful to define a local reference frame at location $\vec{p}(\theta)$ such that $\hat{t}$ is tangential to the path, $\hat{r}$ is in the radial direction, and $\hat{b}$ completes the orthogonal system (Fig. 2.1). Vectors in these directions are given by

$$\vec{t}(\theta) = \frac{d\vec{p}}{d\theta} = r\hat{\theta} + p_z'(\theta)\hat{z} \tag{2.2}$$

$$\vec{b}(\theta) = \vec{t} \times \hat{r} = p_z'(\theta)\hat{\theta} - r\hat{z}. \tag{2.3}$$

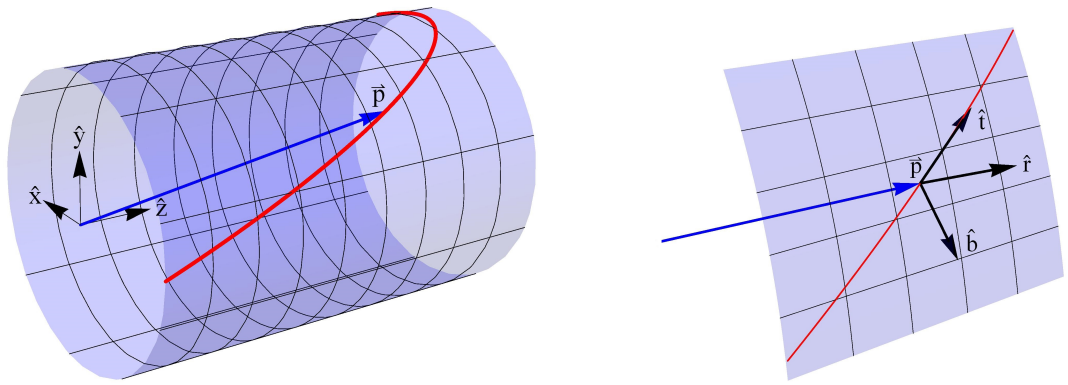

Figure 2.1: The local unit tangent, radial, and binormal vectors ($\hat{t}$, $\hat{r}$, $\hat{b}$) are shown at point $\vec{p}$ of a parametric path constrained to the surface of a cylinder.

A periodic function for $p_z(\theta)$

It is seen that the choice of the axial position function $p_z(\theta)$ is sufficient to define both the path and all local coordinate frame directions. It is desirable for the path to contain a symmetry such that it can be repeated axially to create a uniform region away from the start

and end points of repetition. This is accomplished by requiring the axial distance between adjacent repetitions of the path be a constant for all points (independent of θ), meaning

$$|p_z(\theta + 2\pi) - p_z(\theta)| = w, \tag{2.4}$$

where the pitch w is defined as the constant axial distance between paths (Fig. 2.2). It can be shown that the perpendicular distance between adjacent paths $\delta(\theta)$ (in the direction of $\hat{b}$) is approximated by

$$\delta(\theta) = w\hat{z} \cdot \hat{b} = \frac{wr}{|\vec{t}|} = \frac{w}{\sqrt{1 + p_z'(\theta)^2/r^2}}. \tag{2.5}$$

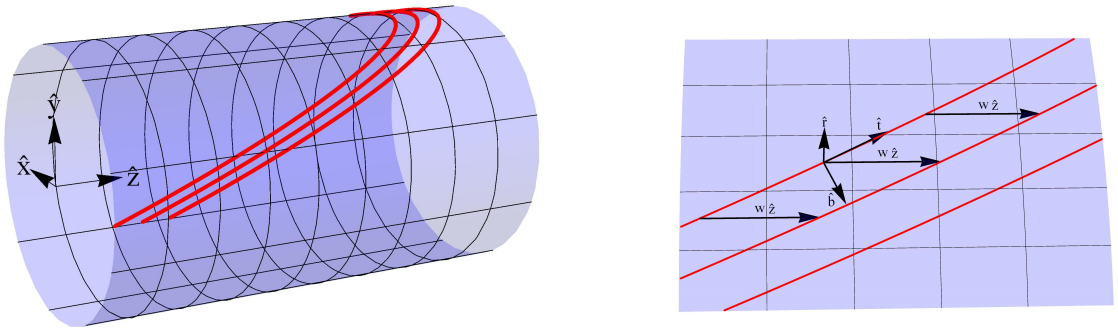

Figure 2.2: A path is shown patterned axially in integer multiples of the pitch length w. This periodic symmetry condition requires the pitch length be constant for all azimuthal angles, and is represented in the figure by the vector $w\hat{z}$ pointing axially between adjacent paths.

A pitch averaged current density

If the path $\vec{p}(\theta)$ represents a continuous line current of magnitude I_0, the perpendicular spacing (Eqn. 2.5) can be used to average the line currents into a 2D cylindrical current sheet with current density

$$\vec{j}(\theta) = \frac{I_0\hat{t}}{\delta(\theta)} = I_0\frac{\vec{t}}{|\vec{t}|}\frac{|\vec{t}|}{wr} = \frac{I_0}{wr}\vec{t} = \frac{I_0}{w}\left(\hat{\theta} + \frac{p_z'(\theta)}{r}\hat{z}\right). \tag{2.6}$$

The current consists of two components: a constant azimuthal portion (generating solenoidal fields) dependent on the pitch, and an axial portion varying with azimuthal angle (generating transverse fields) determined by $p_z'(\theta)$. Because the axial current's azimuthal variation is completely determined by $p_z'(\theta)$, this current expression can be used to derive an axial path expression $p_z(\theta)$ to produce the desired transverse fields.

Relation of current density to magnetic field

It is well known that a cylindrical sheet of axial current at fixed radius r with azimuthal variation $j_z(\theta) = j_{0nz}\cos(n\theta)$ produces a pure "nth" order cylindrical field harmonic within the bore (for example see [42]). The relation between the magnitude of the current j_{0nz} and the generated field harmonic B_n is given by

$$B_n = -\frac{\mu_0 j_{0nz}}{2}\left(\frac{R_{ref}}{r}\right)^{n-1}, \tag{2.7}$$

where r is the radius of the current sheet and R_{ref} is the reference radius for the harmonic description (see Appendix A). To produce cylindrical harmonics with a CCT, the axial component of the pitch averaged current density in Equation 2.6 is related to the ideal $\cos(n\theta)$ current,

$$\frac{I_0}{wr}p_z'(\theta) = j_{0nz}\cos(n\theta). \tag{2.8}$$

It is seen that the yet undetermined function of the parametric path $p_z(\theta)$ is easily related to the desired harmonic through integration such that

$$p_z(\theta) = \frac{wr}{I_0}\frac{j_{0nz}}{n}\sin(n\theta) + \frac{w}{2\pi}\theta, \tag{2.9}$$

where second term in the equation is required to satisfy the specified condition of a continuous path with axial periodicity of pitch length w (see Eqn. 2.4).

Equation 2.9 combined with the definition of the parametric path in Equation 2.1, using the parametric variable $0 \leq \theta \leq 2\pi n_t$, can be used to draw a continuous CCT winding path with n_t turns to generate cylindrical harmonics far from the end effects of the windings. There are three parameters needed for a CCT layer at a fixed radius: I_0, j_{0nz}, and w. In practice it is advantageous to relate the free parameters (design choices) to the physical properties of the path itself. This can be done by defining a midplane tilt angle α, such that

$$\tan(\alpha) \equiv \left.\frac{\vec{t}\cdot\hat{\theta}}{\vec{t}\cdot\hat{z}}\right|_{\theta=0} = \frac{I_0}{wj_{0nz}}, \tag{2.10}$$

where the assumption that the radius is much larger than the pitch ($r \gg w$) is made. With this assumption the path can be written in terms of two free physical parameters, the tilt angle α and the axial pitch length w,

$$p_z(\theta) = \frac{r\cot(\alpha)}{n}\sin(n\theta) + \frac{w}{2\pi}\theta. \tag{2.11}$$

The current density for this path is then given by

$$\vec{j}(\theta) = \frac{I_0}{w}\left(\hat{\theta} + \frac{p_z'(\theta)}{r}\hat{z}\right) = \frac{I_0}{w}\left(\hat{\theta} + \left[\cot(\alpha)\cos(n\theta) + \frac{w}{2\pi r}\right]\hat{z}\right). \tag{2.12}$$

It is important to note a single layer contains three distinct currents: a constant azimuthal current which generates a solenoidal field inside the winding, a $\cos(n\theta)$ axial current which produces transverse harmonics, and a constant axial current which produces an azimuthal field outside the winding. As will be shown, the CCT uses multiple layers to cancel the solenoidal field within the bore and leave only the desired transverse harmonics. The magnitude of the harmonic generated by a single layer using the path in Equation 2.11 is then given by

$$B_n = -\frac{\mu_0 I_0}{2w}\cot(\alpha)\left(\frac{R_{ref}}{r}\right)^{n-1}. \tag{2.13}$$

In practice it is simpler to describe the field independently of the reference radius used in the harmonic representation. This is done by normalizing the coefficient to the reference radius,

$$B_n^* = \frac{B_n}{R_{ref}^{n-1}} = -\frac{\mu_0 I_0}{2w}\cot(\alpha)\frac{1}{r^{n-1}}, \tag{2.14}$$

which corresponds to a polynomial fit of the midplane field using $B_n^* r^{n-1}$. In this case the dipole field is given by B_1^*, the quadrupole gradient by B_2^*, and so on.

Example 1: a dipole layer (n=1)

The path for a CCT dipole layer is given by the $n = 1$ case of Equation 2.11 with Equation 2.1,

$$\vec{p}(\theta) = r\hat{r} + \left[r\cot(\alpha)\sin(\theta) + \frac{w}{2\pi}\theta\right]\hat{z}, \tag{2.15}$$

producing a dipole field within the bore of magnitude

$$B_1 = -\frac{\mu_0 I_0}{2w}\cot(\alpha). \tag{2.16}$$

A solenoidal field is also produced, given by

$$B_z = \mu_0 j_\theta = \frac{\mu_0 I_0}{w}. \tag{2.17}$$

Seventy-five turns of this path for a radius of 25 mm, tilt angle α of 20 deg, and pitch w of 6.96 mm are shown in Figure 2.3.

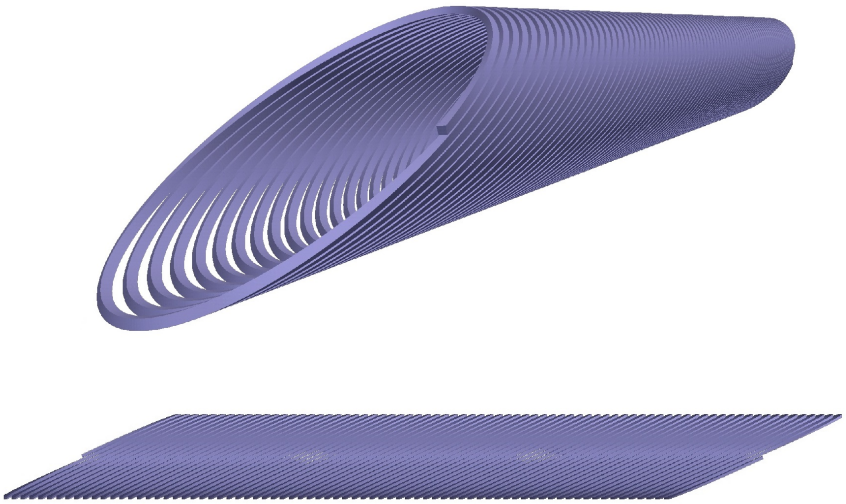

Figure 2.3: Two views of the conductor path for a CCT dipole layer are shown.

Example 2: a quadrupole layer (n=2)

The path for a CCT quadrupole layer is given by the $n = 2$ case of Equation 2.11 with Equation 2.1,

$$\vec{p}(\theta) = r\hat{r} + \left[\frac{r\cot(\alpha)}{2}\sin(2\theta) + \frac{w}{2\pi}\theta\right]\hat{z}, \tag{2.18}$$

producing a quadrupole field within the bore with gradient

$$B_2^* = -\frac{\mu_0 I_0}{2w}\frac{\cot(\alpha)}{r}. \tag{2.19}$$

Seventy-five turns of this path for a radius of 25 mm, tilt angle α of 20 deg, and pitch w of 7.163 mm are shown in Figure 2.4.

Example 3: A combined function dipole and quadrupole layer

The path for a combined function CCT layer is best described using the ratio of the desired harmonics. For example, a dipole with a quadrupole component added can be written as

$$\vec{p}(\theta) = r\hat{r} + \left[r\cot(\alpha)\sin(\theta) + \frac{B_2^* r}{2B_1^*}r\cot(\alpha)\sin(2\theta) + \frac{w}{2\pi}\theta\right]\hat{z}, \tag{2.20}$$

where B_2^*/B_1^* is the ratio of the desired quadrupole gradient to main dipole. Here special attention has to be paid to the meaning of the tilt angle α as Equation 2.10 is not as straight forward for multiple current components.

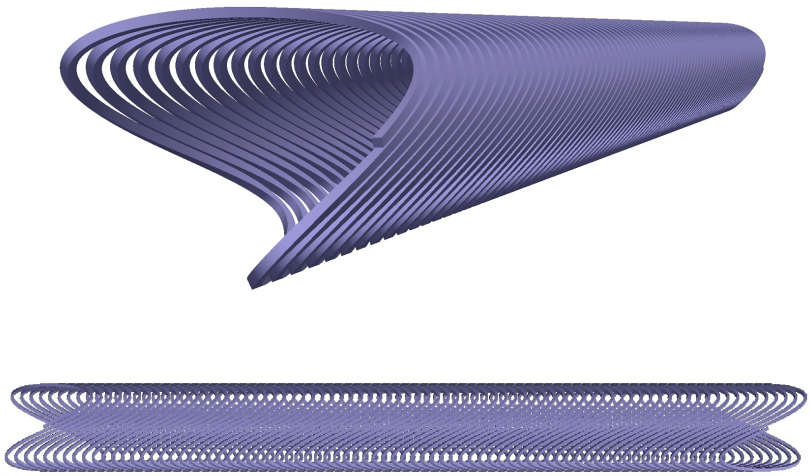

Figure 2.4: Two views of the conductor path for a CCT quadrupole layer are shown.

Extension to a multi-layer magnet

As seen in Equation 2.12, the CCT has two currents that do not produce desired transverse harmonics. The constant azimuthal current produces a solenoidal field inside of the windings, and the constant axial current produces an azimuthal field outside of the windings. A multi-layer approach is used to cancel these undesirable fields. This approach uses pairs of CCT layers where the sign of the tilt angle and direction of current is changed between layers (see Figures 2.5 and 2.6). In this configuration the transverse harmonics produced by each layer sum, while the solenoidal and azimuthal fields cancel (to be shown in Section 2.3).

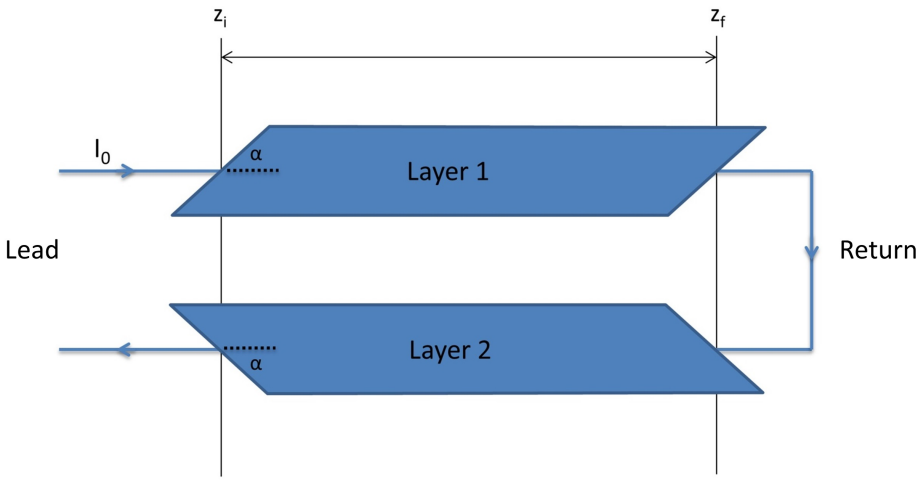

Figure 2.5: A schematic showing the configuration for canceling undesired fields using a pair of CCT layers.

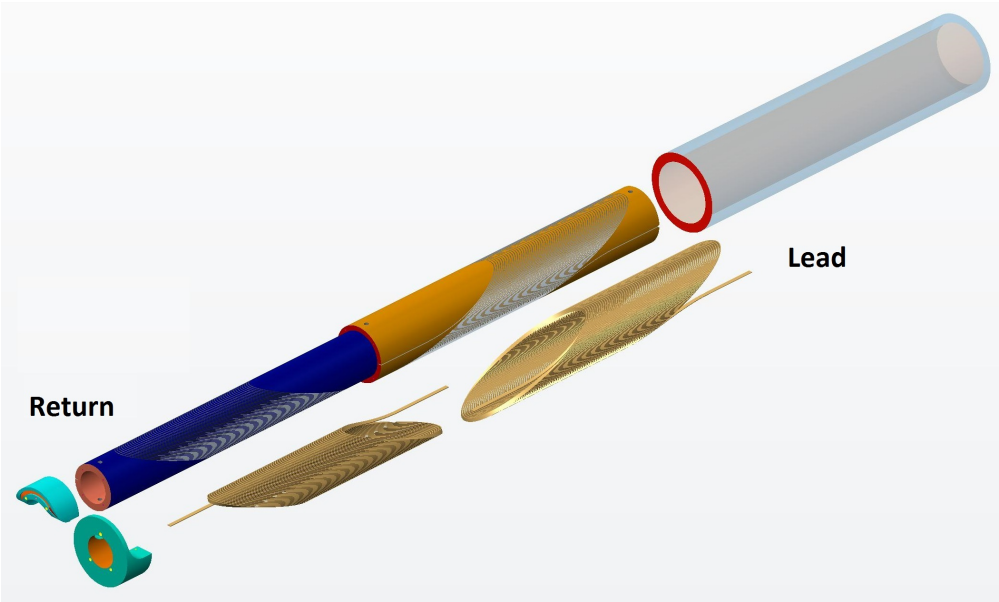

Figure 2.6: A CAD assembly of a pair of CCT layers is shown with angles and current directions as diagrammed in Figure 2.5. The green splice box on the left connects (splices) layer 1 and layer 2 on the return end.

2.3 A vector potential model for a multi-layer CCT: fields, stored energy, and inductance

Section 2.2 averaged the current path of a single CCT layer into a current sheet density, which was then used to find the winding to field relation. Here the current sheet model will be extended to a multi-layer CCT magnet by finding the associated magnetic vector potential. Expressions for the magnetic field, stored energy, and inductance of a "n" harmonic CCT magnet will be derived from this potential.

Finding the vector potential

As seen in Equation 2.12, the equivalent sheet current for a CCT layer is described by three components. These are: a constant azimuthal current, a cos(nθ) axial current, and a constant axial current. If the assumption of alternating tilt angle and current between layers is made, the sheet current density for the "ith" layer of a CCT magnet is

$$\vec{j}_i(\theta) = \frac{I_0}{w}\left((-1)^{i-1}\hat{\theta} + \left[\cot(\alpha)\cos(n\theta) + (-1)^{i-1}\frac{w}{2\pi a_i}\right]\hat{z}\right), \tag{2.21}$$

where a_i is the fixed radius of the layer. The variable r, which previously denoted the radius of the current layer, will now be used for the location at which the field is calculated.

Appendix B derives a magnetic vector potential for a sheet current density containing each of the three current components found in the CCT. By comparison, the current coefficients in Equations B.12, B.17, and B.22 for a CCT layer are given by

$$\begin{aligned} j_{0\theta} &= (-1)^{i-1}\frac{I_0}{w} \\ j_{0zn} &= \cot(\alpha)\frac{I_0}{w} \\ j_{0z} &= (-1)^{i-1}\frac{I_0}{2\pi a_i}. \end{aligned} \tag{2.22}$$

The vector potential resulting from the "ith" CCT layer is then defined by an azimuthal component

$$\vec{A}_{\theta i}(r) = \frac{\mu_0 I_0}{2w}(-1)^{i-1}\begin{cases} r & r < a_i \\ \frac{a_i^2}{r} & r > a_i \end{cases}, \tag{2.23}$$

and axial component

$$\vec{A}_{zi}(r,\theta) = \frac{\mu_0 I_0}{2w}\begin{cases} \cot(\alpha)\frac{a_i}{n}\left(\frac{r}{a_i}\right)^n\cos(n\theta) - (-1)^{i-1}\frac{w}{\pi}\log(a_i) & r < a_i \\ \cot(\alpha)\frac{a_i}{n}\left(\frac{r}{a_i}\right)^{-n}\cos(n\theta) - (-1)^{i-1}\frac{w}{\pi}\log(r) & r > a_i \end{cases}. \tag{2.24}$$

The net vector potential for a multi-layer CCT magnet can be found by a summation of the contribution from individual layers (i.e. a sum over "i").

Multi-layer magnetic fields

The magnetic field generated by a single layer is found using $\vec{B} = \nabla \times \vec{A}$, Equation 2.23, and Equation 2.24. A single CCT layer generates three fields: a solenoidal field inside, transverse harmonics inside, and a constant azimuthal field outside. The field generated by the "ith" layer $\vec{B}_i$ is given by

$$\vec{B}_i(r,\theta) \equiv \begin{pmatrix} \hat{r} & \hat{\theta} & \hat{z} \end{pmatrix} \begin{pmatrix} B_{ri} \\ B_{\theta i} \\ B_{zi} \end{pmatrix}, \tag{2.25}$$

where

$$\begin{pmatrix} B_{ri} \\ B_{\theta i} \\ B_{zi} \end{pmatrix} = -\frac{\mu_0 I_0}{2w} \begin{pmatrix} \cot(\alpha) \left(\frac{r}{a_i}\right)^{n-1} \sin(n\theta) \\ \cot(\alpha) \left(\frac{r}{a_i}\right)^{n-1} \cos(n\theta) \\ 2(-1)^i \end{pmatrix} \qquad r < a_i \tag{2.26}$$

and

$$\begin{pmatrix} B_{ri} \\ B_{\theta i} \\ B_{zi} \end{pmatrix} = -\frac{\mu_0 I_0}{2w} \begin{pmatrix} \cot(\alpha) \left(\frac{r}{a_i}\right)^{-n-1} \sin(n\theta) \\ -\cot(\alpha) \left(\frac{r}{a_i}\right)^{-n-1} \cos(n\theta) + (-1)^i \frac{w}{\pi r} \\ 0 \end{pmatrix} \qquad r > a_i. \tag{2.27}$$

Field in the bore

The magnetic field in the bore of a CCT magnet of N total layers is then

$$\begin{pmatrix} B_r \\ B_\theta \\ B_z \end{pmatrix} = -\frac{\mu_0 I_0}{2w} \begin{pmatrix} \cot(\alpha) \sin(n\theta) \sum_{i=1}^{N} \left(\frac{r}{a_i}\right)^{n-1} \\ \cot(\alpha) \cos(n\theta) \sum_{i=1}^{N} \left(\frac{r}{a_i}\right)^{n-1} \\ -\left[1 - (-1)^N\right] \end{pmatrix} \qquad r < a_1, \tag{2.28}$$

leaving just the "n" harmonic if an even number of layers is used to cancel the solenoid.

Stored energy and inductance

Relation to the vector potential

The stored energy is related to the vector potential and current density by the volume integral

$$E = \frac{1}{2}\int (\vec{A}\cdot\vec{J})\ d\tau. \tag{2.29}$$

For the case of a cylindrical sheet of current density at fixed radius $r = a$, the stored energy per unit of axial length is given by an integration over θ only

$$E' = \frac{a}{2}\int (\vec{A}\cdot\vec{j})\ d\theta, \tag{2.30}$$

where $\vec{j}$ is the linear current density. For a multi-layer magnet with N total layers, the total stored energy can be described by

$$E'_{net} = \frac{1}{2}\begin{pmatrix} I_1 & I_2 & \cdots & I_N \end{pmatrix}\begin{pmatrix} L_{1,1} & L_{1,2} & \cdots & L_{1,j} \\ L_{2,1} & L_{2,2} & \cdots & L_{2,j} \\ \vdots & \vdots & \ddots & \vdots \\ L_{i,1} & L_{i,2} & \cdots & L_{N,N} \end{pmatrix}\begin{pmatrix} I_1 \\ I_2 \\ \vdots \\ I_N \end{pmatrix}, \tag{2.31}$$

where I_i is the current in the "ith" layer, L_{ii} are the self inductances, and L_{ij} are the mutual inductances. This section will show the contribution of each current component to the stored energy of a multi-layer CCT magnet. Finally, as a check of the accuracy, this formulation will be compared to inductance measurements performed on fabricated CCT magnets (CCT1 and CCT2).

Stored energy in the solenoid component

The vector potential due the solenoidal current for a single CCT layer is given in Equation 2.23. For the calculation of the stored energy, the net vector potential at the location of each layer will be found. For a multi-layer CCT magnet of N total layers located at constant increasing radii $a_1, ..., a_{i=N-1}, a_{i=N}$ with current I_i, the vector potential generated by the solenoidal current of the layer located at a_j at the location of the layer i is given by

$$\vec{A}_{\theta ij} = \frac{\mu_0 I_j}{2w}\begin{cases} (-1)^{j-1} a_i & \text{if} \quad i < j \\ (-1)^{j-1}\frac{a_j^2}{a_i} & \text{if} \quad i > j \end{cases}, \tag{2.32}$$

making the net vector potential at the location of the "ith" layer $\vec{A}_{\theta 1(net)}$

$$\begin{pmatrix} \vec{A}_{\theta 1(net)} \\ \vec{A}_{\theta 2(net)} \\ \vdots \\ \vec{A}_{\theta N(net)} \end{pmatrix} = \begin{pmatrix} c_{1,1} & c_{1,2} & \cdots & c_{1,j} \\ c_{2,1} & c_{2,2} & \cdots & c_{2,j} \\ \vdots & \vdots & \ddots & \vdots \\ c_{i,1} & c_{i,2} & \cdots & c_{N,N} \end{pmatrix}\begin{pmatrix} I_1 \\ I_2 \\ \vdots \\ I_N \end{pmatrix} \qquad c_{i,j} = \frac{\mu_0}{2w}(-1)^{j-1}\begin{cases} a_i & \text{if} \quad i < j \\ \frac{a_j^2}{a_i} & \text{if} \quad i > j \end{cases}. \tag{2.33}$$

The stored energy per unit of axial length is given by the combination of Equations 2.21, 2.30, and 2.33. For the case of the solenoidal component of current and vector potential, the

energy $E'_{\theta ij}$ due to the vector potential generated by layer j due to the current density at layer i is

$$E'_{\theta ij} = \frac{a_i}{2}\frac{I_i}{w}(-1)^{i-1}2\pi\vec{A}_{\theta ij}. \tag{2.34}$$

Then, the energy relation is given by

$$\begin{pmatrix} E'_{\theta 1(net)} \\ E'_{\theta 2(net)} \\ \vdots \\ E'_{\theta N(net)} \end{pmatrix} = \begin{pmatrix} c_{1,1} & c_{1,2} & \cdots & c_{1,j} \\ c_{2,1} & c_{2,2} & \cdots & c_{2,j} \\ \vdots & \vdots & \ddots & \vdots \\ c_{i,1} & c_{i,2} & \cdots & c_{N,N} \end{pmatrix} \begin{pmatrix} I_1 \\ I_2 \\ \vdots \\ I_N \end{pmatrix} \qquad c_{i,j} = I_i\frac{\mu_0\pi}{2w^2}(-1)^{i+j-2}\begin{cases} a_i^2 & \text{if } \ i<j \\ a_j^2 & \text{if } \ i>j \end{cases}. \tag{2.35}$$

The net stored energy from the solenoidal component in a CCT magnet is then

$$E'_{\theta(net)} = \frac{1}{2}\begin{pmatrix} I_1 & I_2 & \cdots & I_N \end{pmatrix}\begin{pmatrix} L_{1,1} & L_{1,2} & \cdots & L_{1,j} \\ L_{2,1} & L_{2,2} & \cdots & L_{2,j} \\ \vdots & \vdots & \ddots & \vdots \\ L_{i,1} & L_{i,2} & \cdots & L_{N,N} \end{pmatrix}\begin{pmatrix} I_1 \\ I_2 \\ \vdots \\ I_N \end{pmatrix} \tag{2.36}$$

$$L_{i,j} = \frac{\mu_0\pi}{w^2}(-1)^{i+j-2}\begin{cases} a_i^2 & \text{if } \ i<j \\ a_j^2 & \text{if } \ i>j \end{cases}, \tag{2.37}$$

where L_{ij} are the self and mutual terms in the inductance matrix.

Stored energy in the harmonic component

The vector potential due the harmonic current for a single CCT layer is given by the first term in Equation 2.24. For the calculation of the stored energy, the net vector potential at the location of each layer will be found. For a multi-layer CCT magnet of N total layers located at constant increasing radii $a_1, ..., a_{i=N-1}, a_{i=N}$ with current I_i, the harmonic vector potential generated by a layer located at a_j at the location of the layer i is given by

$$\vec{A}_{zij} = \frac{\mu_0 I_j}{2w}\frac{a_j}{n}\cot(\alpha)\begin{cases} \left(\frac{a_i}{a_j}\right)^n\cos(n\theta) & a_i < a_j \\ \left(\frac{a_i}{a_j}\right)^{-n}\cos(n\theta) & a_i > a_j \end{cases}, \tag{2.38}$$

making the net vector potential at the location of the "ith" layer $\vec{A}_{z1(net)}$

$$\begin{pmatrix} \vec{A}_{z1(net)} \\ \vec{A}_{z2(net)} \\ \vdots \\ \vec{A}_{zN(net)} \end{pmatrix} = \begin{pmatrix} c_{1,1} & c_{1,2} & \cdots & c_{1,j} \\ c_{2,1} & c_{2,2} & \cdots & c_{2,j} \\ \vdots & \vdots & \ddots & \vdots \\ c_{i,1} & c_{i,2} & \cdots & c_{N,N} \end{pmatrix}\begin{pmatrix} I_1 \\ I_2 \\ \vdots \\ I_N \end{pmatrix} \tag{2.39}$$

$$c_{i,j} = \frac{\mu_0}{2w}\frac{a_j}{n}\cot(\alpha)\begin{cases}\left(\frac{a_i}{a_j}\right)^n\cos(n\theta) & \text{if } i<j\\ \left(\frac{a_i}{a_j}\right)^{-n}\cos(n\theta) & \text{if } i>j\end{cases}.$$

The stored energy per unit of axial length is given by the combination of Equations 2.21, 2.30, and 2.39. For the case of the harmonic component of current and vector potential, the energy E'_{zij} due to the vector potential generated by layer j due to the current density at layer i is

$$E'_{zij} = \frac{\mu_0\pi I_i I_j}{2w^2}\cot^2(\alpha)\frac{a_i a_j}{2n}\begin{cases}\left(\frac{a_i}{a_j}\right)^n & \text{if } i<j\\ \left(\frac{a_i}{a_j}\right)^{-n} & \text{if } i>j\end{cases}. \tag{2.40}$$

Then, the energy relation is given by

$$\begin{pmatrix}E'_{z1(net)}\\ E'_{z2(net)}\\ \vdots\\ E'_{zN(net)}\end{pmatrix} = \begin{pmatrix}c_{1,1} & c_{1,2} & \cdots & c_{1,j}\\ c_{2,1} & c_{2,2} & \cdots & c_{2,j}\\ \vdots & \vdots & \ddots & \vdots\\ c_{i,1} & c_{i,2} & \cdots & c_{N,N}\end{pmatrix}\begin{pmatrix}I_1\\ I_2\\ \vdots\\ I_N\end{pmatrix} \tag{2.41}$$

$$c_{i,j} = \frac{\mu_0\pi I_i}{2w^2}\cot^2(\alpha)\frac{a_i a_j}{2n}\begin{cases}\left(\frac{a_i}{a_j}\right)^n & \text{if } i<j\\ \left(\frac{a_i}{a_j}\right)^{-n} & \text{if } i>j\end{cases}.$$

The net stored energy from the harmonic component in a CCT magnet is then

$$E'_{z(net)} = \frac{1}{2}\begin{pmatrix}I_1 & I_2 & \cdots & I_N\end{pmatrix}\begin{pmatrix}L_{1,1} & L_{1,2} & \cdots & L_{1,j}\\ L_{2,1} & L_{2,2} & \cdots & L_{2,j}\\ \vdots & \vdots & \ddots & \vdots\\ L_{i,1} & L_{i,2} & \cdots & L_{N,N}\end{pmatrix}\begin{pmatrix}I_1\\ I_2\\ \vdots\\ I_N\end{pmatrix} \tag{2.42}$$

$$L_{i,j} = \frac{\mu_0\pi}{2w^2}\cot^2(\alpha)\frac{a_i a_j}{n}\begin{cases}\left(\frac{a_i}{a_j}\right)^n & \text{if } i<j\\ \left(\frac{a_i}{a_j}\right)^{-n} & \text{if } i>j\end{cases}, \tag{2.43}$$

where L_{ij} are the self and mutual terms in the inductance matrix.

Stored energy in the constant axial component

The vector potential due the constant axial current for a single CCT layer is given by the second term in Equation 2.24. For the calculation of the stored energy, the net vector potential at the location of each layer will be found. For a multi-layer CCT magnet of N total layers located at constant increasing radii $a_1, ..., a_{i=N-1}, a_{i=N}$ with current I_i, the vector

potential generated by the constant axial current of the layer located at a_j at the location of the layer i is given by

$$\vec{A}_{zc}(r,\theta) = -\frac{\mu_0 I_j}{2\pi}(-1)^{j-1}\begin{cases}\log(a_j) & i<j\\ \log(a_i) & i>j\end{cases}. \tag{2.44}$$

making the net vector potential at the location of the "ith" layer $\vec{A}_{zc1(net)}$

$$\begin{pmatrix}\vec{A}_{zc1(net)}\\ \vec{A}_{zc2(net)}\\ \vdots\\ \vec{A}_{zcN(net)}\end{pmatrix} = \begin{pmatrix}c_{1,1} & c_{1,2} & \cdots & c_{1,j}\\ c_{2,1} & c_{2,2} & \cdots & c_{2,j}\\ \vdots & \vdots & \ddots & \vdots\\ c_{i,1} & c_{i,2} & \cdots & c_{N,N}\end{pmatrix}\begin{pmatrix}I_1\\ I_2\\ \vdots\\ I_N\end{pmatrix} \qquad c_{i,j} = -\frac{\mu_0}{2\pi}(-1)^{j-1}\begin{cases}\log(a_j) & i<j\\ \log(a_i) & i>j\end{cases}. \tag{2.45}$$

The stored energy per unit of axial length is given by the combination of Equations 2.21, 2.30, and 2.45. For the case of the constant axial component of current and vector potential, the energy E'_{zcij} due to the vector potential generated by layer j due to the current density at layer i is

$$E'_{zcij} = (-1)^{i-1}\frac{I_i}{2}\vec{A}_{zcij}. \tag{2.46}$$

Then, the energy relation is given by

$$\begin{pmatrix}E'_{zc1(net)}\\ E'_{zc2(net)}\\ \vdots\\ E'_{zcN(net)}\end{pmatrix} = \begin{pmatrix}c_{1,1} & c_{1,2} & \cdots & c_{1,j}\\ c_{2,1} & c_{2,2} & \cdots & c_{2,j}\\ \vdots & \vdots & \ddots & \vdots\\ c_{i,1} & c_{i,2} & \cdots & c_{N,N}\end{pmatrix}\begin{pmatrix}I_1\\ I_2\\ \vdots\\ I_N\end{pmatrix} \qquad c_{i,j} = \frac{\mu_0 I_i}{4\pi}(-1)^{i+j-1}\begin{cases}\log(a_j) & i<j\\ \log(a_i) & i>j\end{cases}. \tag{2.47}$$

The net stored energy from the constant axial component in a CCT magnet is then

$$E'_{zc(net)} = \frac{1}{2}\begin{pmatrix}I_1 & I_2 & \cdots & I_N\end{pmatrix}\begin{pmatrix}L_{1,1} & L_{1,2} & \cdots & L_{1,j}\\ L_{2,1} & L_{2,2} & \cdots & L_{2,j}\\ \vdots & \vdots & \ddots & \vdots\\ L_{i,1} & L_{i,2} & \cdots & L_{N,N}\end{pmatrix}\begin{pmatrix}I_1\\ I_2\\ \vdots\\ I_N\end{pmatrix} \tag{2.48}$$

$$L_{i,j} = \frac{\mu_0}{2\pi}(-1)^{i+j-1}\begin{cases}\log(a_j) & i<j\\ \log(a_i) & i>j\end{cases}, \tag{2.49}$$

where L_{ij} are the self and mutual terms in the inductance matrix. It is seen that this formulation is poorly defined for a single layer which results in taking the logarithm of a unit of distance (the issue is associated with the axial current not returning). With a second

layer added to return the current, the two layers solution reduces to the expected expression for a simple coaxial cable.

Net stored energy and inductance

It can be shown that $E'_{\theta(net)}$, $E'_{z(net)}$, and $E'_{zc(net)}$ are the only terms generated by the volume integral in Equation 2.30. The net stored energy is then simply given by the sum of these terms. Because $I^T L_1 I + I^T L_2 I = I^T (L_1 + L_2) I$, the total inductance matrix can be found from the sum of the inductance matrices generated by each component. In practice, for a typical even layer CCT magnet, the harmonic energy makes up almost all of the total, with the small remaining portion (about 2%) coming from the solenoid. The constant axial contribution is included in the previous formulation for completeness, but can be ignored in almost all cases. With this assumption, the net stored energy and inductance per unit length for a multi-layer CCT magnet is given by

$$E'_{net} = \frac{1}{2} \begin{pmatrix} I_1 & I_2 & \cdots & I_N \end{pmatrix} \begin{pmatrix} L_{1,1} & L_{1,2} & \cdots & L_{1,j} \\ L_{2,1} & L_{2,2} & \cdots & L_{2,j} \\ \vdots & \vdots & \ddots & \vdots \\ L_{i,1} & L_{i,2} & \cdots & L_{N,N} \end{pmatrix} \begin{pmatrix} I_1 \\ I_2 \\ \vdots \\ I_N \end{pmatrix}, \tag{2.50}$$

$$L_{i,j} = \frac{\mu_0 \pi}{2w^2} \cot^2(\alpha) \frac{a_i a_j}{n} \begin{cases} \left(\frac{a_i}{a_j}\right)^n \\ \left(\frac{a_i}{a_j}\right)^{-n} \end{cases} + \frac{\mu_0 \pi}{w^2} (-1)^{i+j-2} \begin{cases} a_i^2 & \text{if } i < j \\ a_j^2 & \text{if } i > j \end{cases}. \tag{2.51}$$

Comparison to measured inductance of fabricated CCT magnets at LBNL

Table 2.2 shows a comparison between the analytic and measured inductance for two CCT magnets built at Lawrence Berkeley National Laboratory. The straight-section inductance per length for each CCT magnet was approximated by the total measured inductance divided by the magnetic length of the coil (see Appendix A for the definition of magnetic length). This approximation allowed for a comparison with the formulation (which does not include the effect of the ends of the magnet). The magnetic length L_m, inductance per meter L, and total inductance L_{tot} are given in the table. Given the approximation of end effects, reasonable agreement is seen between the formulation and measured results. More information on the design of these magnets and the electrical measurements can be found in Chapters 5 and 6.

Table 2.2: Inductance of Fabricated CCT Magnets

			Predicted		Measured
Magnet	Config.	L_m (m)	L (mH/m)	L_{tot} (mH)	L_{tot} (mH)
CCT1	Layer 1	0.593	0.490	0.291	N/A
	Layer 2	0.547	0.729	0.399	N/A
	Layer 1,2 series	0.570	1.95	1.11	1.19
CCT2-64turn	Layer 1	0.4881	1.242	0.606	0.6
	Layer 2	0.4881	1.919	0.937	1.0
	Layer 1,2 series	0.4881	4.690	2.289	2.4

2.4 Correction of cross-talk in 2-in-1 CCT magnets

High energy hadron colliders typically require a dual bore "2-in-1" magnet with equal and opposite dipole fields. An example of such a design is shown for the LHC in Figure 2.7. This allows for two beams to be stored, traveling in opposite directions in their respective bores, which are then crossed to produce collisions in interaction regions. A key consideration in the design of 2-in-1 magnets is the contribution of the fringe fields from one bore to another referred to as "cross-talk". Because the orientation of the fields is reversed between bores, this cross-talk contributes positively to each bore and boosts the net field. The challenge is to preserve field quality which will be spoiled by the cross-talk if it is not considered and corrected in the magnetic design.

It has been shown in Section 2.2 that the CCT is an effective method for producing combined function fields. A formulation will be developed that uses this capability to control the field quality in a 2-in-1 CCT design. This approach differs from the LHC in that it uses the winding path itself to correct the cross-talk rather than an iron yoke. The flexibility of this method will be shown, with the capability to produce pure or combined function harmonics of excellent field quality in both bores of a 2-in-1 CCT magnet. This process will make use of the harmonics described in Appendix A, but will use slightly different notation necessary to distinguish between the field and current in two bores. For this reason, the formulation for the 2-in-1 CCT will be presented in a section that is self-complete, redefining expressions as necessary.

Field harmonics inside a cos(kθ) current sheet

The field outside and inside a sheet of linear axial current density $j = j_{0k}\cos(k\theta)$ located at radius R is

$$\vec{B}^{in}(z) = B_y + iB_x = -\frac{\mu_0 j_{0k}}{2}\left(\frac{z}{R}\right)^{k-1} \tag{2.52}$$

$$\vec{B}^{out}(z) = B_y + iB_x = \frac{\mu_0 j_{0k}}{2}\left(\frac{z}{R}\right)^{-k-1}, \tag{2.53}$$

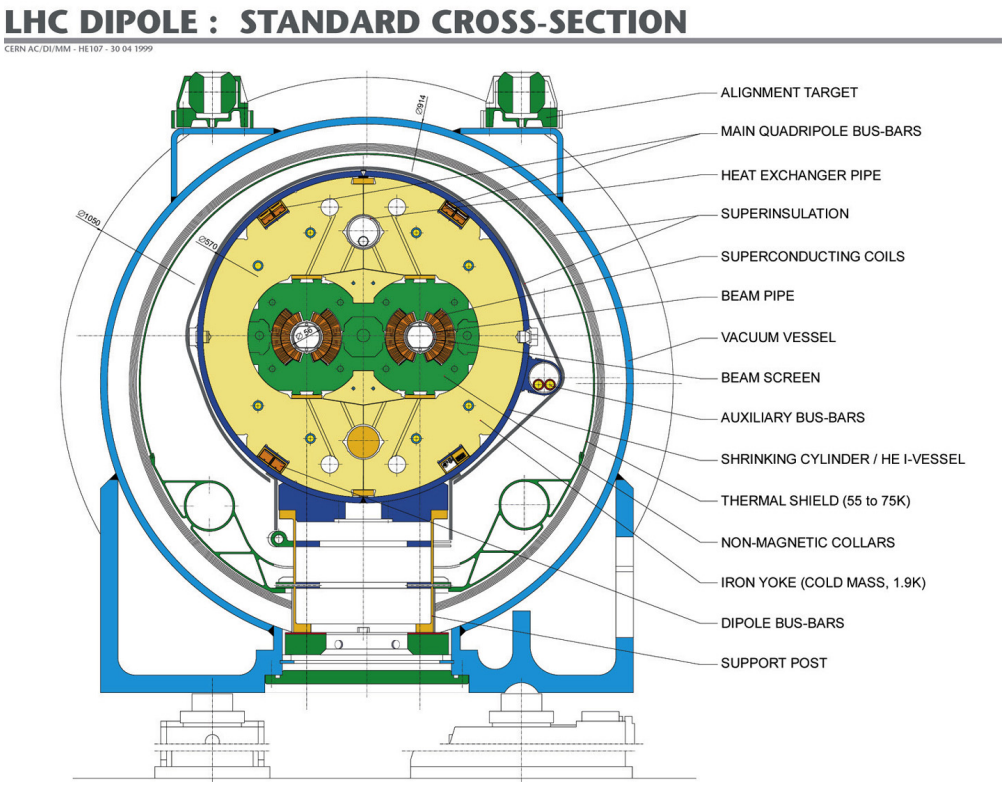

Figure 2.7: The LHC "2-in-1" dual bore dipole magnet is shown. (Fig. from [2])

where the coordinate system $z = x + iy$ can be seen defined in Figure A.1. The field within the bore is typically represented using the harmonics

$$\vec{B}(z) = B_y + iB_x = [B_n + iA_n] \left(\frac{z}{R_{ref}} \right)^{n-1}, \tag{2.54}$$

where R_{ref} is the reference radius. The normal (non-skew) field coefficients produced in the bore of the current sheet are then given by

$$B_n = -\frac{\mu_0 j_{0n}}{2} \left(\frac{R_{ref}}{R} \right)^{n-1}. \tag{2.55}$$

Displaced field harmonics

To determine the harmonics about a point displaced a distance a along the midplane (Fig. 2.8), the field outside a current sheet of $j = j_{0k} \cos(k\theta)$ located at $r' = R$ is rewritten in the displaced coordinate system as

$$\vec{B}^{out} = \frac{\mu_0 j_{0k}}{2} \left(\frac{z'}{R} \right)^{-k-1} = \frac{\mu_0 j_{0k}}{2} \left(\frac{z+a}{R} \right)^{-k-1}. \tag{2.56}$$

Binomial expansion of $(z+a)^{-k-1}$ leads to

$$\vec{B}(z) = \frac{\mu_0 j_{0k}}{2}\left(\frac{R}{a}\right)^{k+1}\sum_{m=1}^{\infty}\binom{-k-1}{m-1}\left(\frac{z}{a}\right)^{m-1}. \tag{2.57}$$

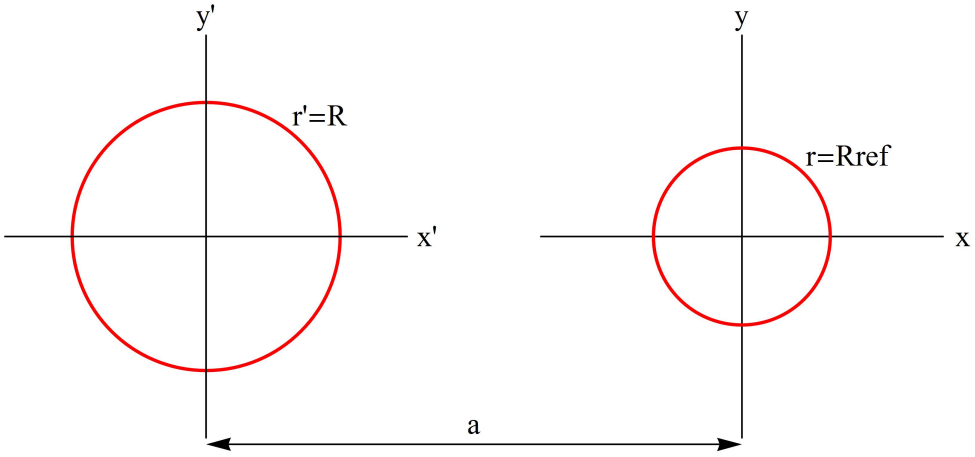

Figure 2.8: Displaced harmonics are calculated at R_{ref} in the $z = x + iy$ system due to current sheet located at $r' = R$ in the $z' = x' + iy'$ system.

Equating with the standard field series representation (Eqn. 2.54), the harmonic coefficients in the displaced expansion are

$$B_n = \frac{\mu_0 j_{0k}}{2}\binom{-k-1}{n-1}\left(\frac{R}{a}\right)^{k+1}\left(\frac{R_{ref}}{a}\right)^{n-1} = \frac{\mu_0 j_{0k}}{2}\left(\frac{R_{ref}}{R}\right)^{n-1}\binom{-k-1}{n-1}\left(\frac{R}{a}\right)^{k+n}. \tag{2.58}$$

Or in the case of negative displacement $(-a)$,

$$\begin{aligned} B_n &= \frac{\mu_0 j_{0k}}{2}(-1)^{k+n}\binom{-k-1}{n-1}\left(\frac{R}{a}\right)^{k+1}\left(\frac{R_{ref}}{a}\right)^{n-1} \\ &= \frac{\mu_0 j_{0k}}{2}(-1)^{k+n}\left(\frac{R_{ref}}{R}\right)^{n-1}\binom{-k-1}{n-1}\left(\frac{R}{a}\right)^{k+n}. \end{aligned} \tag{2.59}$$

Dual bore harmonics

For two bores with a midplane displacement distance of a and current densities of $j_L = j_{Lk}\cos(k\theta)$ and $j_R = j_{Rm}\cos(m\theta)$ around the left and right bore respectively, the harmonics in each bore using a reference radius of R_{ref} are the sum of those contributed by the local

current (inside: Eqn. 2.55) and the current of the other bore (outside: Eqn. 2.58 or 2.59). If B_{nL} and B_{nR} are the harmonics in the left and right bores,

$$B_{nL} = -\frac{\mu_0}{2}\left(\frac{R_{ref}}{R}\right)^{n-1}\left[j_{L(k=n)} - \sum_{m=1}^{\infty} j_{Rm}\binom{-m-1}{n-1}\left(\frac{-R}{a}\right)^{m+n}\right] \tag{2.60}$$

$$B_{nR} = -\frac{\mu_0}{2}\left(\frac{R_{ref}}{R}\right)^{n-1}\left[j_{R(m=n)} - \sum_{k=1}^{\infty} j_{Lk}\binom{-k-1}{n-1}\left(\frac{R}{a}\right)^{k+n}\right]. \tag{2.61}$$

Matrix Form

With this definition, the currents to produce desired multipoles can be found using

$$\begin{pmatrix} B_{L1} \\ B_{L2} \\ \vdots \\ B_{Ln} \\ B_{R1} \\ B_{R2} \\ \vdots \\ B_{Rn} \end{pmatrix} = -\frac{\mu_0}{2}\begin{pmatrix} M_{LR} & If^{n-1} \\ If^{n-1} & M_{RL} \end{pmatrix}\begin{pmatrix} j_{R1} \\ j_{R2} \\ \vdots \\ j_{Rm} \\ j_{L1} \\ j_{L2} \\ \vdots \\ j_{Lk} \end{pmatrix} \tag{2.62}$$

$$M_{LR} = \begin{pmatrix} a_{1,1} & a_{1,2} & \cdots & a_{1,m} \\ a_{2,1} & a_{2,2} & \cdots & a_{2,m} \\ \vdots & \vdots & \ddots & \vdots \\ a_{n,1} & a_{n,2} & \cdots & a_{n,m} \end{pmatrix} \qquad a_{n,m} = -\binom{-m-1}{n-1}\left(\frac{-R}{a}\right)^{m+n} f^{n-1} \tag{2.63}$$

$$M_{RL} = \begin{pmatrix} c_{1,1} & c_{1,2} & \cdots & c_{1,k} \\ c_{2,1} & c_{2,2} & \cdots & c_{2,k} \\ \vdots & \vdots & \ddots & \vdots \\ c_{n,1} & c_{n,2} & \cdots & c_{n,k} \end{pmatrix} \qquad c_{n,k} = -\binom{-k-1}{n-1}\left(\frac{R}{a}\right)^{k+n} f^{n-1} \tag{2.64}$$

where $f = \left(\frac{R_{ref}}{R}\right)^{n-1}$ is the bore fraction of the reference radius and I is the identity matrix. If an equal number of currents (up to $k_{max} = m_{max}$) are used in both bores, the current coefficients to produce desired multipoles up to $B_{L(n=k_{max})}$ and $B_{R(n=m_{max})}$ can be calculated. This allows the exact multipoles up to the order of current ($k_{max} = m_{max}$) to be specified. Multipoles $n > k_{max}$ are still produced as a result of the series, but are left unspecified. The order of current necessary ($k_{max} = m_{max}$) is practically determined by comparison of the field quality specifications to the non-specified multipoles ($B_{n>k_{max}}$).

Relation to CCT winding coefficients

As described in Section 2.2, the parametric path for a CCT winding can be related to a sheet current density. The method for producing a 2-in-1 CCT is to first use the analytic formulation developed for the 2-in-1 to calculate the desired sheet currents for the left-hand $j_{L1} \dots j_{Lk=k_{max}}$ and right-hand $j_{R1} \dots j_{Rm=m_{max}}$ bores. Then, these sheet currents can be used to derive the parametric path for a CCT layer according to

$$\vec{p}(\theta) = R\hat{r} + \left[R\cot(\alpha) \sum_{k=1}^{k_{max}} \frac{j_{Lk}}{j_{L1}} \frac{\sin(k\theta)}{k} + \frac{w}{2\pi}\theta \right] \hat{z} \tag{2.65}$$

for the left-hand bore winding, and

$$\vec{p}(\theta) = R\hat{r} + \left[R\cot(\alpha) \sum_{m=1}^{m_{max}} \frac{j_{Rm}}{j_{R1}} \frac{\sin(m\theta)}{m} + \frac{w}{2\pi}\theta \right] \hat{z} \tag{2.66}$$

for the right-hand bore winding. Here the left-hand bore winding will be shifted to be centered about -$a/2$ and the right-hand winding about +$a/2$ as seen in Figure 2.8.

In this case the main harmonic produced is assumed to be a dipole (j_{L1} and j_{R1}). For a quadrupole 2-in-1 the path would be normalized to j_{L2} and j_{R2}, and for an arbitrary "n" main harmonic it would be normalized to j_{Ln} and j_{Rn}. For this reason it is useful to define normalized winding coefficients

$$\begin{aligned} j^*_{Lk} &= \frac{j_{Lk}}{j_{Ln}} \\ j^*_{Rm} &= \frac{j_{Rm}}{j_{Rn}}, \end{aligned} \tag{2.67}$$

where "n" represents the main harmonic.

Considerations for powering multi-layer 2-in-1 CCT's

The windings around each bore of the 2-in-1 are built up in pairs of layers with alternating tilt angle and current (as previously described). Care must taken that the CCT layers are generated and powered to correctly represent the current density solution from Equation 2.62. To satisfy this, the CCT path is generated using the current density solution and Equations 2.65 and 2.66, with the tilt angle and current alternating between layers. A special consideration is the direction of the current in the windings due to the sign of the current being normalized out of the winding equation. For example, in a reversed dipole 2-in-1 the left-hand CCT needs to be powered opposite of the right. If the right-hand CCT is powered with layer 1 positive and layer 2 negative, the left-hand must have layer 1 negative and layer 2 positive.

Example 1: a 2-in-1 CCT dipole

The fields from a two layer, dual bore dipole generated using the 2-in-1 CCT winding relation were examined. Radii of 50 mm and 60 mm were chosen for layer 1 and layer 2 respectively. A tilt angle of 19 degrees and pitch of 7.627 mm was used for the CCT path, and a spacing between bore centers of 140 mm was specified for an example with dramatic cross-talk. The number of conductor turns for each layer was 350. Two cases were considered: one where no cross-talk was corrected, and one where the cross-talk was corrected up to the b_9 harmonic. CCT windings were generated for each of these cases using a combination of the solution of Equation 2.62 and the winding relations in Equations 2.65 and 2.66. The field harmonics from these windings were then calculated in the commercial software Opera3D [43] and compared to the predictions of the formulation. The methods used for the modeling in Opera3D can be found described in Chapter 3. For both cases a reference radius of 30 mm was used for the harmonic calculation, and a pure dipole (positive in the left bore and negative in the right bore) with all other harmonics zero ($B_{L2} \cdots B_{Lm_{max}} = 0.0$, $B_{R2} \cdots B_{R_{max}} = 0.0$) was specified.

No correction

A dual bore dipole with no correction has only one component of current density $k_{max} = m_{max} = 1$. The 2-in-1 solution is then trivial and reduces the winding equation to the single bore CCT dipole path specified in Equation 2.15. As expected, a large amount of cross-talk between bores can be seen in the results shown in Table 2.3 and Figure 2.9. Desired field quality is of the order of several units of field error, making this uncorrected case far from acceptable.

Corrected up to b_9

The results for the case of the 2-in-1 CCT dipole corrected up to b_9 are shown in Table 2.4 and Figure 2.9. It is seen that by adding combined function currents, the field error can be brought below one unit for all the non-dipole harmonics up to b_9. This is an example of how the cross-talk in a dual bore dipole can be effectively managed using the CCT's capability to produce combined function fields.

Table 2.3: Uncorrected 2-in-1 Harmonic Comparison

	Layer 1		Layer 2		Formulation		Opera3D	
n	$j^*_{L(k=n)}$	$j^*_{R(m=n)}$	$j^*_{L(k=n)}$	$j^*_{R(m=n)}$	b_{Ln}	b_{Rn}	b_{Ln}	b_{Rn}
1	1	1	1	1	10^4	10^4	10^4	10^4
2	0	0	0	0	577.11	-577.10	576.9	-576.73
3	0	0	0	0	185.50	185.50	185.26	185.27
4	0	0	0	0	53.00	-53.00	53.00	-52.96
5	0	0	0	0	14.20	14.20	14.23	14.23
6	0	0	0	0	3.65	-3.65	3.66	-3.64
7	0	0	0	0	.91	.91	0.90	0.89
8	0	0	0	0	.22	-.22	0.23	-0.22
9	0	0	0	0	0.05	0.05	0.06	0.06

The current winding coefficients (normalized to the dipole: $n = 1$ in Equation 2.67) and calculated harmonics (in units) are shown for an example CCT 2-in-1 dipole with no correction. The calculated harmonics are normalized to B_1 of their own bore.

Table 2.4: Corrected 2-in-1 Harmonic Comparison

	Layer 1		Layer 2		Formulation		Opera3D	
n	$j^*_{L(k=n)}$	$j^*_{R(m=n)}$	$j^*_{L(k=n)}$	$j^*_{R(m=n)}$	b_{Ln}	b_{Rn}	b_{Ln}	b_{Rn}
1	1	1	1	1	10^4	10^4	10^4	10^4
2	-0.0856	0.0856	-0.1371	0.1371	0	0	-0.652	-0.652
3	-0.0446	-0.04461	-0.0819	-0.0819	0	0	-0.398	-0.398
4	-0.0205	0.0205	-0.0425	0.0425	0	0	-0.074	-0.074
5	-0.0088	-0.0088	-0.0201	-0.0201	0	0	0.013	0.013
6	-0.0036	0.0036	-0.0086	0.0086	0	0	-0.024	-0.024
7	-0.0014	-0.0014	-0.0033	-0.0033	0	0	-0.024	-0.024
8	-0.0005	0.0005	-0.0010	0.0010	0	0	0.007	0.007
9	-0.0002	-0.0002	-0.0002	-0.0002	0	0	0.011	0.011

The current winding coefficients (normalized to the dipole: $n = 1$ in Equation 2.67) and calculated harmonics (in units) are shown for an example CCT 2-in-1 dipole with correction currents added up to b_9. The calculated harmonics are normalized to B_1 of their own bore.

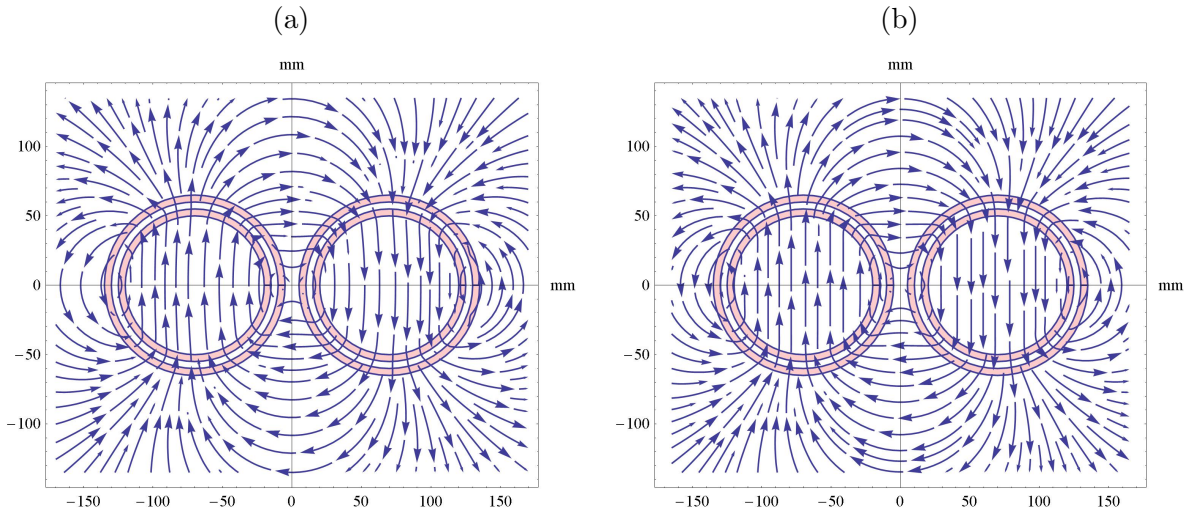

Figure 2.9: Streamlines for the uncorrected (a) and corrected (b) 2-in-1 CCT dipole are shown.

2.5 Fields in a multi-layer thick winding CCT dipole magnet

Field due to a single, thick CCT dipole layer

The derivation of the path for a single CCT layer was presented in Section 2.2 with the assumption the conductor has little or no radial thickness (thin wire averaged into a thin current sheet). This description will now be extended to a CCT dipole layer of some radial thickness as would be needed to model the fields generated by a Rutherford cable. The inner edge of the conductor is defined at $r = a_1$ and the outer at $r = a_2$. The total magnetic field produced is the sum of the fields produced by each of the three current density terms in Equation 2.12.

Field produced by the $cos(\theta)$ current $j_z = \frac{I_0 cot(\alpha)}{w} cos(\theta)$

For a thin winding at fixed radius a with linear current density $j_z(\theta) = j_{0z} cos(n\theta)$ the field generated is

$$\begin{vmatrix} B_r \\ B_\theta \end{vmatrix} = \frac{-\mu_0 j_{0z}}{2} \left(\frac{r}{a}\right)^{n-1} \begin{vmatrix} sin(n\theta) \\ cos(n\theta) \end{vmatrix} \qquad r < a_1$$

inside the winding, and

$$\begin{vmatrix} B_r \\ B_\theta \end{vmatrix} = \frac{\mp\mu_0 j_{0z}}{2} \left(\frac{r}{a}\right)^{-n-1} \begin{vmatrix} sin(n\theta) \\ cos(n\theta) \end{vmatrix} \qquad r > a_2$$

outside the winding [44]. For a thick dipole winding ($n = 1$) starting at $r = a_1$ and extending to $r = a_2$ the linear current density j_{0z} is replaced by $J_{0z} da$, where J_{0z} is the current per area. The field contribution from a thin sheet is integrated radially to find the field generated by a conductor with radial thickness. The integrals are

$$\begin{vmatrix} B_r \\ B_\theta \end{vmatrix} = \frac{-\mu_0 J_{0z}}{2} \int_{a_1}^{a_2} da \begin{vmatrix} sin(\theta) \\ cos(\theta) \end{vmatrix} \qquad r < a_1$$

$$\begin{vmatrix} B_r \\ B_\theta \end{vmatrix} = \frac{\mu_0 J_{0z}}{2} \left[-\int_r^{a_2} dR \mp \int_{a_1}^{r} \left(\frac{r}{a}\right)^{-2} da \right] \begin{vmatrix} sin(\theta) \\ cos(\theta) \end{vmatrix} \qquad a_1 < r < a_2$$

$$\begin{vmatrix} B_r \\ B_\theta \end{vmatrix} = \frac{\mp\mu_0 J_{0z}}{2} \int_{a_1}^{a_2} \left(\frac{r}{a}\right)^{-2} da \begin{vmatrix} sin(\theta) \\ cos(\theta) \end{vmatrix} \qquad r > a_2$$

for the three regions of interest. Performing the integration results in fields of

$$\begin{vmatrix} B_r \\ B_\theta \end{vmatrix} = \frac{-\mu_0 I_0 cot(\alpha)}{2w} \begin{vmatrix} sin(\theta) \\ cos(\theta) \end{vmatrix} \qquad r < a_1$$

$$\begin{vmatrix} B_r \\ B_\theta \end{vmatrix} = \frac{-\mu_0 I_0 cot(\alpha)}{2w(a_2-a_1)}\left[a_2 \mp \frac{a_1^3}{3r^2} + \left(-1 \pm \frac{1}{3}\right) r\right] \begin{vmatrix} sin(\theta) \\ cos(\theta) \end{vmatrix} \qquad a_1 < r < a_2$$

$$\begin{vmatrix} B_r \\ B_\theta \end{vmatrix} = \mp \frac{\mu_0 I_0 cot(\alpha)}{2w(a_2-a_1)} \frac{a_2^3 - a_1^3}{3r^2} \begin{vmatrix} sin(\theta) \\ cos(\theta) \end{vmatrix} \qquad r > a_2$$

where the substitution of the CCT dipole current density $J_{0z} = \frac{I_0 cot(\alpha)}{w(a_2-a_1)}$ has been made.

Field produced by the constant axial current $j_z = \frac{I_0}{2\pi r}$

Ampere's law $\int B \cdot dl = \mu_0 I_{enc}$, with an enclosed current of

$$I_{enc} = \int_0^{2\pi}\int_{a_1}^{r} \frac{j_z}{a_2-a_1} r dr d\theta = 2\pi \int_{a_1}^{r} \frac{I_0}{2\pi r(a_2-a_1)} r dr d\theta = I_0 \frac{(r-a_1)}{a_2-a_1}, \tag{2.68}$$

can be used to find the azimuthal field resulting from the CCT's constant axial current. This field is

$$B_\theta = \begin{cases} 0 & : r < a_1 \\ \frac{\mu_0 I_0}{2\pi r} \frac{r-a_1}{a_2-a_1} & : a_1 < r < a_2 \\ \frac{\mu_0 I_0}{2\pi r} & : r > a_2 \end{cases}$$

which outside of the winding is equivalent to the field from a single wire carrying current I_0 at the center of the bore.

Field produced by the constant azimuthal current $j_\theta = \frac{I_0}{w}$

For an infinite solenoid with inner and outer radii of a_1 and a_2, the field is

$$B_z = \begin{cases} \mu_0 J_\theta (a_2 - a_1) & : r < a_1 \\ 0 & : r > a_2 \end{cases}$$

where J_θ is the averaged azimuthal current density (in current per area). The field within the conductor of this solenoid can be approximated with a linear fall off from the inner to outer radius. Incorporating this with the CCT's azimuthal current density leads to solenoidal fields of

$$B_z = \begin{cases} \frac{\mu_0 I_0}{w} & : r < a_1 \\ \frac{\mu_0 I_0}{w} \frac{a_2-r}{a_2-a_1} & : a_1 < r < a_2 \\ 0 & : r > a_2 \end{cases}$$

in the three regions of interest.

Total field produced by a single, thick CCT dipole layer

The total field generated by a thick CCT dipole layer is the sum of the contribution from each of the three current components. This can be written as

$$\begin{vmatrix} B_r \\ B_\theta \\ B_z \end{vmatrix} = -\frac{\mu_0 I_0 cot(\alpha)}{2w} \begin{vmatrix} sin(\theta) \\ cos(\theta) \\ -2tan(\alpha) \end{vmatrix} \qquad r < a_1$$

$$\begin{vmatrix} B_r \\ B_\theta \\ B_z \end{vmatrix} = -\frac{\mu_0 I_0 cot(\alpha)}{2w} \begin{vmatrix} f_r sin(\theta) \\ f_\theta cos(\theta) - f_{\theta 2}\frac{wtan(\alpha)}{\pi} \\ -2f_z tan(\alpha) \end{vmatrix} \qquad a_1 < r < a_2$$

$$\begin{vmatrix} B_r \\ B_\theta \\ B_z \end{vmatrix} = -\frac{\mu_0 I_0 cot(\alpha)}{2w} \begin{vmatrix} f_r^o sin(\theta) \\ f_\theta^o cos(\theta) - \frac{wtan(\alpha)}{\pi r} \\ 0 \end{vmatrix} \qquad r > a_2$$

where radial form factors

$$\begin{aligned} f_r(r, a_1, a_2) &\equiv \tfrac{a_2 - \frac{a_1^3}{3r^2} - \frac{2}{3}r}{a_2 - a_1} \\ f_\theta(r, a_1, a_2) &\equiv \tfrac{a_2 + \frac{a_1^3}{3r^2} - \frac{4}{3}r}{a_2 - a_1} \\ f_{\theta 2}(r, a_1, a_2) &\equiv \tfrac{r - a_1}{r(a_2 - a_1)} \\ f_z(r, a_1, a_2) &\equiv \tfrac{a_2 - r}{a_2 - a_1} \\ f_r^o(r, a_1, a_2) &\equiv \tfrac{a_2^3 - a_1^3}{3r^2(a_2 - a_1)} \\ f_\theta^o(r, a_1, a_2) &\equiv -\tfrac{a_2^3 - a_1^3}{3r^2(a_2 - a_1)} \end{aligned} \tag{2.69}$$

have been defined. Figure 2.10 shows this formulation plotted for a CCT dipole layer.

Multi-layer current density

A CCT dipole uses multiple layers to cancel the undesirable solenoidal field produced in the bore of a single layer. For this purpose a total of N layers can be defined with the sign of the midplane angle α and the current I_0 changed for every other layer. In this case the path of the "ith" layer becomes

$$\vec{p_i}(\theta) = r_i cos(\theta)\hat{i} + r_i sin(\theta)\hat{j} + \left((-1)^{i-1} r_i cot(\alpha) sin(\theta) + \frac{w\theta}{2\pi}\right)\hat{k} \tag{2.70}$$

where α represents $|\alpha|$. This leads to a current density in the "ith" layer of

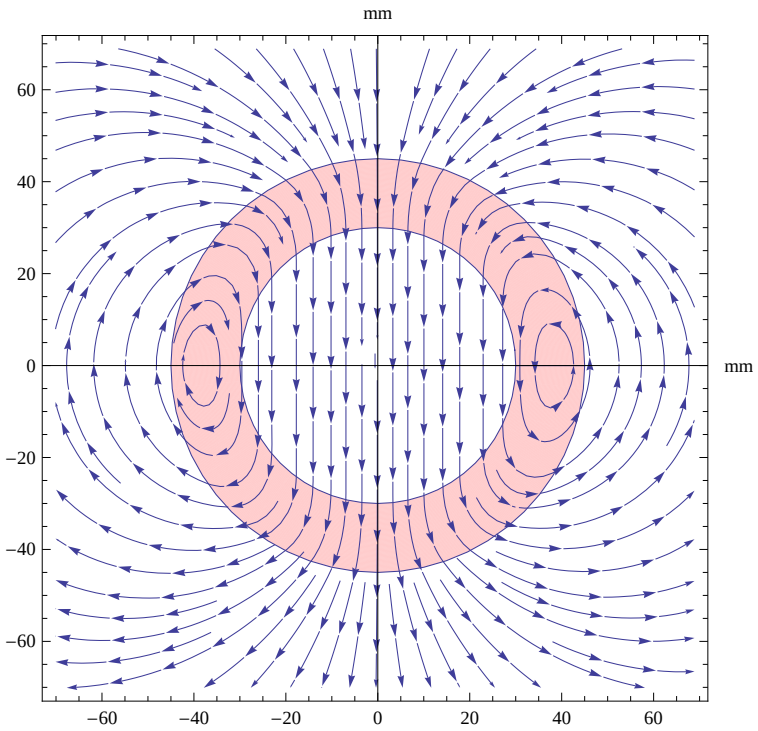

Figure 2.10: The 2D streamlines for the transverse field generated by a single CCT dipole layer of radial thickness are shown.

$$\begin{vmatrix} j_{ri} \\ j_{\theta i} \\ j_{zi} \end{vmatrix} = \frac{I_0}{w} \begin{vmatrix} 0 \\ (-1)^{i-1} \\ cot(\alpha)cos(\theta) + (-1)^{i-1}\frac{w}{2\pi r} \end{vmatrix}.$$

Muli-layer thick coil fields

A radial thickness for each of the N conductor layers is defined such that the inner radii are given by $a_{11}, a_{12}, \cdots, a_{1i}, \cdots a_{1N-1}, a_{1N}$ and the outer radii $a_{21}, a_{22}, \cdots, a_{2i}, \cdots a_{2N-1}, a_{2N}$. With these definitions the field produced by the "ith" CCT layer is given by

$$\begin{vmatrix} B_r \\ B_\theta \\ B_z \end{vmatrix} = -\frac{\mu_0 I_0 cot(\alpha)}{2w} \begin{vmatrix} sin(\theta) \\ cos(\theta) \\ -2(-1)^{i-1}tan(\alpha) \end{vmatrix} \qquad r < a_{1i}$$

$$\begin{vmatrix} B_r \\ B_\theta \\ B_z \end{vmatrix} = -\frac{\mu_0 I_0 cot(\alpha)}{2w} \begin{vmatrix} f_r(r, a_{1i}, a_{2i})sin(\theta) \\ f_\theta(r, a_{1i}, a_{2i})cos(\theta) - (-1)^{i-1}\frac{wtan(\alpha)}{\pi r}\frac{r-a_{1i}}{a_{2i}-a_{1i}} \\ -2(-1)^{i-1}tan(\alpha)\frac{a_{2i}-r}{a_{2i}-a_{1i}} \end{vmatrix} \qquad a_{1i} < r < a_{2i}$$

$$\begin{vmatrix} B_r \\ B_\theta \\ B_z \end{vmatrix} = -\frac{\mu_0 I_0 cot(\alpha)}{2w} \begin{vmatrix} f_r^o(r, a_{1i}, a_{2i}) sin(\theta) \\ f_\theta^o(r, a_{1i}, a_{2i}) cos(\theta) - (-1)^{i-1} \frac{w tan(\alpha)}{\pi r} \\ 0 \end{vmatrix} \qquad r > a_{2i}.$$

Field inside the bore $r < r_{bore}$

Using superposition, the field inside the bore is the summation over all N layers for the case of $r < a_{i1}$. This leads to

$$\begin{vmatrix} B_{rbore} \\ B_{\theta bore} \\ B_{zbore} \end{vmatrix} = -\frac{\mu_0 I_0 cot(\alpha)}{2w} \begin{vmatrix} N sin(\theta) \\ N cos(\theta) \\ -[1 - (-1)^N] tan(\alpha) \end{vmatrix}.$$

Note if there are an even number of layers, the solenoidal field completely cancels and is zero. If there are an uneven number of the layers, the magnitude of the solenoidal field will be equal to the contribution from a single layer.

Field within an arbitrary layer

Using superposition and ignoring the small field contribution from the pitch to B_θ, the field within the conductor of the "ith" layer is

$$\begin{vmatrix} B_r \\ B_\theta \\ B_z \end{vmatrix} = -\frac{\mu_0 I_0 cot(\alpha)}{2w} \begin{vmatrix} \left(\sum_{k=1}^{i-1} f_r^o(r, a_{1k}, a_{2k}) + f_r(r, a_{1i}, a_{2i}) + \sum_{k=i+1}^{N} \right) sin(\theta) \\ \left(\sum_{k=1}^{i-1} f_\theta^o(r, a_{1k}, a_{2k}) + f_\theta(r, a_{1i}, a_{2i}) + \sum_{k=i+1}^{N} \right) cos(\theta) \\ -2 \left((-1)^{i-1} f_z(r, a_{1i}, a_{2i}) + \sum_{k=i+1}^{N} (-1)^{k-1} \right) tan(\alpha) \end{vmatrix},$$

which reduces to

$$\begin{vmatrix} B_r \\ B_\theta \\ B_z \end{vmatrix} = -\frac{\mu_0 I_0 cot(\alpha)}{2w} \begin{vmatrix} \left(\sum_{k=1}^{i-1} f_r^o(r, a_{1k}, a_{2k}) + f_r(r, a_{1i}, a_{2i}) + (N - i) \right) sin(\theta) \\ \left(\sum_{k=1}^{i-1} f_\theta^o(r, a_{1k}, a_{2k}) + f_\theta(r, a_{1i}, a_{2i}) + (N - i) \right) cos(\theta) \\ -2 \left((-1)^{i-1} f_z(r, a_{1i}, a_{2i}) + \frac{1}{2} \left[(-1)^i - (-1)^N \right] \right) tan(\alpha) \end{vmatrix}.$$

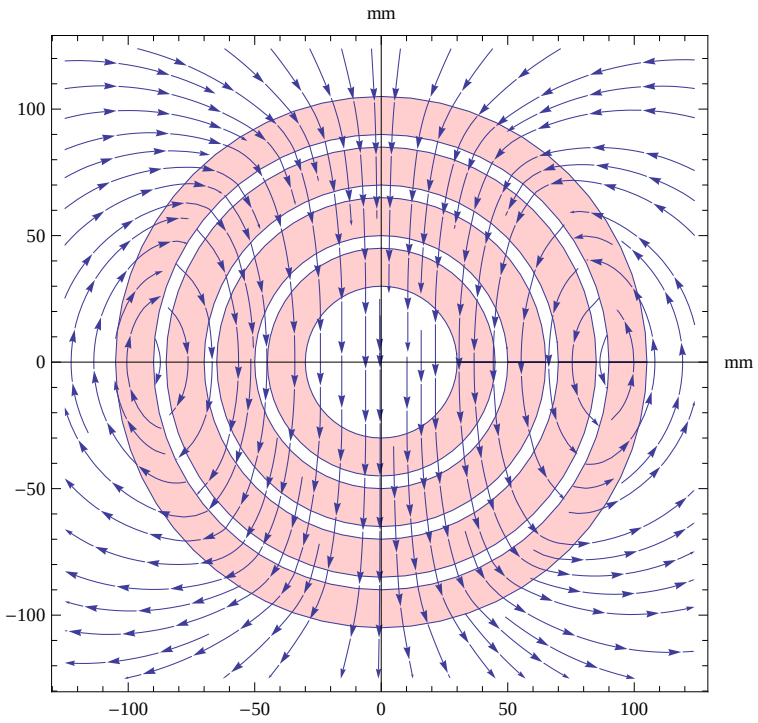

Figure 2.11: The 2D streamlines for the transverse field generated by a four layer CCT dipole magnet are shown.

Here the cancellation of the solenoidal field is determined by the number of layers above the layer of interest (since the solenoidal field outside the layer is assumed zero). This means in an even layer magnet, even though the solenoidal field within the bore may be zero, this will not be the case in every layer. This is due to the solenoidal field varying across the winding combined with the possibility of an odd number of layers above it. The size of this variation is not proportional to the total number of layers, but only the single "extra" layer above it that does not cancel. The transverse fields for a four layer CCT dipole are shown plotted in Figure 2.11.

2.6 Lorentz forces and pressures in a multi-layer thick winding CCT dipole magnet

Rib Pressure

A Frenet-Serret coordinate system following the central path of the conductor is defined using coordinates β, γ, and r. As seen in Figure 2.12, β is along the direction of the conductor path (direction of current), r is in the radial direction, and γ completes the right hand

system. Note since γ is perpendicular to the conductor path and the radial direction, it is also perpendicular to the face of the rib next to the conductor.

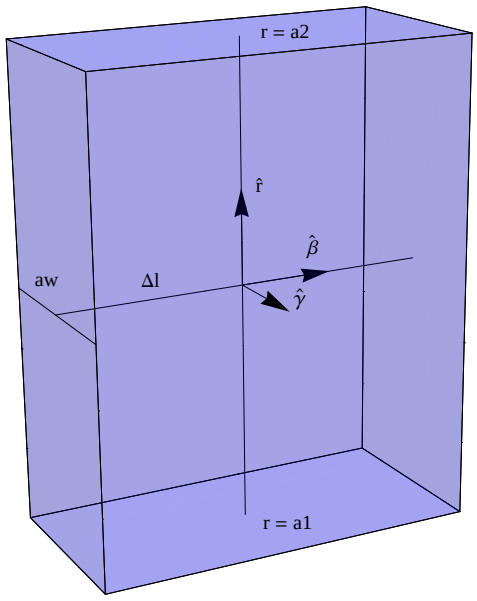

Figure 2.12: Conductor volume element showing the Frenet-Serret frame $(\beta(\theta), \gamma(\theta), r(\theta))$ following the center of the conductor path.

Since the β coordinate is defined in the direction of the current, the Lorentz force per volume in this frame only has r and γ components

$$\vec{f_{vol}} = \vec{J} \times \vec{B} = -JB_\gamma \hat{r} + JB_r \hat{\gamma}. \tag{2.71}$$

To approximate the pressure in the radial and rib direction the force is taken to be a constant throughout the conductor volume element (Fig. 2.12) and given by the value at the center of the (r, β, γ) frame. The pressure is then taken to be this force divided by the respective area of the face in question so that

$$p_\gamma = \frac{f_\gamma vol}{\Delta l(a_2 - a_1)} = \frac{f_\gamma \Delta l(a_2 - a_1)aw}{\Delta l(a_2 - a_1)} = f_\gamma aw \tag{2.72}$$

$$p_r = \frac{f_r vol}{aw\Delta l} = \frac{f_r \Delta l(a_2 - a_1)aw}{aw\Delta l} = f_r(a_2 - a_1), \tag{2.73}$$

where p_γ is the pressure on the rib, and p_r is the pressure in the radial direction. If I_0 is the magnitude of the current in the conductor, $J = \frac{I_0}{aw(a_2 - a_1)}$,

$$p_\gamma = \frac{B_r I_0}{a_2 - a_1} \tag{2.74}$$

$$p_r = -\frac{B_\gamma I_0}{aw}. \tag{2.75}$$

Substituting B_r for an arbitrary layer, the pressure on the rib due to the Lorentz forces for "ith" layer is

$$p_\gamma = -\frac{\mu_0 I_0^2 cot(\alpha)}{2w(a_2 - a_1)} \left(\sum_{k=1}^{i-1} f_r^o(r, a_{1k}, a_{2k}) + f_r(r, a_{1i}, a_{2i}) + (N - i) \right) sin(\theta), \tag{2.76}$$

where the radial form factors f_r^o and f_r are given in Equation 2.69.

This pressure is an approximation of the transverse stress on the Rutherford cable in the situation where the Lorentz forces do not accumulate (are completely captured by the mandrel ribs) and there is no bending of the structure. Equation 2.76 was compared to results from a finite element model. This model uses Biot-Savart to calculate the fields from a segmented CCT conductor path. It then calculates the Lorentz forces on each segment of the conductor and the approximate pressure based on the width of the Rutherford cable. A comparison between the results of this model and the formulation for a single 4.5 T CCT layer can be seen in Figure 2.13. The pressure on the rib is seen increasing from zero on the midplane (θ=0) to a maximum of around 4.5 MPa at the pole ($\theta = \pi/2$). A similar comparison was made for a four layer 18 T dipole (Fig. 2.14). This shows a maximum transverse cable stress of less than 20 MPa. If this is an accurate approximation for the CCT (stress interception and no bending), it shows an order of magnitude reduction in the conductor stress when compared to the traditional design approaches. This reduction in stress is the primary motivation for an in-depth investigation of the CCT for high field Nb_3Sn dipoles (see Section 1.3).

Radial Pressure

The radial pressure is given by

$$p_r = -\frac{B_\gamma I_0}{aw}, \tag{2.77}$$

which requires a description of the magnetic field in the γ direction. With the β direction defined by path normal

$$\hat{\beta} = \frac{\vec{n}}{|n|} = \frac{r\hat{\theta} + (rcot(\alpha)cos(\theta) + \frac{w}{2\pi})\hat{z}}{\sqrt{r^2 + (rcot(\alpha)cos(\theta) + \frac{w}{2\pi})^2}}, \tag{2.78}$$

a unit vector in the γ direction is found to be

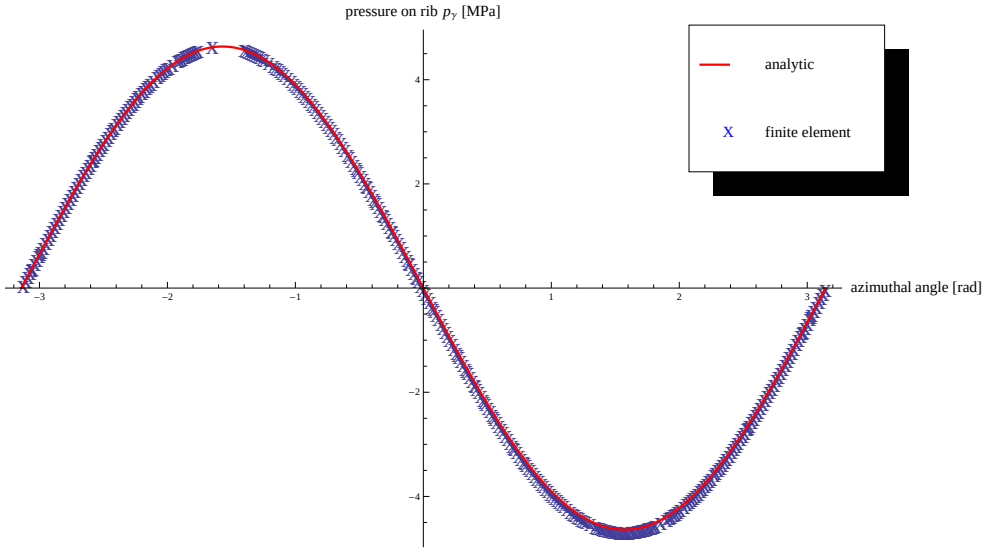

Figure 2.13: Comparison of Equation 2.76 with finite element results for a single 4.4 T layer: a_1=28 mm, a_2=43 mm, α=20 deg, w=7.34 mm, and I_0=16.1 kA.

$$\hat{\gamma} = \hat{\beta} \times \hat{r} = \frac{-r\hat{z} + (rcot(\alpha)cos(\theta) + \frac{w}{2\pi})\hat{\theta}}{\sqrt{r^2 + (rcot(\alpha)cos(\theta) + \frac{w}{2\pi})^2}}. \tag{2.79}$$

Then, the field in the γ direction can be found using

$$B_\gamma = B_\theta(\hat{\theta} \cdot \hat{\gamma}) + B_z(\hat{z} \cdot \hat{\gamma}) = \frac{-rB_z + B_\theta(rcot(\alpha)cos(\theta) + \frac{w}{2\pi})}{\sqrt{r^2 + (rcot(\alpha)cos(\theta) + \frac{w}{2\pi})^2}}, \tag{2.80}$$

which for a single layer results in

$$B_\gamma = -\frac{\mu_0 I_0 cot(\alpha)}{2w\sqrt{r^2 + (rcot(\alpha)cos(\theta) + \frac{w}{2\pi})^2}} \left(2rf_z tan(\alpha) + f_\theta cos(\theta)(rcot(\alpha)cos(\theta) + \frac{w}{2\pi})\right). \tag{2.81}$$

The radial pressure for a single CCT layer is then

$$p_r = \frac{\mu_0 I_0^2 cot(\alpha)}{2wa_w\sqrt{r^2 + (rcot(\alpha)cos(\theta) + \frac{w}{2\pi})^2}} \left(2rf_z tan(\alpha) + f_\theta cos(\theta)(rcot(\alpha)cos(\theta) + \frac{w}{2\pi})\right). \tag{2.82}$$

This pressure can be seen compared to results from the finite element model in Figure 2.15. The radial pressure is seen varying opposite of the rib pressure, decreasing from a maximum at the midplane to a minimum at the pole. The increased magnitude of the pressure is a

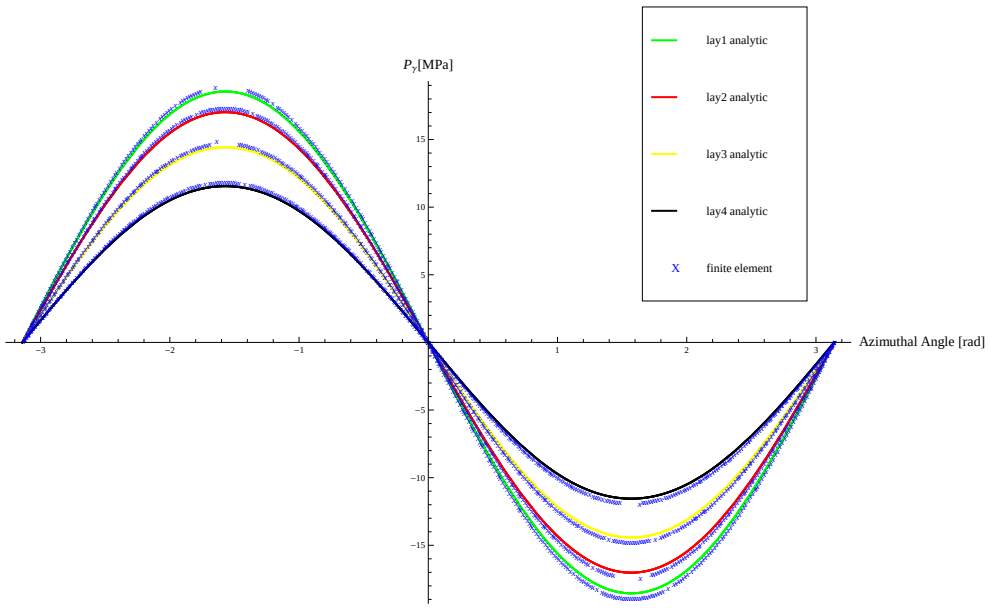

Figure 2.14: Comparison of Equation 2.76 with finite element results for a four layer 18 T dipole: inner radius of 28 mm, 15.35 mm layer radial thickness, 0.55 mm spacing between layers, w=7.34 mm, α=20 deg, and I_0=16.1 kA.

result of the cable cross section having a thickness in the radial direction that is about eight times larger than the transverse direction.

This approach can be extended for a multi-layer CCT magnet with field

$$B_\gamma = -\frac{\mu_0 I_0 cot(\alpha)}{2w\sqrt{r^2+(rcot(\alpha)cos(\theta)+\frac{w}{2\pi})^2}}\left(2rtan(\alpha)\left[(-1)^{i-1}f_z(r,a_{1i},a_{2i})+\frac{1}{2}\left((-1)^i-(-1)^N\right)\right]\right.$$
$$\left. + \; cos(\theta)\left(rcot(\alpha)cos(\theta)+\frac{w}{2\pi}\right)\left[\sum_{k=1}^{i-1} f_\theta^o(r,a_{1k},a_{2k})+f_\theta(r,a_{1i},a_{2i})+(N-i)\right]\right), \quad (2.83)$$

leading to a radial pressure in the "ith" layer varying as

$$p_r = \frac{\mu_0 I_0^2 cot(\alpha)}{2wa_w\sqrt{r^2+(rcot(\alpha)cos(\theta)+\frac{w}{2\pi})^2}}\left(2rtan(\alpha)\left[(-1)^{i-1}f_z(r,a_{1i},a_{2i})+\frac{1}{2}\left((-1)^i-(-1)^N\right)\right]\right.$$
$$\left. + \; cos(\theta)\left(rcot(\alpha)cos(\theta)+\frac{w}{2\pi}\right)\left[\sum_{k=1}^{i-1} f_\theta^o(r,a_{1k},a_{2k})+f_\theta(r,a_{1i},a_{2i})+(N-i)\right]\right). \quad (2.84)$$

Comparison of the multi-layer radial pressure to the finite element model is seen in Figure 2.16.

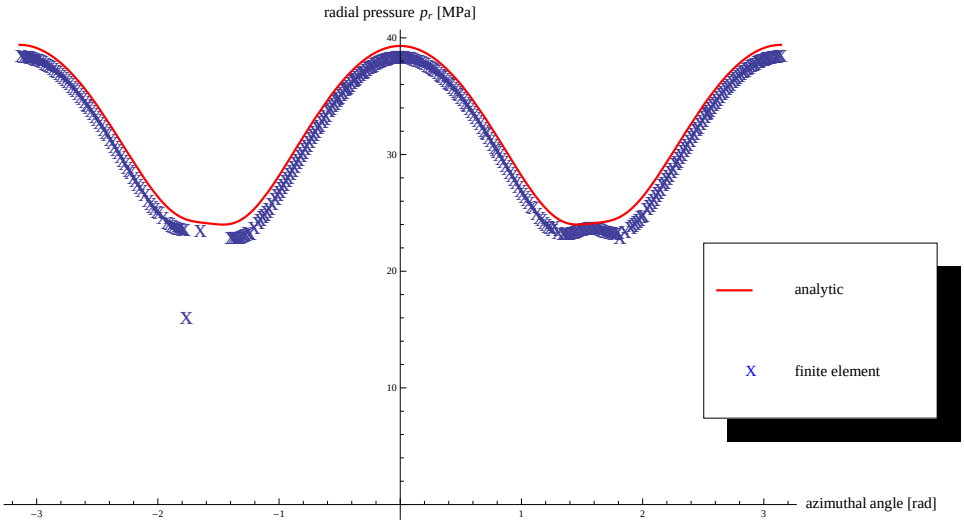

Figure 2.15: Comparison of Equation 2.82 with finite element results for a single 4.4 T layer: a_1=28 mm, a_2=43 mm, α=20 deg, w=7.34 mm, and I_0=16.1 kA.

2.7 Limitations of the analytic model

The formulation in Sections 2.2, 2.3, 2.4, and 2.5 makes several assumptions. The first is the region of interest is far enough from the ends of the magnet (in the straight-section). The second is the pitch is much smaller than the radius, and the third is the average current density is sufficiently accurate to describe the conductor. It is good practice to verify analytic representations using finite elements models during the design process, and here special care should be taken for magnets of very small bore and or short axial length. A critical calculation in the design of superconducting magnets is the maximum field on the conductor, necessary for determining the short-sample performance. A calculation of the maximum field at the conductor requires a specification of the true geometry of current which leads to a rise of field at the conductor when compared with the bore. In many cases, the pitch averaged current used in this analytic model is insufficient for this calculation.

The cable pressure in Section 2.6 is only an accurate approximation of the Lorentz force induced conductor stress in the case where there is no accumulation of force or bending of the mandrel. In reality the mandrels are not infinitely rigid and bending will occur, making this formulation the best case scenario. In practice the analytic pressure presented is best used for understanding the effect of forces within the magnet (general tendencies), and not to predict the stress state of the conductor. It serves to complement a detailed structural analysis done using a finite element model (to be discussed in Chapter 3).

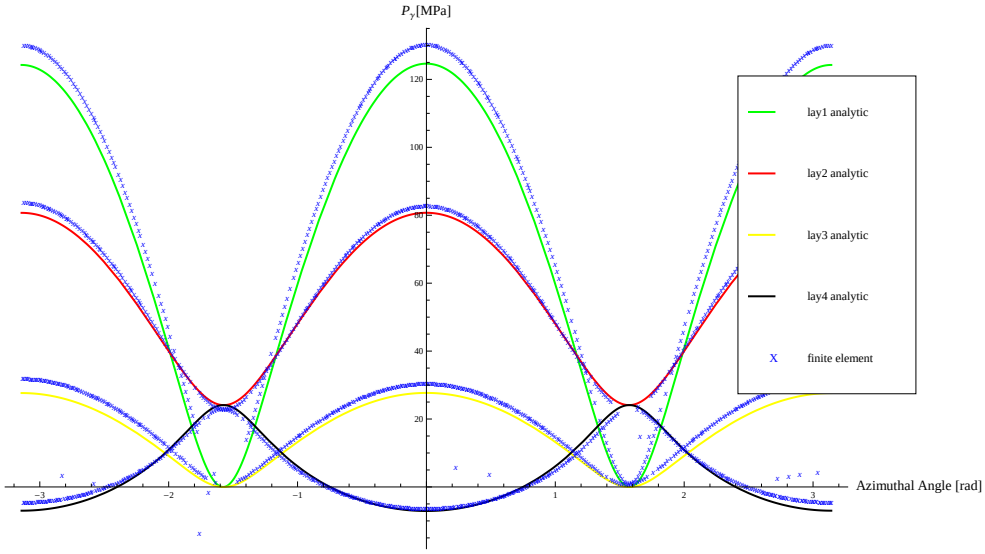

Figure 2.16: Comparison of Equation 2.84 with finite element results for a four layer 18 T dipole: inner radius of 28 mm, 15.35 mm layer radial thickness, 0.55 mm spacing between layers, w=7.34 mm, α=20 deg, and I_0=16.1 kA.

2.8 The 3D periodic symmetry region of the CCT

The CCT conductor path creates a region of symmetry in the mandrel that is axially periodic. This is a direct result of the periodic constraint placed on the path in Equation 2.4. The symmetry region mates end-to-end, and with conductor included can be repeated in a laminated fashion to form a complete CCT layer (Fig. 2.17, Fig. 2.18). A symmetry region for each layer and a laminated outer structure of the same axial thickness can be combined to form a symmetry region for the magnet as a whole.

The axial thickness of the laminated region is determined by the pitch of the conductor path. The pitch is defined as the turn-to-turn axial distance at the midplane and is calculated using

$$w = \frac{a_w + \delta_{rib}}{\sin \alpha}, \tag{2.85}$$

where a_w is the conductor width, δ_{rib} is the rib thickness at the midplane, and α is the tilt angle. This represents the period distance over which the symmetry region repeats, allowing the entire magnet to be built of this region displaced axially by integer numbers of the pitch.

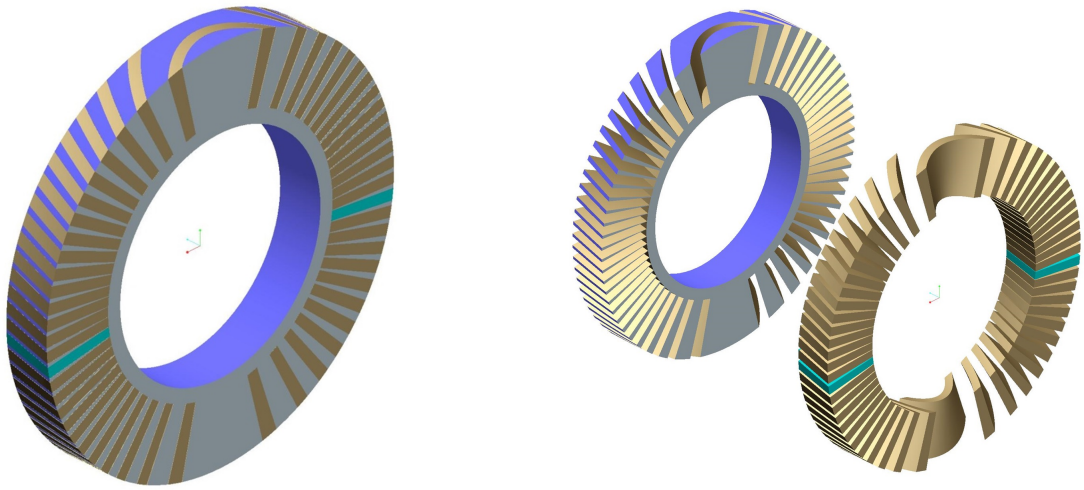

Figure 2.17: The conductor and mandrel forming the minimum symmetry region for one CCT layer is shown together and then separated. This symmetry can be repeated axially to form a CCT layer in a laminated fashion.

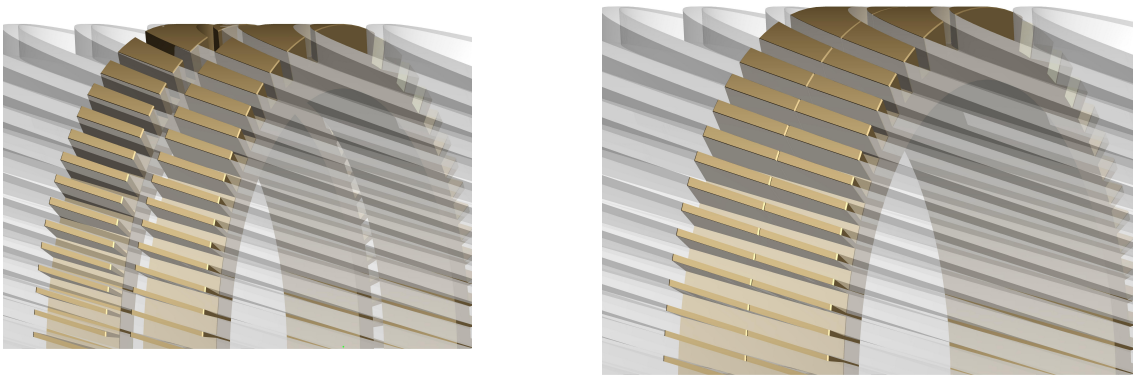

Figure 2.18: Two adjacent mandrel laminations are shown with a displacement and then mated. These laminations are identical and the conductor channels match perfectly end to end, representing the periodic symmetry in the winding path.

Comparison to the traditional straight-section symmetry

Traditional magnet designs have a 2D axial symmetry far from the ends (in the straight-section). This symmetry is typically used for the majority of the magnetic and structural analysis because of the dramatic reduction of finite element model size compared with the 3D model. The CCT has a fundamentally different straight-section symmetry consisting of a 3D periodic region (see Fig. 2.19 for a comparison). This symmetry has a similar advantage of

drastically reducing finite element model size, but requires the development of new analysis methods and boundary conditions due to its 3D nature.

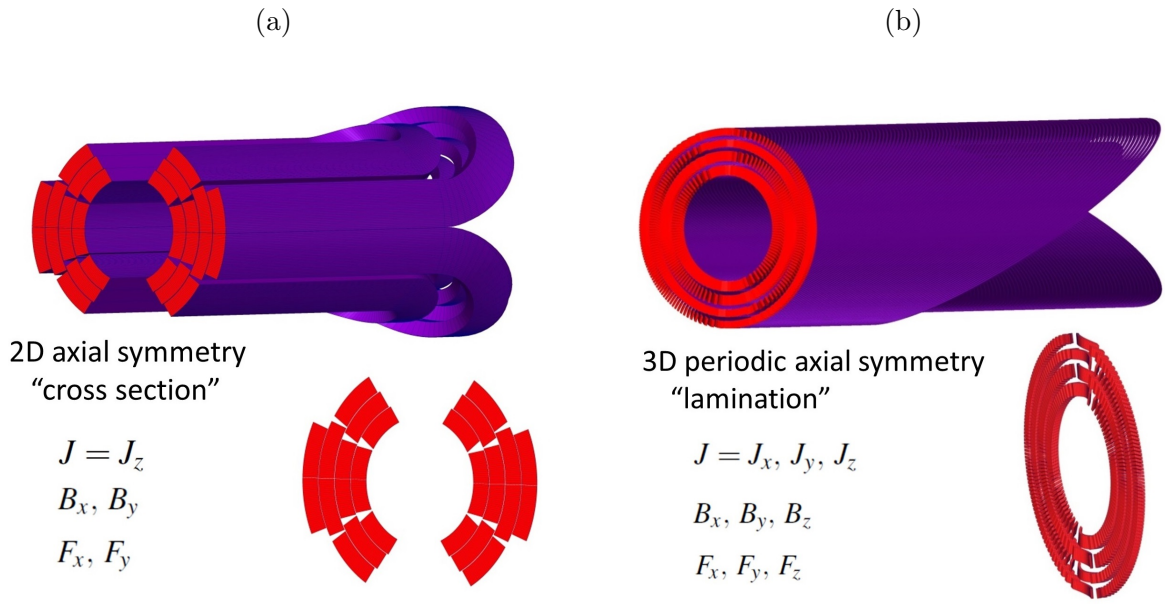

Figure 2.19: The 2D axial symmetry of a traditional cosine-theta dipole "cross section" (a) is shown compared to the 3D periodic symmetry region of the CCT "lamination" (b).

2.9 Magnetic and structural boundary conditions for the 3D symmetry

Boundary conditions for magnetic modeling

Magnetic modeling using the symmetry region requires periodic current and field conditions. These conditions maintain continuity when the region is patterned axially. They are enforced by requiring the fields and current at like positions on the two axial faces of the region are equal. Figure 2.20 shows an example symmetry region through a CCT dipole. The conditions for periodicity are

$$\begin{aligned} \vec{B}_1(x, y, z_1) &= \vec{B}_2(x, y, z_2) \\ \vec{J}_1(x, y, z_1) &= \vec{J}_2(x, y, z_2) \end{aligned} \tag{2.86}$$

where $\vec{B}$ and $\vec{J}$ are the magnetic field and current density at face 1 and face 2 as marked in the figure. These are the outer axial faces of the region (with thickness of a single pitch length w) such that $z_2 = z_1 + w$. The application of these conditions to finite element models will be discussed in Chapter 3.

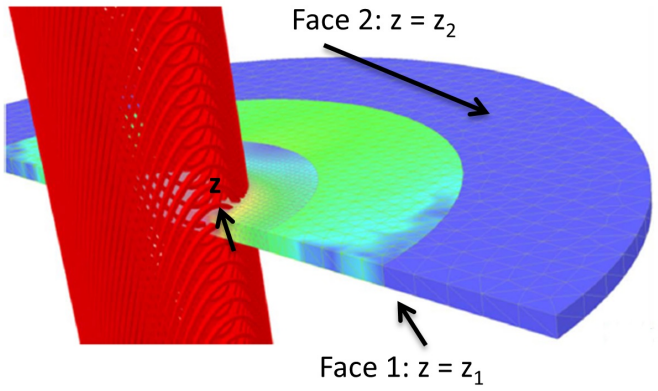

Figure 2.20: A periodic symmetry region is shown meshed around the conductor of a CCT dipole. The outer axial faces of this region are used for the specification of the periodic field and current conditions.

Boundary conditions for structural modeling

The periodic symmetry is enforced by relating the displacement of matching nodes on the two axial faces of the region. For matching nodes on face 1 and face 2 (Fig. 2.21), the constraint equations

$$\begin{aligned} u_{x2} - u_{x1} &= 0 \\ u_{y2} - u_{y1} &= 0 \\ u_{z2} - u_{z1} &= \delta_z \end{aligned} \tag{2.87}$$

couple the nodes' transverse displacement (u_x, u_y) and relate their axial displacement (u_z) to the constant length δ_z. This parameter allows for a change of axial length between nodes while still enforcing the periodic requirements of the symmetry region. Three different axial boundary conditions, set by the choice of δ_z, have been developed. Two of these model the extreme behavior of the problem and reproduce 2D plane strain and plane stress solutions when implemented on a 3D axially symmetric model [45]. The third choice is bounded by these two and is closer to the expected behavior of the CCT.

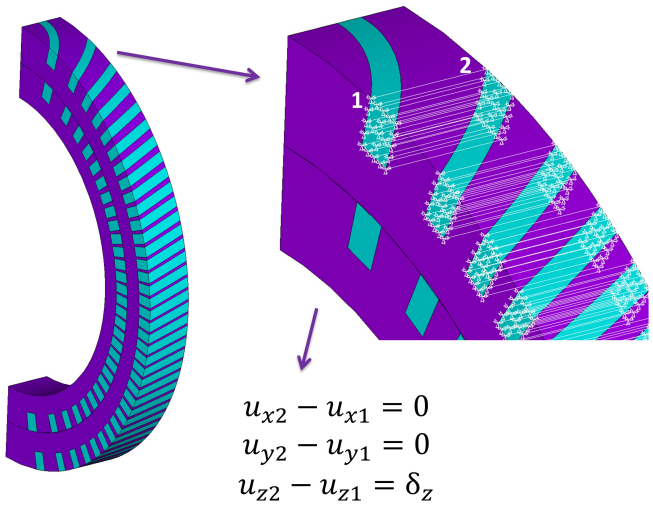

Figure 2.21: A two layer symmetry region of conductor and mandrels is shown. The constraint equations between lamination face nodes are shown graphically for the conductor of layer two.

Condition 1: Generalized Plane Strain

The generalized plane strain condition is implemented by setting $\delta_z = 0$ for all nodes on the constrained axial faces. The nodes are allowed to move axially, but required that as a pair they displace such that the axial length between them remains unchanged. Fixing the length between axial faces results in the development of large axial stress and force on the constrained surface during cooldown of the region. This condition is relevant to a highly unlikely test configuration where the ends of the magnet are held such that it is not allowed to strain axially, even during cooldown.

Condition 2: Single Strain

The second condition, closest to the expected behavior of CCT, is the choice of a single length change $\delta_z \neq 0$ for all constrained nodes. This is similar to *Condition 1*, but now the axial length of the region changes by a constant related to thermal contraction during cooldown. The single value for δ_z is determined such that the net force on the outer axial faces (surface between repeated magnet symmetry regions) is zero. This force is calculated by integrating the stress normal to the surface, and for a single component (CCT layer or structural element) is given by

$$F_i = \int_{S_i} \sigma_n dS_i, \tag{2.88}$$

where S_i represents the outer surface of the ith component. For this boundary condition, δ_z is chosen such that the sum of F_i over all components is zero (Eqn. 2.89). While net forces may develop on the faces of individual components, the net force over the entire magnet symmetry region surface is required to be zero. This condition is relevant to the test configuration where the magnet is allowed to strain axially, but all components (layers and structure) are tied together such that they strain the same. This boundary condition is closest to the expected behavior of a CCT magnet that has been impregnated such that the layers are all bonded together, or a CCT magnet with sufficient friction between layers that the strain is tied together at the layer to layer interface.

$$\sum_i F_i = 0 \tag{2.89}$$

Condition 3: Generalized Plane Stress

The generalized plane stress condition is implemented by choosing a unique δ_z for each component such that the net force on the face of that individual component is zero (Eqn. 2.90). The value of δ_z for each component is primarily determined by its thermal contraction. A CCT layer with the conductor and mandrel bonded is treated as a single component with the same δ_z used for both, with δ_z chosen such that the net normal force on the layer is zero (*Condition 2* for mandrel and conductor).

$$F_i = 0 \quad \text{for all i components} \tag{2.90}$$

This boundary condition is applicable for a CCT magnet with perfect slip planes between layers. In this case each layer is allowed to have its own axial strain such that no net axial force builds up for each individual layer. Methods for the implementation of these boundary conditions in finite element structural models will be introduced in Chapter 3.

Chapter 3

Finite Element Modeling of CCT Dipoles

3.1 Brick element representation of the conductor

The design of CCT magnets in this thesis assumes conductor in the form of a Rutherford cable. This cable is made up of individual strands which contain the superconducting material along with copper for stabilization. To reduce complexity and calculation time, the representation of the conductor used in this chapter will remain at the cable level. The electrical and mechanical properties of the strands are averaged across the cross section of the cable, such that the conductor is modeled by a rectangular cross section of uniform properties following the CCT path. This continuous conductor is then discretized into eight node brick elements as needed for finite element calculations.

To produce the brick elements, a rectangular cross section corresponding to the cable dimensions (described by four points) is placed at discrete intervals along the central path of the CCT winding. For a dipole, this path is given by Equation 2.15. The orientation of the cable cross section about the central path is chosen such that the cable height is aligned with the radial direction. This allows for winding mandrel channels to be machined with a cutter moving radially inward with respect to a cylindrical surface. The connection of adjacent cross sections generates the eight node brick elements. The level of discretization can be controlled by using equal steps $d\theta$ of the parametric variable θ, such that $n_{div} = 2\pi/d\theta$ is the number of divisions created per CCT turn. Figure 3.1 shows an example of the conductor generated for a single CCT dipole turn using 120 eight node brick elements.

3.2 Magnetic modeling in Opera3D

As will be shown in the design of CCT1 and CCT2 (Chapters 5 and 6), CCT magnets can achieve excellent straight-section and integrated field quality without the use of iron. For

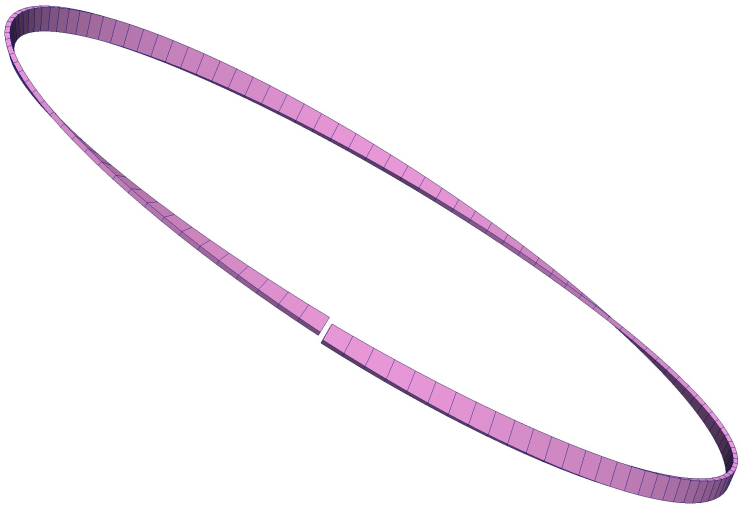

Figure 3.1: A single CCT dipole turn discretized into eight node brick elements is shown.

this reason it is likely the role of iron in CCT magnets will be limited to the reduction of stray fields. In this case, field quality and field at the conductor calculations can be performed without the consideration of iron (which can be added later based on the stray field specifications of the accelerator). Without the mesh required for calculations using iron, the Post-Processor of the commercial software Opera3D can be used [43].

The conductor geometry for each CCT layer is imported into the Post-Processor of Opera3D in 8-node brick element form. Here, the eight nodes of each discretized element described in Section 3.1 are written to a ".cond" file along with the average current density of the element. The format of a ".cond" file is shown in Figure 3.2. Here, only the first two brick elements of a single layer are included in order to show the required header and footer. The current density corresponds to the power supply current divided by the cross section of the cable. The current type is set to "1.0" to represent a full 3D treatment of the conductor geometry. If a value of "-1.0" is used, the current density will be approximated as a line current at the center of the brick. This may be used to speed up calculations far from the conductor, or more generally in situations where less accuracy is required.

After setting the units in the Post-Processer, the ".cond" file can be loaded to import the conductor. Once the conductor for all layers has been imported, the generation of the 3D magnetic model is complete. This model can be used for calculation of both straight-section and integrated harmonics, as well as the field at the conductor needed for the determination of the short-sample limit. It can also be used to calculate the Lorentz forces, providing the operational loads for the structural analysis. The 3D periodic symmetry and magnetic boundary conditions (discussed in Sections 2.8 and 2.9) are relevant to straight-section cal-

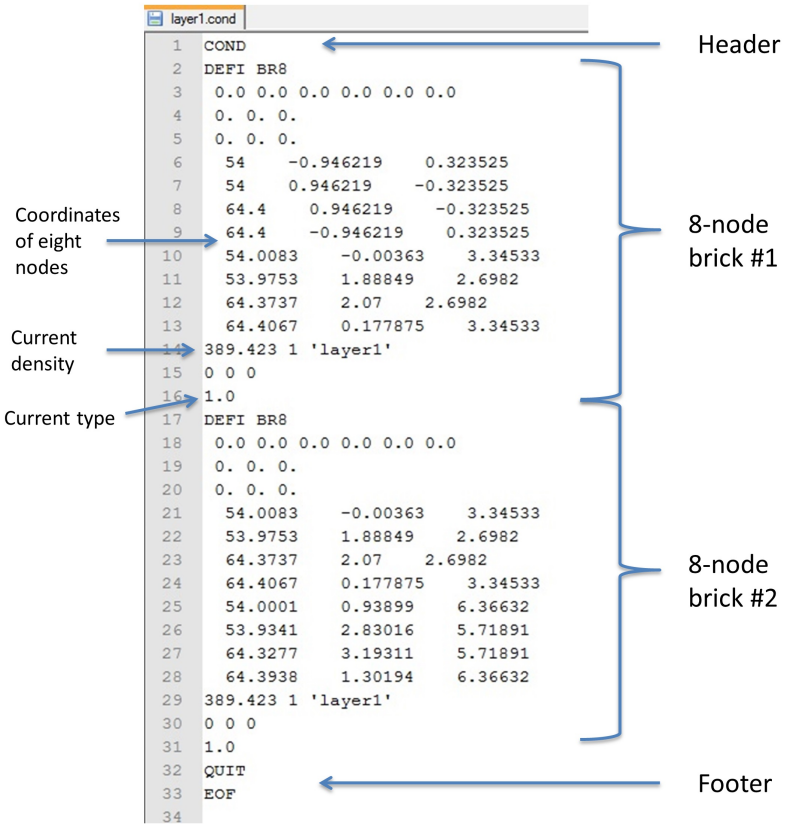

Figure 3.2: An example of a .cond file "layer1.cond" is shown for importing the first two 8-node brick element conductors into Opera3D.

culations only (far from ends). This symmetry is useful in reducing computation time for Opera3D models requiring a mesh (for example, when real iron is included). To implement the periodic boundary conditions described in Section 2.9, the "PERIODICITY" command is used. For example, the command

```
PERIODICITY NSETS=1 DX1=0 DY1=0 DZ1=7.2 ROTX1=0 ROTY1=0 ROTZ1=0 ANGLE1=0 TYPE1=positive OPTION1=MATCH
```

can be used in the Modeler before the generation of the mesh. This forces the potential and geometry to be the same on both sides of a symmetry model with example axial pitch length $w = 7.2$ (consider Figure 2.20 with $z_1 = 0$ and $z_2 = 7.2$).

3.3 Structural modeling in ANSYS

A method for mechanical modeling of the CCT using the commercial software ANSYS [46] was developed. This method implements the 3D periodic symmetry region and structural

boundary conditions described in Sections 2.8 and 2.9. Additional information on the structural modeling of CCT dipoles can be found in [47].

Generation of the model geometry

The first step in the creation of the ANSYS model is the generation of the conductor geometry. The conductor is modeled with a solid rectangular cross section corresponding to the height and width of the Rutherford cable used. The central path of this cable for each conductor layer is generated using Equation 2.15. The rectangular cable cross section is then placed at discrete intervals along this path. This models the continuous cable using discrete brick elements (as previously described in Section 3.1). A pitch length is cut out of this path at the center of the winding, and then sliced at 180 degrees (see Fig. 3.3). This generates the conductor brick elements of the symmetry region to be used in ANSYS. Only 180 degrees of region is chosen to reduce the size of the model. This is an approximation, as the 180 degree symmetry is slightly broken by the axial pitch of the CCT winding.

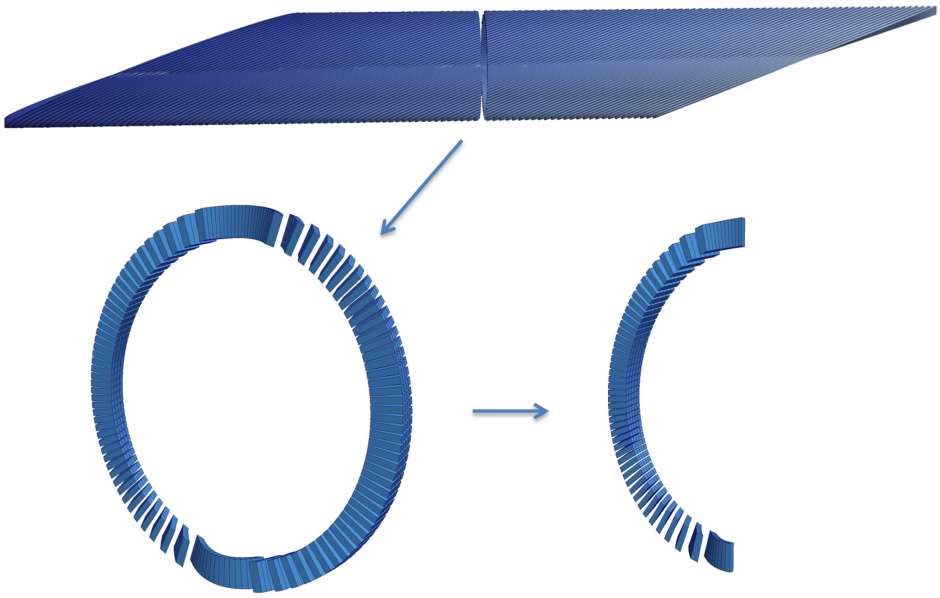

Figure 3.3: The method for generating the 180 degree symmetry region from the brick element path is illustrated for a CCT dipole conductor layer.

The eight corners specifying each conductor brick element are generated as keypoints in ANSYS. The areas of each brick are created from these keypoints followed by the generation of a volume from the areas. Then, the volumes of adjacent conductors are merged as the final step in the generation of the conductor geometry. A winding mandrel for each layer is generated by a cut-out boolean operation between a thick walled cylinder and the conductor.

Finally, the geometry of any structure outside the CCT layers is generated using a 2D cross section extruded a pitch length in the axial direction. For example, figure 5.11 shows the final result of this process in ANSYS for CCT1.

Meshing the geometry

The ANSYS model is meshed using the 20 node volume element type SOLID186. A meshing process was developed to ensure the two outer axial faces of the model have the exact same mesh. It is crucial to mesh these faces the same due to the periodic boundary conditions (see Section 2.9). These conditions are applied between like nodes on these two faces requiring there be a matching node on each face. The method developed begins by meshing one of the two faces using the surface element MESH200. This is a "mesh-only" element type in ANSYS that does not contribute to the solution (no material properties, real constants, etc.). This surface mesh is then copied to the other axial face using the MSHCOPY command. Then a VMESH command is used to mesh the volume with SOLID186 elements, where the "mesh-only" surface elements already created force the generation of a mesh that is the same on the two outer faces. The conductor bricks are meshed with hexahedral elements, and the more complex mandrel geometry is meshed using less accurate tetrahedral elements.

Applying the loads

Three load steps are typically considered: assembly, cooldown, and operation. The first is an "assembly" step where any pre-stress from an outer structure is applied, the second is a "cooldown" of the model from room temperature to liquid helium (4.2 or 1.9 K), and the third is the application of the "operation" Lorentz forces due to energization of the magnet. The first load is dependent on whether an outer pre-loading structure is used, and when necessary is usually applied by means of an interference between surfaces. The second load step is applied by first specifying room temperature with the TREF command and then the temperature to be cooled down to using the BFUNIF,TEMP command.

The application of the Lorentz force loads is more complicated. First the centroid location of each ANSYS conductor mesh element is exported. These locations are imported into the Opera3D magnetic model so the Lorentz force at each centroid can be calculated. This Lorentz force is then exported from the Opera3D model back to the ANSYS model where force at each element's centroid is distributed equally on that element's nodes. It is typical to solve the ANSYS model in the order of these load steps to simulate the magnet at each point from assembly to operation. This results in three solutions corresponding to the following: assembly loads; assembly and cooldown loads; and assembly, cooldown, and operation loads. This incremental loading method has been previously applied to other magnet designs such as the LARP quadrupoles [48].

Applying the boundary conditions

The 180 degree symmetry of the model is specified by fixing the azimuthal displacement of all the nodes at the poles (± 90 degrees). The model is further constrained by fixing the displacement of a single node at the midplane (0 degrees) in the axial and azimuthal directions. The periodic boundary condition is applied to each pair of matching nodes on the axial faces using the constraint in Equation 2.87. A script is used to find the node numbers of the two matching nodes (based on having the same transverse positions), after which the constraint equation is applied. The value of δ_z used is determined by the choice of one of the three axial boundary conditions discussed in Section 2.9.

The axial boundary condition most frequently used is the "single-strain" condition, which applies a single δ_z value to the entire model. As described in Section 2.9, the value of δ_z is chosen such that the net axial force is zero on the outer faces of the entire model. The correct value for this parameter can be determined by solving the ANSYS model with two guesses for δ_z and using the net force results to interpolate the zero net force value. An example of this process is shown in Figure 3.4. To calculate the net axial force the nodes on the outer face of the region are selected and a FSUM command is used.

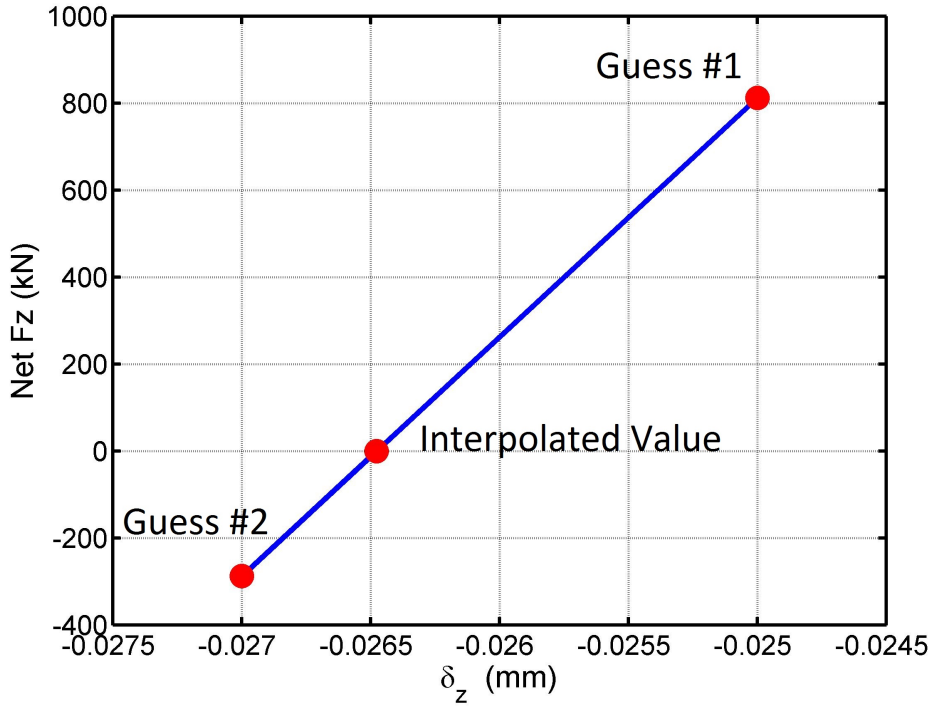

Figure 3.4: An example of two guesses and the interpolated zero force value for δ_z is shown. Each case represents a solution of the ANSYS model with the "single-strain" condition using the respective value for δ_z.

Stress and strain results in a local cable frame

It is valuable to have a method for viewing the conductor stress results in a coordinate system local to the conductor path, allowing for the determination of the tangential, transverse, and radial stress within the cable. This requires post-processing beyond what is contained in ANSYS due to no global coordinate system being aligned with the 3D path of the conductor. A method was developed to export the conductor stress and strain from ANSYS, convert the results to the local conductor frame, and display them in the open source software ParaView [49].

The definitions for the local tangential $\hat{t}$ and transverse $\hat{b}$ directions are found in Equations 2.2 and 2.3, and illustrated in Figure 2.1. For a CCT dipole layer, Equation 2.15, the tangential, radial, and transverse direction unit vectors in cartesian coordinates are given by

$$\begin{aligned}
\hat{t} &= \frac{-\sin\theta\hat{x} + \cos\theta\hat{y} + \left[\cot\alpha\cos\theta + \frac{w}{2\pi r}\right]\hat{z}}{\sqrt{1 + \left[\cot\alpha\cos\theta + \frac{w}{2\pi r}\right]^2}} \\
\hat{r} &= \cos\theta\hat{x} + \sin\theta\hat{y} \\
\hat{b} &= \frac{\left[\cot\alpha\cos\theta + \frac{w}{2\pi r}\right]\left[-\sin\theta\hat{x} + \cos\theta\hat{y}\right] - \hat{z}}{\sqrt{1 + \left[\cot\alpha\cos\theta + \frac{w}{2\pi r}\right]^2}},
\end{aligned} \tag{3.1}$$

where the sign of the tilt angle α alternates between layers in a multi-layer CCT dipole magnet. These unit vectors can be used to transform stress and strain results from the global cartesian coordinate system x, y, z to the local system t, r, b using

$$\begin{aligned}
\sigma_{trb} &= Q \cdot \sigma_{xyz} \cdot Q^T \\
\epsilon_{trb} &= Q \cdot \epsilon_{xyz} \cdot Q^T,
\end{aligned} \tag{3.2}$$

where σ_{xyz} is the Cauchy stress tensor in the cartesian frame, ϵ_{xyz} is the strain tensor in the cartesian frame, and Q is the transformation matrix to the local frame given by Equation 3.1 and

$$Q = \begin{pmatrix} t_x & t_y & t_z \\ r_x & r_y & r_z \\ b_x & b_y & b_z \end{pmatrix}. \tag{3.3}$$

To calculate the local stress and strain tensors (Eqn. 3.4 and 3.5) the conductor element nodes are first selected in ANSYS and a NLIST command is used to export the node locations to a data file. Then a PRNSOL command is used with the relevant option to export the nodal ANSYS solution results (stress or strain tensor for each node) in the cartesian coordinate system. A script is then run that calculates the values of r, θ for each node and evaluates Equations 3.1 and 3.3 to find Q for each node. Finally, the nodal ANSYS results are transformed into the local conductor coordinate frame for each node using Equation 3.2.

$$\sigma_{trb} = \begin{pmatrix} \sigma_{tt} & \sigma_{tr} & \sigma_{tb} \\ \sigma_{rt} & \sigma_{rr} & \sigma_{rb} \\ \sigma_{bt} & \sigma_{br} & \sigma_{bb} \end{pmatrix} \tag{3.4}$$

$$\epsilon_{trb} = \begin{pmatrix} \epsilon_{tt} & \epsilon_{tr} & \epsilon_{tb} \\ \epsilon_{rt} & \epsilon_{rr} & \epsilon_{rb} \\ \epsilon_{bt} & \epsilon_{br} & \epsilon_{bb} \end{pmatrix} \tag{3.5}$$

Figure 3.5 shows an example of this process for a single conductor layer. Three images show the conductor stress displayed in the global cylindrical coordinate system in the ANSYS postprocessor. This stress is then shown converted to a local frame and displayed in the program ParaView with the approximate 180 degree symmetry expanded to a full turn. This allows the determination of the tangential σ_t, radial σ_r, and transverse σ_b stress at all points along the conductor path. Because of the 3D path of the cable, all three cylindrical coordinates are only aligned with the local frame at the pole location ($\theta = \pm 90$ degrees) where $t = \theta$, $r = r$, and $b = z$. This allows for a convenient check of the transformation results in the pole region where $\sigma_t = \sigma_\theta$, $\sigma_r = \sigma_r$, and $\sigma_b = \sigma_z$.

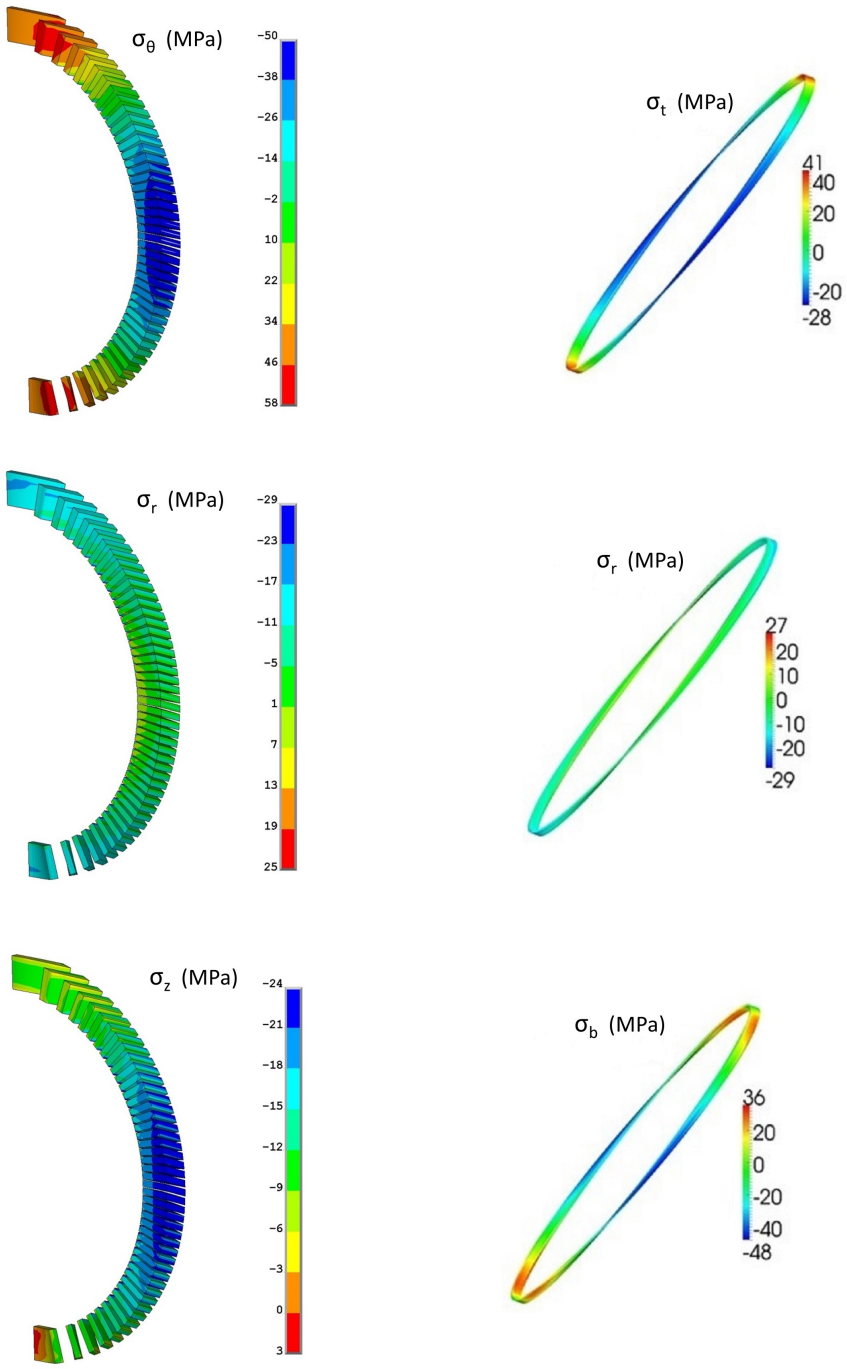

Figure 3.5: ANSYS stress results for a single conductor layer are shown using the ANSYS viewer in the global cylindrical frame (r, θ, z). The stress results are also shown converted to a local conductor frame (t, r, b) and plotted in the program ParaView as a single continuous conductor turn.

Chapter 4

Design Choices and Optimization for High Field CCT Dipoles

4.1 Goals and overview

This chapter seeks to present important considerations for the design of high field CCT dipoles. Rather than developing a fixed step by step optimization process, the goal is to identify and discuss key design choices such that the reader gains an understanding of what drives the scaling and efficiency of the CCT design. Section 4.2 begins the chapter with a discussion of the efficiency of the CCT for producing dipole fields. Next, Section 4.3 develops the formulation for the amount of conductor used in a single layer and a multi-layer magnet. Section 4.4 presents a set of design parameters for the CCT. The choice of the key free parameters is discussed in detail in Sections 4.5, 4.6, and 4.7. During this discussion, a method for grading the outer layers of a multi-layer CCT magnet will be presented to reduce the amount of conductor and coilpack size needed to reach a desired dipole field. Finally, Section 4.8 presents a cost comparison study between graded and ungraded Nb_3Sn CCT dipole designs ranging from two to eight layers (11-17 T).

4.2 Efficiency of a CCT layer: comparison to an ideal cosine-theta

A CCT layer has two sources of inefficiency when considering the production of a dipole field. The first is associated with the generation of undesired fields which are canceled between layers (namely the solenoid), and the second is associated with the reduction in current density due to mandrel ribs between turns at the midplane. The inefficiency can be quantified by comparing a CCT dipole layer to an ideal cosine-theta current density of the same thickness. The dipole field produced by an ideal density $J_z = J_{eng}\cos(\theta)$ of radial thickness b_w is

$$B_1 = \frac{\mu_0 J_{eng} b_w}{2}. \tag{4.1}$$

The magnitude of the dipole is dependent only on the current density and radial thickness, and is independent of the radius at which the layer is located. This is an important characteristic of dipole windings that is often misunderstood. It can be shown the dipole produced by a CCT layer of cable width a_w, cable height b_w, and engineering current density $J_{eng} = I_0/a_w b_w$ is given by

$$B_{1CCT} = \frac{\mu_0 J_{eng} b_w}{2} \epsilon_{cct}. \tag{4.2}$$

The efficiency ϵ_{cct} then determines the difference between the dipole field generated by a CCT and an ideal cosine-theta layer. This efficiency can be written as

$$\epsilon_{cct} = \frac{\cos(\alpha)}{1 + \delta/a_w}, \tag{4.3}$$

where δ is the rib thickness between turns at the midplane and α is the tilt angle. The pitch relation to these parameters, as would be needed for the generation of a dipole path using Equation 2.15, is

$$w = \frac{a_w + \delta}{\sin(\alpha)}. \tag{4.4}$$

Assuming a small variation in the choice Rutherford cable widths a_w, the two design choices that affect ϵ_{cct} are the tilt angle and midplane rib thickness. It is seen the effect of the tilt angle is non-linear and behaves as $\cos\alpha$. This means the inefficiency associated with the angle can be kept below 5% with a choice of less than 18 degrees (additional considerations for the choice of an optimal tilt angle will be further discussed in Section 4.5). Despite how it may appear after a first glance at the CCT design, the key contribution to the inefficiency comes from the midplane rib and not from tilting the windings. Experience at LBNL has shown a midplane rib of not less than 15 thousandths of an inch (0.381 mm) is necessary to avoid breakage of the rib during machining of the mandrel channels. With the typical width of a Rutherford cable a_w being near 2 mm, the effect of using a 0.381 mm midplane rib is the reduction of efficiency by 15-20%. With both the effect of the midplane rib and tilt angle considered, typical values for ϵ_{cct} are around 80%.

Eliminating the midplane rib entirely has been identified as an area for future research. In this case, a δ of zero is used so adjacent turns are touching at the midplane. Moving to zero rib would eliminate the breakage issues below 15 thousandths of an inch, but would require the rib be introduced away from the midplane in a way that does not create a sharp edge with the potential to damage the conductor. Care would also have to be taken to prevent turn-to-turn electrical shorts where adjacent turns are touching. This is an area of future study that has the potential to boost the efficiency of a CCT layer to a point where it is more than 95% efficient with respect to an ideal cosine-theta current distribution.

4.3 Conductor length

A key consideration in the design of superconducting magnets is the amount of superconductor used. For high field Nb_3Sn dipole magnets, the cost of the Nb_3Sn superconductor itself is a significant if not dominant fraction of the total magnet cost [50]. When the potential demand for several thousand high field dipoles for a future hadron collider is considered, it is of extreme importance to minimize the amount of conductor (and thus cost) needed to reach the desired dipole field.

Path length of a CCT turn

Section 2.2 describes a CCT turn using a parametric path confined to the surface of a cylinder. If this surface is at fixed radius r, the length of a parametric path is given by

$$l = \int ds, \tag{4.5}$$

where in cylindrical coordinates

$$ds = \sqrt{dr^2 + r^2 d\theta^2 + dz^2} = \sqrt{r^2 + \left(\frac{dz}{d\theta}\right)^2} d\theta. \tag{4.6}$$

Using the path previously derived for a dipole layer (Equation 2.15),

$$ds = r\sqrt{1 + \left(\cot(\alpha)\cos(\theta) + \frac{w}{2\pi r}\right)^2} d\theta. \tag{4.7}$$

The length of a single turn is then given by

$$l_{turn} = r\int_0^{2\pi} \sqrt{1 + \left(\cot(\alpha)\cos(\theta) + \frac{w}{2\pi r}\right)^2} d\theta \approx r\int_0^{2\pi} \sqrt{1 + \cot^2(\alpha)\cos^2(\theta)} d\theta, \tag{4.8}$$

which can be expressed in terms of elliptic integrals. It is seen that the conductor length of a single turn is linearly proportional to the radius and a constant determined by the tilt angle

$$l_{turn}(r, \alpha) = C_l(\alpha) r \qquad C_l(\alpha) \approx \int_0^{2\pi} \sqrt{1 + \left(\frac{\cos(\theta)}{\tan(\alpha)}\right)^2} d\theta. \tag{4.9}$$

Path length of a CCT layer

A CCT layer is different from traditional designs in that it has no variation of the conductor path along the length of the magnet. The conductor in the straight-section and end region

is formed by the same expression for a single turn patterned axially. In this case, the total conductor length of a CCT dipole layer is simply given by

$$l_{lay}(r, \alpha, n_{turns}) = l_{turn} n_{turns} = r C_l(\alpha) n_{turns} \tag{4.10}$$

where n_{turns} is the total number of turns making up the layer.

In some cases it is desirable to know the conductor length based on the geometric properties of the layer. In particular it is convenient to know the amount of conductor used per magnetic length. For a CCT layer with sufficient straight-section, the magnetic length L_m is given by the distance between the first and last turn on the midplane (see Figure 4.1). This makes the number of turns for a given magnetic length $n_{turns} = L_m/w$. Considering the definition of the pitch in Equation 4.4, the path length for a CCT layer as a function of radius, tilt angle, and magnetic length can be written as

$$l_{lay}(r, \alpha, L_m) = \frac{L_m l_{turn}}{w} = \frac{L_m}{a_w + \delta}\, r\, \sin\alpha\, C_l(\alpha). \tag{4.11}$$

Length of strand in a multi-layer CCT magnet

The parametric path length of a CCT layer given in Equations 4.10 and 4.11 is representative of the length of Rutherford cable used. Given the assumption each layer has the same number of turns, the total cable path length per magnetic length for a multi-layer dipole magnet of n_{lay} layers is

$$\frac{l_{cable}}{L_m} = \sum_{i=1}^{n_{lay}} \frac{l_{turn}(i)}{w}, \tag{4.12}$$

where $l_{turn}(i)$ is the single turn length of the "ith" layer. Given that the layers in a multi-layer magnet may be graded by changing the number of strands, the overall strand length used per magnetic length is

$$\frac{l_{strand}}{L_m} = \sum_{i=1}^{n_{lay}} \frac{l_{turn}(i) n_s(i)}{w} \tag{4.13}$$

where $n_s(i)$ is the number of strands in the cable of the "ith" layer.

4.4 Design parameters

A set of design parameters can be seen in Table 4.1 for a CCT layer and in Table 4.2 for a CCT magnet. The central radius r, cable width a_w, midplane rib δ, and tilt angle α define the pitch and parametric path for the center of the layer's Rutherford cable according to Equation 2.15. Here the choice has been made to replace the pitch w with the cable width a_w and the midplane rib δ (Equation 4.4). This provides a more physically intuitive set of parameters. To complete the description of a layer, either the number of turns n_{turns},

magnetic length L_m, or the tip-to-tip physical length L_{tot} can be specified. In this case the tip-to-tip physical length L_{tot} was chosen to better correspond to accelerator specifications.

Table 4.1: CCT Layer Parameters

Parameter	Type	Criteria
r	fixed	set by specification of clear bore then radial buildup
a_w	fixed	set by typical Rutherford cable
δ	fixed	set by machining limit
L_{tot}	fixed	set by specification of physical length
b_{spar}	fixed	set by fabrication, bending stiffness
b_w	semi-free	key design choice, but must be practically windable
α	free	key design choice

Assumptions about which parameters are set by magnet specifications are seen in the tables. It is assumed the clear bore of the magnet will be specified. This combined with a radial buildup of spar thicknesses b_{spar} and cable heights b_w set the central radii r for each layer. It is also assumed the physical length available for the magnet in the accelerator L_{tot} will be a fixed specification. There are also some parameters which are fixed by practical considerations. For example, the width of the Rutherford cable a_w is fixed as two strand diameters with some compaction factor. There is also a practical restriction on the cable height b_w related to the hard way bend radius in the pole region. If the layer radius is too small or the cable height is too large, the hard way bend can result in damage to the cable during winding. The minimum thickness of the midplane rib δ is also practically restricted based on machining experience at LBNL (previously discussed in Section 4.2).

Table 4.2: CCT Magnet Parameters

Parameter	Type	Criteria
I_0	semi-free	may not exceed short-sample limit
n_{lay}	free	key design choice

With the assumption a certain number of parameters are fixed by the magnet specifications and practical considerations, only several key design choices remain. With the power supply current I_0 fixed by the short-sample, these free parameters are the tilt angle α, cable height b_w (corresponding to the number of strands), and number of layers n_{lay}. Section 4.5 will examine the choice of the tilt angle α in detail, and show for a fixed physical L_{tot} there is an optimal angle to maximize the integrated dipole field. The other two free parameters are closely coupled. There is a trade-off between the cable height b_w of the innermost layer and number of layers n_{lay} needed to reach a desired dipole field. This trade-off will be discussed in detail in Section 4.6.

4.5 Choice of midplane tilt angle α

The tilt angle α is a key design choice for a CCT magnet. This section will examine the effect of the tilt angle on magnet geometry, conductor use, and integrated dipole field. It will be shown that an "optimal" tilt angle exists which maximizes the integrated dipole field for a fixed magnet length.

Geometric effects

The geometric total length L_{tot}, end length L_e, and magnetic length L_m of a single layer are defined in Figure 4.1. The number of turns n_{turns} to make the total length L_{tot} can be determined from the pitch w and the end length $L_e(\alpha, r)$, both of which are non-linear functions of the midplane tilt angle α.

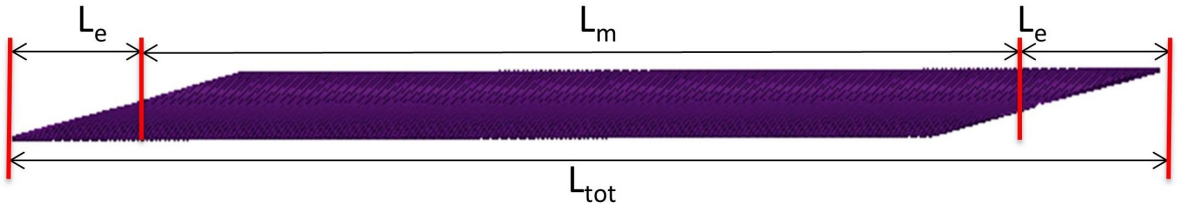

Figure 4.1: A single CCT layer is shown with the total physical length L_{tot}, end length L_e, and magnetic length L_m indicated.

As the tilt angle decreases, both the end length

$$L_e = \frac{r}{\tan \alpha} \tag{4.14}$$

and pitch (Equation 4.4) increase. If the total physical length L_{tot} is kept constant, this results in a smaller number of turns n_{turns} and decreased magnetic length $L_m = w n_{turns}$. In summary, the geometric effect of changing α for a fixed magnet length L_{tot} is to determine the end and straight-section fractions of the total magnet length. Reducing the tilt angle converts straight-section length into end length. Figure 4.2 and 4.3 illustrate this behavior for a typical CCT layer with a total length of 2.2 m.

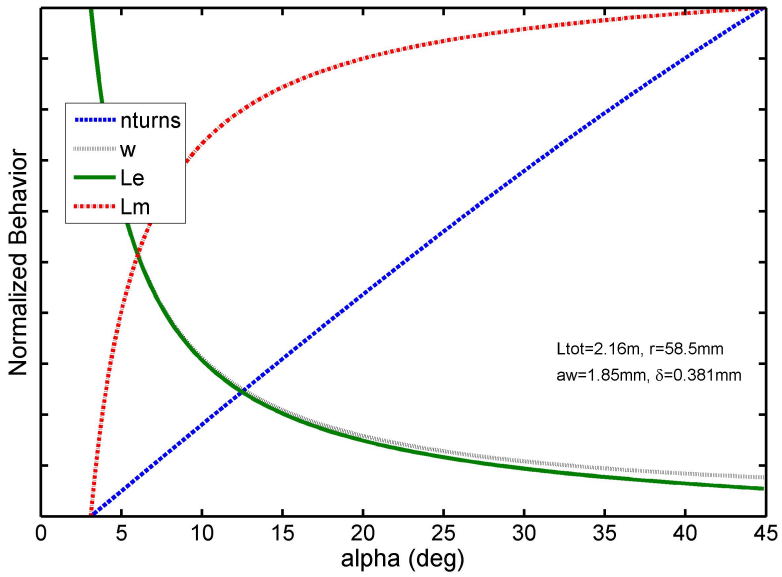

Figure 4.2: Normalized behavior of the pitch, number of turns, and end length is shown as a function of tilt angle for a single layer of fixed total length.

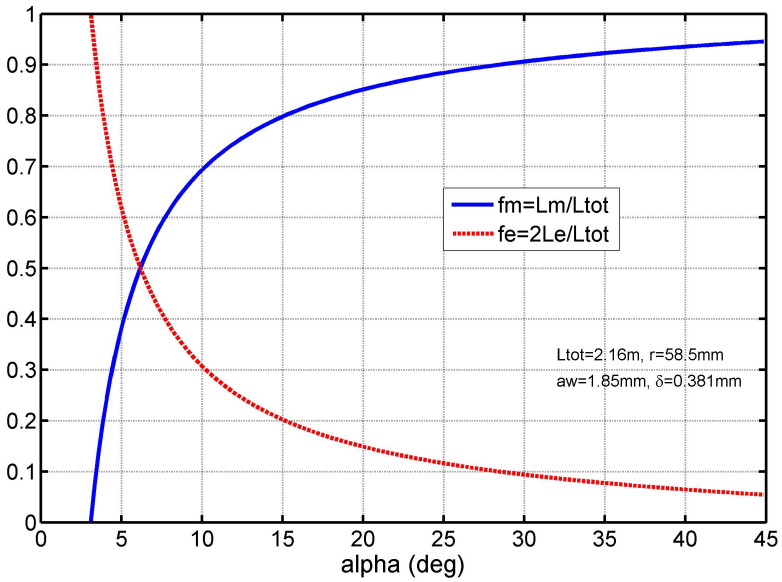

Figure 4.3: The fractional geometric end and straight-section length is shown as a function of tilt angle for a single layer of fixed total length. It is seen that the effect of a smaller tilt angle is to convert straight-section length into end length.

Magnetic effects

The form of dipole harmonics produced along the axis of a single layer is shown in Figure 4.4. As described in Appendix A, the field is expressed in harmonic field units of the central dipole field. For a long layer, the transfer function (load line) for the central dipole field is a function of the tilt angle and is given by

$$T_p = \frac{\mu_0 \cos\alpha}{2(aw+\delta)} \qquad \text{such that} \qquad B_{plat} = T_p I_0. \tag{4.15}$$

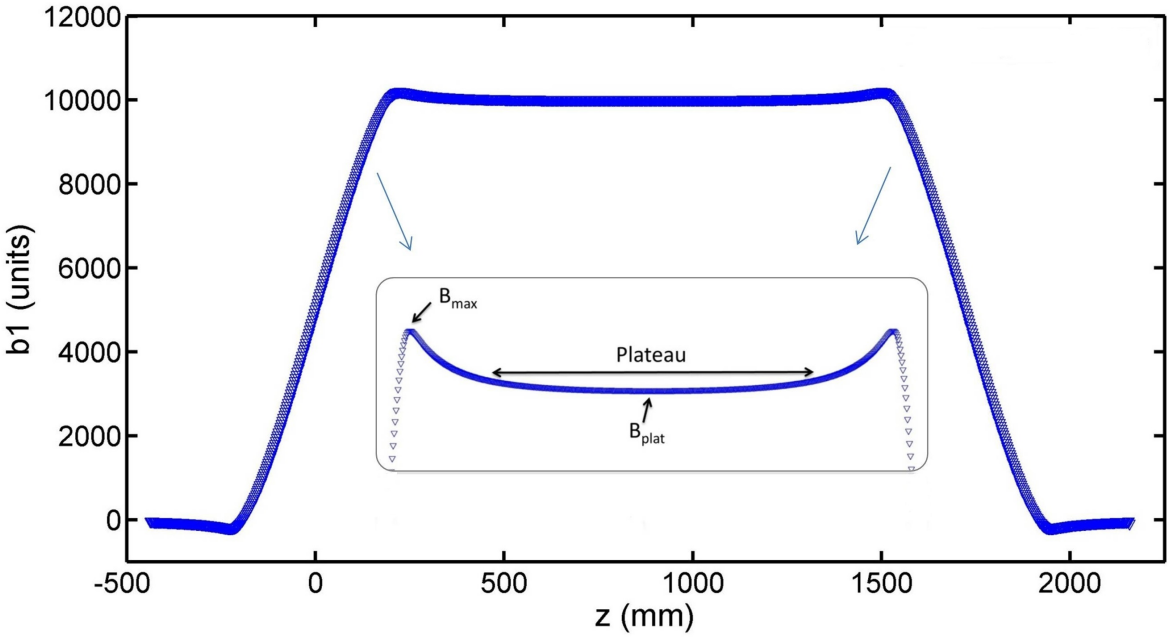

Figure 4.4: Dipole harmonics along the axis of the magnet (z) are shown for a single layer. The zoomed region shows the location of the max and plateau field.

B_{plat} is representative of the field produced by a layer free of end effects. End effects on the dipole field are quantified by the integrated field

$$B_{int} = \int B_1(z)dz. \tag{4.16}$$

The integrated dipole field can be represented by a step function of value B_{plat} and width

$$L_m = \frac{\int B_1(z)dz}{B_{plat}}, \tag{4.17}$$

which is referred to as the magnetic length of the magnet.

For a layer sufficiently long that the ends have a negligible effect on the central field, the magnetic length is equivalent to the geometric straight-section length (see Figure 4.1). In this case $L_m = wn_{turns}$, making the choice of midplane tilt angle α a trade-off between plateau field B_{plat} and magnetic length L_m. The integrated dipole is the product of the two, so for a given total length L_{tot}, radius r, and current I_0 there exists an optimum tilt angle which maximizes the integrated field (Fig. 4.5).

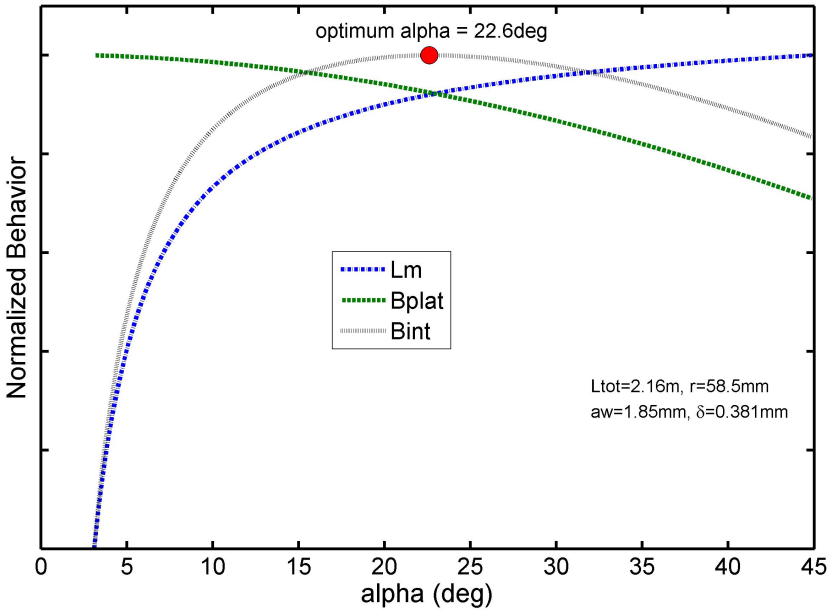

Figure 4.5: The normalized behavior of the magnetic length L_m, plateau field B_{plat}, and integrated field B_{int} are shown for a single layer of fixed total length. There exists a single alpha which maximizes the integrated field. For a given conductor and rib thickness, this optimum angle is a function of layer radius r and total length L_{tot} (see Figure 4.6).

This optimal angle is a function of the total physical length L_{tot} and radius r of the layer. Figure 4.6 shows the optimal angles for a selection of layer lengths and radii. The general trend of increasing optimal angle for decreasing total physical length and increasing radius is shown. It is seen that for CCT dipole magnets 10 to 15 meters long, as would be desired for a future hadron collider, the optimal tilt angle is between 10 to 20 degrees. As discussed in Section 4.2, this range of tilt angles contributes very little ($< 5\%$) to the inefficiency of the CCT design.

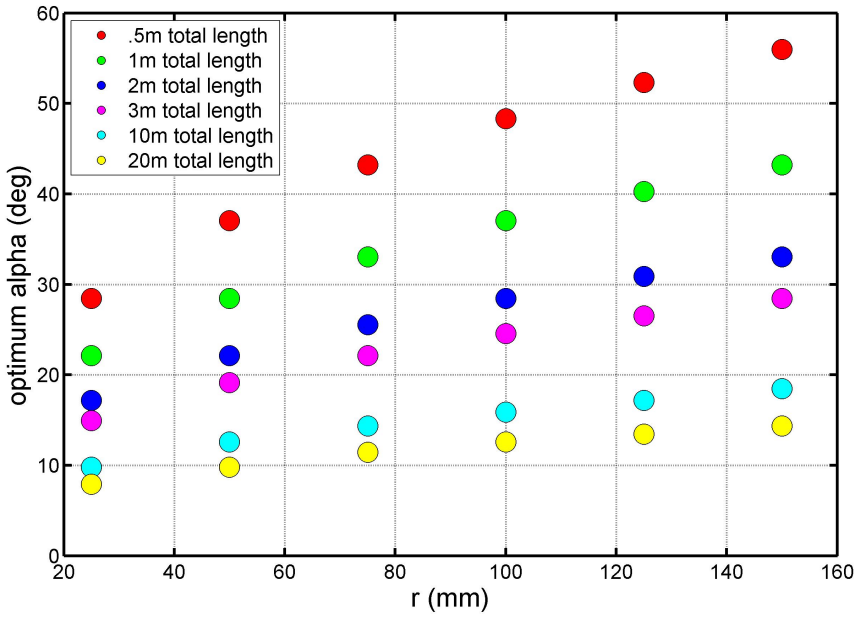

Figure 4.6: The optimial tilt angle that maximizes the integrated dipole field is shown as a function of total physical length and radius.

Conductor usage

The conductor path length for a single layer is also non-linearly dependent on the midplane tilt angle α. The factor C_l can be used to relate the length of a single turn to its radius as seen in Equation 4.9. This factor is dependent only on the tilt angle, with the dependence shown in Figure 4.7. As expected, the behavior is seen diverging as α tends to zero and approaching that of a circle (2π) as α increases. Of greater importance is the amount of conductor used in a layer for a given fixed physical length, which can be estimated using Equation 4.11.

Figure 4.8 adds the layer's conductor use to the example of the optimal tilt angle shown in Figure 4.5. It is seen that increasing the tilt angle also increases the total amount of conductor in the layer for a fixed physical length. This increase behaves fairly linearly in the region near the optimal tilt angle. The ultimate choice for the tilt angle is a trade-off between maximizing the integrated dipole by choosing the optimal angle, and reducing of the amount of conductor by decreasing the angle past this point.

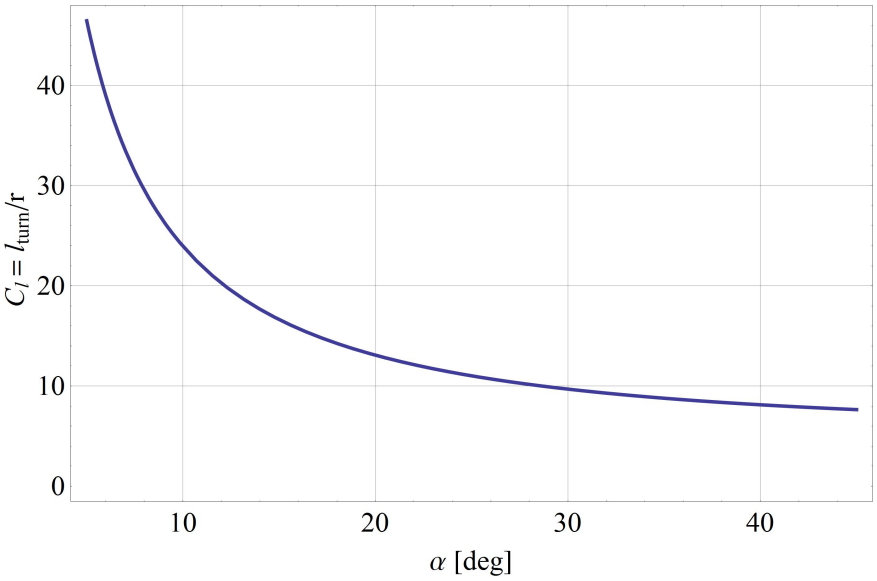

Figure 4.7: The factor relating the radius to the length of a single CCT turn C_l is shown for varying tilt angle α.

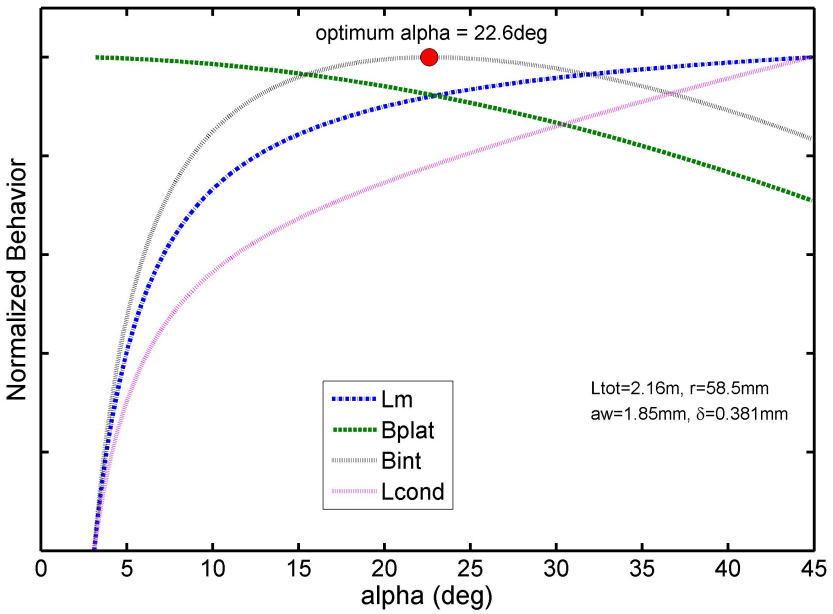

Figure 4.8: The normalized conductor use as a function of tilt angle for a 2.2 m CCT layer is shown added to Figure 4.5.

4.6 Choice of cable height (strand number) for the innermost layer

Equation 4.2 can be rewritten in terms of the current I_0 such that the dipole field from a single CCT layer is

$$B_{1CCT} = \frac{\mu_0 I_0}{2a_w}\epsilon_{cct}. \tag{4.18}$$

Once again it is seen that field produced by a dipole layer is independent of the layer's radius. It is also important to note that when the current is considered, the dipole field is also independent of the cable height b_w of the layer (which will be used for current density grading in Section 4.7). If the same pitch w, tilt angle α, and power supply I_0 are used for all layers in a multi-layer CCT magnet, each layer contributes the same magnitude dipole field.

This means the net dipole field in the bore of a multi-layer CCT can be written as

$$B_{1net} = \frac{\mu_0 I_0}{2a_w}\epsilon_{cct} n_{lay}, \tag{4.19}$$

where I_0 is the power supply current and n_{lay} is the number of layers. The short-sample limit of the conductor has not yet been considered. This limit requires $I_0 < J_{ess}(B_{cond})a_w b_w$, where $J_{ess}(B_{cond})$ is the engineering short-sample current density based on the properties of the superconductor. The short-sample current density is a function of the field at the conductor B_{cond}, the maximum value of which is found in the first layer. This means the height and width of the cable used in the first layer set the short-sample current I_0, and thus the individual dipole field contribution for all layers. Because the width of the cable a_w is fixed at slightly less than two times the strand diameter, the relevant design choice is the cable height b_w. This means to reach a desired dipole field there is a trade-off between the height b_w of the innermost layer and the total number of layers n_{lay}.

One way to illustrate this trade-off is by making the simple assumption the field in the bore determines the short-sample of the first layer. In reality there will be a rise in field at the windings which requires a numerical calculation. For the sake of simple analytic scaling this will be disregarded (Section 4.8 will show scaling with the rise of field at the conductor numerically calculated). With this assumption, the trade-off between b_w for the innermost layer and n_{lay} for a desired net dipole field B_{1net} is given by

$$b_w(B_{1net}) = \frac{2B_{1net}}{\mu_0 \epsilon_{cct} n_{lay} J_{ess}(B_{1net})}. \tag{4.20}$$

This relation is shown in Figure 4.9 assuming a typical Nb_3Sn short-sample current density. The solid lines represent the case of a CCT with perfect efficiency $\epsilon_{CCT} = 1$ which bounds the achievable field. This perfect case corresponds to the tilt angle and midplane rib thickness going to zero (see Section 4.2). The markers correspond to typical CCT designs

with an efficiency of $\epsilon_{CCT} \approx 0.8$. The clear trade-off between number of layers and the cable height of the innermost layer is seen. From this perspective it is desirable to use the largest possible cable for the innermost layer. This reduces the number of layers to reach a desired dipole field which corresponds to a reduction in conductor, stored energy, inductance, and complexity. The maximum size that can be used is determined by the practicality of winding the cable around the hard way bend in the pole region of the first layer. The bend radius is directly related to the clear bore, allowing the use of a larger cable for increased bore size.

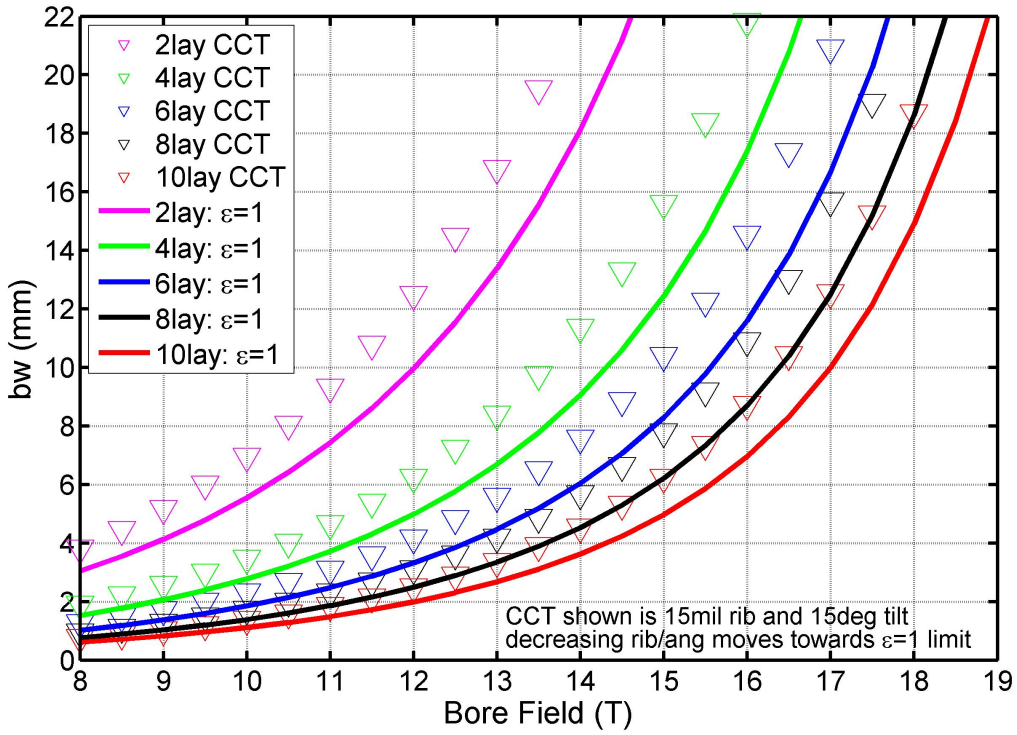

Figure 4.9: Equation 4.20 is shown plotted given a typical Nb_3Sn short-sample current density curve.

4.7 Current grading by reducing strand number

As was discussed in Section 4.6, the power supply current I_0 is set by the short-sample current density and the radial thickness of the innermost conductor layer. Once the power supply current is set, the dipole field contribution is the same for all layers as seen in Equation 4.18. This contribution is independent of the radial thickness b_w of the layer. In simple terms, the power supply current I_0 determines the field produced by a dipole layer and the

radial height of the cable b_w determines the short-sample. The power supply current is set based on the innermost layer where the field at the conductor is the highest. The field at the conductor falls off radially, meaning the maximum field at the outer layers will be lower than the innermost. If all layers use the same size cable (which was chosen based on the maximum field at the inner layer), the current density in the outer layers will be well below the short-sample limit.

To bring the outer layers closer to the short-sample limit, the current density is increased by reducing the cable height b_w. In practice this means the number of strands in the outer layers is reduced in proportion to the drop in field at the conductor. Figure 4.10 shows an example of grading that was performed for the eight layer Nb_3Sn dipole CCT2 (design details in Chapter 6). The current density in the superconductor within the strand is shown. In (a) all layers use 23 strands like the innermost layer, whereas in (b) the number of strands in the outer layers is reduced to bring the load lines closer to the short-sample limit. Because the power supply current does not change (the number of the strands in the innermost layer remains fixed), the bore dipole field is unaffected by the grading.

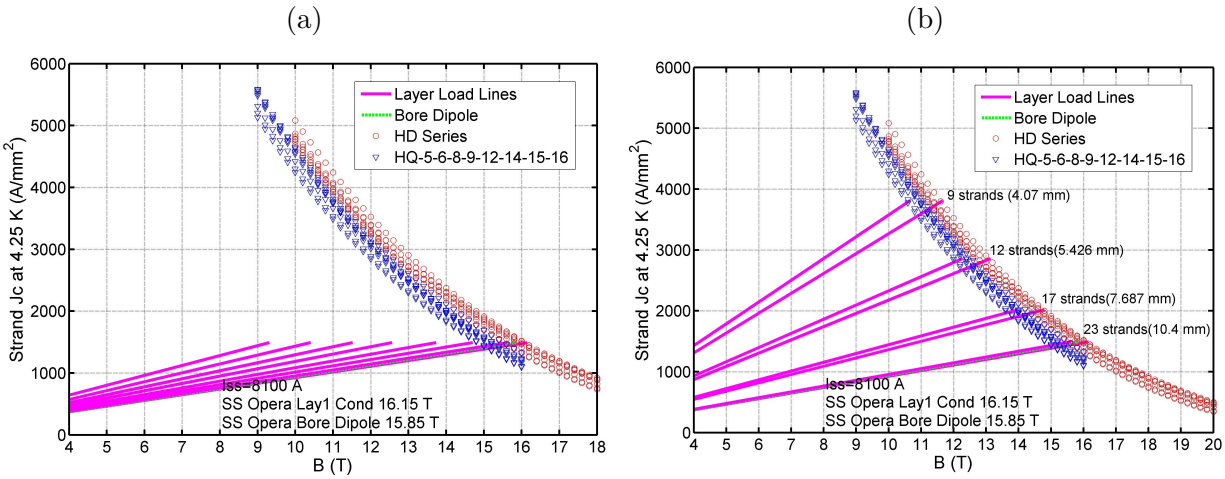

Figure 4.10: The load lines for the conductor layers of an ungraded (a) and graded (b) eight layer CCT dipole are shown.

Grading saves conductor and reduces the total diameter of the magnet (see, for example, the cross section comparison for CCT2 in Figure 4.11), while still reaching the same dipole field in the bore. These savings are increased for a large number of layers. In the eight layer example shown, 44% less conductor was used after grading. It is important to note in this particular case the field at the conductor of all layers remained above 10 T, so the use of NbTi for the outer layers was not considered. The CCT design is well suited for this style of grading due to the use of a winding mandrel for each individual layer. With this approach, the channel height of each layer is easily adjusted to accommodate a cable with a different

number of strands. The stress interception provided by the mandrels in the CCT design is also of key importance, as it allows for aggressive grading that is not limited by conductor stress. Grading of a traditional magnet design (with accumulation of Lorentz forces) rapidly increases conductor stress, leaving very little room for grading before the stress limits of strain-sensitive Nb_3Sn are reached [51].

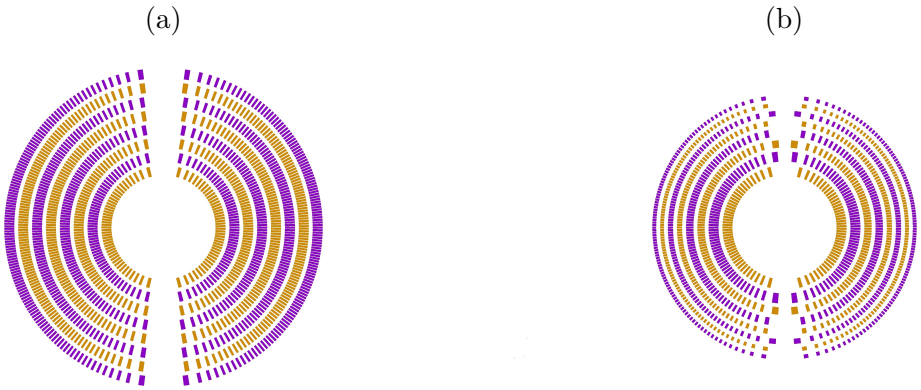

Figure 4.11: The ungraded (a) and graded (b) conductor cross sections are shown for the eight layer Nb_3Sn dipole design CCT2.

The method for grading a CCT dipole begins with the innermost layer and works outward. The maximum number of strands is chosen for the first layer such that the cable remains practically windable around the hard way bend in the pole region. This minimizes the total number of layers as discussed in Section 4.6. After this, the field at the following pair of layers is calculated (using Opera3D, for example). The number of strands in this pair is then reduced to bring the current density to the short-sample point. This process is repeated, working outwards, until all pairs of CCT layers have been graded. It is important to update the magnetic model as the number of strands is changed, as the location of the outer layers will move radially inward as the layers beneath them are graded. CCT2 was graded in pairs of layers to limit the number of unique cables needed to four. For maximum savings, the grading process can be performed on an individual layer basis. An example of grading by individual layer will be presented in Section 4.8.

4.8 A cost study of the CCT design for high field

The design of a future hadron collider will require the selection of a main dipole field. Should Nb_3Sn be used, it is thought this selection will be in the 10-16 T range [8, 4]. The goal of this study is to better understand the characteristics of CCT designs in this dipole field range, with an ultimate focus on the conductor cost. This focus is due to the cost of the superconductor itself being a significant if not dominant fraction of the total magnet cost for a Nb_3Sn CCT [50]. In reality, both the cost and performance of Nb_3Sn is expected to change before the date at which such a collider may be built. The value of this study lies not necessarily in the resultant numbers, but rather in understanding how CCT design scales to high field.

Assumptions

The assumptions for magnet designs used in this study are shown in Table 4.3. A large bore was chosen to allow for the potential inclusion of an HTS insert, but for the interested reader a method for scaling the final results to different bore sizes will be presented. All assumed parameters are based on practical experience with CCT design and construction at LBNL. Conservative values were used in all cases except the choice of the conductor. Here the "best of the best" Nb_3Sn, based on extracted strand measurements of HD3 coil-2, was selected.

Table 4.3: Assumptions for the CCT Designs

1.	100 mm clear bore diameter	space for HTS insert, winding practicality
2.	22 strand cable for layer 1	test windings show this near the hard way bend limit
3.	4 mm radial spar thickness	ANSYS results on coilpack bending (Chapter 5)
4.	0.8 mm strand (HD3 coil 2)	"best of the best" Nb_3Sn (Fig. 4.12)
5.	15 mil midplane rib	CCT1/CCT2 experience (Chapter 5, 6)
6.	0.125 mm insulation	CCT1/CCT2 experience (Chapter 5, 6)
7.	15 deg tilt angle	optimal angle for 10 m magnetic length
8.	4.2 K operation	1.9 K will add additional margin
9.	all layers have same n_{turns}	same magnetic length for every layer

Table 4.4: Assumption for Nb_3Sn Strand Cost

35 kg billet	70,000 ($)
0.8 mm strand	7910 (m/billet)
0.8 mm strand	= 8.85 ($/m)

The cost of Nb_3Sn conductor is expected to drop if demand is increased (as would be the case for a Nb_3Sn hadron collider). To avoid speculating on this subject, a conservative estimate for the current cost of Nb3Sn strand was assumed [53]. This assumption is seen

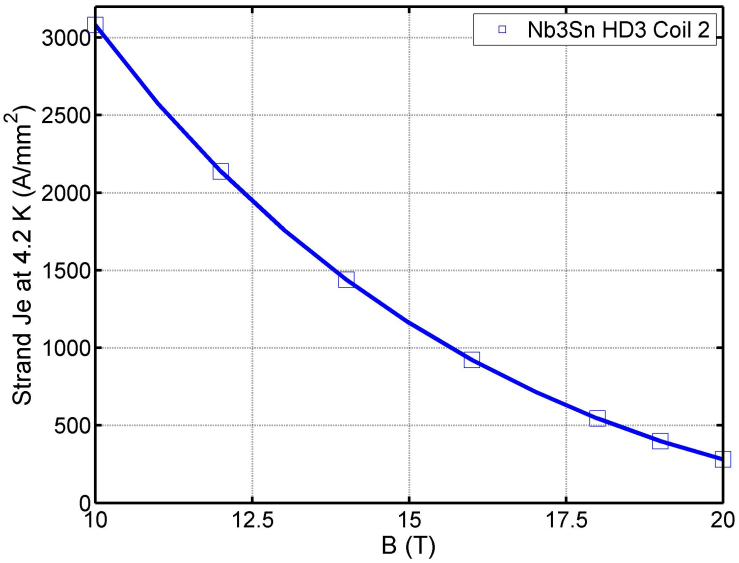

Figure 4.12: A fit [52] of the Nb_3Sn strand current density for HD3 coil-2 is shown.

in Table 4.4. The results of this study are easily scaled in a linear fashion to represent a different cost per meter for the Nb_3Sn strand. Equation 4.13 can be used to determine the total strand length in a multi-layer CCT magnet. Based on the assumption of strand cost, the conductor cost per meter of magnetic length is then given by

$$8.85(\$/m)\sum_{i=1}^{nlay}\frac{l_{turn}(i)*n_s(i)}{w}. \tag{4.21}$$

Method

Based on the assumptions, a magnetic model was generated for four CCT dipole designs using 2, 4, 6, and 8 layers. These designs initially used a 22 strand cable for all layers, which corresponds to a cable height of around 10 mm. This thickness was selected based on a clear bore of 100 mm and experience winding CCT coils at LBNL. The maximum field at the conductor was calculated for each design in Opera3D, and then short-sample current and fields were determined. Each model was then graded by adjusting the number of strands in the outer layers according to the method described in Section 4.7. This process resulted in eight total designs, four ungraded and four graded, which produce between 11 and 17 tesla at short-sample. The total Nb_3Sn strand used per meter of magnetic length was compared between the eight cases. By associating the conductor cost with length of strand, the cost scaling by number of layers and dipole field was estimated for both the ungraded and graded cases.

Results

The reader interested in detailed results for each of the designs is referred to Appendix C. In this appendix the maximum field at each conductor layer, load lines, layer radii, number of strands, and conductor usage can be found for all eight designs. In this section, the focus will remain on a comparison between the key results and the scaling. Table 4.5 gives a summary of the short-sample results. Here there is no difference between the graded and ungraded cases, due to the number of strands in the innermost layer remaining the same. It is seen that when the short-sample limit of the conductor is considered, the increase in field from adding an additional pair of layers slowly tapers off. For example, an increase from two to four layers gains 3 T, while an increase from six to eight layers only gains 1 T.

Table 4.5: Short-Sample Summary

n_{lay}	Bore Dipole	Max Field at Cond.	Current
2	11.29 T	12.75 T	20.55 kA
4	14.25 T	14.95 T	12.94 kA
6	15.82 T	16.26 T	9.52 kA
8	16.81 T	17.19 T	7.58 kA

Table 4.6 summarizes the length and cost of the conductor for all eight designs. The net cost of each case is also shown plotted as a function of bore dipole in Figure 4.13. It is seen that the benefits of grading start small and grow rapidly as the number of layers is increased. This is a result of an increased reduction in the number of strands and radii when grading the outermost layers.

Table 4.6: Conductor Cost Summary

	Ungraded			Graded		
n_{lay}	L_{cable}/L_m	L_{strand}/L_m	\$/m of L_m	L_{cable}/L_m	L_{strand}/L_m	\$/m of L_m
2	251	5520	48.9 k\$/m	250	4940	43.7 k\$/m
4	603	13.26 k	117.4 k\$/m	585	9.58 k	84.8 k\$/m
6	1055	23.2 k	205.5 k\$/m	991	13.8 k	122.1 k\$/m
8	1609	35.39 k	313.2 k\$/m	1462	17.7 k	156.8 k\$/m

A second observation is the large increase in expense for the last 1-2 T of the very high field designs. Increasing the dipole field requires adding additional layers, which has already been shown to have diminishing returns at higher field. Another issue is the increased conductor use due to the additional layers being at larger radii (especially for the ungraded case). With these effects combined, it is clear from the figure these last 1-2 tesla are very expensive. This cost has several implications for the choice of operating dipole field for a future collider. The first is the non-linear increase in cost associated with a higher dipole field should be considered in the context of the net cost (including the tunnel, etc.) and

performance of the accelerator. The second implication is the importance of being able to operate the magnet with as small a short-sample margin as possible. The choice of margin determines to how much of the expensive last few tesla are needed. The necessary margin is then a key consideration for very high field magnets. This requirement is unknown for the CCT, and for this reason there is a series of Nb_3Sn CCT dipole tests planned at LBNL to determine the performance of the design at high field (Chapter 6).

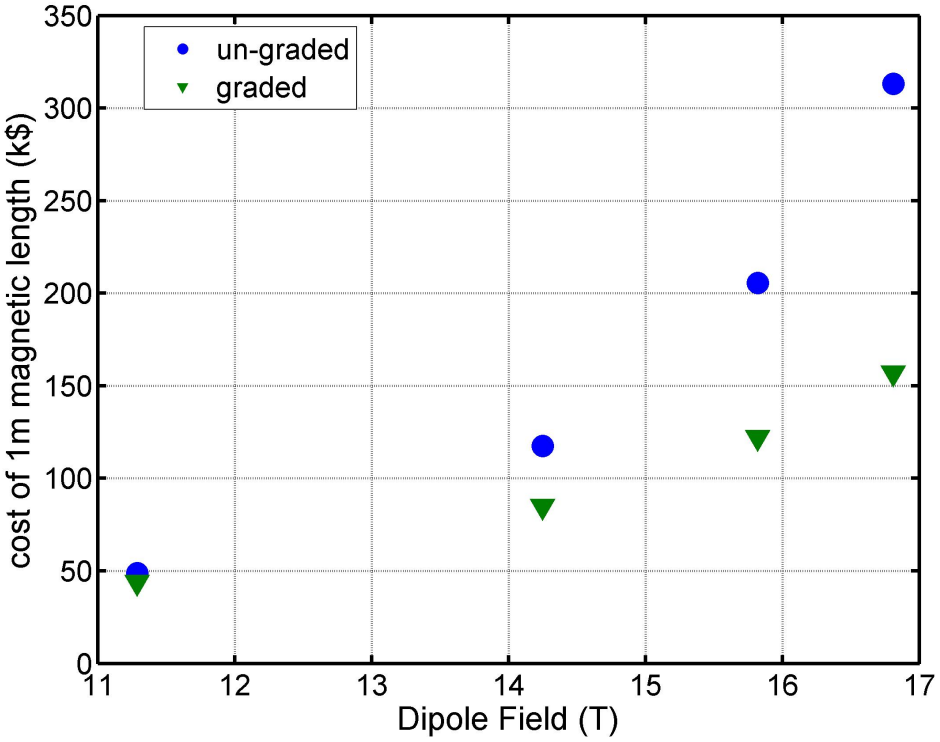

Figure 4.13: The conductor cost of one meter of magnetic length for varying dipole fields is shown for a 100 mm bore CCT.

A bore size dependent model for the ungraded results

The clear bore of a dipole magnet is a key specification that was not taken into consideration in the previous cost study (all eight designs had a 100 mm bore). To account for this, a scaling of the conductor cost with bore size was developed for an ungraded CCT magnet. An analytic scaling for the graded case was not considered due to the number of strands per layer being dependent on a numerical, not analytic, field at the conductor calculation. For a multi-layer CCT dipole with clear bore radius r_{bore} and radial mandrel spar thickness b_{spar} between all layers, the central radius of the "ith" layer is

$$r(i) = r_{bore} + ib_{spar} + (i - 1/2)b_w, \tag{4.22}$$

where b_w is the radial width of the cable (ungraded means this is the same for all layers).

The conductor costs for an ungraded CCT magnet of n_{lay} total layers is then

$$\text{cost/m of L}_m = 8.85(\$/m)\frac{C_l n_s}{w}\sum_{i=1}^{n_{lay}}[r_{bore} + ib_{spar} + (i - 1/2)b_w], \tag{4.23}$$

which simplifies to

$$\text{cost/m of L}_m = 8.85(\$/m)\frac{C_l n_s}{w}\left(n_{lay}r_{bore} + \frac{1}{2}n_{lay}(n_{lay}+1)b_{spar} + \frac{1}{2}n_{lay}^2 b_w\right). \tag{4.24}$$

Equation 4.24 is shown plotted in Figure 4.14 as a function of the number of layers, using the same parameters (with the exception of clear bore) as the cost study. The conductor cost of each of the eight 100 mm clear bore designs are shown in solid markers. As expected, the markers for the ungraded case lie on the 100 mm scaling relation. This scaling can be used to determine the conductor savings by going to a smaller bore size, which increases in significance for a large number of layers (high field).

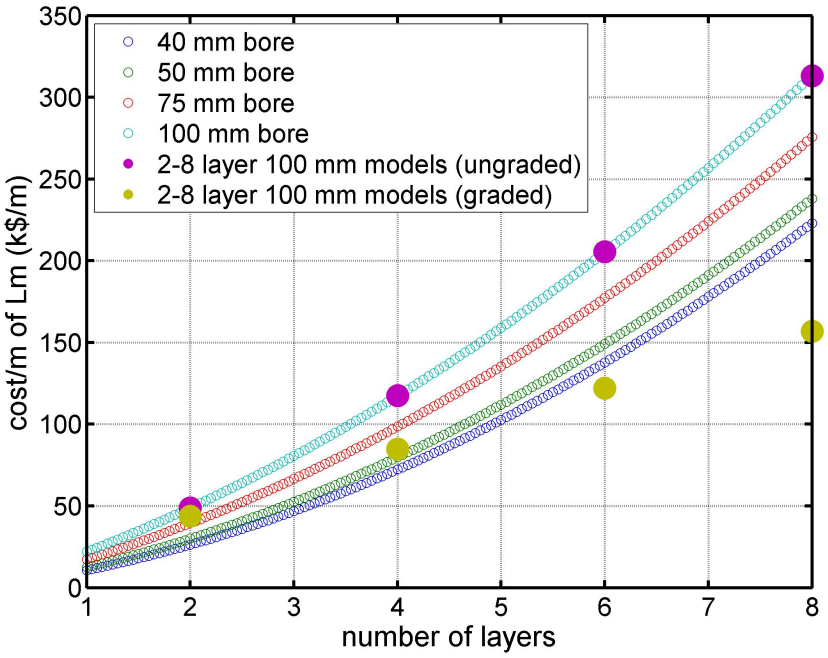

Figure 4.14: The scaling of conductor cost as function of number of layers for the ungraded case is shown for a selection of clear bore diameters.

Chapter 5

CCT1: a 2.5T NbTi Proof-of-Principle Dipole

5.1 Introduction and goals

CCT1 is a 2.5 T superconducting CCT dipole magnet that was built and tested at Lawrence Berkeley National Laboratory (LBNL) as a first step towards a high field Nb_3Sn dipole. While CCT1 was designed for relatively low field using NbTi conductor, key aspects for a high field CCT magnet (such as Rutherford cables and winding mandrels for stress interception) were implemented. CCT1 is the first published test of a CCT dipole built in a configuration that scales to high field, serving as a proof-of-principle step before moving on to the increased complexity and cost associated with a Nb_3Sn magnet. As with the design and construction of any first prototype, many lessons were learned along the way. In most cases magnetic and structural modeling techniques were developed for CCT1 as needed during the design. The development of these tools will have a lasting impact by being easily adaptable for the analysis of future CCT designs.

Overall, bringing CCT1 from the conceptual stage to the construction and test of a real superconducting magnet has been an invaluable experience that will continue to guide the CCT magnet program at LBNL. This chapter will present this process by following the design, construction, and test of CCT1. It will begin with a report on the magnetic and structural design of the magnet. Then the manufacturing of winding mandrels, winding of the coil, and final preparation for the test will be discussed. The test configuration and plan will be described and the test results for the short-sample performance and field quality of CCT1 will be given. Finally, a perspective on the test results and their impact in both the fields of High Energy Physics and Ion Beam Cancer Therapy will be given. Additional information on the design, construction, and test of CCT1 can be found in the following references [47, 54, 55, 56].

5.2 Design

CCT1 is a two layer CCT dipole designed to reach 2.5 T in a 50 mm clear bore using NbTi conductor. A winding mandrel approach was taken, with each CCT layer consisting of cabled conductor wound into channels machined into a thick-walled cylinder. These mandrels serve to position the conductor for field quality and provide structural support against the operating Lorentz forces. The two CCT layers nest one inside the other, and are then assembled into an external structure which provides pre-stress or additional support against the Lorentz forces. Two external structures were modeled during the design: a complex key, bladder, and shell structure (as seen in the Figure 5.1) and a simple shell structure.

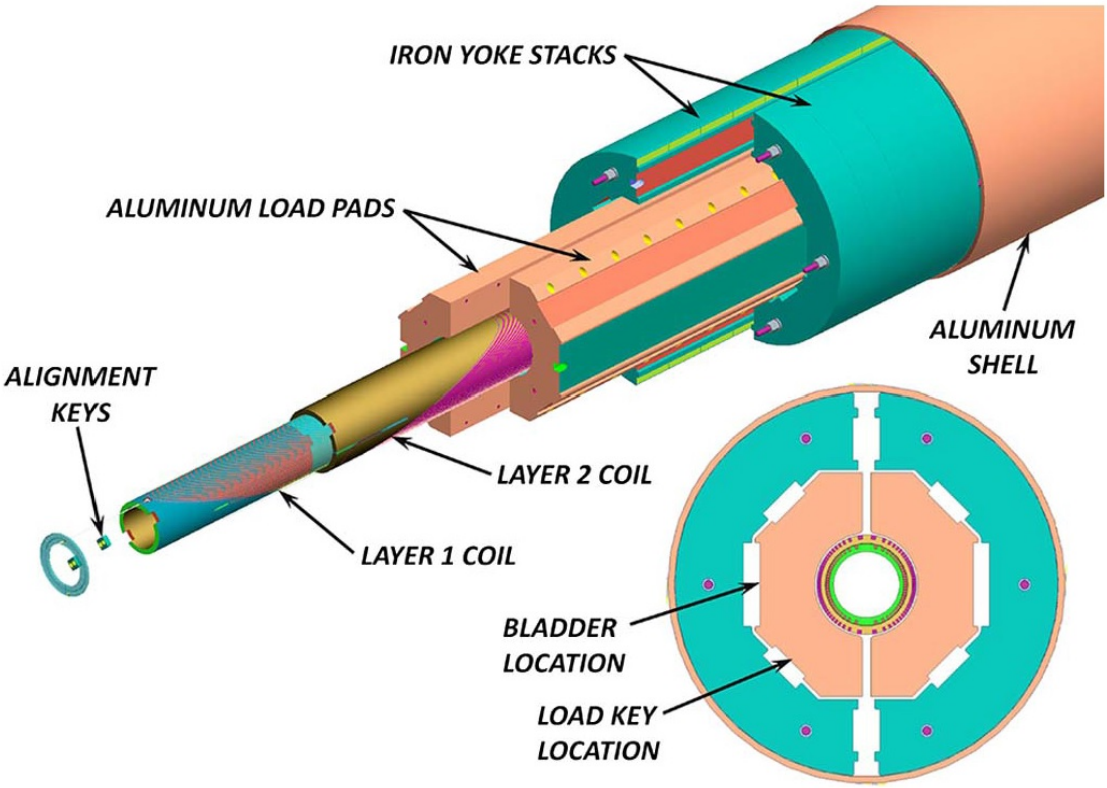

Figure 5.1: An exploded view of CCT1 with an external key, bladder, and shell loading structure is shown.

NbTi conductor remaining from the SSC project was chosen for use in CCT1. The "SSC outer" strand was cabled into an eight strand Rutherford cable whose properties can be seen in Table 5.1. The cable was then insulated with a 0.15 mm thick braid of S-glass insulation. A central path for 78 turns of this cable was generated using the CCT dipole Equation 2.15. A tilt angle of 15 degrees, pitch of 7.604 mm, and central radii of 30 mm for layer 1 and

36.59 mm for layer 2 was used (see Fig. 5.2). The mandrel channels for the cable were chosen with a slightly oversized cross section of 3.02 by 1.59 mm. Combined with the pitch and tilt angle this resulted in a minimum rib thickness between turns of 0.381 mm at the midplane.

Table 5.1: SSC Outer NbTi Cable Parameters

Filament Diameter	6.0 μm
Strand Diameter	0.648 mm
Strand J_c (5T, 4.2K)	2750 A/mm^2
Strand Cu/SC	1.8
No. Strands	8
Cable Width, bare	2.72 mm
Cable Width, ins.	3.02 mm
Cable Thickness, bare	1.07 mm
Cable Thickness, ins.	1.37 mm

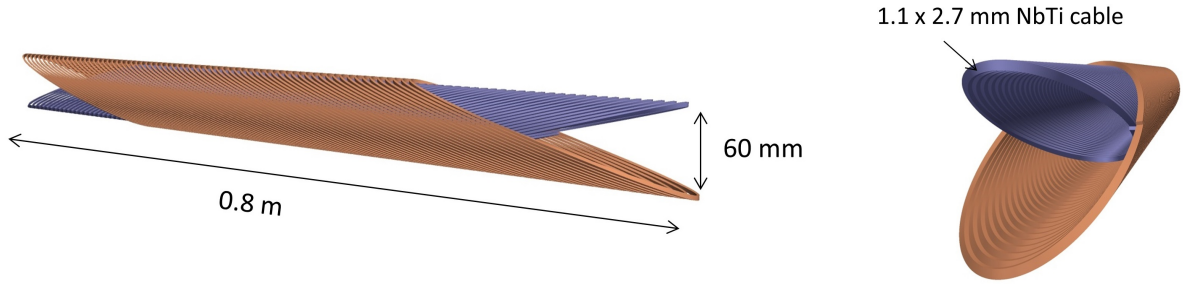

Figure 5.2: The two conductor layers of CCT1 are shown.

The radial thickness of the thick-walled cylinders used for the winding mandrels was chosen to leave an inner wall thickness (spar) of approximately 3 mm after machining the channels. A 0.25 mm radial gap was left between the OD of mandrel 1 and the ID of mandrel 2 for a G10 sheet to serve as a slip plane during the assembly of layer 1 into layer 2 (see Table 5.2 and Figure 5.3). A 6061 aluminum alloy was chosen as the mandrel material for its availability and ease of machining. It is important to note aluminum is incompatible with the heat treatment for Nb_3Sn (around 650^0 C), which will require a change to a mandrel material with a higher melting point for future Nb_3Sn CCT magnets.

Conductor use

The amount of conductor used in the two layers of CCT1 can be seen in Table 5.3.

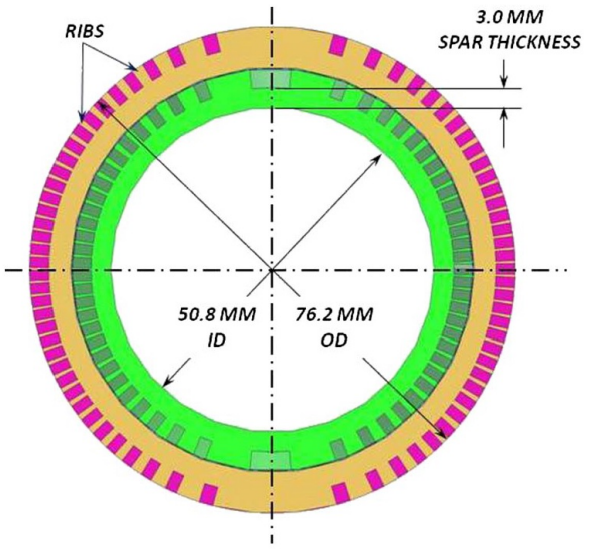

Figure 5.3: A cross section of CCT1's mandrels is shown.

Table 5.2: CCT1 Mandrel Properties

Lay	Min. Rib (mm)	Spar (mm)	Ri (mm)	Ro (mm)	Channel (mm)	Length (mm)
1	0.381	3.08	25.40	31.50	1.59/3.02	841.13
2	0.381	3.33	31.75	38.10	1.59/3.02	841.13

Table 5.3: CCT1 Conductor Use

Layer	# turns	L-one-channel (m)	L-all-channel (m)	# strands	L-strand (m)
1	78	.4987	38.90	8	311.2
2	78	.6086	47.47	8	379.8
total			86.4 m		691 m

Outer structure

The first option considered for the outer structure of CCT1 is a key, bladder, and shell loading structure (Fig. 5.1 and 5.4) that was developed at LBNL for Nb_3Sn magnets [19]. This structure inflates bladders between the yoke and loading pads during the assembly of the magnet. Keys are inserted and the bladders deflated such that a variable pre-stress is applied to the conductor layers based on the thickness of the key. For traditional Nb_3Sn high field magnets, precise control of pre-stress is desired to prevent conductor movement and reduce training. A key motivation for the CCT design, as described in Section 1.3, is to reduce or eliminate the required pre-stress for high field magnets containing strain-sensitive Nb_3Sn.

A complex key and bladder loading structure is not a requirement for a low field and NbTi magnet such as CCT1. This structure was instead considered for the flexibility it provides to study and potentially test CCT1 with different values of pre-stress. This allows for an investigation of pre-stress in CCT dipole magnets, studying the key motivation for developing the CCT concept for high field. While this option was studied and may potentially be used for future high field CCT Nb_3Sn dipoles, the decision was made to test CCT1 in a simpler configuration where the two layers were assembled into an aluminum shell of 20 mm radial wall thickness.

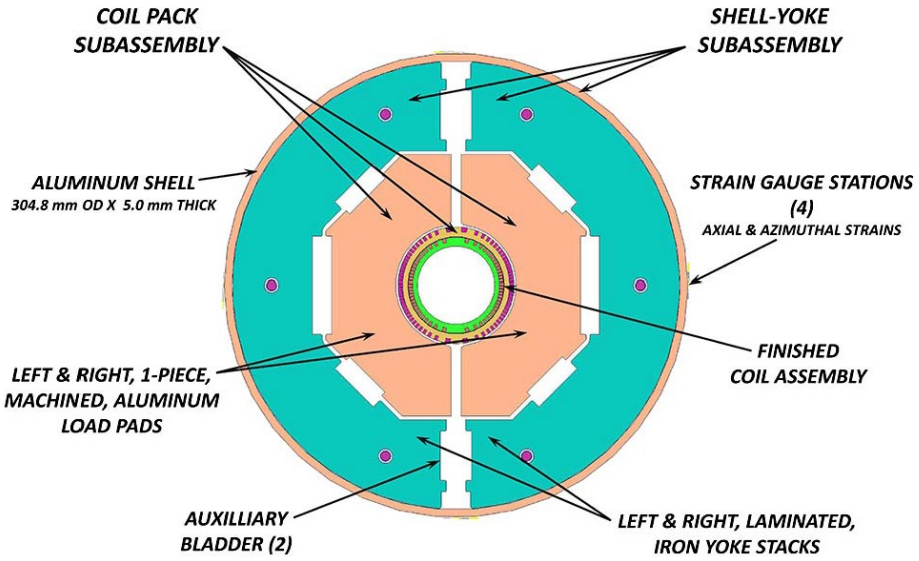

Figure 5.4: A cross section of the key and bladder outer structure considered for variable loading of CCT1 is shown.

5.3 Magnetic modeling

A magnetic model for CCT1 was generated in Opera3D using the method described in Section 3.2. While iron was considered in some studies, for example with a key and bladder outer structure, the results shown in this section correspond to the iron free configuration in which CCT1 was tested. As will be described in Section 5.5, layer 2 was manufactured with 6 less turns (72 instead of 78) due to a mix-up with the CAD model sent to the machine shop. The results presented in this section are representative of the design, with 78 turns in each layer, while any modeling predictions for the test results found in Section 5.6 were calculated based on the magnet as it was manufactured. The field harmonic representation used in this section for both local and integrated harmonics can be found described in Appendix A.

Integrated dipole field and magnetic length

The magnetic length of a dipole magnet is defined as the length of a step function of the integrated dipole field. Figure 5.5 shows the dipole harmonic along the length of CCT1 calculated at 2/3 of the bore radius using Opera3D and a current of 4050 A. This data was fit and then integrated axially (along z) through the magnet to find an integrated dipole of 1485.6 Tmm. A magnetic length of 590.4 mm was calculated for CCT1 by simply dividing this value by the central dipole field of 2.516 T.

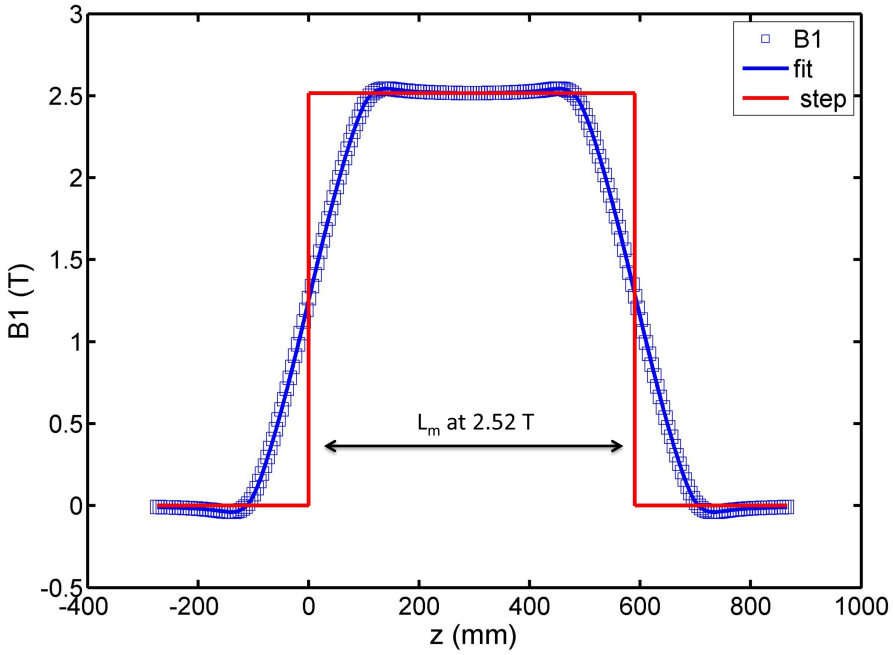

Figure 5.5: The dipole harmonic (B_1) along the length of CCT1 is shown. The equivalent dipole step function at the central field of 2.52 T is shown with the magnetic length L_m indicated.

Harmonic content in straight-section

The field errors in the straight-section of CCT1 were calculated at the axial center of the magnet using the Opera3D model. Table 5.4 shows the results of this calculation up to the 9th harmonic. It is seen that CCT1 has excellent predicted field quality, < 1 unit of field error, at 66.66% of the 25.4 mm clear bore radius.

Table 5.4: CCT1: Straight-Section Harmonics from Opera3D (in units of B_1)

Ref. (mm)	% of Apert.	b_2	b_3	b_4	b_5	b_6	b_7	b_8	b_9
16.93	66.6%	-0.03	-0.25	<0.01	0.06	<0.01	-0.01	<0.01	<0.01

Harmonic content through the ends of the magnet

The ends break the symmetry of the magnet inducing axial variation of the higher order harmonics. To reduce the negative effects of this behavior on the beam, it is desirable that the higher order harmonics integrate to zero through the ends of the magnet. For a typical accelerator magnet this requires a difficult and time-consuming optimization of the conductor path in the end region. The CCT design has the advantageous property of the higher order harmonics naturally integrating to zero through the ends (see Figure 5.6 for example). This is due to the ends of a CCT dipole being of "Lambertson" type. The reference [57] explains the characteristics of a Lambertson end and why it is ideal for achieving zero integrated higher order harmonics.

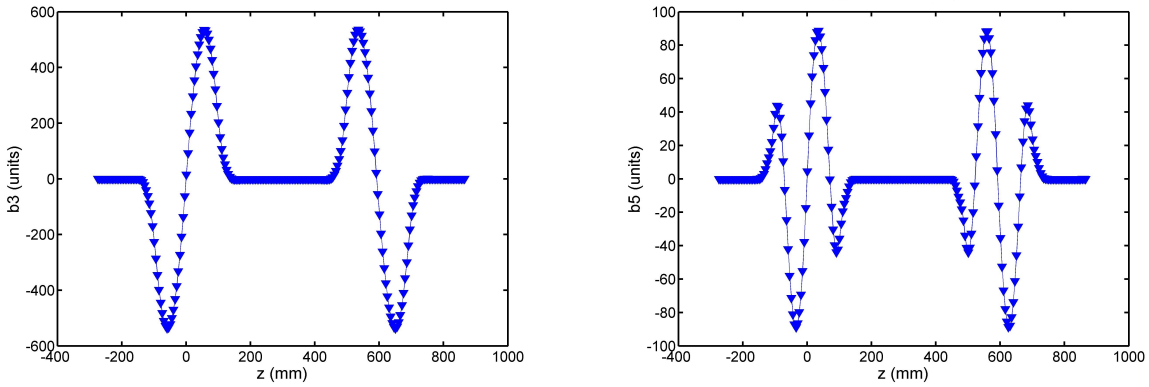

Figure 5.6: The sextupole (b_3) and dodecapole (b_5) harmonics are shown along the length of CCT1. The harmonics are calculated in Opera3D at 2/3 of the clear bore.

To describe the higher order field error through the ends of a dipole magnet, integrated harmonics are defined

$$\bar{b}_n = \frac{\int B_n(z)dz}{B_1^{SS} L_m}, \tag{5.1}$$

where B_1^{SS} is the dipole harmonic in the straight-section and L_m is the magnetic length. Calculated values of $\bar{b_n}$ for CCT1 are shown in Table 5.5. The natural field quality of CCT1, with no optimization of the ends, is shown by the low values for these integrated harmonics.

Table 5.5: CCT1: Integrated Harmonics from Opera3D (in units)

Ref. (mm)	% of Apert.	$\bar{b}_2$	$\bar{b}_3$	$\bar{b}_4$	$\bar{b}_5$	$\bar{b}_6$	$\bar{b}_7$	$\bar{b}_8$	$\bar{b}_9$
16.93	66.6%	-1.11	-0.83	-0.29	-0.09	-0.09	-0.06	-0.02	-0.01

Solenoidal Field

The solenoidal field along the length of CCT1 can be seen in Figure 5.7. As a result of cancellation between oppositely tilted and powered layers, the value of the solenoidal field in the center (straight-section) of the magnet is only 0.003 T. Axial variation of the solenoidal field through the ends of the magnet results in a region where the solenoidal field does not cancel. As seen in the figure, this variation tends toward integrating to zero.

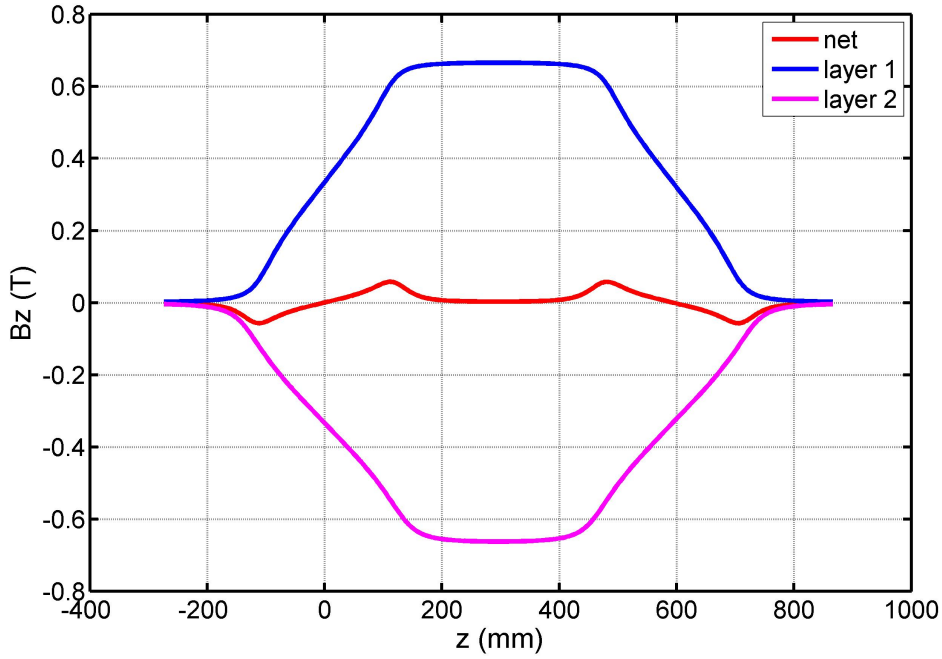

Figure 5.7: The solenoidal field (Bz) is shown along the length of CCT1.

Field at the conductor and short-sample

The field at the conductor of CCT1 was calculated in the Opera3D model, and found to be a maximum at the pole in the end region. Because the test of CCT1 includes no iron, this provides a linear load line for the field at the conductor. Figure 5.8 shows the short-sample limit for CCT1 based on this load line and a Bottura fit [58] for the NbTi conductor

properties in Table 5.1. The expected short-sample fields are 2.5 T in the bore and 3.1 T at the conductor, corresponding to a short-sample magnet current of 4050 A.

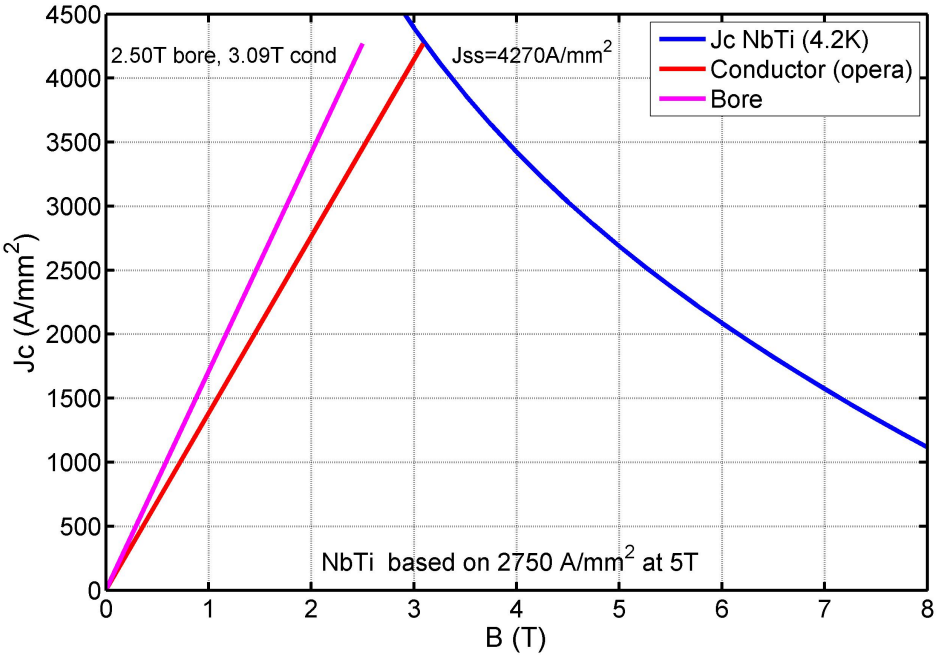

Figure 5.8: The load line for CCT1 is shown for current density in the superconductor.

Stored energy and inductance

Using the analytic formulation in Section 2.3, the predicted inductance matrix for CCT1 is

$$L_{CCT1}\left[\frac{mH}{m}\right] = \begin{pmatrix} 0.490 & 0.366 \\ 0.366 & 0.729 \end{pmatrix}, \tag{5.2}$$

resulting in a total inductance of 1.95 mH/m. The stored energy of CCT1 at the short-sample current of 4050 A in both layers is then 16.0 kJ/m. The predicted inductance of CCT1 was compared to electrical measurements performed on the magnet (found in Table 5.8). Good agreement was found between the predicted and measured value. This comparison is summarized in Table 5.6.

5.4 Structural modeling

Two different test configurations were considered during the structural modeling of CCT1. The first included the use of a complex key and bladder external loading structure, and the

Table 5.6: CCT1 Inductance

		Predicted		Measured
	L_m (m)	L (mH/m)	L_{tot} (mH)	L_{tot} (mH)
Layer 1	0.593	0.490	0.291	N/A
Layer 2	0.547	0.729	0.399	N/A
Layer 1,2 series	0.570	1.95	1.11	1.19

second only the two layers themselves (no external structure). One goal for the structural modeling of CCT1 was to study the stress interception properties of the CCT, and as a result better understand what kind of external structure is best suited to the CCT design. An additional goal was to study the effect of different boundary conditions and develop the necessary methods for structural analysis. To accomplish this, ANSYS models for both configurations were generated by the process described in Section 3.3. These models were solved with different loads and boundary conditions to study stress interception in CCT1 and the importance of external structure.

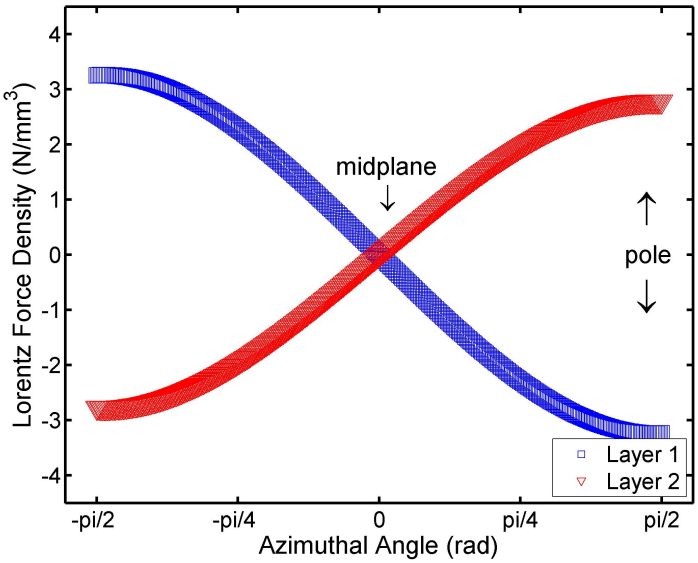

Figure 5.9: The Lorentz force density directed towards the mandrel ribs is shown for CCT1. The results displayed were calculated at the center of the conductor using Opera3D.

Lorentz forces in CCT1

The Lorentz forces in a CCT dipole magnet are azimuthally asymmetric and can be described by two components. The first component is normal to the ribs between adjacent turns, and

the second is oriented in the radial direction normal to the cylindrical mandrel surface. The Lorentz force density in these two directions for CCT1 is shown in Figures 5.9 and 5.10. It is seen that the Lorentz force intercepted by the ribs (perpendicular to the conductor path and radial direction) vary from a minimum of zero at the midplane to a maximum at the poles. A beneficial feature of the CCT design is the size of the mandrel ribs are inherently dimensioned similar to the magnitude of the forces they intercept. They start thin at the midplane and reach their thickest point in the pole region. As seen in the figure, there is an inversion of the force on the ribs for an oppositely canted layer. This results in an axial shearing force between the two layers with a maximum in the pole region.

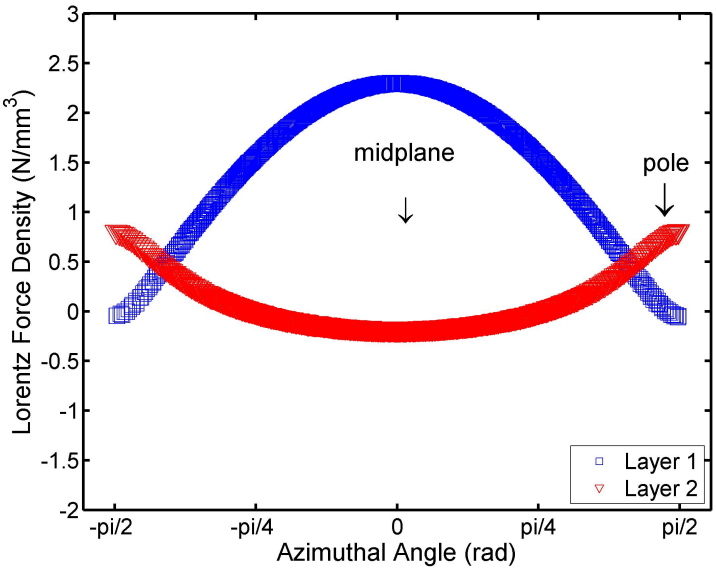

Figure 5.10: The Lorentz force density directed in the radial direction is shown for CCT1. The results displayed were calculated at the center of the conductor using Opera3D.

The radial Lorentz force in layer 1 of CCT1 can be seen varying opposite of the force in the rib direction. The radial force starts at a maximum on the midplane and decreases to a minimum in the pole region. These forces act to move the conductor out of the channel. For each layer the radial forces are partially captured by the spar of the layer above it or the external structure in the case of the final layer. As will be seen in the structural analysis, the asymmetry of both the rib and radial forces leads to bending of the coilpack (CCT layers) from a circular to an elliptical shape. This can induce both high stress concentrations and field errors. A key consideration for the outer structure of a CCT dipole is its role in preventing this Lorentz force induced bending by providing pre-stress and rigidity.

Generation of the ANSYS model

The ANSYS models were created using the periodic CCT symmetry region assuming 180 degree symmetry, as described in Section 3.3, and seen for CCT1 in Figure 5.11. The geometry was generated from keypoints and meshed using the SOLID186 element type. A mesh copy operation was used to ensure the outer axial faces of the region were identically meshed. This created pairs of matching nodes for the constraint equations implementing the boundary conditions. The contact surfaces between the conductor and mandrel of each layer were bonded, and all the constant radius contact surfaces were allowed to slide with no friction.

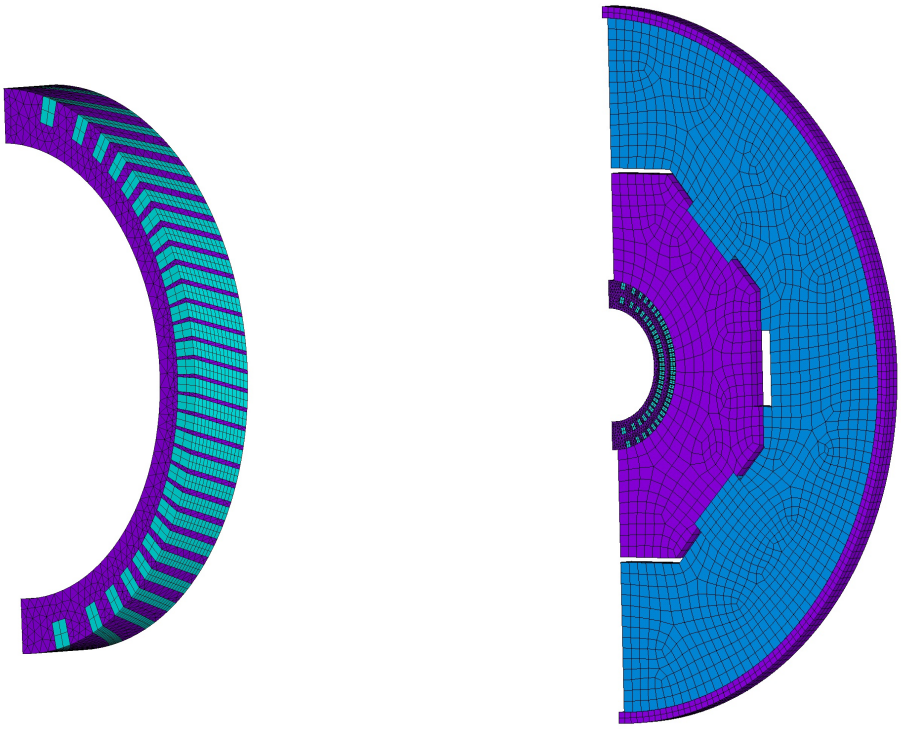

Figure 5.11: The 3D periodic symmetry region used for structural calculations in ANSYS is shown for layer 1 of CCT1 and for both layers assembled into a key, bladder, and shell structure.

Three load steps were solved for each of three axial boundary conditions studied. First the assembly load was produced by applying an interference between the keys and the pad (to simulate bladder pressure). A second load step was then solved with a cooldown of the model to 4.3 K. The third and final load step was solved with the operating Lorentz forces applied to the conductor elements. This was done by calculating the Lorentz force at the centroid location of each ANSYS conductor mesh element using Opera3D and then

distributing it equally on the nodes of the element. For all reported results a key interference of 0.1 mm was applied for the assembly, and the Lorentz force loads were calculated using a current of 5 kA.

Investigation of all three axial boundary conditions for CCT1

Table 5.7 shows the values of δ_z used to implement each of the three axial boundary conditions described in Section 2.9 for CCT1 and the resultant normal forces. F_z is the normal stress integrated over an entire 360 degree face, and the axial length change δ_z is normalized by the pitch length. The plane stress results are rounded to show zero force across individual components and zero net force across the conductor and mandrel in each bonded layer. The behavior of CCT1 is expected to be closest to the "Single Strain" boundary condition where all components share the same axial length change. This is due to the planned epoxy impregnation of the coil pack, and the structural support at the ends of the magnet tying the motion of multiple components together. Outside of Table 5.7 all presented results were calculated with the "Single Strain" boundary condition.

Table 5.7: CCT1 Axial Boundary Condition Results

		0.1 mm Key Interference		Cooldown to 4.3 K		Operation at 5 kA	
		δ_z/w ($\mu\epsilon$)	$F_z(kN)$	δ_z/w ($\mu\epsilon$)	$F_z(kN)$	δ_z/w ($\mu\epsilon$)	$F_z(kN)$
Generalized Plane Strain	L1 Mandrel	0	-3	0	202	0	272
	L1 Conductor	0	0	0	33	0	34
	L2 Mandrel	0	-6	0	266	0	272
	L2 Conductor	0	-1	0	38	0	40
	Pad	0	-9	0	6028	0	6022
	Yoke	0	-17	0	21683	0	21681
	Shell	0	39	0	1898	0	1902
			$\sum F_z = 3$		$\sum F_z = 30148$		$\sum F_z = 30223$
Single Strain	L1 Mandrel	-0.3	-3	-2307	80	-2308	85
	L1 Conductor	-0.3	0	-2307	6	-2308	8
	L2 Mandrel	-0.3	-6	-2307	104	-2308	109
	L2 Conductor	-0.3	-1	-2307	7	-2308	9
	Pad	-0.3	-10	-2307	2674	-2308	2667
	Yoke	-0.3	-19	-2307	-3852	-2308	-3863
	Shell	-0.3	39	-2307	980	-2308	984
			$\sum F_z = 0$		$\sum F_z = -1$		$\sum F_z = -1$
Generalized Plane Stress	L1 Mandrel	36	0	-3694	10	-3807	10
	L1 Conductor	36	0	-3694	-10	-3807	-10
	L2 Mandrel	71	0	-3698	10	-3793	10
	L2 Conductor	71	0	-3698	-10	-3793	-10
	Pad	5	0	-4160	0	-4155	0
	Yoke	1	0	-1963	0	-1962	0
	Shell	-85	0	-4593	0	-4612	0

Stress interception in CCT1

The effectiveness of mandrels to prevent the accumulation of Lorentz force induced stress was studied by means of a comparison. A second ANSYS model identical to CCT1 was generated with the mandrel spar of layer 1 removed. In this model the ribs between turns no longer provide internal structural support, behaving similar to wedges in a traditional sector coil design. The stress distribution within layer 1 of this sparless model was compared to CCT1 and an analytic calculation of the accumulated stress in an equivalent sector coil [59]. The results of this comparison are shown in Figure 5.12. The ANSYS result shown

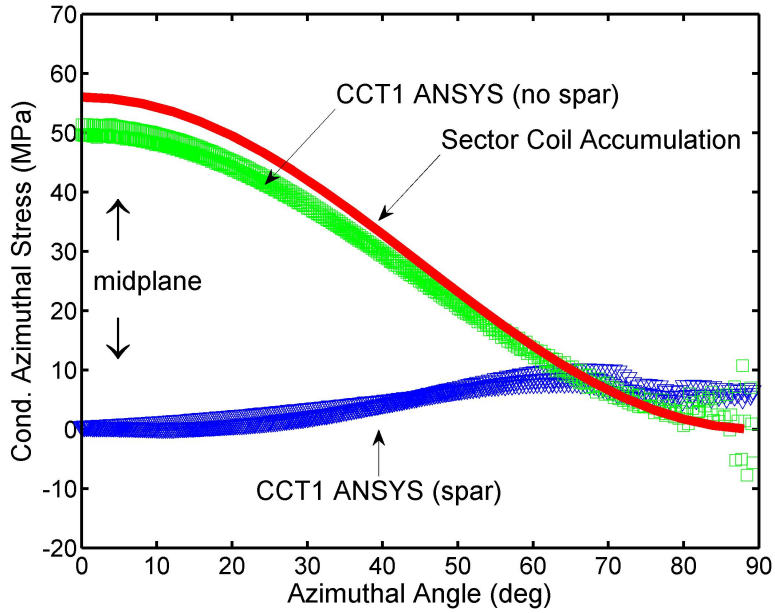

Figure 5.12: The Lorentz force induced azimuthal stress (difference between cooldown and operation) for the conductor of CCT1 is compared to results from a model with the inner mandrel spar removed (no interception) and to the predicted azimuthal stress within an equivalent sector coil. The stress in the CCT model with interception is seen reduced to near the single turn level.

is the difference in azimuthal conductor stress between the cooldown and operation load steps, representing the effect of the Lorentz forces on the model. The conductor in high field accelerator dipoles is typically pre-stressed with an outer structure (during assembly and cooldown) such that no part of the coil goes into tension during operation. It is seen that the ANSYS model with no internal interception of Lorentz forces (spar removed) behaves similar to a sector coil and requires a pre-stress of 50 MPa. The ANSYS results with the spar included show the stresses intercepted and reduced to the integration of the Lorentz

force over individual turns (0 - 8 MPa) as opposed to the integration over the coil pack (0 - 50 MPa).

CCT1 operating stress

The stress during operation for the conductor and structure of CCT1 is shown in Figure 5.13. Due to the interception of forces, the operating conductor stress is dominated by the pre-stress applied during assembly and cooldown. Even with a minimum assembly bladder preload (0.1 mm key interference), the coil is still pre-stressed beyond the requirement. The majority of this develops during cooldown and is applied asymmetrically to the coil by the aluminum mandrels. While this pre-stress is excessive for CCT1, the external structure was still considered for the test as a step towards high field Nb_3Sn CCT magnets where it may be necessary.

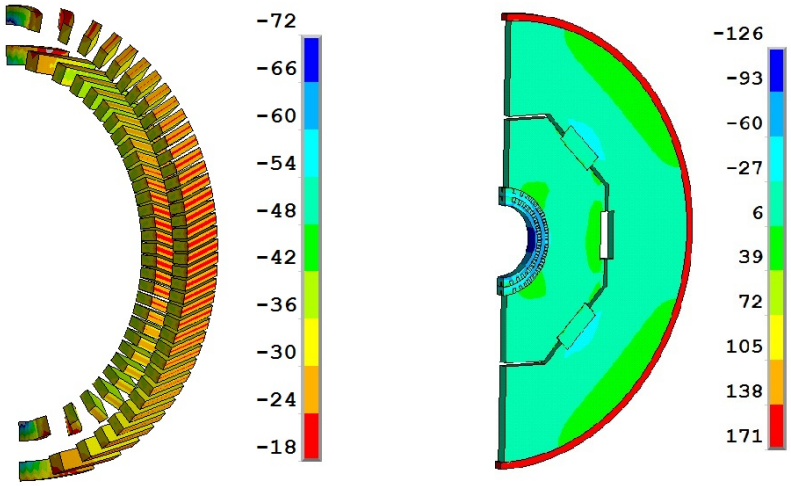

Figure 5.13: Operating azimuthal conductor stress in MPa is shown for CCT1 conductor and structure.

CCT1 stress without an outer structure

For CCT1, the low required pre-stress suggests the consideration of testing without an outer structure. The shell based structure of the CCT1 ANSYS model was removed, and the two remaining mandrels and conductor layers were bonded to reflect the epoxy impregnation. Conductor stress after cooldown and operation are shown in Figure 5.14.

Even without an external structure, a pre-stress develops on the coil during cooldown due to the difference in thermal contraction between the aluminum mandrels and conductor

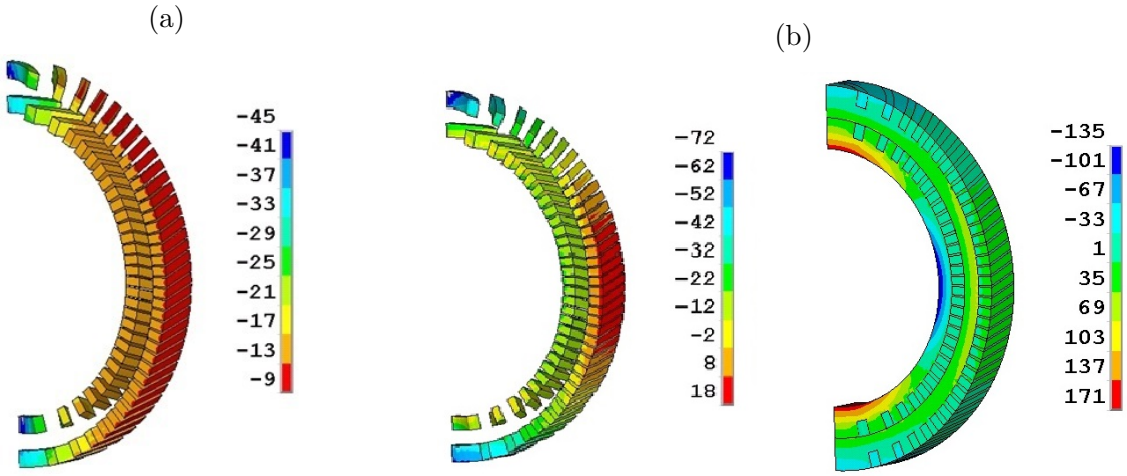

Figure 5.14: Azimuthal stress in MPa is shown for CCT1 without an external structure for cooldown (a) and operation (b). Without an external structure providing rigidity the coil pack is susceptible to bending under the azimuthally asymmetric Lorentz force loads.

windings. During operation, stress concentrations and tension appear due to the bending of aluminum mandrels under the Lorentz force loads (Fig. 5.14). In addition to applying any necessary pre-stress to the coil, an external structure can be incorporated into the CCT design to oppose the radial Lorentz forces and prevent bending of the coil pack. Given the low pre-stress requirements in the CCT due to Lorentz force interception, future design studies may be more focused toward removal of external structure by improving the rigidity of the internal structure and the pre-stress it provides.

5.5 Fabrication

The two winding mandrels for CCT1 were fabricated by CNC machining of 6061 aluminum alloy tubes (Fig. 5.15). The continuous rectangular channel (3.02 x 1.60 mm) forming the CCT path was created by many passes of a 1.60 mm diameter ball-end mill. At all times this mill was kept oriented radially with respect to the cylindrical surface. The cut depth for each pass was set to a conservative 0.13 mm for the machining of layer 1. This resulted in a machine cutting time of 18 hours. Based on the experience with layer 1, the single pass cut depth was increased to 0.254 mm for layer 2. This increase, combined with a slightly longer conductor path, led to a machining time of 10 hours. As a result of a mix-up in the CAD model transferred to the machine shop, layer 2 was machined to have only 72 turns and not the 78 turns in the design.

Following the machining, both winding mandrels were anodized in Cal Berkeley colors with a choice of gold for layer 1 and blue for layer 2 (Fig. 5.16). This was done to pro-

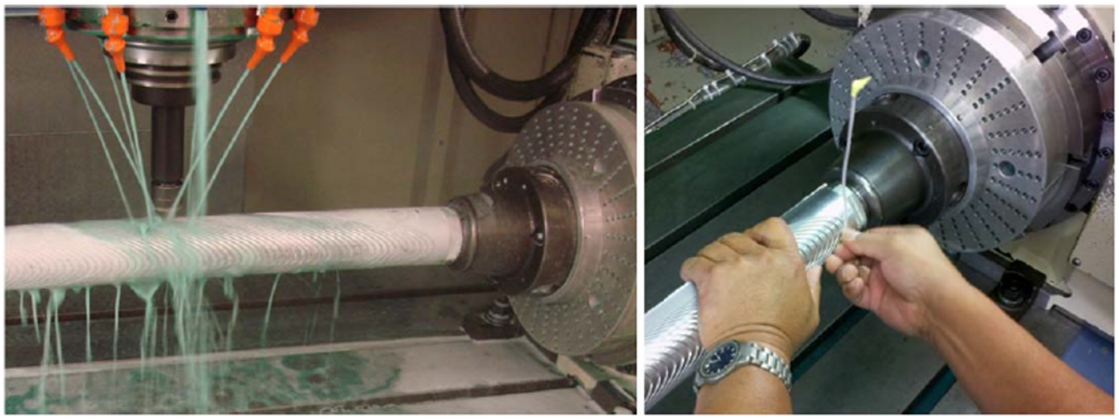

Figure 5.15: The CNC machining of an aluminum winding mandrel for CCT1 is shown.

vide additional protection against electrical shorts between the mandrel and the insulated conductor. After being anodized, each layer was wound by hand with insulated cable. A continuous winding between layer 1 and layer 2 was first attempted. In this scheme layer 1 was wound and then inserted into layer 2, after which a special transition within the mandrels themselves brought the conductor from layer 1 to layer 2 with no break or splice necessary (Fig. 5.17). It proved difficult to insert layer 1 into layer 2 with a tight fit and the continuous transition. During the attempt, the insulation of the conductor of layer 1 was damaged, but this was not realized until after the winding of layer 2 had been completed.

Figure 5.16: The anodized mandrels for layer 1 and layer 2 of CCT1 are shown. The mandrels were wound with conductor by hand with no additional applied tension.

As a result of the damage caused during assembly with a continuous transition, it was decided to break the conductor between layers and rewind layer 1. The transition was cut and the two layers were separated from each other. Then the conductor of layer 1 was removed (because of the insulation damage) and then rewound with new insulation. After this, layer 1 was reinserted into layer 2 with 0.05 mm sheets of G10 between them acting as a slip plane (Fig. 5.17). After assembling the layers together a splice was made outside the magnet to connect the conductor of layer 1 to layer 2. Experience with CCT1 has shown it is desirable to keep R&D CCT magnets as modular as possible by isolating the fabrication and winding of individual layers (with a final assembly of the layers together at the end).

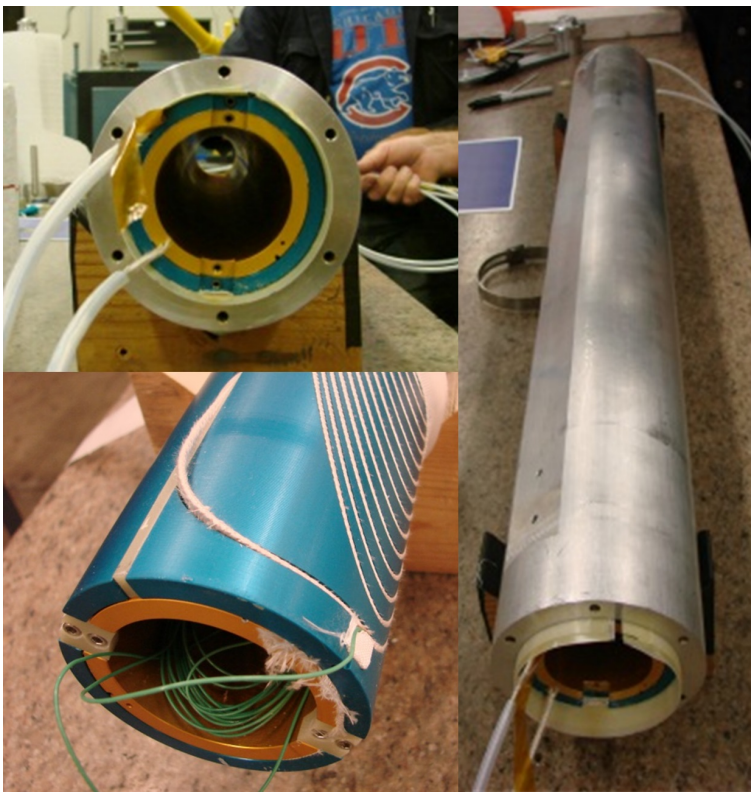

Figure 5.17: Layer 1 and layer 2 of CCT1 are shown assembled one inside the other and then into an outer aluminum shell. The bottom left image shows the continuous transition between layers that was later replaced with a splice outside the magnet.

After the assembly of layer 1 into layer 2, both layers were inserted into a 20 mm thick aluminum shell (Fig. 5.17). Similar to the assembly of layer 1 and layer 2, G10 sheets were used between layer 2 and shell to provide a slip plane while pushing one into the other. While the initial design of CCT1 considered a complex external loading structure, a simple shell was chosen to reduce cost and expedite the test. Epoxy impregnation of the magnet

(to prevent conductor motion) was considered and then decided against. The low forces in the CCT combined with the added benefit of liquid helium bathing the conductor were the primary factors in this decision. There was interest in impregnating CCT1 after the test and performing a second test to study the merits of impregnation, but this was decided against due to funding constraints.

A set of electrical tests were performed on CCT1 after the fabrication and assembly of the magnet. Measurements of the inductance L_s, capacitance C_s, and resistance R_s were taken in series mode. The measured values as a function of frequency can be seen in Table 5.8. These AC values are influenced by eddy currents induced in the aluminum mandrels and shell. A fit for the DC value of inductance was performed, leading to a value of 1.19 mH. This value was used for comparison with the analytic model for inductance of CCT1 in Table 5.6.

Table 5.8: CCT1 Electrical Measurements

Freq.	Ls (μH)	Q	Cs (mF)	Rs (mΩ)
20 Hz	456.9	0.005	-138.7	1080
30 Hz	336.7	0.06	-83.6	1090
100 Hz	156.7	0.09	-16.16	1150
1 kHz	35.9	0.18	-0.7059	1290
10 kHz	17.04	0.61	-0.0149	1760
30 kHz	12.15	1.05	-0.00232	2180
100 kHz	10.1	1.99	-0.0002516	3170
300 kHz	8.69	2.66	-0.0000324	6150

5.6 Test results

CCT1 was tested at a temperature of 4.2 K at LBNL's Superconducting Magnet Test Facility. Several tests were performed with goals of determining the short-sample performance and field quality of the magnet. A 26 mm long rotating field coil of 18.2 mm radius (72% of the clear bore) was used for magnetic measurements. After being cooled down to 4.2 K, the magnet current was ramped towards the calculated short-sample limit of 4050 A. During these ramps the rotating field coil was used to measure the field harmonics in the straight-section of the magnet. The results of these measurements for the first three allowed harmonics (b_3, b_5, and b_7) are shown in Figures 5.18 and 5.19. All other measured harmonics up to b9 were less than two units.

Some variation of the harmonics with magnet current is seen with the largest occurring for the sextupole (b_3). A possible explanation for this behavior is radial movement of the

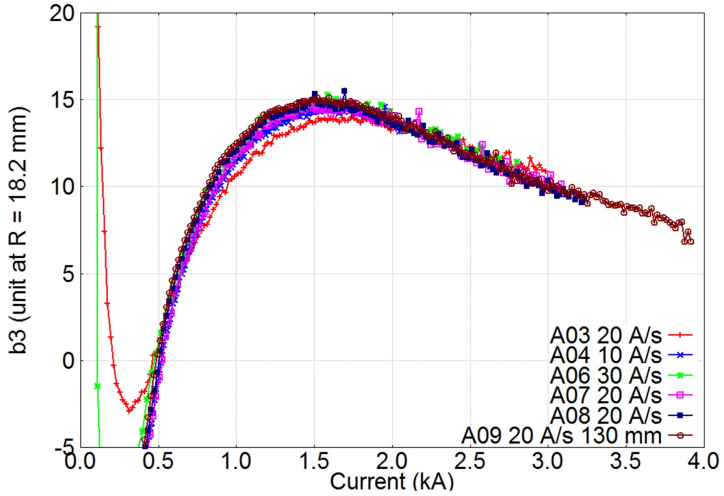

Figure 5.18: The straight-section sextupole (b_3) is shown as function of magnet current for the six current ramps of CCT1.

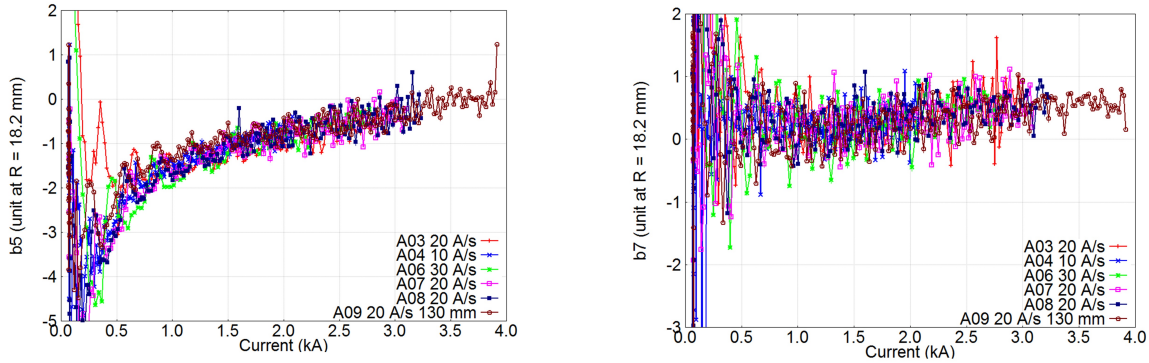

Figure 5.19: The straight-section b_5 and b_7 harmonics are shown as function of magnet current for the six current ramps of CCT1.

conductor in the channel due to the Lorentz forces. The conductor of CCT1 was not epoxy impregnated, and the channels provide little restraint in the radial direction. A calculation was made to determine the sensitivity of b_3 field errors to radial displacement of the conductor at either the pole or the midplane. A radial displacement δr was applied to the conductor in the Opera3D model, varying as $\delta r = \epsilon_{max} \cos\theta$, such that there is a maximum displacement ϵ_{max} at the pole. A linear relationship between ϵ_{max} and b_3 was observed, with layer 1 providing 46.1 units/mm and layer 2 providing 25.4 units/mm of max radial displacement. The b_3 harmonic observed in CCT1 would then correspond to 0.1-0.2 mm of radial displacement, which is well within what would be expected of an unimpregnated coil free to move within the channel. This level of sextupole field error is higher than the acceptable limit for a typical accelerator. It is hoped that the planned epoxy impregnation

of future CCT magnets will prevent conductor movement and eliminate the sextupole field error.

In addition to the straight-section harmonics measured during the current ramps, one scan of the harmonics through the end of CCT1 was made at a fixed current. Figure 5.20 shows the measured sextupole as a function of axial distance through the end. A comparison between the measured and predicted harmonics is made. The tendency of CCT end harmonics to integrate to zero is seen in both the prediction and the measurement.

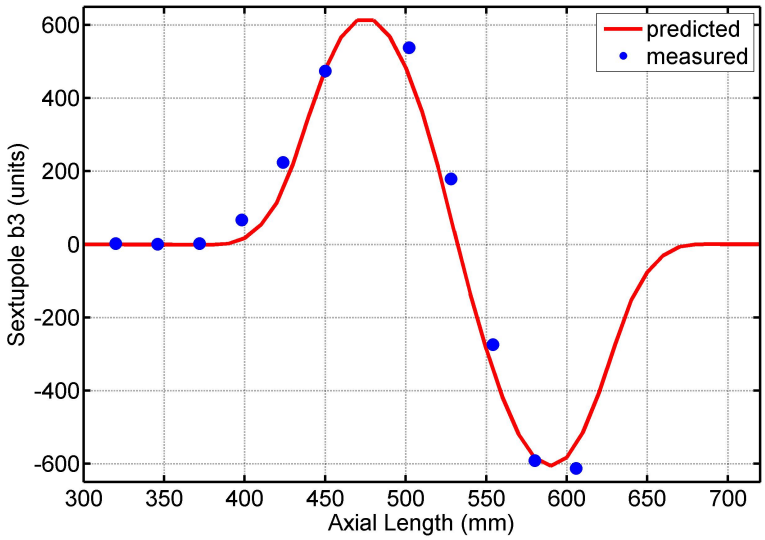

Figure 5.20: The measured sextupole harmonic (b_3) as a function of axial position through one end of CCT1 is shown.

Six quenches were observed in CCT1 before nearly reaching the calculated short-sample limit (Fig. 5.21). Of these six, only two occurred inside the magnet itself with the other four quenches occurring in the leads. The quenches occurring outside of the coil are not thought to be indicative of the performance of the magnet but rather the result of minimal mechanical support of the leads after leaving the magnet. The final quench (in the coil) was observed at 96% of the calculated short-sample limit with an extremely high quench propagation velocity. One possible explanation for this is a distributed quench in the homogeneous field region of layer 1 due to reaching the short-sample limit of the conductor. Several more current ramps were planned to check the repeatability of the maximum quench current, but a lack of helium stopped the test at this point.

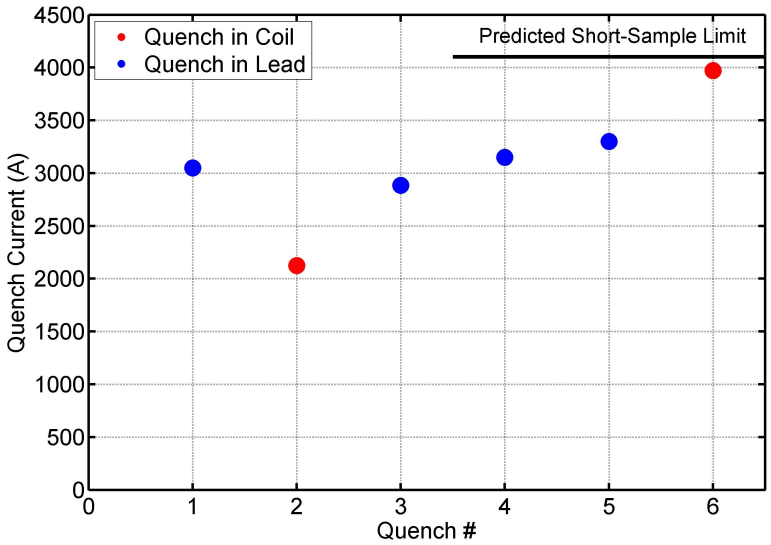

Figure 5.21: Training quenches during the test of CCT1 are shown.

5.7 Perspective on test results

While being low field and NbTi, CCT1 provides the first published test results of a superconducting CCT dipole in a configuration that scales to high field. The magnet reached 96% of the calculated short-sample limit with only one previous quench in the coil. The field quality of the CCT design was shown by both straight-section and integrated harmonic measurements. As a result of these measurements, the importance of conductor radial restraint (or the use of epoxy impregnation) for field quality in future CCT magnets was realized. Ultimately, the goal of establishing a successful proof-of-principle test before moving on to a high field Nb_3Sn dipole was accomplished.

As a result of the successful test of CCT1, the LBNL Superconducting Magnet Program began a staged program towards the test of a 16 T Nb_3Sn dipole. The details of this design will be presented in Chapter 6. The test results also had implications for curved CCT magnets for use in Ion Beam Cancer Therapy gantries. Performance of a CCT magnet was shown at the field level (2-3 T) desired for a proton gantry magnet. As a result of the interest this generated, a design study for a curved CCT proton gantry magnet was completed. This study will be presented in Chapter 9.

Chapter 6

CCT2: a 16T Nb_3Sn Dipole Design

6.1 Introduction and goals

CCT2 is a superconducting Nb_3Sn dipole magnet designed to produce a short-sample bore field of 16 T, which can be boosted to 18 T with the inclusion of a Bi2212 HTS insert. Staged tests of CCT2 are planned at LBNL as part of the high field base program, with the goal of investigating the performance of the CCT design at a field relevant to a future hadron collider. The Nb_3Sn CCT program was started following the successful proof-of-principle test of CCT1 to take the next steps towards this goal.

This chapter will present the design of CCT2 and progress towards the construction of the magnet. Magnetic and structural analysis will be shown for configurations with and without the HTS insert. A method for current grading of the outer layers to reduce the amount of conductor needed will be described. The winding mandrel approach developed for CCT1 will be shown extended to a Nb_3Sn CCT, with the introduction of a new mandrel material, reaction tooling, and epoxy impregnation technique. The reaction and impregnation of a five turn Nb_3Sn CCT layer testing this process will be described. Finally, a report will be given on the progress towards fabrication, winding, and assembly of the first two layers. These two layers will be tested with NbTi as the first step in a staged plan towards 16 T. Additional information on the design, test plan, and initial fabrication of CCT2 can be found in the following references [60, 61].

6.2 Design

CCT2 is an eight layer CCT dipole designed to reach 16 T in a 90 mm clear bore using Nb_3Sn conductor (Fig. 6.1). A winding mandrel approach was taken, with each CCT layer consisting of cabled conductor wound into channels machined into a thick-walled cylinder. These mandrels serve to position the conductor for field quality and provide structural support against the operating Lorentz forces. The eight CCT layers nest one inside the other, and

are then assembled into an external shell structure which provides additional support against the Lorentz forces.

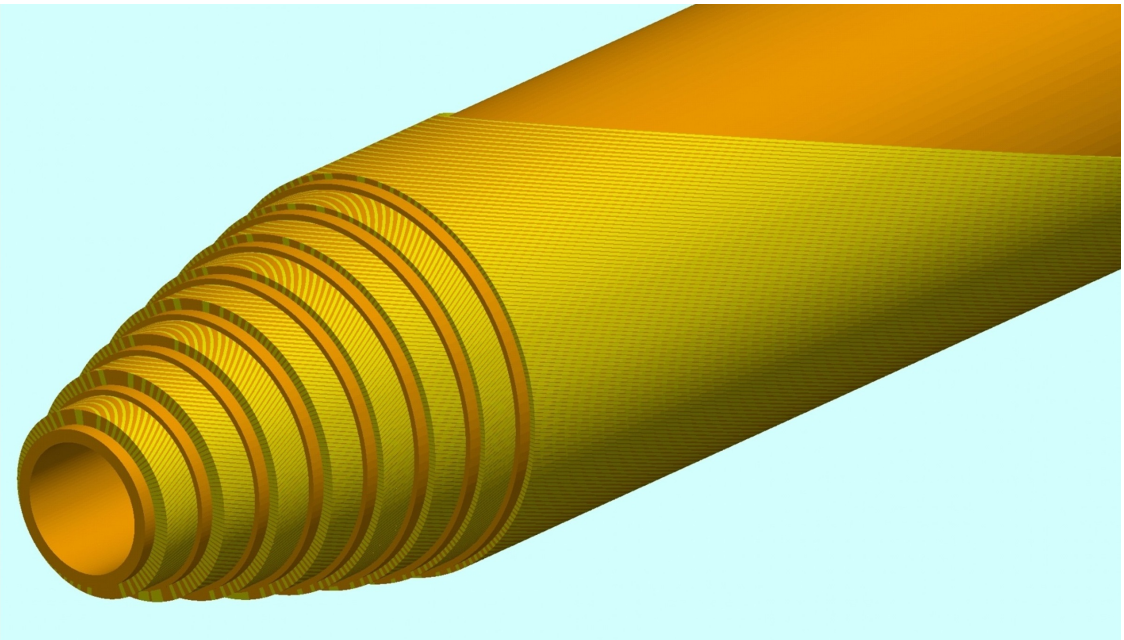

Figure 6.1: The eight graded conductor layers and mandrels of CCT2 are shown.

Table 6.1: 60/61 RRP Nb_3Sn Wire (HD3 Coil-2)

Diameter	0.8 mm
J_c (12T,4.2K)	3554 A/mm^2
J_c (15T,4.2K)	1935 A/mm^2
Non-Cu frac.	0.606

The same Nb_3Sn strand was considered for all eight conductor layers. The critical current used is based on a fit [52] of extracted strand measurements performed on HD3 coil-2 Ta-alloyed 60/61 RRP Nb_3Sn strand. This fit is representative of the highest J_c Nb_3Sn strand currently available. The properties of HD3 coil-2 strand are given in Table 6.1, with the only difference being an assumed non-copper fraction of 49% for CCT2. Each pair of layers in CCT2 uses a Rutherford cable with the number of these strands adjusted based on the maximum field on the conductor of that layer. This "grades" the conductor, and increases the current density of the outer layers where the field is lower (explained in detail in Section 4.7). As a result of this grading, four different size Rutherford cables are used. The number of strands in each cable and the approximate height and width of the mandrel channels for the insulated cable are given in Table 6.2.

Table 6.2: Rutherford Cables for CCT2

Layer	# Strands	Channel (mm)
1,2	23	2.0/10.4
3,4	17	2.0/7.69
5,6	12	2.0/5.43
7,8	9	2.0/4.07

All eight conductor layers were chosen with a tilt angle of 19 degrees and pitch of 7.627 mm. This results in a minimum rib thickness at the center of the cable of 0.483 mm. The rib thickness of CCT2 was increased with respect to CCT1 because of an increased "key-stone" effect on the ribs when placing a larger rectangular conductor on a curved surface. It was found that the minimum rib thickness at the ID of the cable of CCT2 was close to 0.381 mm due to the key-stone effect. The number of turns in all eight layers was chosen to be 132 to produce a magnetic length of nearly 1 m. These eight conductor layers can be seen in Figure 6.2.

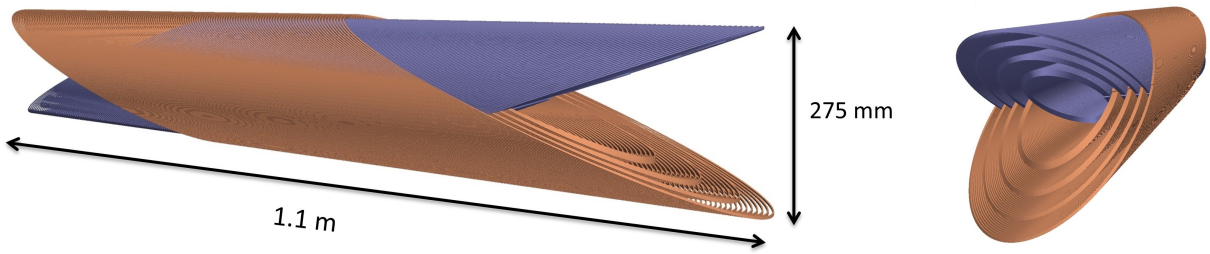

Figure 6.2: The eight conductor layers of CCT2 are shown.

The radial thickness of the thick-walled cylinders used for the winding mandrels was chosen to leave an inner wall thickness (spar) of 9 mm for the first layer, and 4 mm for layers 2-8. The increased spar thickness for layer 1 was chosen to reduce Lorentz force induced bending which will be further discussed in the section on structural modeling. The 954 aluminum bronze alloy was chosen as the mandrel material. This bronze was chosen for its availability, strength, ease of machining, and compatibility with the Nb_3Sn heat treatment reaction. The mandrel dimensions for all eight layers of CCT2 can be found in Table 6.3, and a picture of a fabricated aluminum bronze mandrel for the first layer can be seen in Figure 1.4. The amount of conductor used in CCT2 can be found in Table 6.4.

Table 6.3: CCT2 Nb_3Sn Mandrel Properties

Lay	Spar (mm)	Ri (mm)	Ro (mm)	Channel (mm)	Length (m)
1	9.0	45.0	64.4	2.0/10.4	1.2
2	4.0	64.4	78.8	2.0/10.4	1.2
3	4.0	78.8	90.4	2.0/7.69	1.2
4	4.0	90.4	102.1	2.0/7.69	1.2
5	4.0	102.1	111.6	2.0/5.43	1.2
6	4.0	111.6	121.0	2.0/5.43	1.2
7	4.0	121.0	129.0	2.0/4.07	1.2
8	4.0	129.0	137.1	2.0/4.07	1.2

Table 6.4: CCT2 Conductor Use

Layer	# turns	L-one-channel (m)	L-all-channel (m)	# strands	L-strand (m)
1	132	.807	106.5	23	2450
2	132	1.00	132.5	23	3046
3	132	1.18	156.0	17	2650
4	132	1.34	177.0	17	3008
5	132	1.48	196.0	12	2351
6	132	1.61	212.9	12	2555
7	132	1.73	228.7	9	2057
8	132	1.84	243.2	9	2189
total			1.45 km		20.3 km

6.3 Magnetic modeling

A magnetic model for CCT2 was generated in Opera3D using the method described in Section 3.2. The field harmonic representation used in this section for both local and integrated harmonics can be found described in Appendix A.

Integrated dipole field and magnetic length

The magnetic length of a dipole magnet is defined as the length of a step function of the integrated dipole field. Figure 6.3 shows the dipole harmonic along the length of CCT2 calculated at 2/3 of the bore radius using Opera3D and a current of 8100 A. This data was fit and then integrated axially through the magnet to find an integrated dipole of 1.567×10^4 T mm. A magnetic length of 0.987 m was calculated for CCT2 by simply dividing this value by the central dipole field of 15.87 T. Each CCT layer is seen contributing equally to both the dipole field and magnetic length.

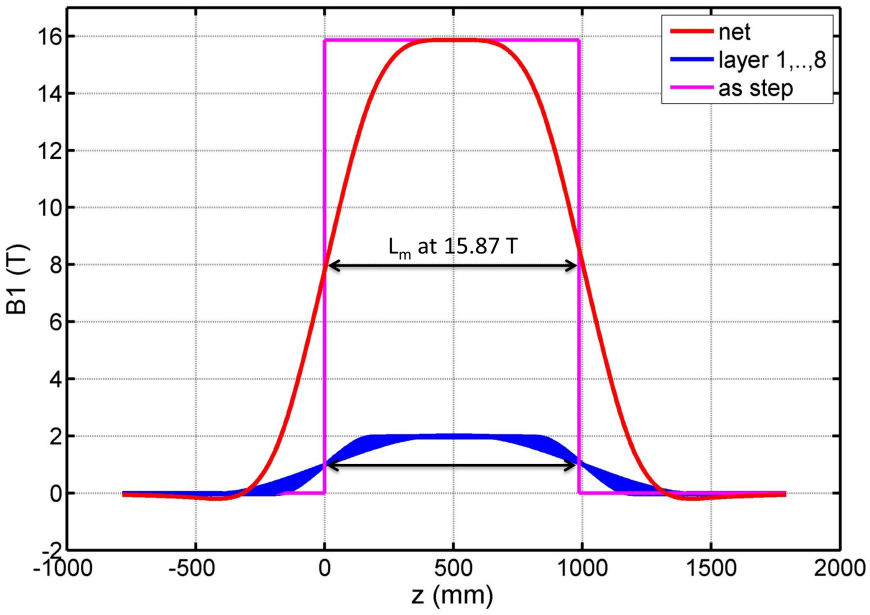

Figure 6.3: The dipole harmonic (B_1) along the length of CCT2 is shown. The equivalent dipole step function at the central field of 15.87 T is shown with the magnetic length L_m indicated.

Harmonic content in straight-section

The field errors in the straight-section of CCT2 were calculated at the axial center of the magnet using the Opera3D model. Table 6.5 shows the results of this calculation up to the 9th harmonic. CCT2 has excellent predicted field quality, < 1 unit of field error, at 67% of the 45 mm clear bore radius.

Table 6.5: CCT2: Straight-Section Harmonics from Opera3D (in units of B_1)

Ref. (mm)	% of Apert.	b_2	b_3	b_4	b_5	b_6	b_7	b_8	b_9
30.0	66.6%	-.05	-.22	<0.01	<0.01	<0.01	-.01	<0.01	.01

Solenoidal Field

The on-axis solenoidal field along the length of CCT2 can be seen in Figure 6.4. As a result of cancellation between oppositely tilted and powered layers, the value of the solenoidal field in the center of the magnet should approach zero (for example, see the solenoidal field of CCT1

in Figure 5.7). For the case of CCT2, the length of the magnet is not large enough such that the solenoidal field completely cancels in the straight-section. The length of CCT2 was kept short to test the performance of a high field CCT dipole without the cost of fabricating a long magnet or the need for a long cryostat. For a long length CCT2, as would be desired for a hadron collider, this solenoidal field would cancel in the straight-section of the magnet.

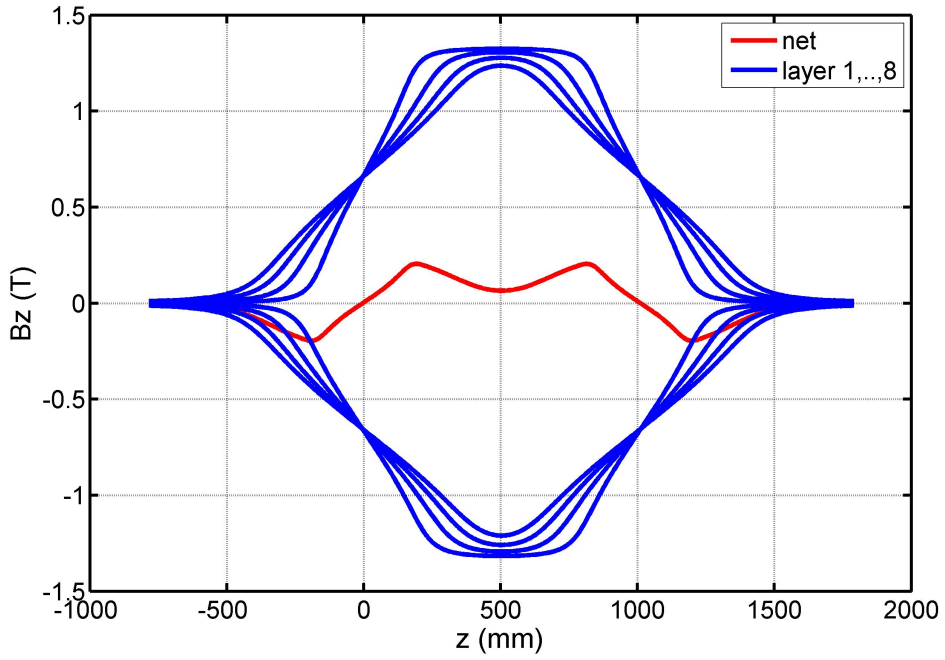

Figure 6.4: The axial variation of the on-axis solenoidal field of CCT2 is shown.

Harmonic content through the ends of the magnet

The ends break the symmetry of the magnet inducing axial variation of the higher order harmonics. To reduce the negative effects of this behavior on the beam, it is desirable that the higher order harmonics integrate to zero through the ends of the magnet. For a typical accelerator magnet this requires a difficult and time consuming optimization of the conductor path in the end region. The CCT design has the advantageous property of the higher order harmonics naturally integrating to zero through the ends (see Figure 6.5). This is due to the ends of a CCT dipole being of "Lambertson" type. The reference [57] explains the characteristics of a Lambertson end and why it is ideal for achieving zero integrated higher order harmonics.

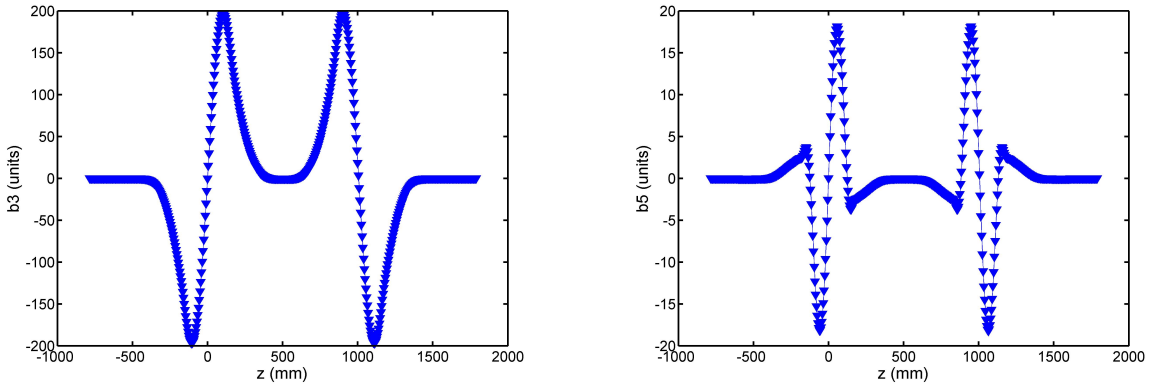

Figure 6.5: The sextupole (b_3) and dodecapole (b_5) harmonics are shown along the length of CCT2. The harmonics are calculated in Opera3D at 2/3 of the clear bore.

To describe the higher order field error through the ends of a dipole magnet, integrated harmonics are defined

$$\bar{b}_n = \frac{\int B_n(z)dz}{B_1^{SS} L_m}, \tag{6.1}$$

where B_1^{SS} is the dipole harmonic in the straight-section and L_m is the magnetic length. Calculated values of $\bar{b_n}$ for CCT2 are shown in Table 6.6. The natural field quality of CCT2, with no optimization of the ends, is shown by the low values for these integrated harmonics.

Table 6.6: CCT2: Integrated Harmonics from Opera3D (in units)

Ref. (mm)	% of Apert.	$\bar{b}_2$	$\bar{b}_3$	$\bar{b}_4$	$\bar{b}_5$	$\bar{b}_6$	$\bar{b}_7$	$\bar{b}_8$	$\bar{b}_9$
30.0	66.6%	-0.40	-0.18	-0.05	-0.02	-.01	-0.02	<0.01	0.01

Field at the conductor and short-sample

The field at the conductor of CCT2 was calculated in the Opera3D model, and found to be a maximum at the pole of layer 1 in the end region. Because the planned test of CCT2 includes no iron, this provides a linear load line for the field at the conductor. Figure 6.6 shows the field at the conductor load line for each layer in CCT2, and a selection of Nb_3Sn critical current densities from the LNBL HD series dipoles and the LARP HQ quadrupoles. The short-sample limit was based on a fit [52] of the highest critical current of those shown. This "best of the best" critical current density is based on extracted strand measurements of HD3 coil-2 conductor. With this selection, the expected short-sample fields are 15.85 T in the bore and 16.15 T at the conductor. These correspond to a short-sample magnet current of 8100 A.

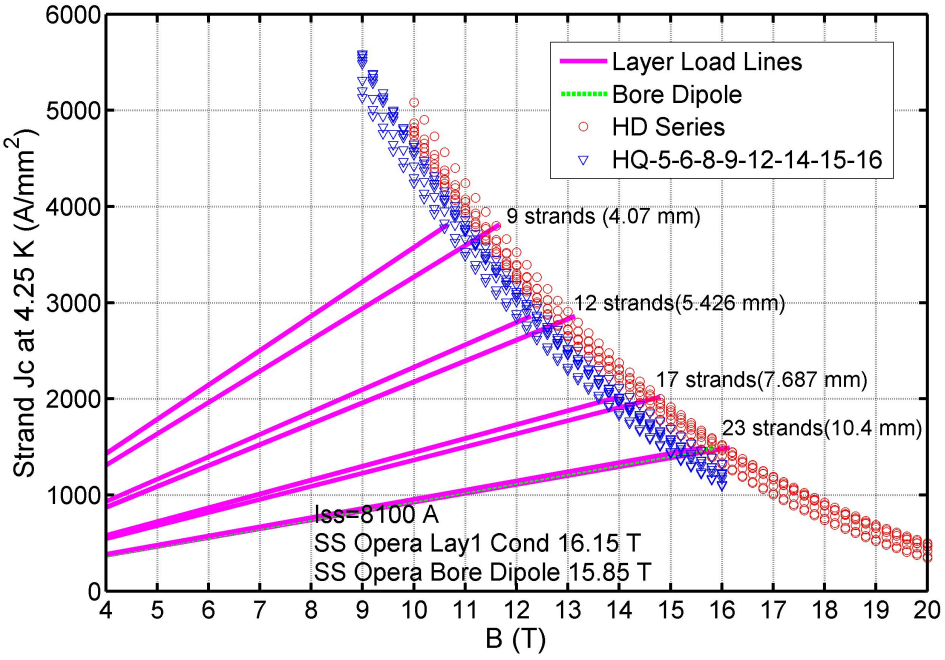

Figure 6.6: The load lines for CCT2 are shown for current density in the superconductor.

Stored energy and inductance

Using the analytic formulation in Section 2.3, the predicted inductance matrix for CCT2 is

$$L_{CCT2}\left[\frac{mH}{m}\right] = \begin{pmatrix} 1.24 & 0.76 & 1.24 & 0.76 & 1.24 & 0.76 & 1.24 & 0.76 \\ 0.76 & 1.92 & 1.18 & 1.92 & 1.18 & 1.92 & 1.18 & 1.92 \\ 1.24 & 1.18 & 2.66 & 1.64 & 2.66 & 1.64 & 2.66 & 1.64 \\ 0.76 & 1.92 & 1.64 & 3.42 & 2.11 & 3.42 & 2.11 & 3.42 \\ 1.24 & 1.18 & 2.66 & 2.11 & 4.20 & 2.59 & 4.20 & 2.59 \\ 0.76 & 1.92 & 1.64 & 3.42 & 2.59 & 4.96 & 3.06 & 4.96 \\ 1.24 & 1.18 & 2.66 & 2.11 & 4.20 & 3.06 & 5.71 & 3.52 \\ 0.76 & 1.92 & 1.64 & 3.42 & 2.59 & 4.96 & 3.52 & 6.46 \end{pmatrix}, \tag{6.2}$$

resulting in a total inductance of 147.09 mH/m. It is seen that the mutual inductance between the large number of layers is the majority contribution to the total inductance. The stored energy of CCT2 at the short-sample current of 8100 A in all eight layers is then 4.83 MJ/m. In Section 6.8 the measured inductance of a short, 64 turn magnet comprised of layers 1 and 2 of CCT2 will be compared to this prediction.

The advantages of grading

Section 4.7 describes the process by which the current density of a CCT magnet can be graded. This method was applied to reach the final graded design of CCT2. A comparison was made between this design and a case where no grading was performed. This corresponds to a version of CCT2 that uses the same cable for all layers (23 strands). The difference in conductor use, stored energy, and inductance can be seen in Table 6.7.

Table 6.7: Grading Savings for CCT2

	Ungraded	Graded	% difference
Total Nb_3Sn Strand	36.29 km	20.31 km	44.0
Stored Energy	5.41 MJ/m	4.83 MJ/m	10.7
Inductance	165.0 mH/m	147.1 mH/m	10.7

6.4 Inclusion of a Bi2212 HTS insert to reach 18 T

The addition of a high temperature superconducting (HTS) insert inside of the eight Nb_3Sn layers was considered to boost the bore dipole field from 16 T to 18 T. This boost in field comes with the cost of reducing the clear bore from 90 mm to 40 mm. The insert is comprised of four CCT layers wound with Rutherford cables made from Bi2212 strand. The reduction in conductor stress offered by the CCT design is especially advantageous for a HTS insert due to Bi2212 being more strain sensitive than Nb_3Sn. A summary of CCT insert development at LBNL using Bi2212 conductor can be found in the following reference [62].

Table 6.8: Bi2212 and Nb_3Sn Mandrel Properties

Lay	Spar (mm)	Ri (mm)	Ro (mm)	Channel (mm)	Length (m)
1	8.0	20.0	31.2	1.8/3.2	1.2
2	3.0	31.2	37.4	1.8/3.2	1.2
3	3.0	37.4	43.6	1.8/3.2	1.2
4	3.0	43.6	49.8	1.8/3.2	1.2
5	4.2	49.8	64.4	2.0/10.4	1.2
6	4.0	64.4	78.8	2.0/10.4	1.2
7	4.0	78.8	90.4	2.0/7.69	1.2
8	4.0	90.4	102.1	2.0/7.69	1.2
9	4.0	102.1	111.6	2.0/5.43	1.2
10	4.0	111.6	121.0	2.0/5.43	1.2
11	4.0	121.0	129.0	2.0/4.07	1.2
12	4.0	129.0	137.1	2.0/4.07	1.2

This insert uses the same winding mandrel approach as CCT1 and CCT2, with use of 954 aluminum bronze as the mandrel material. A 0.8 mm diameter Bi2212 strand with a 100 atm overpressure reaction was considered. This represents the "best of best" measured current density in OST Bi2112 strands [63]. An eight strand Rutherford cable was chosen, corresponding to channel dimensions of 1.8 mm width and 3.2 mm height. A tilt angle of 16.617 degrees and minimum rib thickness of 0.381 mm was used to match the pitch length of the outer Nb_3Sn layers. This allows for the magnetic length of the insert and outer to be matched with 132 turns. The increased spar thickness of the first Nb_3Sn mandrel, added to reduce coilpack bending, was removed and added instead to the mandrel of the first HTS layer. The resultant winding mandrel specifications for all 12 layers are shown in Table 6.8.

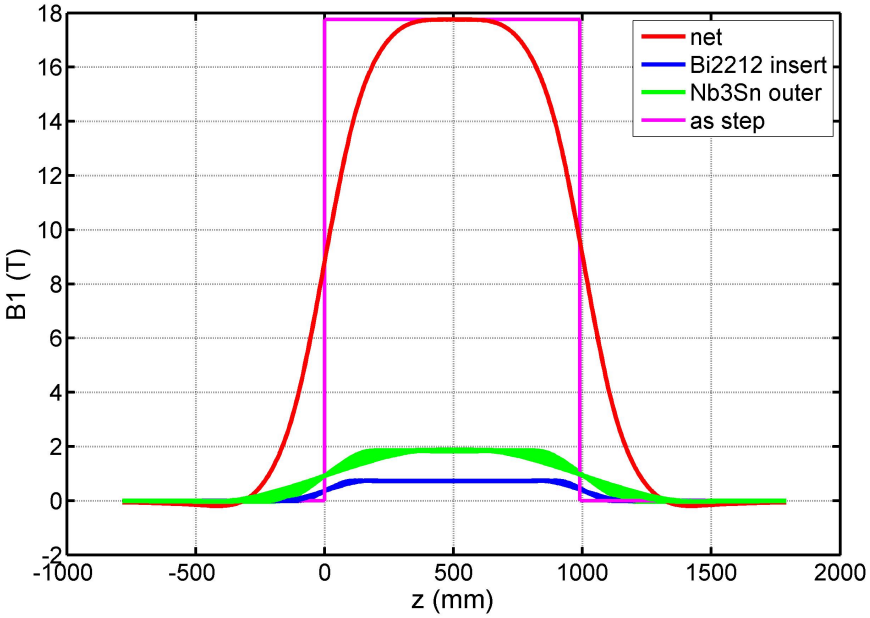

Figure 6.7: The dipole along the length of CCT2 with the Bi2112 insert is shown.

The dipole field profile of the hybrid HTS and Nb_3Sn dipole is shown in Figure 6.7 for the maximum current of 2.62 kA in the HTS layers and 7.58 kA in the Nb_3Sn layers. The contribution to the magnetic length is the same for each individual layer in both the HTS insert and the Nb_3Sn outer. This was accomplished by matching the pitch and using a fixed 132 turns for all twelve layers. The load lines are coupled because changing the current in the HTS insert changes the maximum field at the Nb_3Sn outer and vice versa. In this case there is a set of currents at the short-sample limit for both materials which maximizes the field in the bore. The maximum operating point for this design is 2.62 kA in the HTS and 7.58 kA in the Nb_3Sn, which can be seen as the end of each load line in Figure 6.8. In this

case the maximum field is 18.0 at the first layer of HTS, 16.5 T at the first layer of Nb_3Sn, and 17.7 T in the bore.

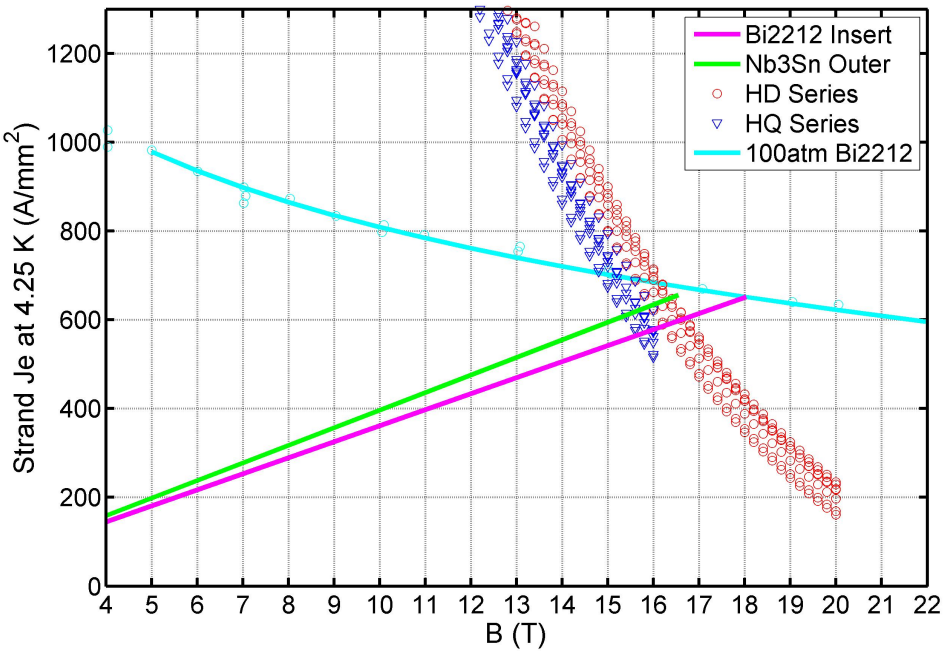

Figure 6.8: The coupled load lines for the hybrid configuration of CCT2 are shown for current density in the strand.

6.5 Structural modeling

Two ANSYS models were created using the CCT's 3D periodic axial symmetry with the method described in Section 3.3 and the "Single Strain" boundary condition described in Section 2.9. The first model is made up of the eight layers of Nb_3Sn and a 25 mm outer aluminum shell. The second model includes the addition of the four layer HTS insert inside the Nb_3Sn model (Fig. 6.9). The Nb_3Sn and HTS layers each require their own operating current and axial boundary condition. These can be found in Table 6.9 and correspond to the short-sample limit. The Lorentz force loads were calculated in Opera3D and then applied to the ANSYS model. All contact surfaces between components are treated as bonded to reflect an epoxy impregnation of the entire structure.

Table 6.9: The Two ANSYS Models

Config.	I Nb_3Sn (kA)	I Bi2212 (kA)	B_{peak} (T)	δ_z/w ($\mu\epsilon$)
Lay 5-12	8.1	N/A	16.15	-3655
Lay 1-12	7.58	2.62	18.02	-3638

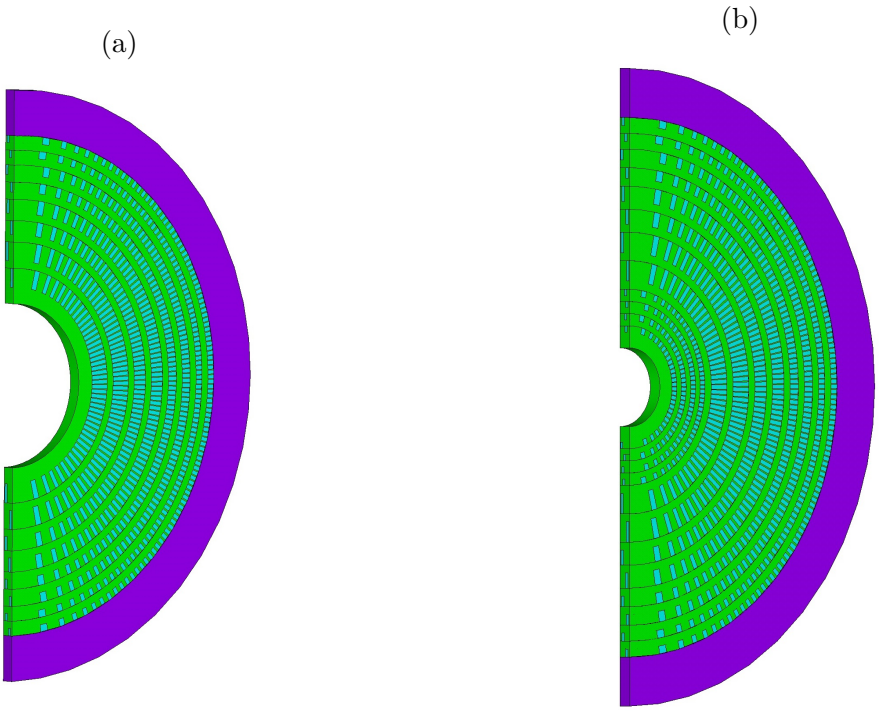

Figure 6.9: The 3D symmetry region of CCT2 is shown in ANSYS without (a) and with (b) the HTS insert.

Results for the 16 T Nb_3Sn outer (no HTS insert)

The conductor stress from the ANSYS solution without the HTS insert was transformed to a local cable coordinate system to find the longitudinal and transverse conductor stress for each layer. The method for this transformation is described in Section 3.3. A summary of the maximum and minimum values for each component is shown in Table 6.10. The highest values are found in the innermost layer. Figure 6.10 shows the three stress components plotted around a single turn for this layer. Maximum and minimum local conductor stress σ_t (along the path), σ_r (radial), and σ_b (perpendicular to the rib) are given.

Results for the 18 T hybrid configuration (with insert)

The maximum and minimum local conductor stresses for this configuration are shown in Table 6.11. The highest stress for each material is again found in the innermost layer as

Table 6.10: Max/Min Local Stress Without the HTS Insert

Layer	Type	σ_t (MPa)	σ_r (MPa)	σ_b (MPa)
1	Nb3Sn	102/-45	28/-51	72/-76
2	Nb3Sn	83/-46	20/-54	40/-67
3	Nb3Sn	47/-42	12/-56	39/-60
4	Nb3Sn	50/-41	7/-56	24/-57
5	Nb3Sn	53/-39	12/-53	24/-50
6	Nb3Sn	52/-35	12/-51	12/-45
7	Nb3Sn	52/-32	20/-43	13/-33
8	Nb3Sn	43/-30	8/-29	11/-26

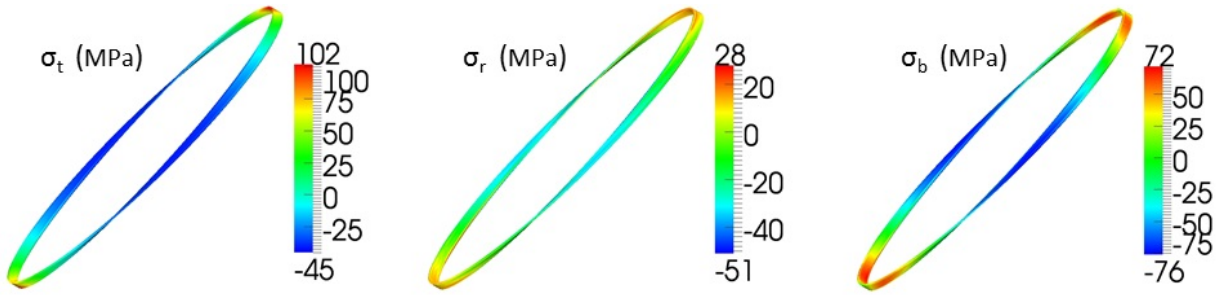

Figure 6.10: Local conductor stress is shown plotted around a single turn for the innermost layer of the eight layers of Nb_3Sn.

positive tension (σ_t) localized to the pole region. This value is 74 MPa in the Bi2212 and 41 MPa in the Nb_3Sn. The variation of the local stress components around these innermost turns is shown in Figure 6.11.

Bending stress and innermost spar thickness

A primary effect of the Lorentz forces is to bend the circular coilpack into an elliptical shape. This can lead to large conductor displacement and localized stress (as seen in Figure 6.12). Two strategies for reducing bending induced stress have been considered. The first and simpler solution is adding to the rigidity of the coilpack by increasing the thickness of the innermost spar at the cost of clear bore. The second approach is adding an outer key, bladder, and shell type structure to directionally pre-stress the coilpack on the midplane [19]. An increased spar thickness was studied first to see if a satisfactory solution could be found without adding the size and complexity of an external loading structure.

Figure 6.13 shows the results of increasing the innermost spar in the eight layer Nb_3Sn ANSYS model. The maximum longitudinal conductor stress in the local frame σ_t and man-

Table 6.11: Max/Min Local Stress With the HTS Insert

Layer	Type	σ_t (MPa)	σ_r (MPa)	σ_b (MPa)
1	Bi2212	74/-35	43/-48	60/-59
2	Bi2212	76/-36	41/-38	43/-47
3	Bi2212	51/-29	36/-32	46/-46
4	Bi2212	59/-32	35/-32	35/-42
5	Nb3Sn	41/-28	27/-29	36/-48
6	Nb3Sn	48/-31	14/-30	25/-50
7	Nb3Sn	37/-33	5/-34	25/-48
8	Nb3Sn	37/-32	8/-36	17/-49
9	Nb3Sn	52/-34	9/-37	16/-44
10	Nb3Sn	52/-30	7/-37	10/-42
11	Nb3Sn	54/-30	16/-32	12/-33
12	Nb3Sn	47/-23	7/-22	10/-28

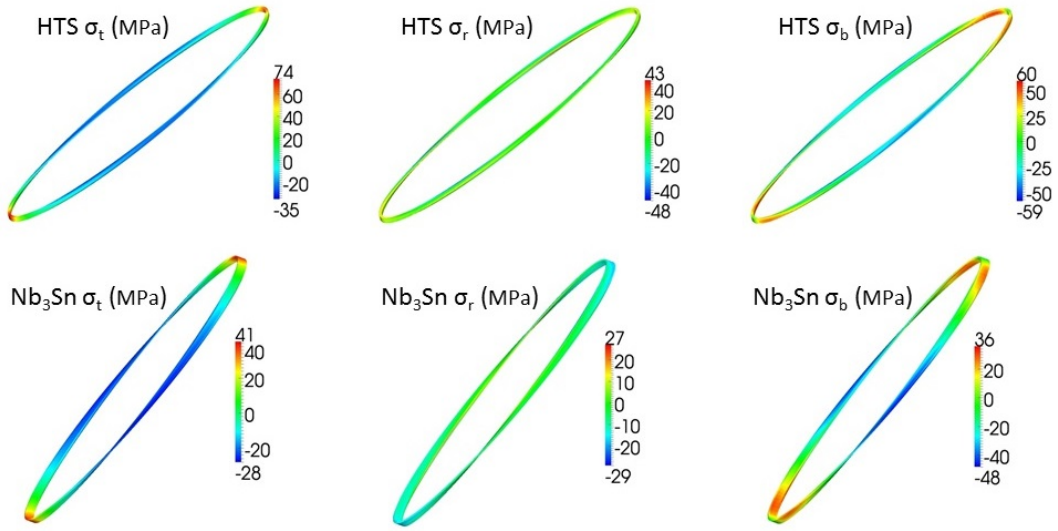

Figure 6.11: Local conductor stress is shown plotted around a single turn for the innermost Bi2212 and Nb_3Sn layer.

drel azimuthal stress σ_θ are shown as functions of the clear bore remaining after increasing the spar. It is seen that the conductor stress can be reduced to as low as 50 MPa by controlling the bending. As a compromise between available clear bore for an insert and conductor stress, an inner spar thickness of 9 mm was chosen for the design. The high stress in the innermost mandrel may require the use of an alternative material other than aluminum bronze or the replacement of the "extra" 5 mm of innermost spar with a high yield strength material bore tube.

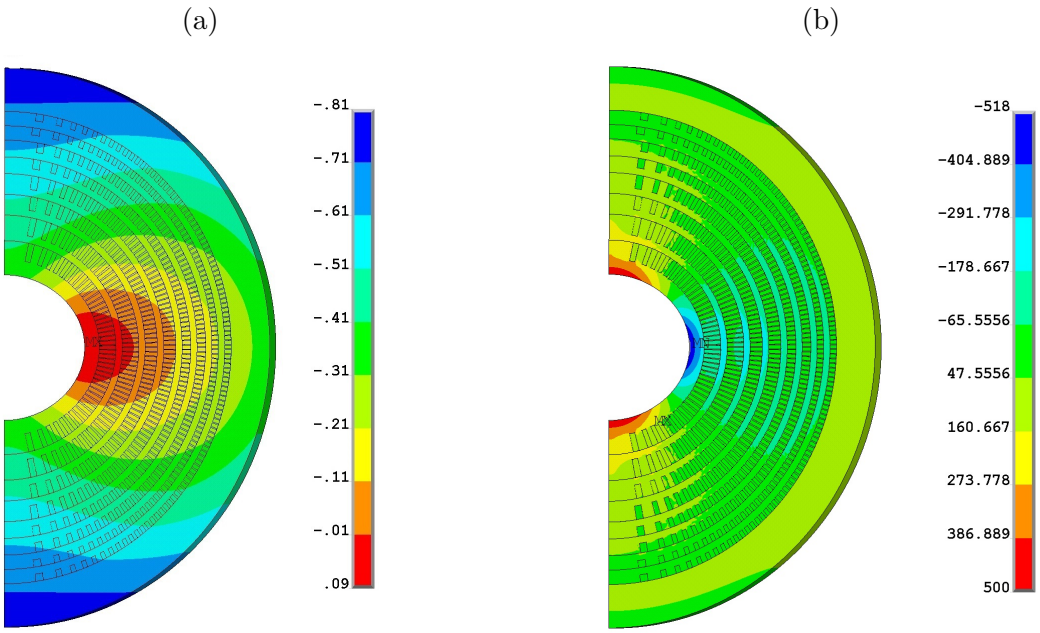

Figure 6.12: (a) Radial displacement in mm is shown for the Nb_3Sn outer. (b) The bending of the coil pack to a non-circular, elliptical shape is seen leading to high stress (in MPa) concentrated on the edge of the inner mandrel.

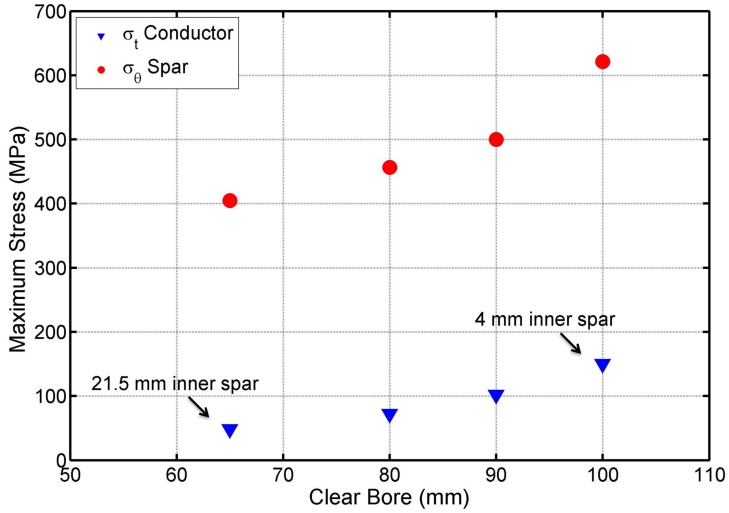

Figure 6.13: The effect of extending the spar of the innermost layer (reducing the clear bore) on the maximum longitudinal conductor and spar stress is shown for the Nb_3Sn layers. Increasing this spar reduces coilpack bending at the cost of clear bore.

6.6 The LBNL fabrication and test plan towards 16 T

Following the successful test of CCT1, a program was put in place at LBNL to move towards the test of the 16 T CCT2 design. This program will seek to incrementally test the CCT design for high field using Nb_3Sn conductor. A short, 64 turn version of Layers 1 and 2 of CCT2 will be fabricated and tested first with NbTi at 5 T and then Nb_3Sn at 10 T. If these tests are successful, the program will move on to full length Nb_3Sn layers. The plan is to incrementally add two layers to each test such that two layers are tested at 10 T, four layers at 13 T, six layers at 15 T, and 8 layers at 16 T. The 64 turn, 5 T NbTi magnet has been constructed and assembled with a test planned in May 2015. Construction has begun on the Nb_3Sn version of this short model, with a test at 10 T planned for fall 2015. The schedule for fabrication and test of the long Nb_3Sn layers will be determined following the short model tests.

6.7 A 5 turn Nb_3Sn reaction and impregnation test

Nb_3Sn CCT magnets require a heat treatment reaction of the conductor and epoxy impregnation. Nb_3Sn is a material that is too brittle to be drawn into a strand. This is overcome by keeping the tin and niobium separated within the strand so it can be drawn in a ductile state. After this, the strand can be made superconducting using a heat treatment reaction. During this reaction the tin diffuses into the niobium and the brittle superconducting Nb_3Sn state is formed. For dipole magnets it is typical to wind the cable while it is ductile and then put the whole coil through reaction. This avoids damaging the brittle conductor during winding, and is referred to as a "wind and react" process.

A 5 turn Nb_3Sn CCT layer was built to develop the "wind and react" process for a CCT (Fig. 6.14). A mandrel was created out of 954 alloy aluminum bronze material with the dimensions of the first layer of CCT2 (Table 6.3). Channels for the leads and five conductor turns were machined, and then wound with Nb_3Sn cable with a sleeved S-glass insulation. A perforated 304 stainless steel sheet 0.46 mm thick was attached over the outer surface of the mandrel using stainless steel hose clamps. This sheet was attached to prevent the conductor from moving radially outward in the channels during the heat treatment. The layer was inserted into the oven and put through the standard Nb_3Sn heat treatment. For this, the temperature of the oven was controlled at 210 ^{0}C for 80 hours, then 400 ^{0}C for 50 hours, and finally 650 ^{0}C for 50 hours.

The mandrel, screen, and clamps were all in good mechanical condition following the reaction. Upon removing the clamps, a slight movement of the conductor outward radially was observed. The measured length changes of the inner diameter, outer diameter, and axial length of the mandrel due to the reaction were all less than 0.1 mm. The length change of the conductor due to the reaction was determined by measuring the leads. The distance to the end of the mandrel for the two leads before and after the reaction can be seen in Table

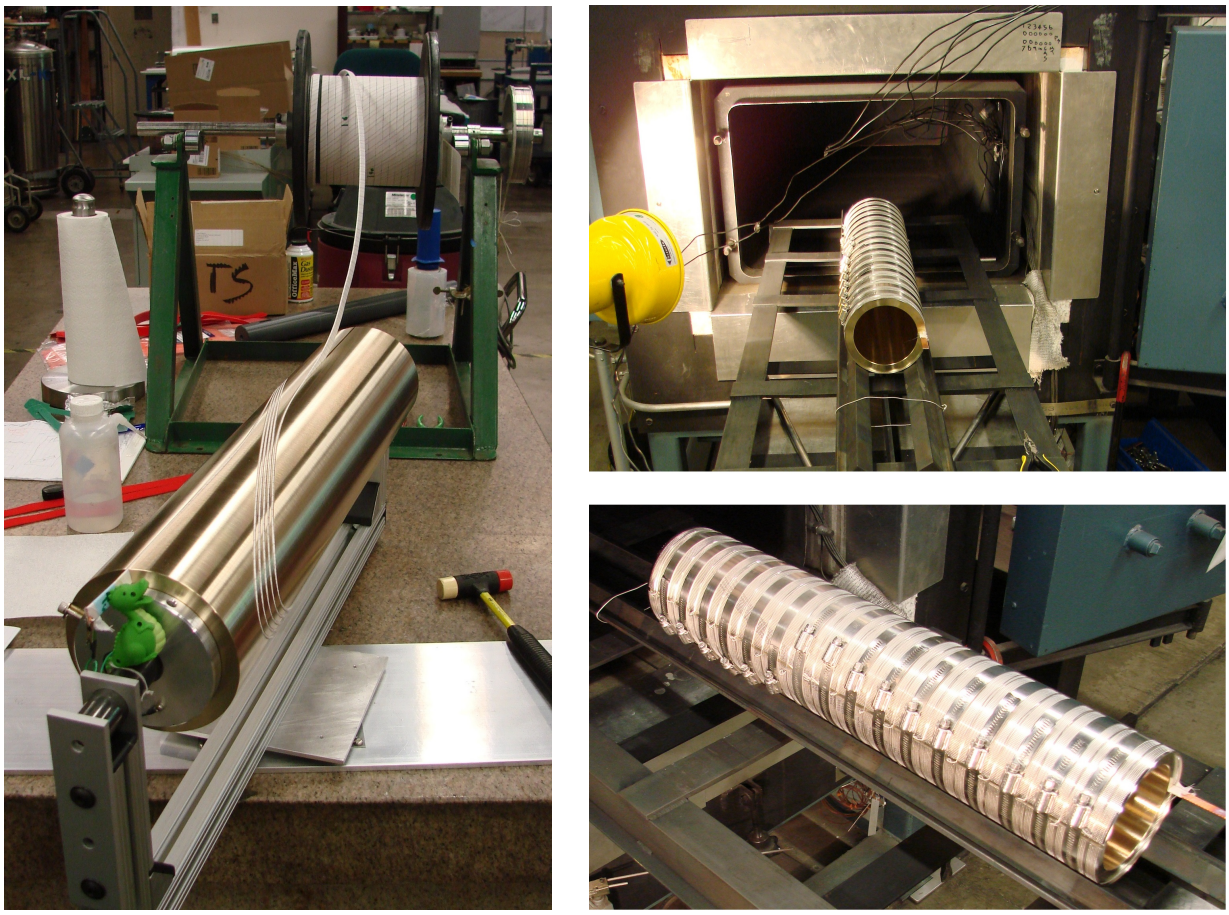

Figure 6.14: The 5 turn mandrel is shown wound with Nb_3Sn cable and then put through the heat treatment reaction.

Table 6.12: CCT2 5-Turn Reaction

	Pre-Reaction	Post-Reaction	Change
Lead In (mm)	52.55	47.45	-5.11
Lead Out (mm)	57.40	52.32	-5.08
Resistance to Mandrel	open	300 Ω	

6.12. A length contraction of approximately 5.1 mm was measured for both. The resistance between the coil and the mandrel was also measured before and after the reaction. This changed from open to approximately 300 Ohms. The increased conductivity through the insulation was thought to be due to a buildup of carbon.

Following the reaction test, the 5 turn model was also used for the development of an impregnation process. Tooling was designed to impregnate the 5 turn model using a shrink

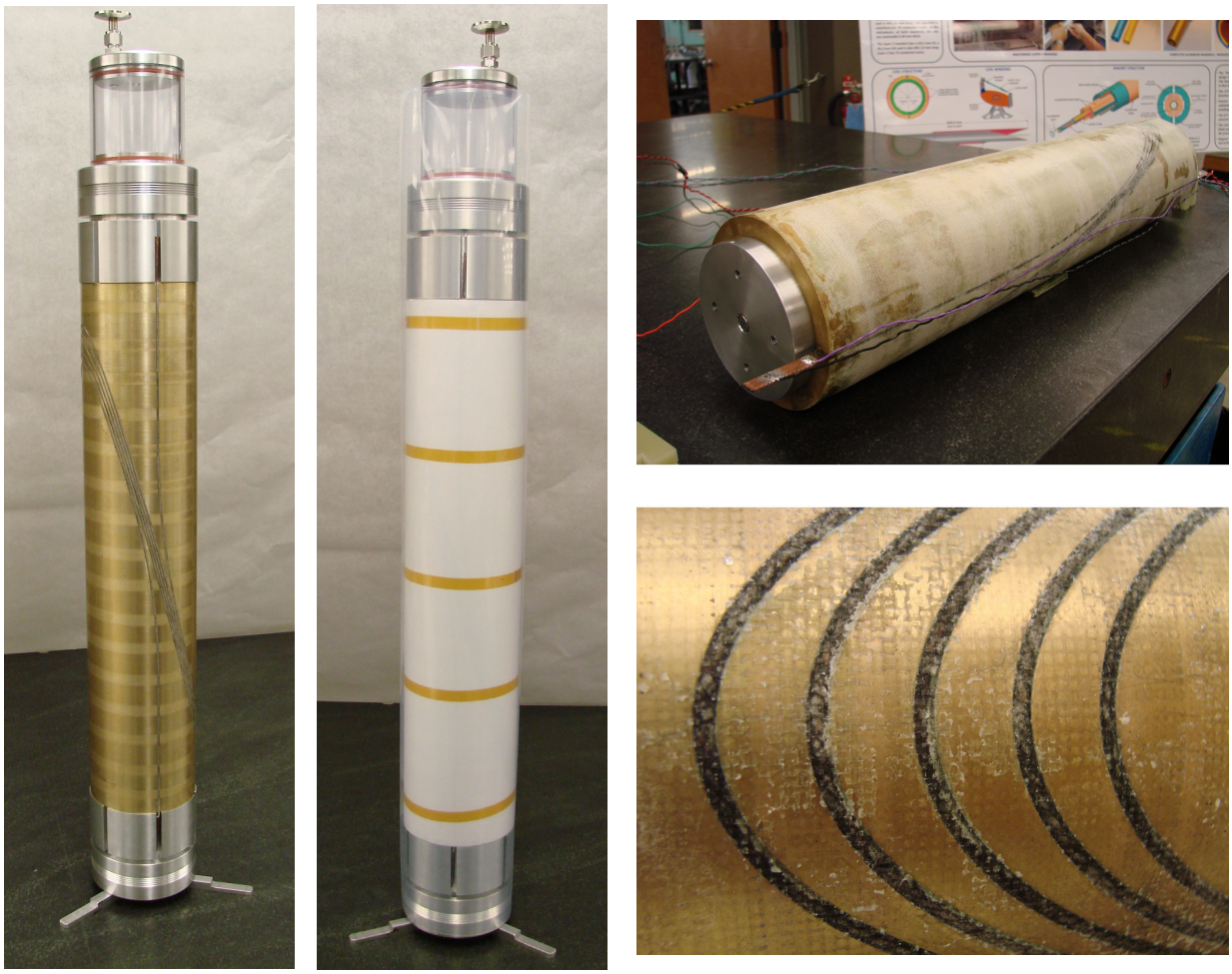

Figure 6.15: The 5 turn impregnation tooling is shown along with the results using beeswax.

tube technique (Fig. 6.15). In this scheme a shrink tubing is contracted onto the OD of the mandrel to form the outer barrier, with two end caps sealing this tubing and providing an epoxy inlet and reservoir. The epoxy then flows in through the inlet, up through the winding channels, and into the reservoir. In addition, a glass and then teflon sheet was placed between the OD of the mandrel and shrink tubing to provide additional wicking. It was decided the first test of this process would be performed using beeswax instead of epoxy. This would allow for the beeswax to be melted out if additional impregnation tests were desired.

Figure 6.15 shows the results of the beeswax impregnation test. The channels were examined for voids in the wax, and the fill was found to be uniform and complete. It appeared the wax traveled through the channel from one lead to the other, completely filling the space around the insulated cable as it went. There is the possibility the wax followed the glass sheet on the OD of the coil and then wicked down into the channels. Further tests

without a glass sheet could be performed to better determine the path of the flow. The resistance between the coil and mandrel was re-measured, and found to have dropped from 300 to 210 Ohms. The cause of the drop in coil to mandrel resistance during reaction and impregnation is not well understood, and was determined to be an area for future study. Overall, the test reaction and impregnation of the 5 turn model was considered a success, and the process developed is being considered for the reaction and epoxy impregnation of future Nb_3Sn CCT layers.

6.8 A 64 turn model of layers 1 and 2: 5 T NbTi

Design and short-sample

As described in Section 6.6 the first planned test in the CCT program at LBNL is a NbTi short model of the first two layers of CCT2. The exact same mandrels and channel dimensions of CCT2 were used with the only difference being a scale down in number of turns from 132 to 64. A shorter model was chosen to reduce cost, and also because of machining length limitations of the in-house CNC machine. The choice of 64 turns results in a very short straight-section of about 20 mm in length (Fig. 6.16). This is the minimum length that can be considered for straight-section field quality measurements due to the length of the rotating field probe that will be used during the test.

A 23 strand cable was made out of the SSC-inner NbTi strand to match the dimensions of the Nb_3Sn cable to be used in the future. The properties of this strand can be seen in Table 6.13. The resulting cable dimensions were 1.35 by 10.05 mm before insulation, and 1.60 by 10.30 mm after a 5 mil thick sleeve of glass insulation was added. The short-sample limit for this two layer NbTi magnet is 5.94 T at the conductor and 5.26 T in the bore. This corresponds to a magnet current of 10.6 kA. The load line for the 64 turn model can be seen in Figure 6.17.

Table 6.13: SSC Inner NbTi Strand Parameters

Filament Diameter	6.0 μm
Strand Diameter	0.808 mm
Strand J_c (5T, 4.2K)	2750 A/mm^2
Strand Cu/SC	1.3

Fabrication and assembly

The mandrels for the 64 turn model were CNC machined out of 954 alloy aluminum bronze similar to CCT1 and the 5 turn model (Fig. 6.18). These layers were wound with the

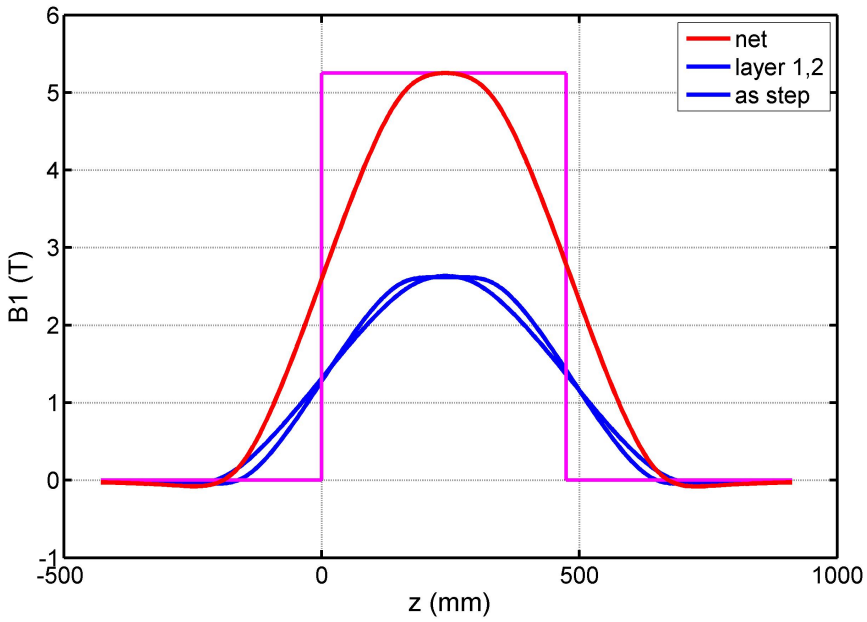

Figure 6.16: The dipole harmonic (B_1) along the length of the 64 turn model is shown for the short-sample current of 10.6 kA.

insulated NbTi Rutherford cable by hand. As a result of the experience with CCT1, the layers were wound separately. A splicing of the two layers together was planned after the epoxy impregnation. Layer 1 was assembled inside of layer 2 with G10 sheets acting as slip planes and insulation between the layers.

A set of electrical tests were performed after the fabrication and assembly of the two layers. Measurements of the inductance L_s, capacitance C_s, and resistance R_s were taken in series mode. The measured values as a function of frequency can be seen in Table 6.15. A fit for the DC value of inductance was performed, leading to a value of 0.6 mH for layer 1 only, 1.0 mH for layer 2 only, and 2.4 mH with the layers connected. These values were used for comparison with the analytic model for inductance of the 64 turn model in Table 6.14.

Table 6.14: CCT2 64-Turn Inductance

		Predicted		Measured
	L_m (m)	L (mH/m)	Ltot (mH)	Ltot (mH)
Layer 1	0.488	1.242	0.606	0.6
Layer 2	0.488	1.919	0.937	1.0
Layer 1,2 series	0.488	4.690	2.289	2.4

After the electrical measurements, two G10 half shells were attached to the OD of layer 2 with a gap left between the shells at both poles for a quench antenna system (Fig. 6.19).

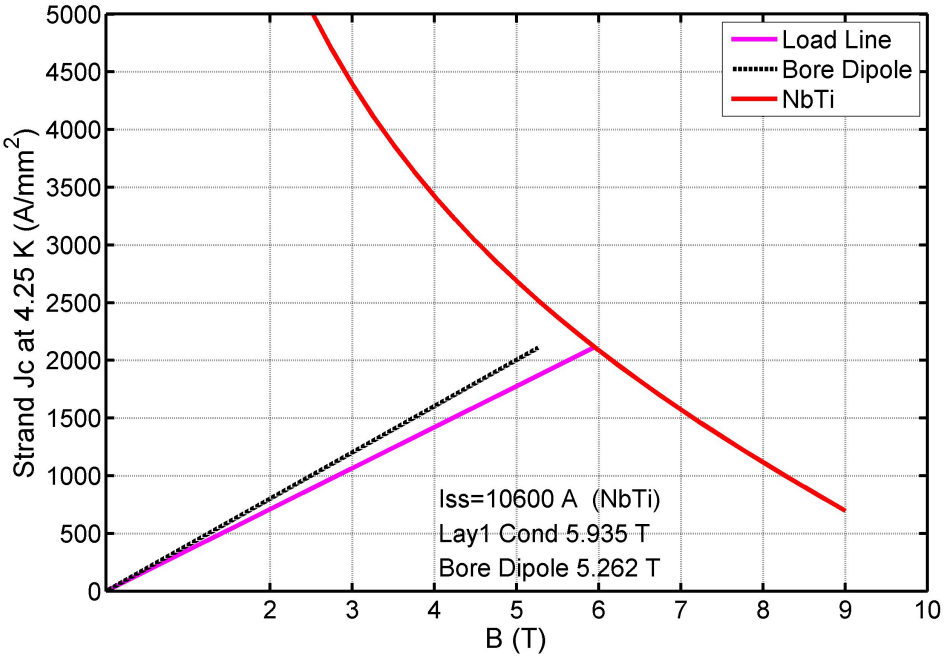

Figure 6.17: The load line for the 64 turn NbTi model is shown for current density in the superconductor.

After attaching the G10 half shells, the whole assembly was inserted into a 20 mm aluminum shell. In this case the G10 half shells provided the slip plane and insulation between layer 2 and the outer shell. The resistance between the coils and the mandrels was monitored during the assembly, with some variation seen. The final resistance between both coils to their respective mandrels was greater than 1.2 MΩ after assembly of the coilpack into the shell. The plan is to impregnate this entire assembly with epoxy using the tooling developed for the 5 turn model. In this case the shell, instead of a shrink tubing, will provide the outer barrier. Following the impregnation, the magnet's performance will be tested at 4.2 K in May 2015.

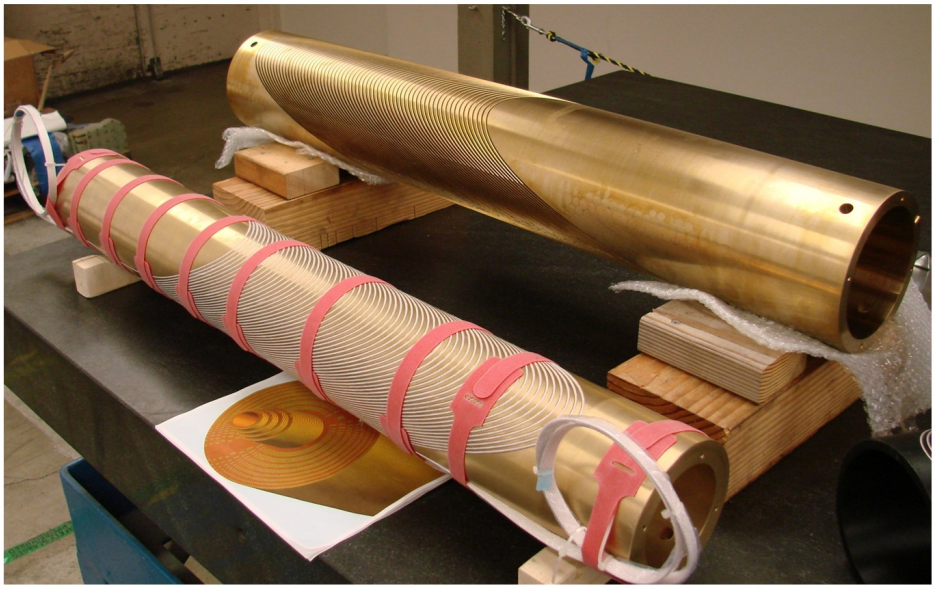

Figure 6.18: The 64 turn layer 1 and 2 mandrels for the NbTi test are shown. Layer 1 is wound with insulated NbTi cable.

Table 6.15: CCT2 64-Turn Electrical Measurements

	Freq.	Ls (μH)	Q	Cs (mF)	Rs (mΩ)
Layer 1 Only	20 Hz	452.3	0.36	-139.5	158.8
	30 Hz	369.4	0.4	-76.2	175.16
	100 Hz	126.6	0.32	-20.17	243.3
	1 kHz	33.3	0.57	-0.7605	366.6
	10 kHz	7.602	0.6	-0.03332	793.4
	30 kHz	4.93	0.97	-0.0057	955.5
	100 kHz	3.83	1.87	-0.00066175	1287
	300 kHz	3.345	3.21	-0.0000841	1965
Layer 2 Only	20 Hz	700.7	0.43	-90.4	204.8
	30 Hz	587.2	0.48	-47.9	228.4
	100 Hz	257.5	0.48	-9.84	334.1
	1 kHz	47.5	0.44	-0.53321	674.3
	10 kHz	8.31	0.5	-0.0348	1040
	30 kHz	6.45	1.03	-0.00436	1180
	100 kHz	5.36	2.11	-0.0004725	1600
	300 kHz	4.79	3.55	-0.00005879	2540
Layer 1,2 Series	20 Hz	1640	0.49	-39.7	421
	30 Hz	1310	0.5	-21.4	491
	100 Hz	433.5	0.38	-5.84	725.5
	1 kHz	66.21	0.36	-0.3825	1150
	10 kHz	14.69	0.5	-0.01725	1840
	40 kHz	9.37	1.04	-0.00169	2270
	100 kHz	8.14	1.75	-0.0003111	2920
	300 kHz	7.47	2.71	-0.000037	5200

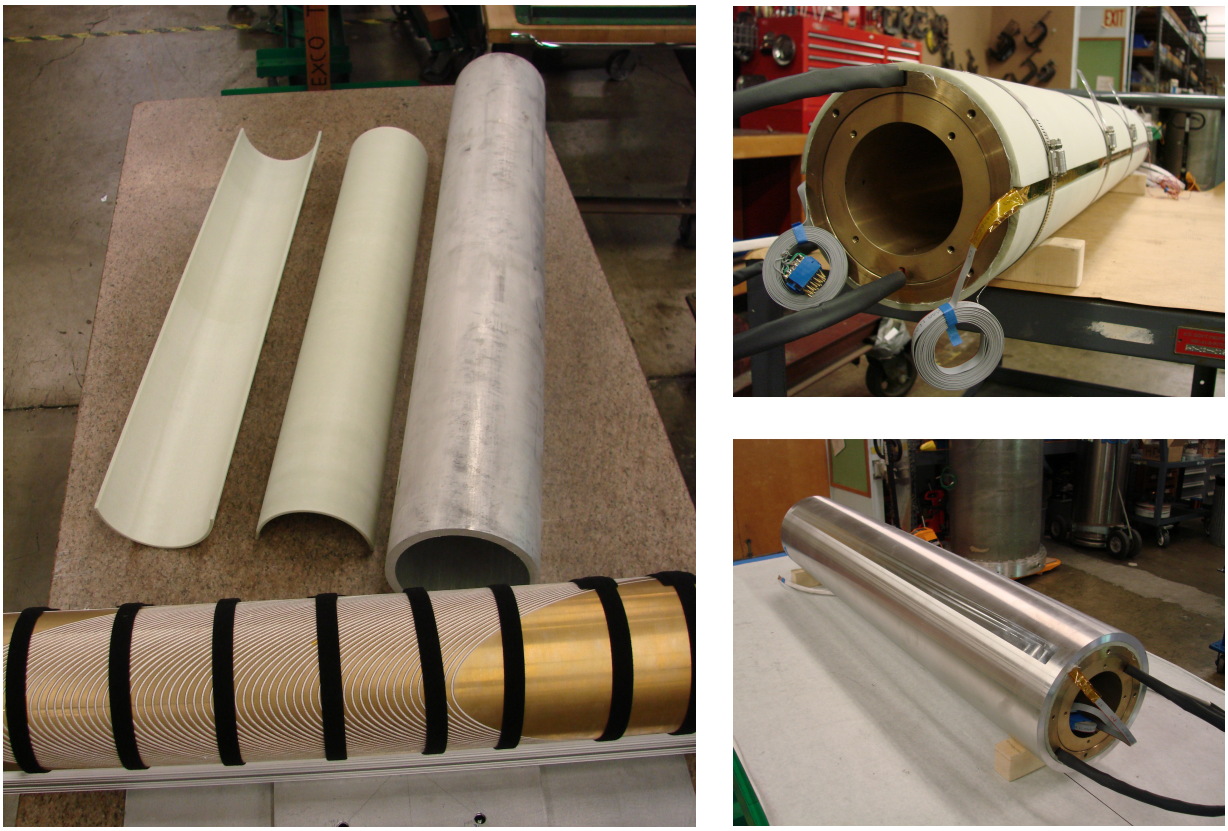

Figure 6.19: The assembly of coil pack into the outer aluminum shell is shown.

Part II

CCT Magnets for Ion Beam Cancer Therapy Gantries

Chapter 7

Introduction and Motivation

7.1 Ion beam cancer therapy

The energy loss of an ion traveling through matter is characterized by a peak immediately before the stopping point. This phenomenon is referred to as the Bragg peak, and results in a region of localized energy deposition with a sharp cut-off (Fig. 7.1). The use of this phenomenon for cancer therapy was first suggested by Robert Wilson in 1942 [64]. He proposed the Bragg peak of protons be used to create a region of high ionization density (which corresponds to biological damage) localized to the volume of the cancer tumor. This proposal was the result of the advancement of accelerator technology at that time, as the proton energy needed to penetrate 4-30 cm into the body (70-220 MeV) was about to be achieved.

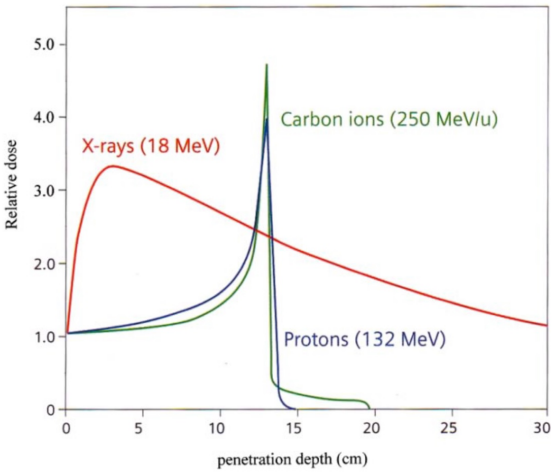

Figure 7.1: A comparison is seen between the depth dose profile of photons and the most commonly used ions for cancer therapy. (Fig. from [65])

The initial radiobiology experiments confirming Wilson's proposal were performed by Cornelius Tobias at the University of California, Berkeley. Following these experiments, the first patients were treated in 1954 using the 184" synchrocyclotron at Lawrence Berkeley National Laboratory under the supervision of John Lawrence. Berkeley lab would go on to treat over 2,500 patients with protons and heavier ions before ending in 1992 for financial reasons. Following the initial experience at Berkeley, other physics laboratories began treating patients. In the late 1950's and early 1960's patients were treated at the Gustav Werner Institute in Uppsala Sweden and at the 160 MeV Harvard Cyclotron in collaboration with Massachusetts General Hospital. The number of physics labs treating patients continued to increase, but it was not until 1990 that the first dedicated hospital facility was developed at Loma Linda [66]. This facility pioneered the delivery of one source beam to multiple treatment rooms and the use of a gantry to treat patients from multiple directions.

The development of ion beam therapy in Japan occurred in parallel with the US and Europe, starting in the late 1970's at the National Institute of Radiological Sciences (NIRS) in Chiba. The development of facilities in Japan has uniquely included a strong focus on treatment with carbon ions. The NIRS facilities provide the majority of the world's experience with carbon, having treated over 8000 patients with carbon ions since 1994. A recent review of the Japanese experience using carbon ions, including a comparison of the efficacy to protons and x-rays, can be found in the following reference [67]. Today there are approximately 60 ion treatment facilities in operation worldwide, and around 110,000 patients have received therapy with ions since the first treatments in the 1950's [68]. There has been increasing demand for ion beam cancer therapy, especially in a hospital-based environment. For example, the number of hospital-based centers has increased from 15 to 40 over the last 15 years.

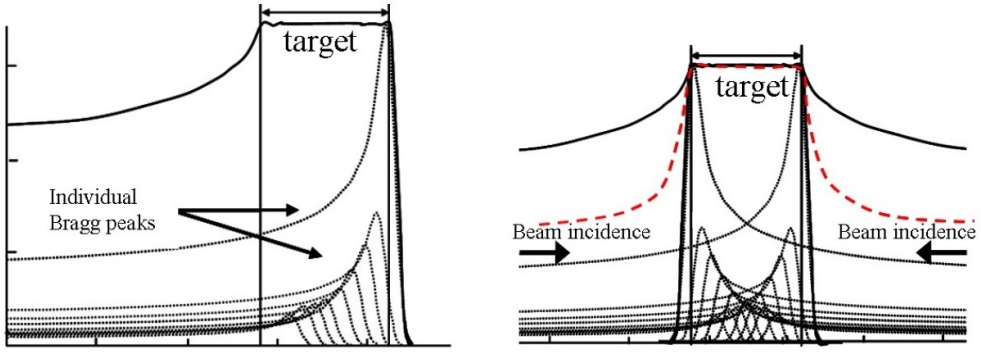

Figure 7.2: The spread-out Bragg peak (SOBP) is shown generated by a single field and by an opposing set of fields. (Fig. from [69])

One of the key treatment planning and technological challenges in the early years was how to manipulate the beam to deliver dose to the full tumor volume. The Bragg peak is typically

only a few millimeters in depth, and the beam cross section from the accelerator only a few millimeters wide. A typical tumor volume is much larger, requiring some manipulation of the beam to treat. The depth of the tumor is covered by using a spread-out Bragg peak (SOBP). With this technique a uniform dose along the length of the beam is achieved by the accumulation of a number of individual Bragg peaks whose depth and intensity are adjusted [70] (Fig. 7.2). In the transverse plane the tumor is covered by first increasing the size of the beam using scattering foils placed in the beam path. The enlarged beam is then collimated to a patient and field specific cross-sectional shape, and compensated to match the edge of the SOBP to the edge of target volume. This technique, referred to as "passive scattering", was developed first and has been used in the majority of treatment facilities to date.

A more advanced treatment that has been developed is called "active scanning". This technique does not change the size of the beam, but rather uses fast scanning magnets and beam energy changes to scan the pencil beam over the volume of the tumor. The scanning magnets provide control over the transverse placement of the beam and the depth of the Bragg peak is adjusted by changing the energy. This gives precise control over dose deposition, and allows for treatment planning which "paints" the tumor volume with a large number of individual beam spots (Fig. 7.3). This method was first proposed in the 1970's [71], and was pioneered at GSI in Germany and at the Paul Scherrer Institute (PSI) in Switzerland in the early 1990's [72, 73]. The precise control available with active scanning allows for improved dose delivery when compared with passive scattering. In particular, the dose to the healthy tissue in front of the tumor can be reduced. Active scanning also provides increased flexibility as no patient specific collimators or compensators are needed. Active scanning is a fairly recent development that is not yet widespread. Given its advantages and successful demonstration, it is expected that active scanning will be used in future state-of-the-art facilities.

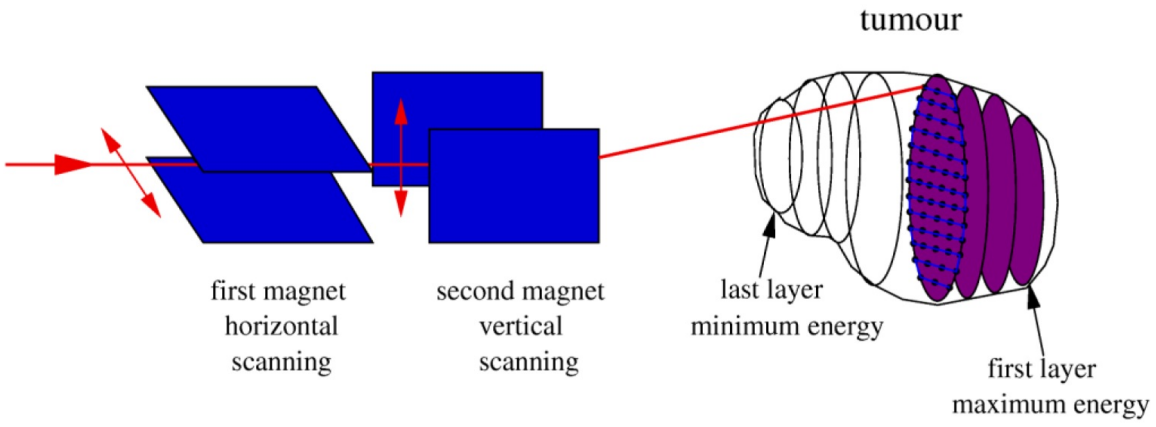

Figure 7.3: Active scanning of the tumor volume. (Fig. from [74])

The treatment capabilities of a facility are enhanced by the use of a rotating beamline called a gantry. This gantry allows for the beam to be positioned in different directions such that the treatment can be performed from multiple angles. A typical treatment facility consists of an accelerator (cyclotron or synchrotron) feeding multiple treatment rooms, one of which may contain a gantry. An example of the recently built Heidelberg Ion Therapy Center (HIT) is shown in Figure 7.4, with the scale of the active scanning gantry (which can treat using heavier ions such as carbon) shown. The cost of a gantry is typically around 25% of the facility and is driven by the large rotating weight on a precise medical device [65]. Proton gantries typically weight approximately 100 tons, with carbon gantries weighing up to 600 tons. A large portion of this weight in active scanning gantries is due to the final bending dipole magnet. For example, the final bending magnet of the HIT carbon gantry is 90 tons, which is 65% of the weight of all rotating beamline components. The final bending magnet has increased weight because of the large aperture. This aperture is needed due to the scanning magnets being upstream in the commonly used "Pavlovic" beam optics layout (Fig. 7.5 and Reference [75]). There is a strong push for the development of lighter, more compact gantries to make treatment facilities more affordable. A large reduction in weight of the post-scanning bending magnet would be a significant step in this direction.

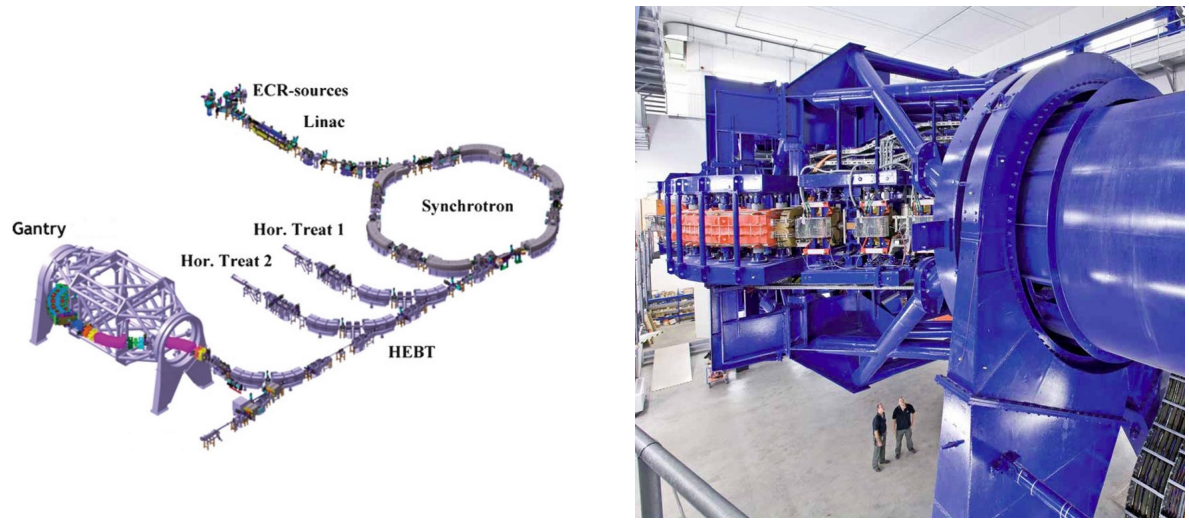

Figure 7.4: The Heidelberg Ion Therapy Center (HIT). (Fig. from [76])

Present day state-of-the-art treatment combines the use of gantries and active scanning (i.e. PSI gantry II for protons and HIT gantry for carbon). This combination provides precise control over the beam and also allows for treatment from multiple directions. A recent joint DOE, NIH, and NCI workshop gathered over 60 world experts and charged them with determining the desired characteristics of a future state-of-the-art beam therapy center and the R&D effort needed before such a facility could be built. The final report of this workshop

can be found in the following reference [77]. The workshop concluded a future facility will have the capability to treat with multiple ion species, use only active scanning, and have at least one gantry. A key component of the recommended R&D effort was developments in gantries and beamlines, with the potential advantage of superconductivity specifically mentioned.

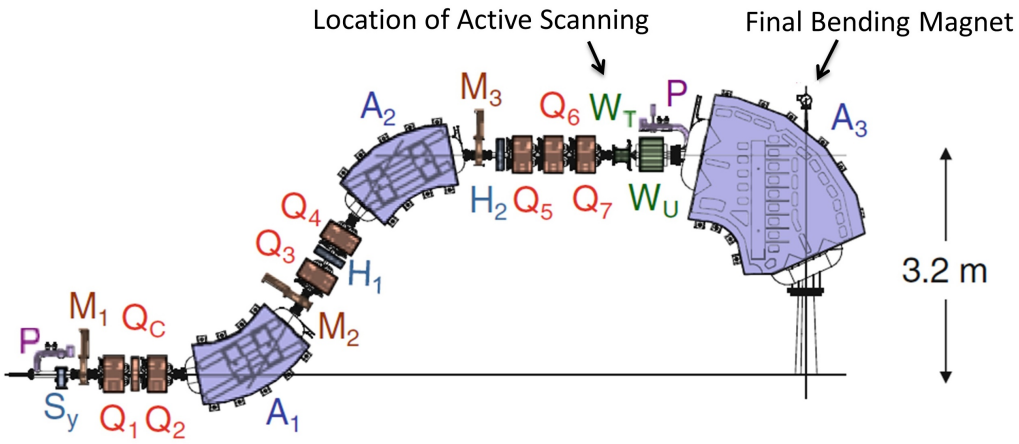

Figure 7.5: A schematic of PSI's proton gantry II is shown with the location of the active scanning and final bending magnet indictaed. (Fig. from [76])

Superconducting magnet technology has two potential advantages for a gantry magnet system. The first is a large reduction in weight. The magnetic field produced by a superconducting magnet is coil-dominated, allowing for the consideration of iron for magnetic shielding only. When compared with resistive magnets relying on the use of a large iron yoke for field generation, superconducting gantry magnets can be up to an order of magnitude lighter. A second advantage of superconducting magnets is the ability to produce much higher fields, opening up the possibility for new and improved beam optics solutions. In particular, the high gradients offered by superconducting quadrupole magnets have been investigated for achromatic gantries [78, 79, 80, 81]. Such gantries have a large beam energy acceptance, showing promise to treat patients with minimal changes in gantry magnet field.

The introduction of superconducting technology in ion therapy gantries does not come without challenges. The large aperture and high degree of curvature present difficulties to traditional superconducting magnet design in terms of field quality, management of Lorentz forces, and magnet fabrication. In addition, a rotating cryogenic system will be required. This system will need to provide sufficient cooling during treatment, which typically includes fast ramping of the magnetic field (up to 0.5 T/s) for beam depth changes. This is a challenging requirement, as field ramping produces AC losses in the conductor and additional

losses in the structure due to eddy currents. Finally, a superconducting system will have to be proven reliable and safe for operation in a medical environment. Patient safety is of upmost concern and will need to be considered in all aspects of design, testing, and certification.

Part II of this thesis will focus on the Canted-Cosine-Theta (CCT) design for superconducting gantry magnets. As will be described in Section 7.2, the CCT design has many advantages for this unique application. Section 7.3 will describe the previous work on superconducting gantries, and present the scope of the thesis research. Chapter 8 will present an extension of the CCT concept and modeling developed for high field Nb_3Sn magnets in Part I to curved CCT magnets. In Chapter 9, the magnetic and structural design of a superconducting CCT magnet for the final bending section of a scanning proton gantry will be described. This design assumes similar optics to today's state-of-the-art gantries, but is an order of magnitude lighter. Chapter 10 will introduce a new superconducting magnet concept called the "Left-Right CCT" (LR-CCT), along with its application to a high momentum acceptance gantry in the form of an "Alternating-Gradient CCT" (AG-CCT). This concept implements both the weight reduction and improved optics advantages of superconductivity previously discussed. Finally, for the reader interested in more information on ion beam cancer therapy, the following textbooks are recommended [76, 82, 83, 84].

7.2 Motivation for a superconducting CCT gantry magnet

As described in Section 7.1, the final bending magnet is a significant contribution to the weight of gantries with active upstream scanning. This magnet has a unique combination of requirements. It must be large aperture, curved over a large angle, produce combined function fields, and be capable of changing field quickly to accommodate beam energy variation (60-220 MeV for protons) during treatment scanning. This is a challenging set of requirements for a superconducting magnet. The highly curved geometry makes both the magnetic design and practical winding of the superconducting coils difficult. The fast field ramping leads to losses in the conductor and magnet structure which can produce a significant heat load to the cryogenic system [85]. Finally, the large bore and bend angle lead to increased net Lorentz forces. These forces can affect field quality and short-sample performance if not managed by the magnet's structure.

The CCT design is well suited to this set of requirements. The concept can be extended to a curved magnet to produce the combined function fields desired for the gantry optics (usually a dipole with a small quadrupole component) [34, 86, 87, 88]. Good field quality can be achieved by careful control of the modulation of the conductor winding path with no external iron necessary. To control the placement of conductor in the curved geometry, the winding mandrel approach developed at LBNL can be extended to a curved magnet. Figure 7.6 show a rapid prototyping model of a curved mandrel used for a winding test. The mandrel channels position the conductor for field quality, and the mandrel ribs and spar

manage the Lorentz forces (previously discussed in Section 1.3).

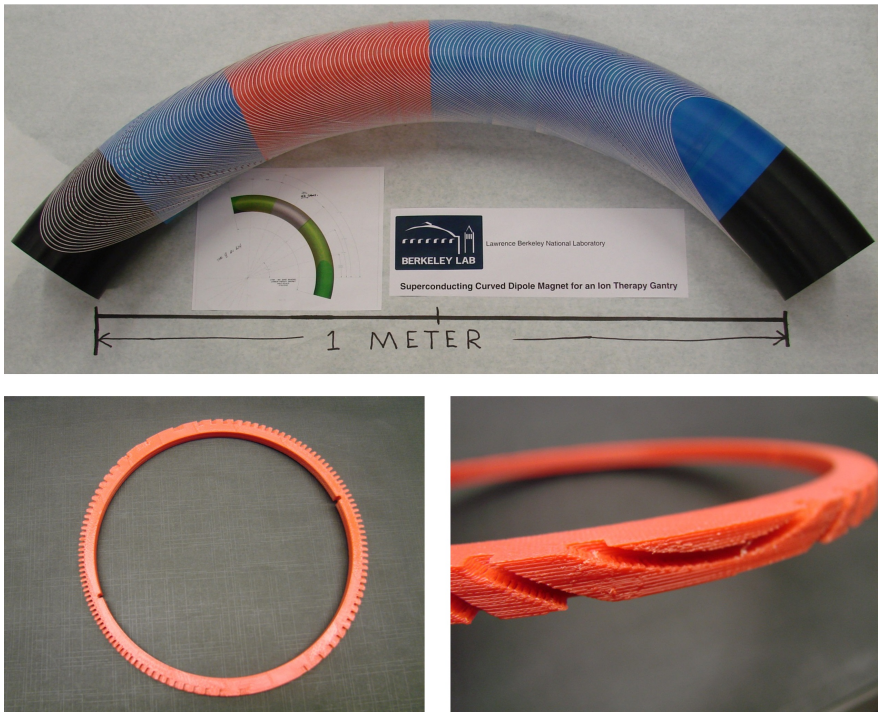

Figure 7.6: A curved rapid prototype mandrel is shown wound with eight strand superconducting cable. The red section was created from stacked laminations.

A practical difficulty associated with the winding of a curved magnet is the tendency of the conductor on the inner edge of the torus to pull off under tension and form a chord across the bend. This problem is inherent to traditional magnet designs that use a 2D cross section extended along the length. With the right choice of parameters, the 3D winding of the CCT remains against the surface of the torus under tension. This allows for the conductor to be wound into the mandrel channels by hand with no additional tooling. The winding mandrel of a curved CCT magnet can also be laminated with slightly tapered laminations in integer numbers of its minimum symmetry [89]. This opens up new manufacturing techniques (such as 3D printing) for the construction of curved mandrels. A laminated approach will also drastically reduce the eddy current losses in the mandrel during field ramping. Figure 7.7 shows an example of the reduction in losses that can be achieved by laminating an aluminum mandrel for proton therapy. It is seen that the ability to laminate the winding mandrel is essential for treatment requiring fast ramping of the magnet.

An alternative approach to solving the AC heat load problem is to eliminate or minimize the need for field ramping during treatment. This can be accomplished by the design of a

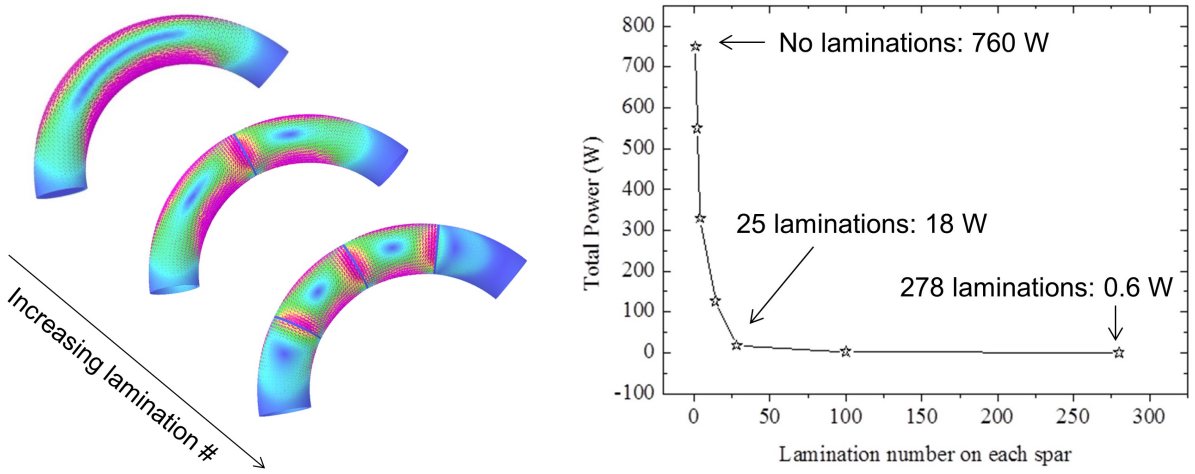

Figure 7.7: Eddy current losses in a proton therapy mandrel. (Figure courtesy of Heng Pan)

gantry with achromatic beam optics. This allows for a range of beam energies to be transported through the gantry without changing the fields of the superconducting magnets. An ideal situation would be one in which the allowable range of energy, quantified as the "momentum acceptance", can cover the depth of the tumor being treated. In this situation the superconducting magnets require one setting and remain unchanged during each treatment field (no ramping or losses). Recent work has shown a gantry using a novel CCT magnet concept, called the "Alternating Gradient CCT" (AG-CCT), can achieve a momentum acceptance close to this ideal case [80]. This is strong motivation for the study of AG-CCT magnets, as the elimination of ramping losses removes one of the key challenges associated with superconducting gantry magnets.

7.3 History, previous work, and scope of thesis

Superconductivity was first introduced into the field of ion beam cancer therapy to reduce the size of proton cyclotrons used for the initial acceleration. The impact of size, or "foot print", of the facility and the associated cost is becoming increasingly important as ion beam therapy moves to hospital-based centers. This is especially true if the industry trend continues towards low barrier to entry facilities that are small, cost-effective, and perhaps have only a single treatment room. With this motivation, there has been a similar push to reduce the size and cost of gantries using superconducting technology.

While there have been many studies in both industry and research laboratories [78, 79, 86, 87, 90, 91, 92, 93], to date only three superconducting designs have been built. The first is a novel design from industry that uses a compact superconducting synchrocyclotron mounted on the gantry itself (Fig. 7.8). This single room proton system, called the MEVION S250, treated its first patient in 2013 and is currently being installed in five additional

hospitals in the US [94]. The second is the superconducting carbon gantry in the final stages of construction at NIRS in Chiba, Japan [95, 96, 97]. This gantry implements upstream scanning and uses superconducting combined function bending magnets (Fig. 7.9). The weight of this gantry (300 tons) is about half of the resistive scanning carbon gantry at the HIT facility. Successful commissioning of this facility, planned for late 2015, will be an important first demonstration of the use of superconducting magnets with upstream active scanning.

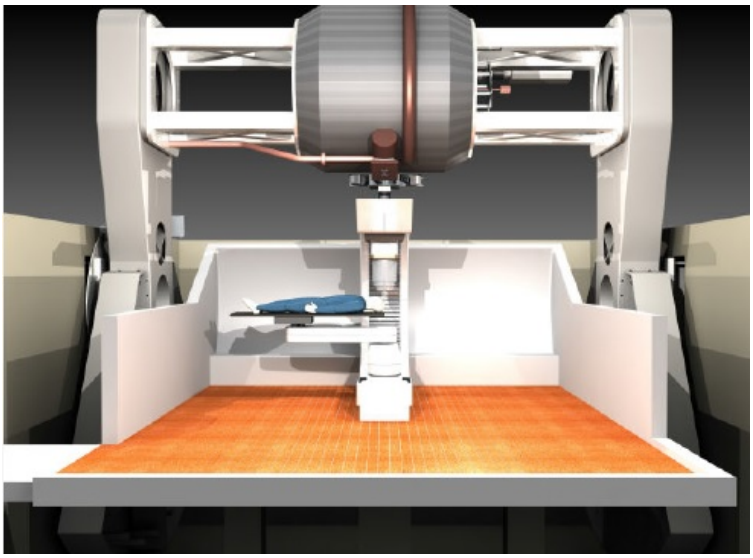

Figure 7.8: An illustration of the MEVION single room proton system. (Fig. from [98])

The use of superconducting magnets for compact, low cost proton gantries is of increasing interest to industry. The approximately 25 ton SC360 design from ProNova solutions appears to be the first such gantry to enter the marketplace. This design is a slightly achromatic double bend system with post-gantry active scanning [99] (Fig. 7.10). The first SC360 has been partially installed in the Provision Center for Proton Therapy in Knoxville Tennessee. Commissioning of the superconducting gantry is expected in late 2015. The success of this project will be an important confirmation of the financial benefits of superconducting gantries for low cost solutions, as the ProNova business model is built around these perceived advantages.

As ion beam cancer therapy continues to grow, the line between research-based facilities seeking to develop and implement new technology and those seeking low barrier to entry solutions may become more defined. Superconductivity could play a large role in both fields. The reduced weight of superconducting gantries shows promise to lower the barrier to entry cost of compact proton facilities, while also opening the door to new research facilities

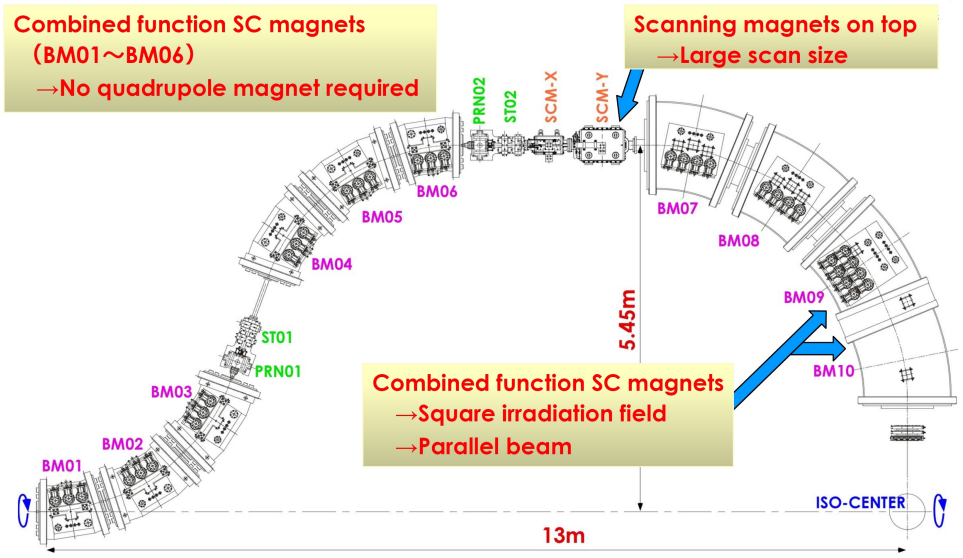

Figure 7.9: An illustration of the NIRS superconducting carbon gantry. (Fig. from [100])

using heavier ions such as carbon. The use of the alternating, high gradient quadrupole fields offered by superconducting magnets for achromatic gantries may also allow for the development of new treatment modes. While the future is never certain and many challenges lie ahead, superconductivity appears poised to have a large impact in the field of ion beam cancer therapy. It is my hope that this development opens the door to treatment for more patients who can benefit from this therapy.

The CCT concept was initially proposed for a Tevatron dipole in 1970. The history of the development of concept for high energy physics was previously described in Section 1.4. The first published record of the concept for a curved, combined function magnet was by Carl Goodzeit in 2007 [34], although the application for ion beam therapy was unmentioned. In 2009 Lawrence Berkeley National Laboratory began a three year LDRD funded study focused on developing technology for carbon therapy gantries. During this study, the CCT concept was identified as an advantageous design for a final bend superconducting gantry magnet in a carbon gantry with upstream scanning. The study of such a magnet was performed with a strong focus on the integration of magnetic design and beam optics. This resulted in a superconducting, combined function CCT design which minimized the carbon beam distortion at the patient location [86, 87].

The overall scope of the ion beam therapy portion of this thesis is to investigate and develop the CCT concept for proton therapy gantries. A new approach to the design of curved CCT magnets will be presented, followed by two magnet design studies. The first study seeks to extend the previous work at LBNL, which was focused on a final bending magnet for an upstream scanning carbon gantry, to a proton therapy gantry. The primary

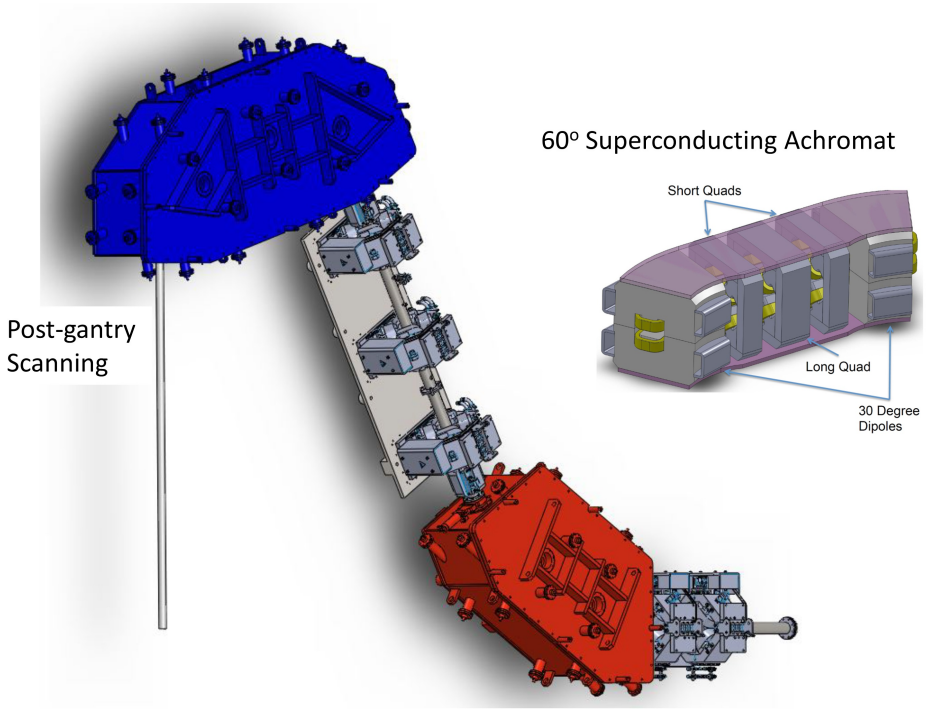

Figure 7.10: An illustration of the ProNova SC360 superconducting proton gantry. (Fig. from [99])

focus will be on the design of the magnet rather than a detailed study of the beam optics. A previously unstudied aspect of this design will be an examination of the behavior and effect of the Lorentz forces within the magnet. The second study is motivated by the goal of investigating new CCT magnet concepts for achromatic proton gantries. The preliminary design of one such concept, called the Alternating Gradient CCT (AG-CCT), will be given.

Chapter 8

Modeling of Curved CCT Magnets

8.1 Introduction and goals

Chapter 2 presented developments for analytic modeling of cylindrical CCT magnets. This chapter seeks to extend this analytic approach to a curved CCT magnet as desired for an ion therapy gantry. This is not without difficulty, as many of the assumptions behind traditional field representation for accelerator magnets are broken by the curved geometry. There are two potential dangers when working in a curved system, each with its own appeal. The first is to stay completely true to the curved geometry, even when this overcomplicates the mathematical approach and makes it too complex to be useful or provide understanding. The second is to oversimplify the problem by drawing too heavily on the familiar expressions for straight magnets, failing to recognize the point at which they are no longer an appropriate approximation. This chapter will seek to present a healthy balance between the two, with the goal of demonstrating both approaches can be useful. It is important to not lose sight of the fact the final field "quality" is a desired effect on beam behavior. The hope is the formulation developed does not distract from this goal, but rather makes it easier to achieve.

Sections 8.2 and 8.3 will describe the toroidal coordinate system and then use these coordinates to develop the formulation for a CCT winding path on a torus. Methods for determining the field to winding relation for a curved CCT magnet will be discussed. A winding path optimization process that has been shown suitable for the design of a gantry magnet will be presented, along with a method for maintaining positive concavity of the winding on the inner edge of the torus. In Section 8.4, 2D toroidal harmonics will be derived to allow for a completely analytic relation between the windings and field. While this relation has not yet been shown necessary for a gantry magnet, it does provide insight into curvature induced field distortions. This complete but complicated approach may be necessary for future applications of curved CCT magnets requiring a higher degree of curvature or field quality.

8.2 Toroidal coordinates

The right hand toroidal system of η, ξ, ϕ is formed by the rotation of bipolar coordinates η and ξ about the vertical axis (Fig. 8.1). Surfaces of constant η are tori, making this system the natural choice for problems with boundary conditions on the surface of a torus. The scale factors for these coordinates are

$$\begin{aligned} h_\eta &= \frac{a}{\cosh\eta - \cos\xi} \\ h_\xi &= \frac{a}{\cosh\eta - \cos\xi} \\ h_\phi &= \frac{a\sinh\eta}{\cosh\eta - \cos\xi}, \end{aligned} \tag{8.1}$$

where $(\pm a, 0)$ are foci of the bipolar system.

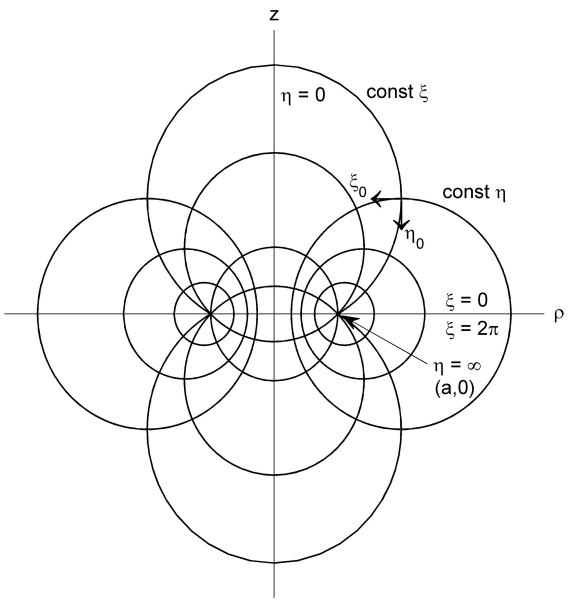

Figure 8.1: Bipolar coordinates $0 < \eta < \infty$ and $0 \leq \xi \leq 2\pi$

8.3 A CCT winding path in toroidal coordinates

Definition of the parametric path

The starting point for the definition of a CCT layer on a curve is a parametric path constrained to the surface of a torus (constant $\eta = \eta_0$) as shown in Figure 8.2. This path can

be parameterized in terms of the toroidal angle ξ as

$$\begin{aligned} \eta &= \eta_0 \\ \xi &= \xi \\ \phi(\xi) &= p_\phi(\xi), \end{aligned} \tag{8.2}$$

where (η, ξ, ϕ) are the toroidal coordinates as defined in Figure 8.1, and $p_\phi(\xi)$ is a yet undefined function of ξ which describes the movement of the path along the bend. It is useful to define a local reference frame at location $\vec{p}(\xi)$ such that $\hat{t}$ is tangential to the path, $\hat{\eta}$ is normal to the surface, and $\hat{b}$ completes the orthogonal system (Fig. 8.2). A vector in the tangent direction is then found to be

$$\vec{t}(\xi) = ak^{-1}\hat{\xi} + ak^{-1}\sinh\eta_0 p'_\phi(\xi)\hat{\phi}, \tag{8.3}$$

where $k \equiv \cosh\eta_0 - \cos\xi$.

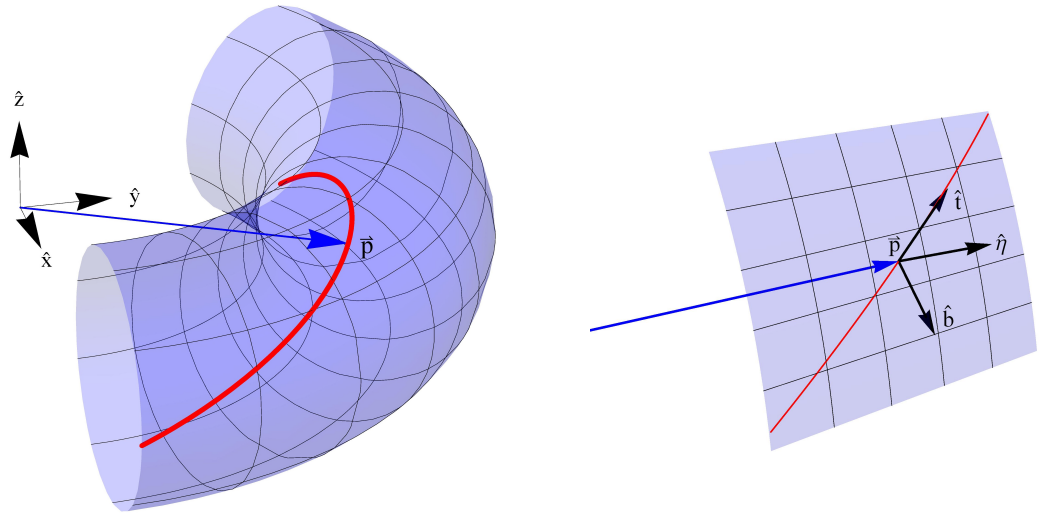

Figure 8.2: The local unit tangent, normal, and binormal vectors ($\hat{t}$, $\hat{\eta}$, $\hat{b}$) are shown at location $\vec{p}$ of a parametric path constrained to the surface of a torus.

A periodic function for $p_\phi(\xi)$

It is seen that the choice of the function $p_\phi(\xi)$ is sufficient to define both the path and the tangential direction. It is desirable for the path to contain a symmetry such that it can be repeated along the bend of the torus (along ϕ) to create a uniform region away from the

start and end points of repetition. This is accomplished by requiring the bend angle between adjacent repetitions of the path be a constant for all points (independent of ξ), meaning

$$|p_\phi(\xi + 2\pi) - p_\phi(\xi)| = \phi_0, \tag{8.4}$$

where the angular pitch ϕ_0 is defined as the constant bend angle between paths (Fig. 8.3). It can be shown the perpendicular distance between adjacent paths $\delta(\xi)$ (in the direction of $\hat{b}$) is approximated by

$$\delta(\xi) = \frac{\rho(\xi)\phi_0\hat{\phi} \times \left(\vec{t}\cdot\hat{\xi}\right)}{|\vec{t}|} = a\phi_0 k^{-1}\left(\sinh^{-2}\eta_0 + p_\phi'^2(\xi)\right)^{-1/2}, \tag{8.5}$$

where $\rho(\xi) = a\sinh\eta_0 k^{-1}$.

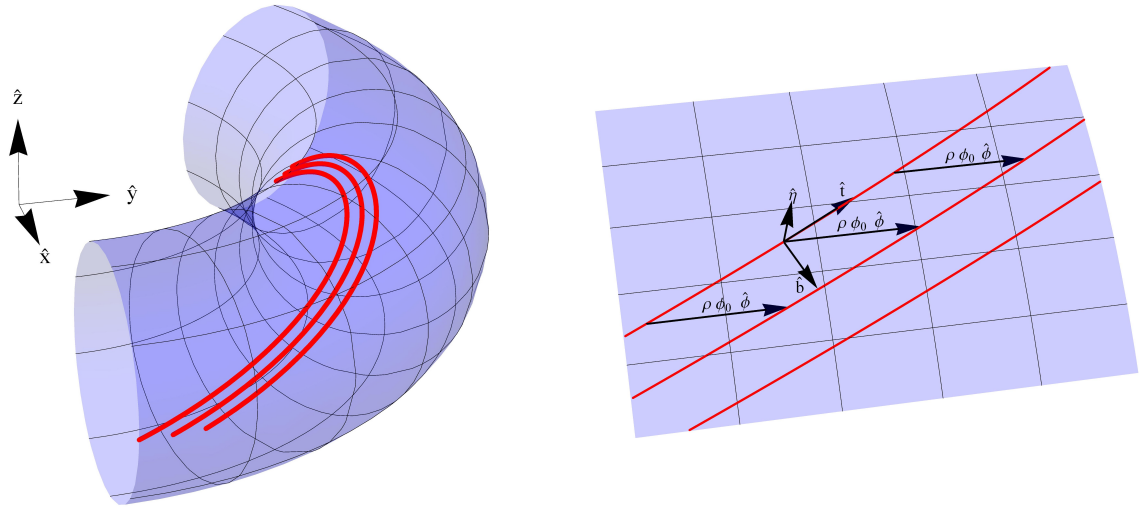

Figure 8.3: A path is shown patterned around the bend in integer multiples of the pitch angle ϕ_0.

A pitch averaged current density

If the path $\vec{p}(\xi)$ represents a continuous line current of magnitude I_0, the perpendicular spacing $\delta(\xi)$ (Eqn. 8.5) can be used to average the line currents into a 2D toroidal current sheet with current density

$$\vec{j}(\xi) = \frac{I_0}{|\delta|}\frac{\vec{t}}{|\vec{t}|} = \frac{I_0}{\rho(\xi)\phi_0}\frac{\vec{t}}{\vec{t}\cdot\hat{\xi}} = \frac{I_0 k}{a\phi_0\sinh\eta_0}\left(\hat{\xi} + \sinh\eta_0\, p_\phi'(\xi)\hat{\phi}\right). \tag{8.6}$$

The current consists of two components: an "azimuthal" portion (generating solenoidal like fields) dependent on the geometry and pitch angle, and an "axial" portion varying with azimuthal angle (generating transverse fields) determined by p'_ϕ. Because the "axial" current's azimuthal variation is determined by p_ϕ, the pitch averaged current density can be used to relate the axial path expression p_ϕ to the produced transverse fields.

Relation to the midplane rib and tilt angle

In practice it is advantageous to relate the formulation to the physical properties of the path. This can be done by defining a midplane tilt angle α on the inner edge of the torus, such that

$$\tan\alpha \equiv \left.\frac{\vec{t}\cdot\hat{\xi}}{\vec{t}\cdot\hat{\phi}}\right|_{\xi=\pi} = \left.\frac{1}{\sinh\eta_0 p'_\phi(\xi)}\right|_{\xi=\pi}. \tag{8.7}$$

Substituting this into Equation 8.5, the midplane perpendicular spacing on the inner edge of the torus can be written as

$$\delta(\xi=\pi) = a\phi_0 \tanh(\eta_0/2)\sin\alpha. \tag{8.8}$$

This location is chosen as it typically corresponds to smallest perpendicular spacing (or rib in the case of a winding mandrel) for a curved dipole.

Relation of current density to magnetic field

In Section 2.2, the pitch averaged current density of a CCT layer on a cylinder was related to the cylindrical multipoles. This allowed for the derivation of a CCT winding path based on desired transverse multipoles (dipole, quadrupole, etc.). In the curved geometry, a similar relation can be found between the CCT winding path and a 2D multipole solution for the magnetic field in toroidal coordinates. Section 8.4 will derive this field expression in terms of toroidal harmonics. This approach is the most complete treatment of the problem, giving a one-to-one relation between the windings and the fields.

There are several practical issues with using toroidal harmonics. The first is they contain associated Legendre functions of half-integer degree (or "toroidal functions") which are difficult to evaluate and understand. The practicality of using toroidal harmonics is also limited by issues with specification of the desired field. Field quality specifications for the desired beam optics will almost certainly be based on cylindrical harmonics, for which there is no easy comparison. In other words, if the toroidal harmonics cannot be adequately related to the desired fields, the ability to produce them is no longer an advantage.

In light of this, a practical method for optimizing the winding path of a curved CCT magnet was developed. Similar to the cylindrical CCT, a sinusoidal series can be assumed for the axial variation of the path such that

$$\begin{aligned} \eta &= \eta_0 \\ \xi &= \xi \\ \phi(\xi) &= C_n \sin(n\xi) + \frac{\phi_0}{2\pi}\xi, \end{aligned} \tag{8.9}$$

where ϕ_0 is the angular pitch, C_n are the winding coefficients, and $0 \leq \xi \leq 2\pi k$ produces k winding turns. The first step in generating a winding is determining the angular pitch from the desired tilt angle and midplane spacing on the inner edge of the torus. Using Equation 8.8, this pitch is given by

$$\phi_0 = \frac{\delta}{a \tanh(\eta_0/2) \sin\alpha}. \tag{8.10}$$

The midplane spacing is typically chosen based on the smallest allowable mandrel rib (the conductor width plus approximately 0.381 mm), and the tilt angle is based on maintaining positive concavity on the inner edge of the bend (to be discussed). A set of sufficiently good winding coefficients C_n can be found numerically. The figure of merit for this optimization is a local cylindrical expansion of the fields on a reference radius located at the center of the bend. If "k" represents the primary desired harmonic for the magnet (i.e. 1=dipole, 2=quadrupole, etc.), the corresponding winding coefficient is fixed as

$$C_{n=k} = \frac{\cot\alpha}{k \sinh\eta_0}, \tag{8.11}$$

which corresponds to a comparison of Equations 8.9 and 8.7 with the assumption only the $C_{n=k}$ winding coefficient is non-zero and the pitch is small. Then, initial guesstimations and a Newton search can be used to optimize the other coefficients (with the series truncated to some maximum $C_{n=nmax}$) until the desired ratio of cylindrical harmonics at the center of the bend is achieved to some tolerance. Despite using cylindrical field expressions in a curved system, this process has proven sufficient for the design of CCT gantry magnets. This process will be used to produce a curved winding path for a combined function proton therapy gantry magnet in Section 9.2.

Restrictions on the concavity of the path

A practical difficulty associated with the winding of a curved magnet is the tendency of the conductor on the inner edge of the torus to pull off under tension and form a chord across the bend. This problem is inherent to traditional magnet designs that use a 2D cross section extended along the length, requiring special tooling or glue to hold the winding in place. With some restrictions on the choice of winding parameters, the 3D path of the CCT can be made to "hug" the inner edge of the torus under winding tension.

This requirement is satisfied if the second derivative of path along the unit vector normal to the surface is positive. Using the formulation developed for the parametric path, this restriction can be written as

$$\frac{a \sinh \eta_0 \left(1 + \left[\cos \xi \cosh \eta_0 - 1\right] p_\phi'^2(\xi)\right)}{(\cosh \eta_0 - \cos \xi)^2} > 0. \tag{8.12}$$

In practice this puts a limitation on how small a tilt angle α can be used for a given geometry. For example, if only the primary winding coefficient in Equation 8.11 is used in Equation 8.9,

$$p'_\phi = \frac{\cos k\xi}{\sinh \eta_0 \tan \alpha}, \tag{8.13}$$

making the condition,

$$\frac{a \sinh \eta_0 \left(1 + \left[\cos \xi \cosh \eta_0 - 1\right] \left(\frac{\cos k\xi}{\sinh \eta_0 \tan \alpha}\right)^2\right)}{(\cosh \eta_0 - \cos \xi)^2} > 0. \tag{8.14}$$

Figure 8.4 shows Equation 8.14 plotted as a function of ξ for a typical magnet geometry for proton therapy (primary harmonic is dipole: k=1, major radius of 774 mm and minor radius of 133 mm: $\eta_0 = 2.45$, a = 762.48). Three different tilt angles are shown. It is seen that a negative concavity is most likely to occur at the inner edge of the torus ($\xi = \pi$) and for a smaller tilt angle. If a positive concavity is desired in all locations, the tilt angle must be chosen greater than 24.5 degrees. If more than one winding coefficient is used, Equation 8.12 must be used with the full derivative of the path (not just the primary coefficient).

8.4 Development of toroidal harmonics

The motivation

There is increasing interest in curved superconducting magnets for both scientific and medical accelerators. Curved designs are presently needed for the Facility for Antiproton and Ion Research (FAIR) at GSI [101, 102], for the Nuclotron-based Ion Collider Facility (NICA) at Dubna [103], and in the medical community for the size and weight reduction of ion therapy gantries (as will be investigated in this thesis). The design of a high aspect ratio magnet system, with a large aperture to bending radius ratio, presents challenges in both field description and conductor placement. It is typical to expand the central magnetic field of an accelerator magnet in terms of circular multipoles (see Appendix A). This expansion directly relates to allowable fields from the solution of the potential equation in cylindrical coordinates with axial symmetry. For a curved magnet this symmetry is no longer valid, as the curvature requires the 2D potential be axisymmetric about the vertical bending axis.

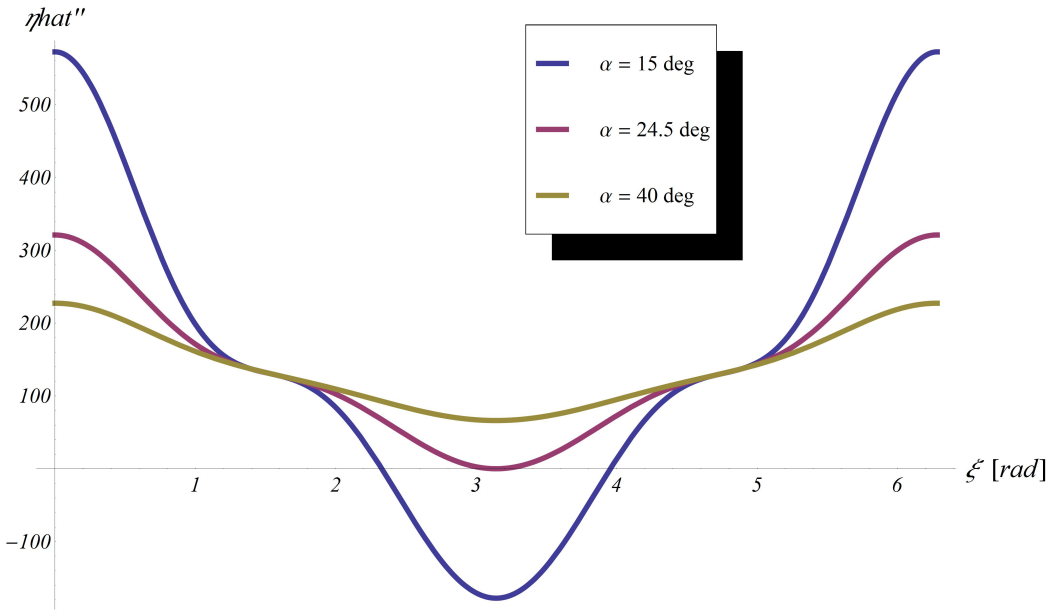

Figure 8.4: The concavity of the CCT winding path as a function of the azimuthal toroidal angle is shown for three different tilt angles.

To account for the effect of curvature, previous analytic work made use of a scalar potential in local cylindrical coordinates solved by expansion and then truncation of the potential equation using the inverse aspect ratio of the torus (approximate R-separation) [104, 105]. This section will present the alternate approach of expanding the fields in toroidal harmonics, which correspond to the solution of the axisymmetric vector potential equation in toroidal coordinates. The solution of the vector Laplace equation in toroidal coordinates is briefly outlined and the current relation found for boundary conditions on the surface of a torus.

A vector potential in toroidal coordinates

Assuming axial symmetry $\vec{A} = A_\phi(\eta, \xi)$ with $\nabla \cdot \vec{A} = 0$, the vector Laplacian [106] in toroidal coordinates is given by

$$\vec{\nabla}^2 \vec{A} = \frac{1}{h_\eta h_\xi} \frac{\partial}{\partial \eta} \left[\frac{h_\xi}{h_\eta h_\phi} \frac{\partial}{\partial \eta} \left(h_\phi A_\phi \right) \right] + \frac{1}{h_\eta h_\xi} \frac{\partial}{\partial \xi} \left[\frac{h_\eta}{h_\xi h_\phi} \frac{\partial}{\partial \xi} \left(h_\phi A_\phi \right) \right]. \tag{8.15}$$

Substitution of coordinate dependent scale factors (Eqn. 8.1) produces

$$\vec{\nabla}^2\vec{A} = \frac{k^2}{a^2}\left[\frac{\partial^2 A_\phi}{\partial\eta^2} + \frac{\partial^2 A_\phi}{\partial\xi^2} + \coth\eta\frac{\partial A_\phi}{\partial\eta} - k^{-1}\left(\sinh\eta\frac{\partial A_\phi}{\partial\eta} + \sin\xi\frac{\partial A_\phi}{\partial\xi}\right) + \frac{A_\phi}{\sinh^2\eta}\right], \tag{8.16}$$

where $k \equiv \cosh\eta - cos\xi$. The technique of R-separation can be employed, using the substitution $A_\phi(\eta,\xi) = \sqrt{k}\ u(\eta,\xi)$ to reduce Equation 8.16 to

$$\vec{\nabla}^2\vec{A} = \frac{k^{5/2}}{a^2}\left[\frac{\partial^2 u}{\partial\eta^2} + \frac{\partial^2 u}{\partial\xi^2} + \coth\eta\frac{\partial u}{\partial\eta} + \left(\frac{1}{4} + \frac{1}{\sinh^2\eta}\right)u\right]. \tag{8.17}$$

A separable solution $u = G(\eta)H(\xi)$ can be found for $\vec{\nabla}^2\vec{A} = 0$. Assuming sinusoidal behavior in ξ, $H(\xi) = a_n\cos(n\xi) + b_n\sin(n\xi)$, the resultant "radial" equation in η can be formulated into an associate Legendre equation

$$\left(1 - Z^2\right)\frac{d^2G}{dZ^2} - 2Z\frac{dG}{dZ} + \left[(n-1/2)\Big[(n-1/2)+1\Big] - \frac{1}{1-Z^2}\right]G = 0, \tag{8.18}$$

for which the general solution is associate Legendre functions [107] with argument $Z = \cosh\eta$. Combining the separable solution with the R substitution leads to a general solution for the vector potential of

$$A_\phi = k^{1/2}\left[a_n\cos(n\xi) + b_n\sin(n\xi)\right]\left[c_nP^1_{n-1/2}(\cosh\eta) + d_nQ^1_{n-1/2}(\cosh\eta)\right]. \tag{8.19}$$

Application to boundary conditions on a torus

The form of the vector potential inside and outside a torus surface of constant $\eta = \eta_0$ can be determined. Considering the divergence of the Legendre functions at the limits of η and choosing a solution symmetric about the midplane leads to

$$\begin{aligned} A^{in}_\phi &= a_nk^{1/2}\cos(n\xi)Q^1_{n-1/2}(\cosh\eta) \quad bore \quad (\eta > \eta_0) \\ A^{out}_\phi &= b_nk^{1/2}\cos(n\xi)P^1_{n-1/2}(\cosh\eta) \quad outside \quad (\eta < \eta_0) \end{aligned} \tag{8.20}$$

where the constants a_n and b_n are determined by the boundary conditions at $\eta = \eta_0$. Using the continuity of the potential, the magnetic boundary conditions, and the Wronskian of the toroidal functions, the surface current density can be expressed as

$$J_\phi(\eta_0,\xi) = J_{0n}k^{3/2}\cos(n\xi), \text{ where} \tag{8.21}$$

$$J_{0n} = \frac{a_n}{a\mu_0\sinh\eta_0}\frac{n^2-1/4}{P^1_{n-1/2}(\cosh\eta_0)}. \tag{8.22}$$

This can be compared to ϕ component of the pitch averaged current density in Equation 8.6 to find the relation between the CCT winding path and the toroidal harmonics in the straight-section.

The resultant fields from this solution are given by $\vec{B} = \nabla \times \vec{A}$. The 2D fields in the toroidal coordinate system are then given by

$$B_\eta = \frac{k}{a}\left(\frac{\partial A_\phi}{\partial \xi} - k^{-1}\sin\xi A_\phi\right) \tag{8.23}$$

$$B_\xi = \frac{k}{a}\left(-\frac{\partial A_\phi}{\partial \eta} - \frac{A_\phi}{\tanh\eta} + k^{-1}\sinh\eta A_\phi\right). \tag{8.24}$$

Evaluating these for the vector potential inside and outside of the torus given in Equation 8.20,

$$B_\eta^{in} = \frac{-a_n k^{3/2}}{a}\left(n\sin n\xi + \frac{1}{2}k^{-1}\sin\xi\cos n\xi\right)Q^1_{n-1/2}(\cosh\eta) \tag{8.25}$$

$$B_\eta^{out} = \frac{-b_n k^{3/2}}{a}\left(n\sin n\xi + \frac{1}{2}k^{-1}\sin\xi\cos n\xi\right)P^1_{n-1/2}(\cosh\eta) \tag{8.26}$$

$$B_\xi^{in} = \frac{-a_n k^{3/2}}{a}\left(\frac{n+\frac{1}{2}}{\tanh\eta}Q^1_{n-1/2} - \frac{1}{2}\sinh\eta k^{-1}Q^1_{n-1/2} - \frac{n+\frac{1}{2}}{\sinh\eta}Q^1_{n-3/2}\right)\cos n\xi \tag{8.27}$$

$$B_\xi^{out} = \frac{-b_n k^{3/2}}{a}\left(\frac{n+\frac{1}{2}}{\tanh\eta}P^1_{n-1/2} - \frac{1}{2}\sinh\eta k^{-1}P^1_{n-1/2} - \frac{n+\frac{1}{2}}{\sinh\eta}P^1_{n-3/2}\right)\cos n\xi. \tag{8.28}$$

Effects of curvature

The primary effect of curvature is a breaking of the left-right symmetry of the field as the focus of the coordinates moves away from the center of the bore aperture. This effect scales with the aspect ratio of the torus

$$\epsilon = R/R_0, \tag{8.29}$$

where R is the minor (bore) radius and R_0 is the major (bend) radius. Figure 8.5 shows the behavior of the quadrupole-like toroidal harmonic (n=2) in the bore of three different aspect ratio tori. The Legendre polynomials needed for the fields were evaluated using the DTOR algorithm [108]. It is seen that the curvature induced distortion of the fields is reduced for decreasing aspect ratio. As expected, in the limit of the aspect ratio approaching zero the traditional cylindrical quadrupole fields are recovered. A typical aspect ratio for a proton gantry magnet is $\epsilon = 125/775$, making the distortion of a single toroidal harmonic close to the central figure for this application.

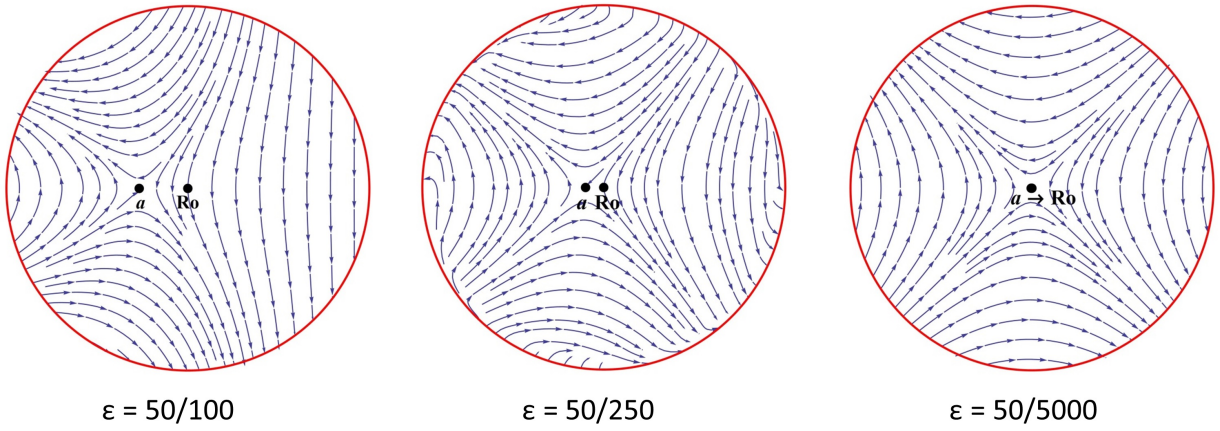

Figure 8.5: The quadrupole-like toroidal harmonic (n=2) is shown for a fixed bore radius R and increasing major radius R_0. The Legendre polynomials needed for the fields were evaluated using the DTOR algorithm [108]. As the aspect ratio of the torus $\epsilon = R/R_0$ tends to zero, the fields are seen approaching those of a straight cylindrical quadrupole.

Chapter 9

A Curved CCT Design Study for a Proton Therapy Gantry

9.1 Design criteria and goals

This chapter will study the application of the CCT concept to a superconducting, final bending magnet for a proton therapy gantry. A magnetic and structural design study will be presented, with the goal of determining the feasibility and advantages of the CCT for this application. Gantry beam optics with active scanning performed upstream of this final bending magnet is assumed. This corresponds to today's state-of-the-art treatment, as well as the greatest potential for gantry weight reduction using superconducting technology. A set of gantry characteristics impacting the design of the final bending magnet are assumed in Table 9.1. These are not hard requirements, but are instead a set of guidelines for the generation of magnet parameters representative of the needs of a typical proton gantry with upstream scanning.

Table 9.1: Proton Gantry Guidelines

Max proton energy	230 MeV
Bending radius	775 mm
Bending angle	90 degrees
Scanning location	0.5 m upstream
Isocenter location	1.0 m downstream
Isocenter field size	20 x 20 cm
Approximate optics	point-to-parallel (inf. SAD)

A set of design criteria for the CCT final bending magnet of this study is assumed in Table 9.2. These criteria are based on the gantry guidelines, as well as what was learned during the design and fabrication of the 2.5 T dipole CCT1 (see Chapter 5). They provide the baseline requirements for the magnetic and structural design to be presented in the

following sections. A small quadrupole field component was added to the main dipole to allow for point-to-parallel beam optics during scanning (to be further explained in Section 9.2), and criteria limiting the power supply current was added to maintain compatibility with "dry" conduction cooling based cryogenics. The necessary current and temperature margin for a superconducting gantry magnet operating in a medical environment is an area for future study. What was believed to be a conservative requirement of 30-40% current margin was assumed.

Table 9.2: CCT Gantry Magnet Design Criteria

Criteria		Motivation
Clear bore diameter	250 mm	desired treatment field
Bending radius	774 mm	desired bend
Bending angle	90 degrees	desired angle
Dipole field	3.0 T	230 MeV protons, 774 mm bend
Quadrupole field	-1.938 T/m	first order point-to-parallel optics
Mandrel spar thickness	> 3.0 mm	CCT1 experience
Minimum mandrel rib	> 0.381 mm	CCT1 experience
Winding curvature P''_η	> 0	maintain contact on inner bend
Current	< 500 A	cryocooler operation
Operating current margin	30-40%	estimated

9.2 Magnetic design

Desired fields for point-to-parallel optics

The beam optics of a scanning gantry allow for the beam at the patient location to be moved over the tumor cross-section using horizontal and vertical deflections at the scanning magnet location (see Fig. 7.3). For a gantry with scanning upstream of the final bend, a "point-to-parallel" beam optics solution can be considered. Figure 9.1 illustrates point-to-parallel behavior in the horizontal plane only. These optics map a change in angle or "kick" at the scanning magnet location to a change in parallel position at the exit of the bending magnet. This allows for a parallel drift from the end of the bending magnet to the location of the patient (in this case at the isocenter of the rotation), resulting in an infinite source-to-axis distance (SAD).

One approach to approximating point-parallel-optics is to require the focusing strength of the final bending magnet be the same in both the horizontal and vertical plane. This can be accomplished by changing the edge angles of the bend, or by adding higher order components to the magnetic field (the weak focusing aspects of sector bends can be found

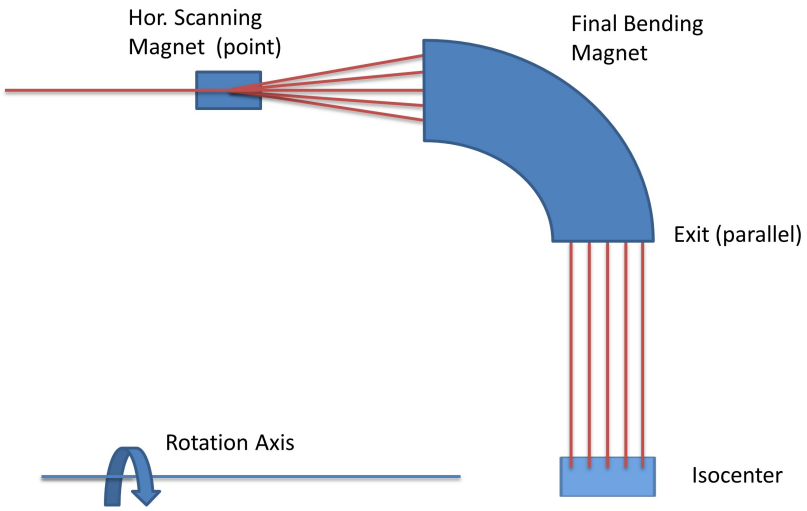

Figure 9.1: An illustration of point-to-parallel optics in the horizontal plane.

described in most introductory accelerator physics textbooks e.g. [109, 110]). The combined function field approach will be considered for this design, as the CCT concept has been shown to be well suited to the addition of higher order fields. To a first order approximation, a quadrupole field of gradient

$$B_2^* = -\frac{B_1}{2\rho} \tag{9.1}$$

can be combined with the dipole field to produce equal focusing in both planes. Given the specifications in Table 9.2, the desired quadrupole component for this design has a field gradient of -1.938 T/m.

An optimized conductor path to produce the desired fields

Section 8.3 discussed methods for optimizing the conductor winding path of a curved CCT magnet to produce desired fields. For this design, the method of optimizing winding coefficients for a parametric path in toroidal coordinates was chosen. Here the field is calculated on a reference radius forming a circle at the middle of the bending angle ($\phi = 45^o$), with the reference circle centered about the bending radius ρ. The figure of merit for the coil optimization was a local cylindrical expansion of these fields compared to the desired 3.0 T dipole and -1.938 T/m quadrupole. While these harmonics are not a true 2D solution for a curved system (such a treatment would require the use of toroidal harmonics), particle tracking through coils generated by this optimization process has shown sufficient accuracy in producing the desired beam behavior.

As was previously discussed in Chapter 8, it is important to not lose sight of the fact the final field "quality" of a magnet system is producing the desired effect on the beam.

This is especially true in a highly curved system where the assumptions behind traditional field expressions begin to break down. Figure 9.2 shows the resultant optimized coil path and straight-section fields for the two layer design. The local harmonic field components at increasing reference radii for these results are shown in Table 9.3. As a result of the optimization, the desired straight-section field components are met to within a fraction of a percent. The quality of this solution for point-to-parallel gantry beam optics will be examined using particle tracking through the coils in Section 9.4.

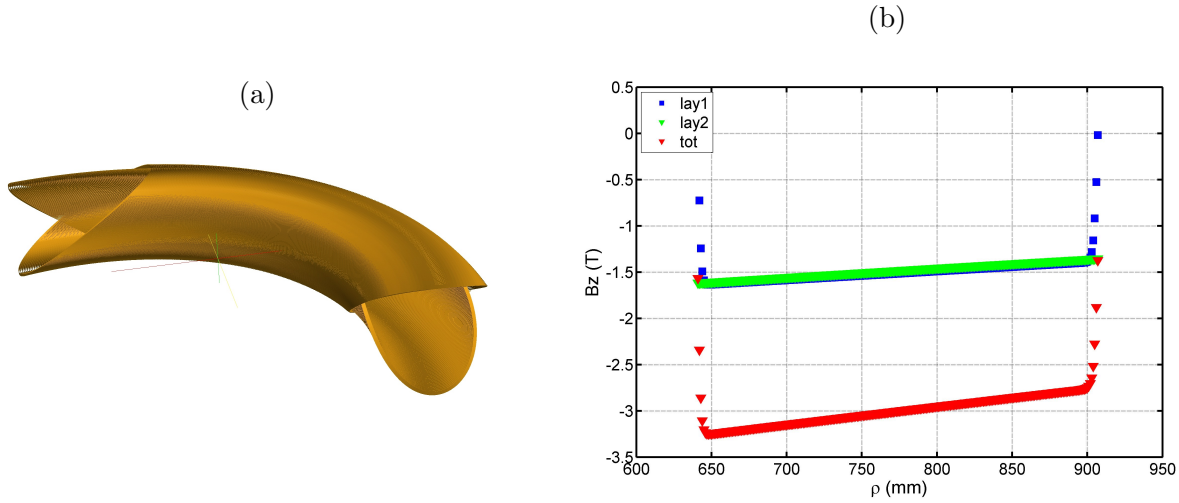

Figure 9.2: (a) The two conductor layers optimized for the combined dipole and quadrupole fields. (b) The contribution of each layer to the transverse field on the midplane and their sum as function of distance across the bore of the straight-section.

Table 9.3: Straight-Section Cylindrical Harmonics

ref. rad. (mm)	% of clear bore	B_1^* (T)	B_2^* (T/m)	B_3^* (T/m^2 10^3)	B_4^* (T/m^3 10^4)
12.5	10%	-3.0005	1.9373	-2.82	-.0575
31.25	25%	-3.001	1.9373	-2.44	3.99
82.5	66%	-3.0045	1.9369	0.258	32.7
93.75	75%	-3.0057	1.9368	1.16	42.5

Positive concavity

An important consideration during the optimization of the coil path is maintaining positive concavity on the inner edge of the torus. This allows for the winding to be placed without

additional tooling, due to its tendency to "hug" the ID of the torus under tension and not pull off to form a chord across the bend. Section 8.2 described the restrictions on the path to achieve this. For this design, the initial tilt angles which set the primary winding coefficient and pitch angle were chosen to be 32.14 degrees for layer 1 and 32.89 degrees for layer 2. These tilt angles were chosen to produce the same pitch angle for both layers. A larger magnitude was also chosen to produce a coil far from containing negative concavity. For example, both are much larger than the limiting tilt angle of 24.5 degrees shown in Figure 8.4 for the geometry of layer 1 with the assumption of only a dipole winding coefficient. Equation 8.12 was evaluated for the set of winding coefficients used for each layer to check the concavity of this solution. The result is shown in Figure 9.3. While the behavior is slightly different than the single coefficient case shown previously in Figure 8.4, the concavity of this solution is far from negative in all areas of the winding.

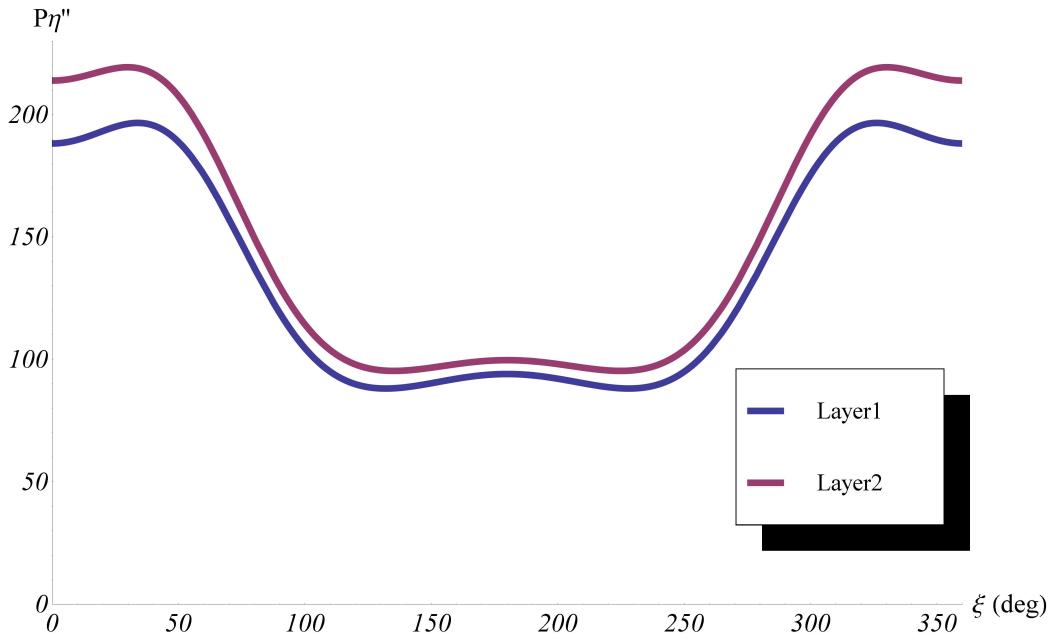

Figure 9.3: The concavity of the CCT winding path as a function of the azimuthal toroidal angle is shown for layer 1 and layer 2 of the design.

Minimum rib thickness

A second consideration during coil generation is the minimum perpendicular distance between conductor channels. The experience machining aluminum and aluminum bronze mandrels has shown a rib thickness of greater than 15 mils (0.381 mm) is necessary to avoid breakage. The rib thickness as a function of toroidal azimuthal angle for layer 1 of this

design is shown in Figure 9.4. An analytic prediction using Equation 8.8 with a 2.0 mm channel subtracted off is compared to results exported from a finite element model of the coil. Good agreement is seen, with a minimum rib thickness of 0.48 mm on the midplane of the inner edge of the torus ($\xi = \pi$). The maximum and minimum rib values for both layers are given in Table 9.4. In this design, both layers have a minimum rib thickness well above the 15 mil requirement.

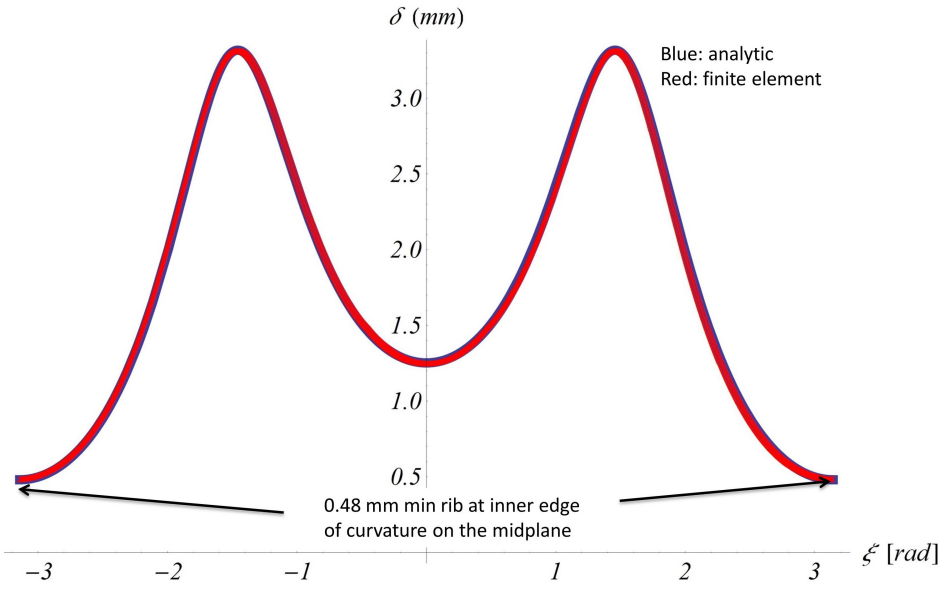

Figure 9.4: Comparison of analytic (blue) and finite element (red) perpendicular rib thickness between channels is shown as a function of toroidal azimuthal angle for the winding of layer 1.

Table 9.4: Gantry Magnet Rib Thickness

Layer	δ_{max} (pole)	δ_{min} (ID midplane)	specification
1	3.32 mm	0.48 mm	$\delta_{min} > 0.381$ mm
2	3.30 mm	0.48 mm	$\delta_{min} > 0.381$ mm

Integrated harmonics and magnetic length

The desired dipole field profile along the length of the magnet will bend the reference particle traveling on axis by ninety degrees. For a CCT magnet, the value of the integrated dipole along the length can be adjusted by adding or removing conductor turns. The number of turns in this design was adjusted to get as close as possible to the ninety degree bend

condition. The closest integer number of turns to this condition was found to be 230 turns per layer. Figure 9.5 shows the calculated dipole field as a function of the distance along the path of the reference particle for this design. A magnetic length of 1218.45 mm at -3.0 T was calculated from the integrated dipole field. This value is close to, but slightly less than, the physical bend length of $\rho\pi/2 = 1215.8$ mm.

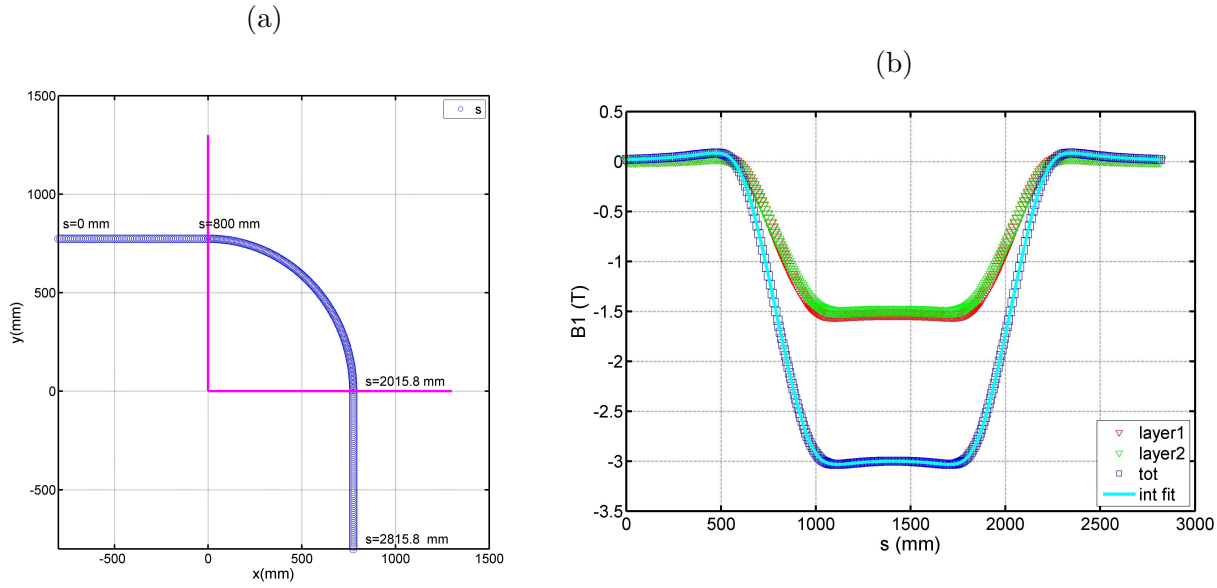

Figure 9.5: (a) The path of integration through the dipole. (b) The dipole harmonic as a function of distance along the path.

Load lines and shortsample

The field at the conductor of layer 1 was first estimated using a line current Biot-Savart method. The magnitude of the field at the bottom of the conductor channel was calculated using a line current placed at the center of the channel. This is an approximation that will underestimate the field at the conductor, but can be used to study the field profile within the windings without the long computation times using the full conductor geometry in software such as Opera3D. The result of this calculation is shown in Figure 9.6. A maximum field at the conductor is seen near the end poles of the magnet which is typical for dipoles.

The field at the conductor in the end region of the coil was then recalculated using Opera3D with the full conductor geometry. A maximum field at the conductor of 3.93 T was found using a net current of 7990 A. Given the lack of iron in the system, this provides a linear load line for the design (see Fig. 9.7). To provide the necessary margin and reduce the power supply current to less than 500 A, 23 strands electrically insulated from one another were chosen as the conductor for both layers. This corresponds to a mandrel channel size

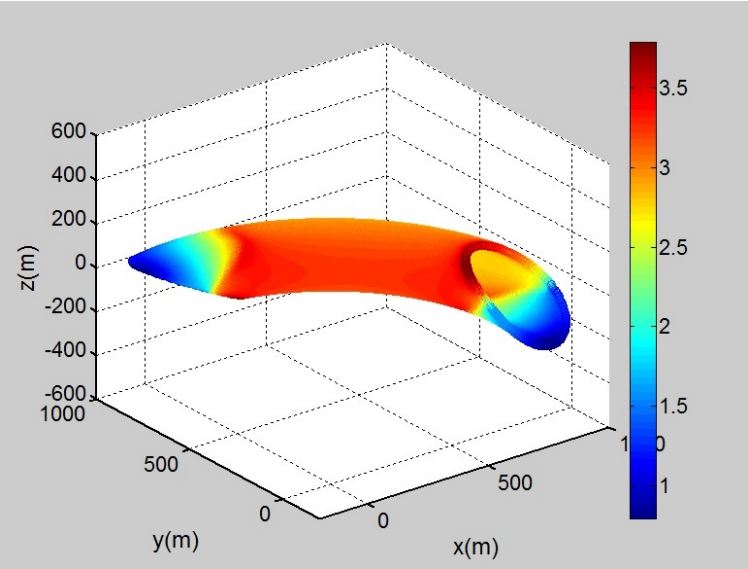

Figure 9.6: The distribution of the field at the conductor is shown for layer 1.

of approximately 2.0 mm in width and 10.0 mm in height. The strand parameters used for the short-sample calculation were based on the 0.8 mm diameter SSC Inner NbTi listed in Table 9.5. As seen in Figure 9.7, this conductor choice results in approximately 30% current margin. If necessary, additional margin can be gained by increasing the channel height and adding more strands.

Table 9.5: SSC Inner NbTi Strand Parameters

Filament Diameter	6.0 μm
Strand Diameter	0.808 mm
Strand J_c (5T,4.2K)	2750 A/mm^2
Strand Cu/SC	1.3

9.3 Magnet geometry, structure, and weight

Conductor geometry and use

The magnet geometry is based on a two layer approach where each layer consists of a winding mandrel (cylindrical torus) with channels to guide the conductor. The size of the channels for both layers is 2.0 x 10.0 mm, corresponding to 23 strands of 0.8 mm diameter, and each mandrel has a 3.0 mm spar. This makes the total radial thickness of each layer 13 mm. The radial buildup for both layers is shown in Table 9.6 where the ID of the inner layer results

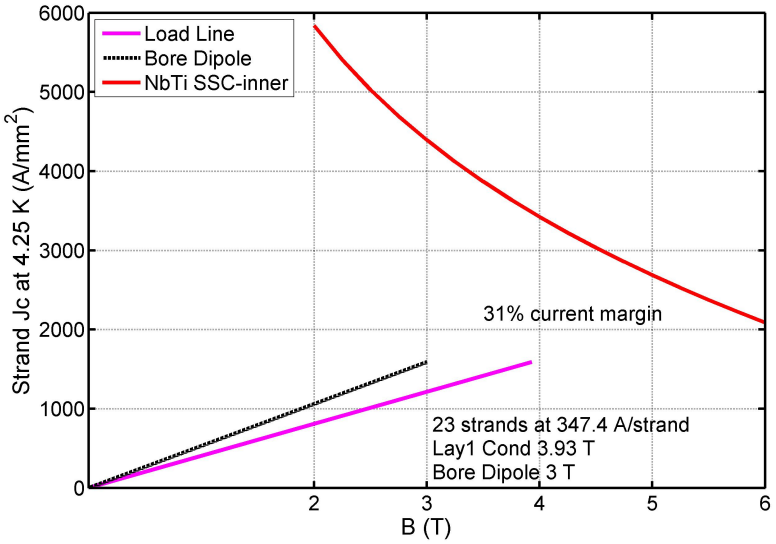

Figure 9.7: The load line and short sample is shown for the design.

in a clear bore diameter of 250 mm. The total radial width of the coilpack is 26 mm. With these parameters, the amount of conductor required for this design is given in Table 9.7.

Table 9.6: Radial Buildup (in mm)

Layer	IR-spar	IR-cond	OR-cond
1	125	128	138
2	138	141	151

Table 9.7: Conductor Use

Layer	# turns	L-one-channel (m)	L-all-channel (m)	# strands	L-strand (km)
1	230	1.237	284.7	23	6.55
2	230	1.340	308.1	23	7.09
tot			592.8 m		13.64 km

Structure and weight

The two cylindrical CCT magnets fabricated to date, CCT1 and CCT2, both use an aluminum outer shell as the only external structure. A similar approach is being considered for

the gantry magnet, using a 20 mm thick aluminum shell outside layer 2. With this assumption, the weight of the mandrels, conductor, and outer shell of the magnet can be estimated. The use of 954 aluminum bronze alloy for the mandrel material is assumed. Table 9.8 estimates this weight assuming a total bend angle of 130 degrees for the mandrels and shell. This angle is extended larger than 90 degrees to include both end regions of coil windings.

Table 9.8: Estimated Weight

	Volume ($10^3 cm^3$)	Density (g/cm^3)	Weight (kg)
Mandrel 1	13.2	7.45	98.1
Mandrel 2	14.6	7.45	108.5
Shell	35.5	2.7	95.9
Channel/Cond.	11.9	8.96	106.2
tot.	75.1		408.8

This estimation does not include contributions from the cryostat and iron necessary for shielding of the stray field. The use of iron for shielding only should result in a significant reduction in iron volume when compared with a resistive gantry magnet. Iron shielding is application specific, with the design tailored to the maximum allowable field in the locations to be shielded. For this reason, the weight of iron needed for shielding this design was not speculated.

9.4 Beam tracking

A short beam tracking study was performed to confirm the approximate point-to-parallel optics. The goal of this study was not to develop an in-depth understanding of the beam optics, but rather to confirm the magnet design performs close what is desired. To accomplish this, protons were tracked from the location of the scanning magnets to the isocenter of the gantry. The horizontal and vertical scanning magnets were approximated at the same location and assumed to be 0.5 m upstream of the final bending magnet. The isocenter was assumed to be 1.0 m downstream of the bend.

Twenty five particles were tracked, each starting at the scanning magnet location with a different initial angle (kick). These kicks were equally spaced between ± 30 mrad. The particles were then tracked in discrete steps using the equations of motion and a Runge-Kutta integrator. At each step of the tracking (particle location), the magnetic field for the equations of motion was calculated from the central path of the coils. The tracking then takes into account the full 3D coil geometry and the associated 3D fields. This is advantageous, as it allows for complete treatment of the end fields and any field distortions present. In this case, no assumptions are needed for fringe field behavior or harmonic representation of the field.

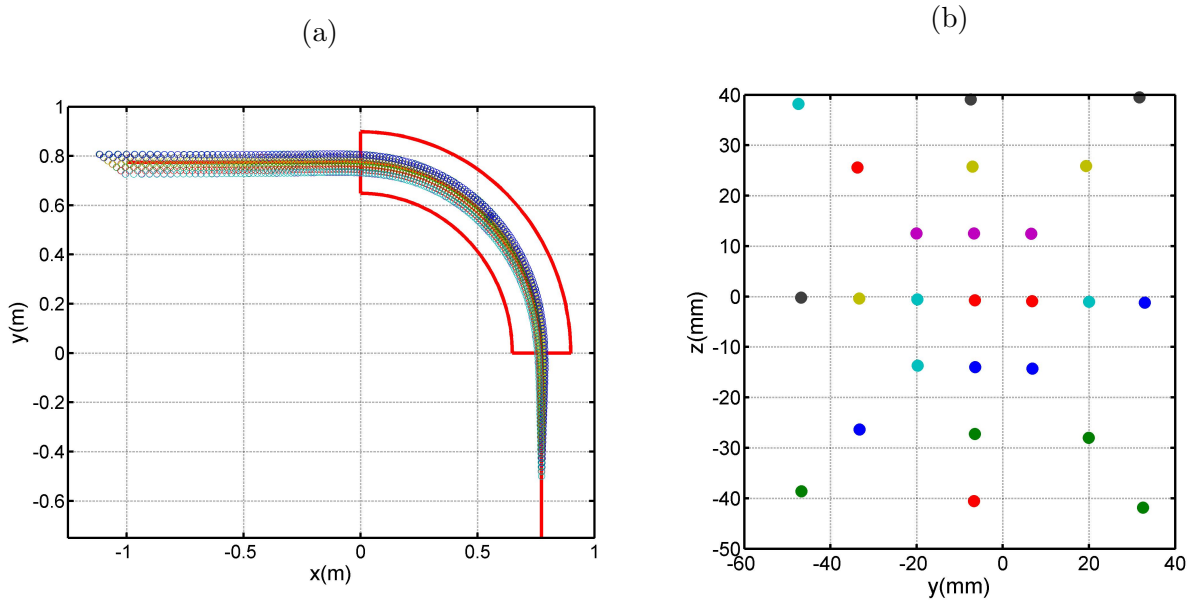

Figure 9.8: Results for tracking through the CCT layers are shown.

The results of the tracking are shown in Figure 9.8. Figure (a) shows the path of the particles projected into the horizontal plane. The kicker location and start of the tracking can seen in the bottom right of the figure (note the slightly different orientation when compared with previous figures). The final grid of particles at the isocenter location is shown in Figure (b). An ideal point-to-parallel system would show a perfect map between initial kick angle and final isocenter position. Some shift and distortion of the distribution is seen in the results for the CCT magnet. This could be corrected with a non-linear kick map or by further optimization of the fields. In a design study including a full treatment of the beam optics, the fields would be further optimized including the consideration of the distortion of the beam spot itself. For the example of such a study for a carbon therapy magnet see [86]. In this case the beam behavior was close enough to what is desired that the coil design could be considered for a study of the Lorentz forces and a structural analysis.

9.5 Lorentz forces

The Lorentz forces of the design were calculated to gain an initial understanding of their magnitude and direction. The goal was to determine what deformation the Lorentz forces would create. The results of two different calculations were examined. The first is the variation of the Lorentz forces around a single turn at the center (straight-section) of the torus, and the second is the variation of the Lorentz forces along the length of the bend. One gives an idea of the local forces (deforming the bore), and the other focuses on the distributed forces (deforming the full torus). The expectation was the forces would deform

the bore from a circular to an elliptical shape in the straight-section (typical of a dipole magnet), and straighten the bend of the torus along the length. Following this study, the forces were applied as loads in an ANSYS model of the design. Section 9.6 will present a study of boundary conditions for the torus, the Lorentz force induced displacement, and stress using the ANSYS model.

Method for calculating the Lorentz forces

The level of detail desired for the Lorentz forces in this study is at the order of a single conductor brick. Calculation of the variation of the forces across the conductor is time intensive, and would become necessary if an analysis of the conductor stress state was desired (as was performed for CCT1 and CCT2 using the 3D periodic symmetry). This detailed conductor stress calculation will be saved for a later study. To calculate the Lorentz forces desired for this study, the conductor turns were discretized into eight node brick elements as described in Section 3.1. The net Lorentz force on a single brick can then be estimated using

$$\vec{f} = I_0(\vec{L} \times \vec{B}), \tag{9.2}$$

where I_0 is the net current, $\vec{L}$ is a vector representative of a line current at the center of the brick, and $\vec{B}$ is the magnetic field at the center of the brick.

Using a line current Biot-Savart method to calculate the field at the center of the brick is problematic due to a singularity when the contribution of the brick itself is considered. To avoid this issue and long calculation times using the full conductor geometry (requiring an Opera3D model), the field at the center of each brick was estimated as the average of the field calculated slightly radially above and below the center. This is similar to the calculation of the force on a current sheet, where the average takes into effect the discontinuity of the field parallel to the surface required by the magnetic boundary conditions.

Figure 9.9 shows the coordinate system used for the Lorentz force results. The ρ coordinate is along the direction from the central bending axis to the location of calculation, the ϕ coordinate is along the bend, and the z coordinate is aligned with the central bending axis. The location at which the Lorentz force has been calculated will be described by the local azimuthal angle θ for the straight-section results, and by the bend angle ϕ for the results along the length of the torus.

Lorentz forces in the straight-section

Figure 9.10 shows the Lorentz forces in the center (straight-section) of this design as a function of azimuthal angle. The variation of the three force components are shown, along with an illustration of the primary Lorentz force actions on a single turn. The behavior is similar to what is seen for a straight CCT dipole. This is characterized by "radial" forces

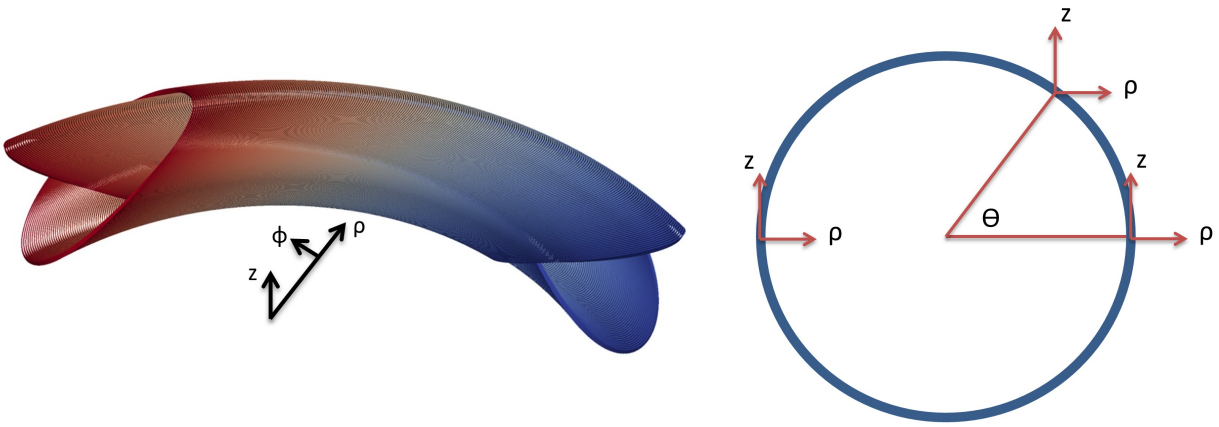

Figure 9.9: The coordinate system for the Lorentz force results is shown.

tending to bend the turn from a circular to elliptical shape at the midplane, and opposite "axial" forces at the poles. Due to the curved and combined function nature of this design, the f_ρ component is unbalanced with a net positive force of 1.8 kN. If this is distributed along the length it will attempt to straighten out the bend of the torus.

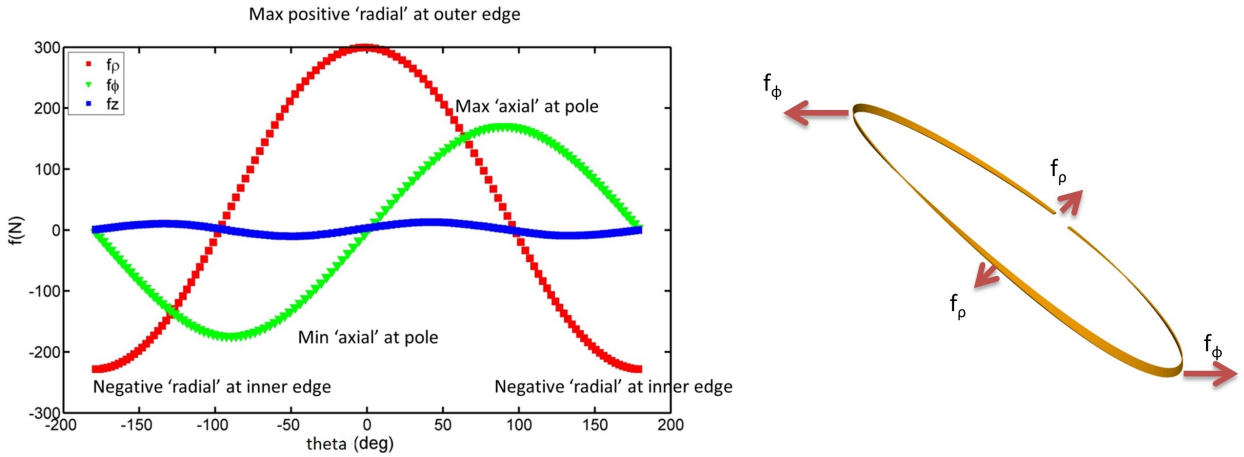

Figure 9.10: The Lorentz forces of a single straight-section turn are shown as a function of azimuthal angle.

Lorentz forces along the length

Figures 9.11 and 9.12 show the Lorentz forces along the length of this design as a function of bend angle. Here, the force shown for each bend angle is representative of the net force within an angular pitch length of ϕ_0 centered about the bend angle. The variation of the

three force components are shown, along with an illustration of the primary Lorentz force actions on the bend of the magnet. As expected, the forces along the length attempt to straighten out the bend. The forces in the end region attempt to collapse the windings into the bending plane, and the opposite "axial" forces at the poles produce shear between the two layers. These results give a basic understanding of the Lorentz forces within the magnet, which can be used during the design of the magnet structure, cryostat, or any other structural member which will resist these forces.

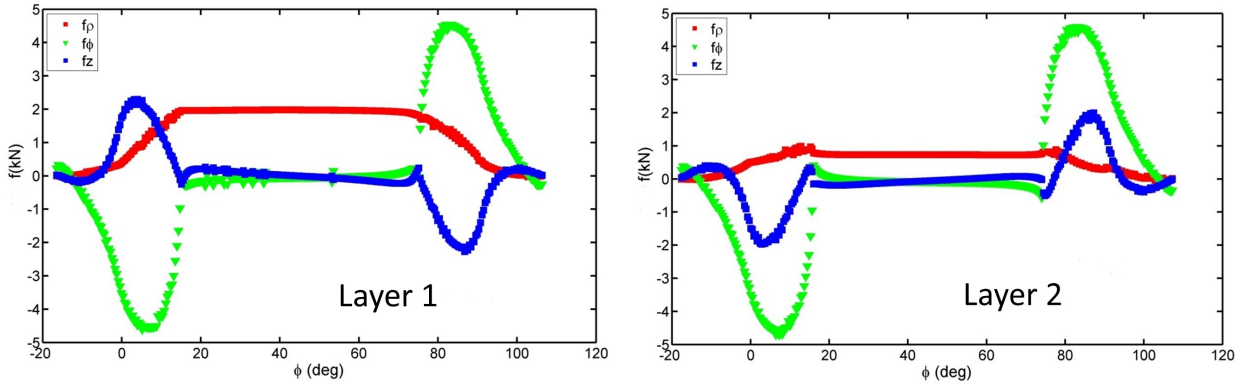

Figure 9.11: The Lorentz forces along the length of each layer are shown as a function of bend angle.

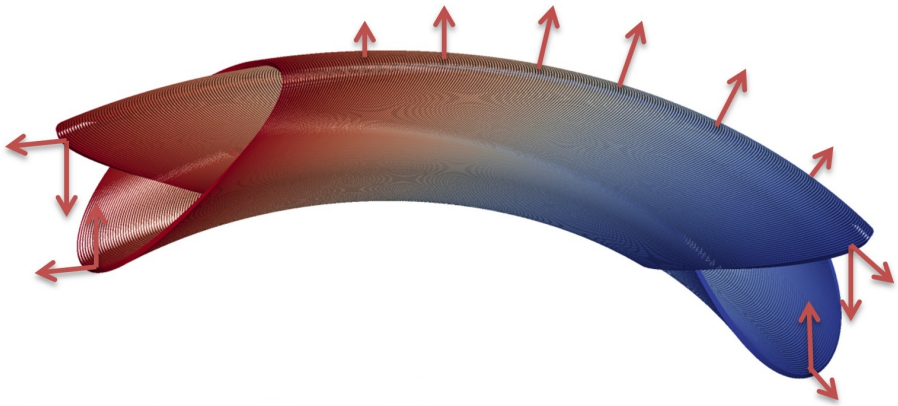

Figure 9.12: An illustration of the primary actions of the Lorentz forces along the bend of the magnet is shown.

9.6 Structural modeling in ANSYS

An ANSYS model was created to study the displacement and stresses induced during cooldown and operation of the magnet. Two thick-walled aluminum bronze tubes sized to the mandrels were generated, followed by an outer aluminum shell of 20 mm radial thickness (Fig. 9.13). A sequential loading of the model was considered, starting with a cooldown to 4.2 K followed by the application of the Lorentz forces at the maximum operating current. For the second load step, the Lorentz forces previously calculated in Section 9.5 were applied to the mandrel tubes. This model does not include the detail of the mandrel channels, due to the difficulty of meshing and solving a large model with small features (minimum rib on the order of 0.5 mm). This a non-conservative approximation, as the channels will reduce the stiffness of the mandrels. A future calculation including the detail of the conductor and channels could be performed using the concept of the minimum 3D symmetry (see Section 3.3) extended to a curved CCT magnet. Given the relatively low field and use of NbTi conductor, it was decided to focus on a study of the large scale behavior of the curved magnet rather than a detailed straight-section model including the conductor.

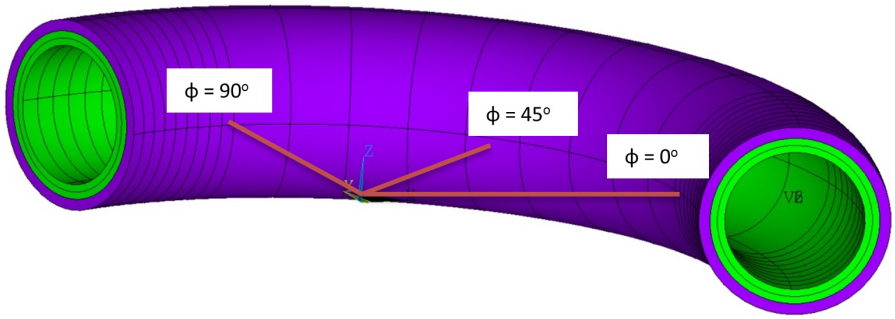

Figure 9.13: The ANSYS model and locations of applied boundary conditions are shown.

Without knowledge of how the magnet interfaces to the cryostat and the gantry, two different boundary conditions were studied with the hope of bounding the possible behavior. The first condition leaves the ends of the magnet free and restricts the nodes at the center to remain in the 45^o plane. This reflects a situation where the ends of the magnet are allowed to deform under Lorentz forces seeking to straighten the bend. The second condition leaves the center of the magnet free and restricts the ends to remain in the 0^o and 90^o planes. This probes the opposite extreme. For both boundary conditions, the contact surfaces between all layers were bonded to reflect epoxy impregnation of the entire magnet.

Boundary condition #1: center fixed in plane

The first boundary condition forces the center of the model to stay in plane. This is accomplished by selecting all the nodes at $\phi = 45^o$ and constraining their displacement in ϕ with the condition $u_\phi = 0$. Then the nodes at the pole ($\rho = \rho_0$) were reselected and restricted with $u_\rho = 0$, and the nodes at the midplane ($z = 0$) were reselected and constrained with $u_z = 0$. Following this, the ANSYS model was solved for a cool down to 4.2 K and then with the Lorentz force loads. Figure 9.14 shows the Lorentz force induced displacement. As expected, a straightening of the torus as well as a bending of the central cross section from a circular to an elliptical shape is seen.

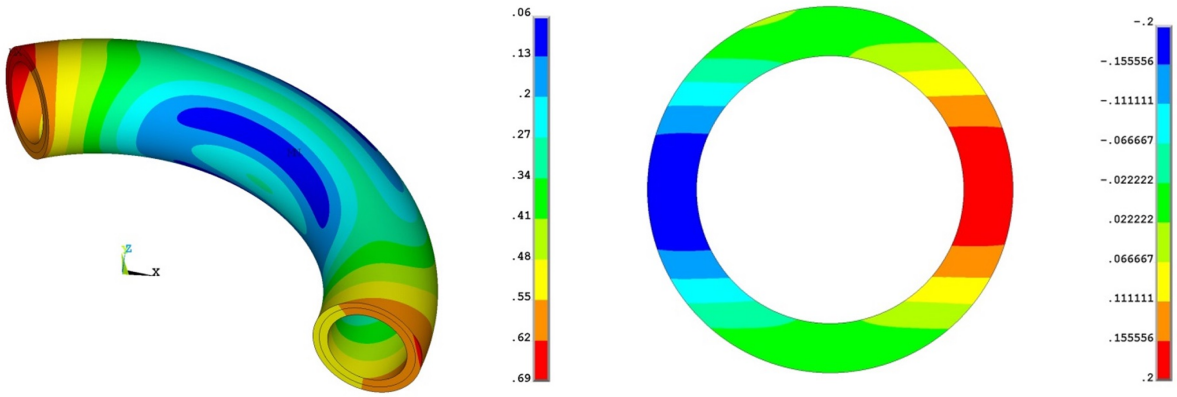

Figure 9.14: The net displacement (in mm) is shown along the length, and the displacement along ρ (in mm) is shown for a central cross section.

Figure 9.15 shows the Lorentz force induced von Mises stress. It is seen that the stress is concentrated towards the center of the bend. The highest stress concentrations are found at the midplane and pole on the inner edge near the bore. This concentration is a result of bending induced stress due to the deformation of the bore from a circular to an elliptic shape. The maximum value of near 120 MPa is well below the 220 MPa yield point of 954 aluminum bronze considered for the mandrel material. The effect of the cooldown was also investigated and found to be minimal. The behavior is characterized by the aluminum shell shrinking onto the bronze mandrels to apply a slight amount of pre-stress. The maximum von Mises stress with both the Lorentz forces and cooldown included was 140 MPa.

Boundary condition #2: ends fixed in plane

The second boundary condition restricts the nodes in the end regions to stay in plane. This is accomplished by selecting all the nodes at $\phi = 0^o$ and $\phi = 90^o$ and constraining their

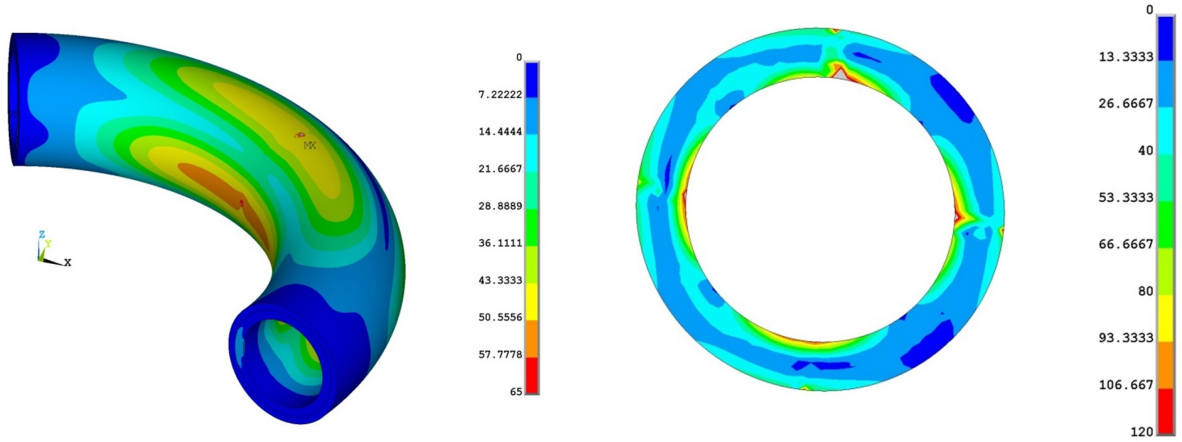

Figure 9.15: The von Mises stress (in MPa) is shown along the length and for a central cross section.

displacement in ϕ with the condition $u_\phi = 0$. Then the nodes at the midplane ($z = 0$) were reselected and restricted with $u_z = 0$. The ANSYS model was then solved for a cool down to 4.2 K and again after the application of the Lorentz force loads. Figure 9.16 shows the Lorentz force induced displacement. This boundary condition prevents the straightening of the torus previously seen, but does not prevent a bending of the central cross section from a circular to an elliptical shape.

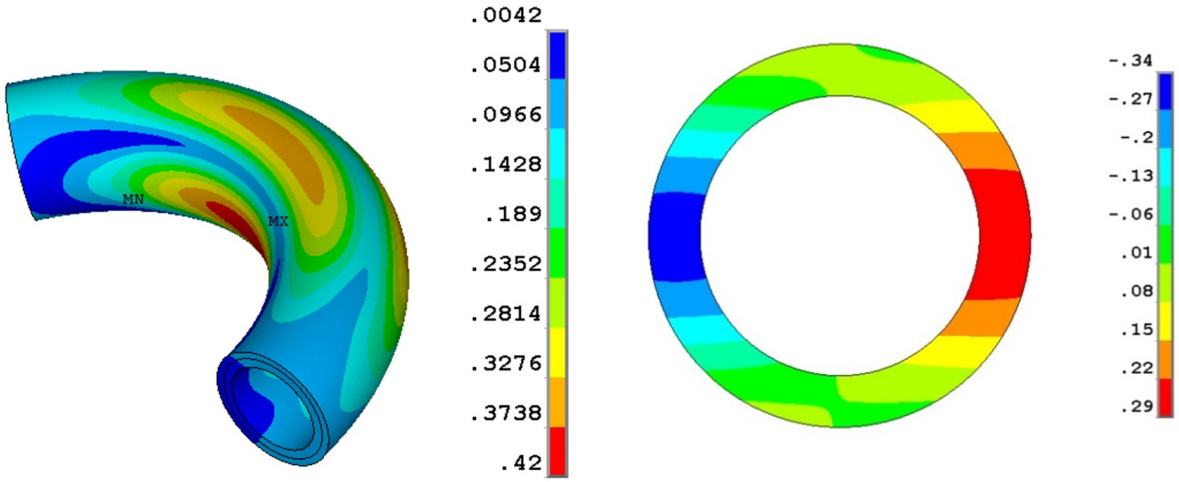

Figure 9.16: The net displacement (in mm) is shown along the length, and the displacement along ρ (in mm) is shown for a central cross section.

Figure 9.15 shows the Lorentz force induced von Mises stress. Similar to the first boundary condition, the highest stress concentrations are found at the midplane and pole on the inner edge near the bore. This is bending induced stress due to the deformation of the bore from a circular to an elliptic shape. The maximum value of near 162 MPa is below the 220 MPa yield point of 954 aluminum bronze considered for the mandrel material. The effect of the cooldown was also investigated and found to be minimal. The net effect is the aluminum shell shrinking onto the bronze mandrels to apply a slight amount of pre-stress. The maximum von Mises stress with both the Lorentz forces and cooldown included was 192 MPa.

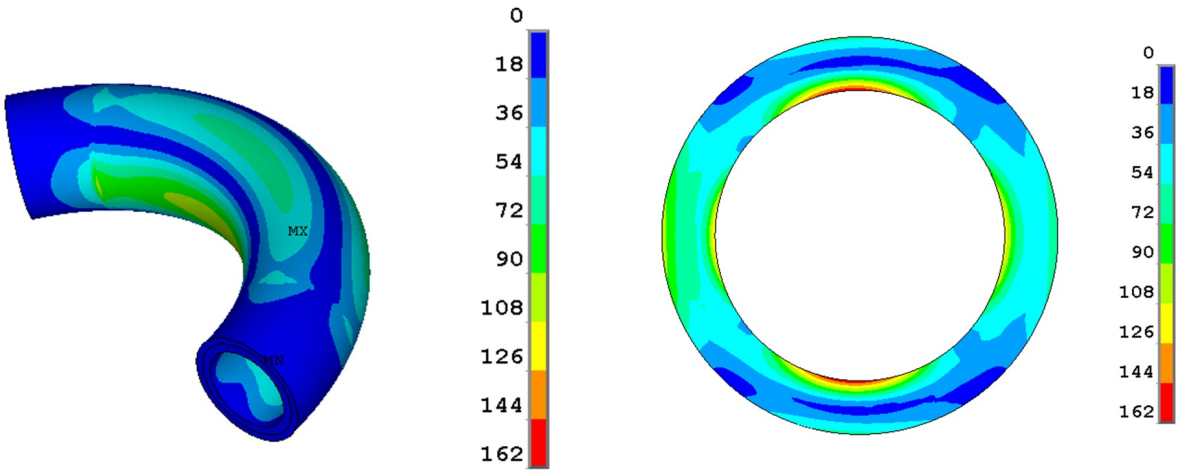

Figure 9.17: The von Mises stress (in MPa) is shown along the length and for a central cross section.

9.7 Conclusion

This design study focused on an initial investigation of the magnetics and structure, with the goal of better understanding the feasibility of using a curved CCT for a final bending magnet in a proton therapy gantry. It was shown a two layer design can be optimized to produce the desired fields, which was verified by particle tracking through the coils. The short-sample limit of the design was calculated and the feasibility of using existing NbTi strand was demonstrated. The distribution of the Lorentz forces was determined to better understand the primary deformations the structure resists. These Lorentz forces were used in an ANSYS model to study two different boundary conditions expected to bound the behavior. A reasonable magnitude of displacements and stresses was found for both conditions. This gives initial confidence a curved winding mandrel approach to the structural design is feasible for this application.

The application of this feasibility based study to the needs of a specific gantry will require a more detailed analysis. One key aspect is the design of the cooling system for the gantry. This system will need to provide adequate cooling of the magnet during gantry specific rotation and magnet field ramping during the treatment. Given the rotation and operation in a hospital environment, it is likely this system will be based on a "dry" conducting cooling approach. The feasibility of such a system to manage the AC losses in the conductor and eddy current losses in the magnet structure will need to be demonstrated.

Chapter 10

The AG-CCT: a New Magnet Concept for an Achromatic Gantry

10.1 The AG-CCT concept

The AG-CCT concept consists of multiple CCT quadrupole winding sections placed in sequence on a curve such that the effective current direction is reversed between sections. This produces alternating quadrupole field regions along the length of the bend whose individual integral strengths can be tuned by the location of the current polarity transitions. A simple transition scheme to reverse the current between sections has been developed to allow for the use of one continuous winding and power supply. This transition scheme nests the ends of each section inside the next, resulting in an alternating focusing system that is both compact and efficient.

The method for changing the current direction between sections makes use of the axial periodicity of CCT windings. Changing the direction of this period switches the direction of the axial current and thus the transverse fields. To generate an AG-CCT winding, a winding path is first optimized to produce quadrupole fields in the straight-section (for example using the method described in Section 8.3). This winding can then be regenerated with sections of alternating axial period based on the desired integrated strengths of the focusing and defocusing regions. Then, a short reverse bend is added to transition between alternating sections and maintain one continuous winding. Figure 10.1 illustrates the concept and transition scheme by showing a single quadrupole winding layer split into five sections (FDFDF). A close up of the coil transition between an F and D section is shown with the current direction at the transition location indicated.

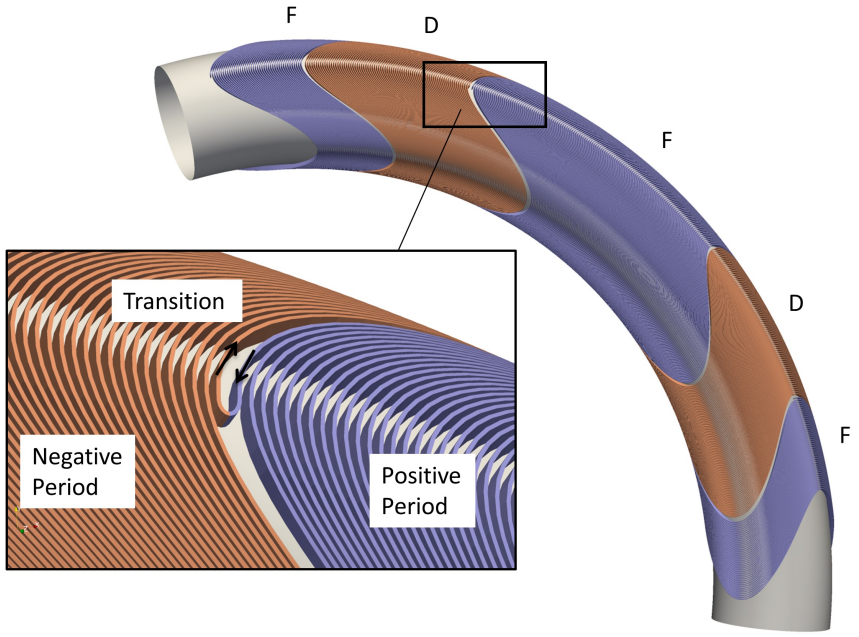

Figure 10.1: A single alternating focusing quadrupole layer is shown with five sections (FDFDF). The transition scheme between sections of opposite axial period is enlarged with the current direction indicated. This scheme allows for the coil to be generated with one continuous winding, where the relative integral strength of the sections can be tuned by adjusting the number and location of transition points.

10.2 Desired magnetic fields for an achromatic proton gantry

The high gradients offered by superconducting quadrupole magnets have recently been investigated for use in achromatic gantries [78, 79, 80, 81]. Such gantries have a large beam energy acceptance, showing promise to treat patients with minimal changes in gantry magnet field. This study will focus on the needs of one particular gantry design which implements the AG-CCT concept. While the focus will primarily be on the superconducting magnets needed for this gantry, a detailed study including the beam optics can be found in the following reference [80]. The beam optics layout implements AG-CCT magnets in three locally achromatic bending sections (B1, B2, and B3 in Figure 10.2).

The first two bending sections B1 and B2 are identical with a total bending angle of 75 degrees. The final bending section B3 is 90 degrees and has an increased bore size due to being downstream of the scanning magnets. All sections contain two field components. The first is a constant dipole field along the length to provide the bending, and the second is an alternating quadrupole field to increase the momentum acceptance. It has been shown this optics layout can provide a 25% momentum acceptance, ranging asymmetrically from -5%

to 20% off momentum. Figure 10.3 shows several proton depth ranges that can be covered using this acceptance.

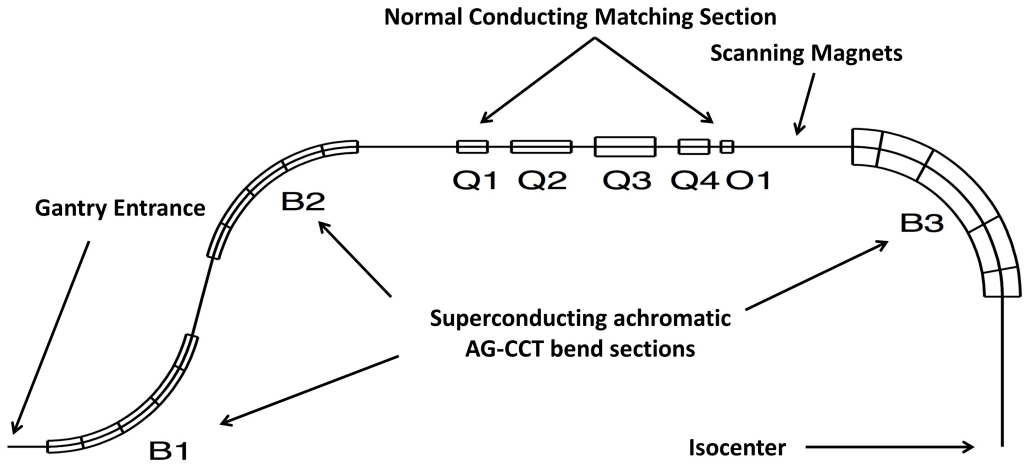

Figure 10.2: A diagram of the proton gantry is shown with the three locally achromatic AG-CCT bending sections (B1, B2, and B3) indicated.

With such a range it is conceivable some tumors could be treated without changing the magnetic field of the superconducting magnets during each treatment direction. This has the advantage of eliminating the difficulty associated with losses in the superconductor and magnet structure during fast field ramping. The design of the magnets in this study will focus on the highest operating point in Figure 10.3 ($B\rho = 1.87$ Tm) corresponding to the maximum current and field in the superconducting magnets. The desired fields will be specified using the Sharp Cut Off Fringe Field (SCOFF) model. In the SCOFF model, fields are represented by step functions of the central field with the length adjusted for the desired integrated harmonic (see the definition of magnetic length in Appendix A).

For a curved magnet it is easiest to specify the magnetic length in terms of the bend angle assuming a constant bend radius. Table 10.1 and Figure 10.4 show the desired fields for both bending sections in terms of the SCOFF model. The field magnitudes are based on the maximum magnet operating current, which takes advantage of the momentum acceptance of the gantry to be 20% less than the maximum proton energy. While both sections have the same dipole field, the alternating quadrupole field in the 75 degree bends is approximately three times as high. This higher gradient is achievable due to the smaller aperture of the 75 degree sections.

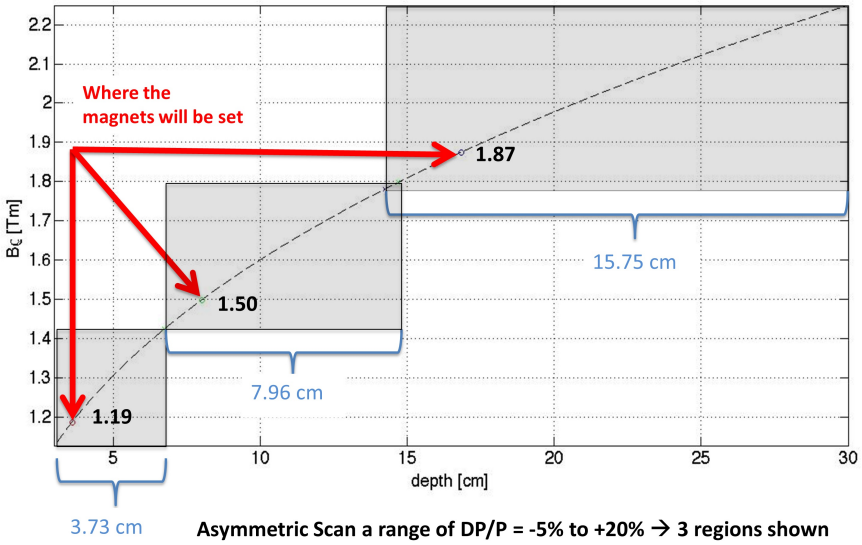

Figure 10.3: Several proton depth ranges covered by the 25% momentum acceptance of the gantry are shown.

Table 10.1: Desired SCOFF Model Fields for the AG-CCT Bends

	B1, B2 (75 °)	B3 (90 °)
Bore aperture (mm)	100	300
Bending radius (m)	1.25	1.25
Bend angle (degree)	75	90
Dipole (T)	1.5	1.5
Gradient (T/m)	48.74	17.43
F Angle (degree)	13.38	10.02
D Angle (degree)	15.80	17.79
F Angle (degree)	16.63	34.39
D Angle (degree)	15.80	17.79
F Angle (degree)	13.38	10.02

10.3 Preliminary design of an AG-CCT magnet system for the desired fields

A preliminary magnet design study was performed to verify the feasibility of using the AG-CCT concept for the desired gantry fields presented in Section 10.2. A four layer design was considered for both the 75 degree and 90 degree bending sections. Each bending section contains two AG-CCT quadrupole layers nested inside two outer CCT dipole layers (Fig. 10.5). The conductor is positioned in grooved winding mandrels which also provide

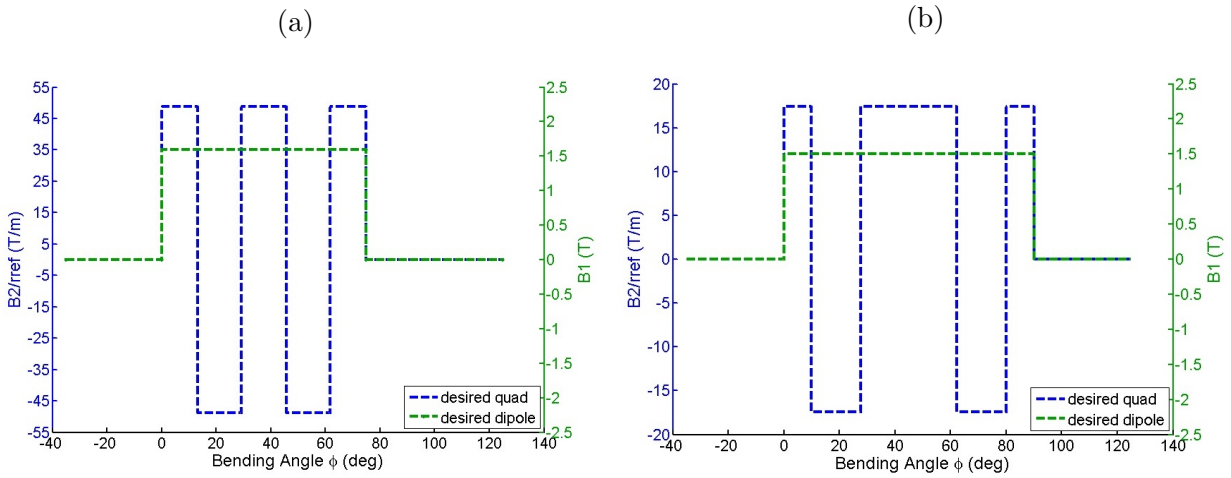

Figure 10.4: The desired SCOFF fields from Table 10.1 are shown for the 75 degree bends B1 and B2 (a) and the 90 degree bend B3 (b).

structural support. The winding mandrel parameters resulting from this approach are shown in Table 10.2, where the channel depth was determined by the number of strands per layer (to be discussed when the short-sample is presented).

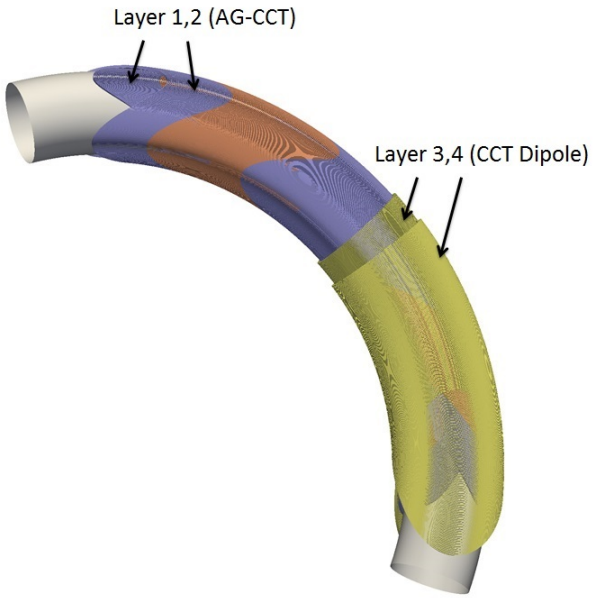

Figure 10.5: The four CCT layer approach to the bending sections is shown.

Table 10.2: Winding Mandrel Geometry (in mm)

		75 degree (B1,B2)				90 degree (B3)			
Lay	Type	Ri	Ro	Wall	Channel	Ri	Ro	Wall	Channel
1	AG-CCT	50	64.3	14.3	2.0/11.3	150	169	19.0	2.0/16.0
2	AG-CCT	64.3	78.6	14.3	2.0/11.3	169	188	19.0	2.0/16.0
3	CCT dipole	78.6	85.1	6.5	2.0/3.5	188	196.2	8.2	2.0/5.2
4	CCT dipole	85.1	91.6	6.5	2.0/3.5	196.2	204.4	8.2	2.0/5.2

Coil generation and fields

A curved CCT conductor path for each of the bends was optimized using the winding coefficient method described in Section 8.3. The figure of merit for the two inner layers was a pure quadrupole field, and the figure of merit for the outer two layers was a pure dipole. In this case a cylindrical expansion of the fields on a reference radius at the center of the bend was compared to the desired fields. Following the coil winding optimization, a current was chosen for the dipole and quadrupole layers to match the desired magnitude of the SCOFF harmonics (see Table 10.1). The quadrupole coils were then broken up into five sections with alternating current to match the SCOFF model. Here an integer number of turns was chosen to match the SCOFF model bend angle considering each turn has a constant angular pitch ϕ_0.

Particle tracking was then performed through the coils. The SCOFF model idealizes the field profile along the length, meaning a final optimization of the windings was needed to account for the differences. Similar to the proton final bending magnet study (Section 9.4), the tracking was performed using the full coil geometry which included all 3D field effects and fringe fields. This directly coupled the final optimization of the coil to the beam behavior, eliminating the need for a final field quality specification which is difficult in an alternating curved system. During the beam tracking study, the sectioning of the quadrupole coils and the magnitude of the field gradients were adjusted. The final break up and field gradients of the AG-CCT sections that produced the desired beam behavior is given in Table 10.3.

Table 10.3: Post Particle Tracking: AG-CCT Split

	75 degree (B1,B2)			90 degree (B3)		
type	nturns	bend (deg)	gradient (T/m)	nturns	bend (deg)	gradient (T/m)
F	62	13.4	50.6	44	10.3	19.7
D	73	15.8	-50.6	79	18.6	-19.7
F	77	16.6	50.6	137	32.2	19.7
D	73	15.8	-50.6	79	18.6	-19.7
F	62	13.4	50.6	44	10.3	19.7
tot.	347	75		383	90	

An example of the resultant straight-section fields are shown for the 75 degree bend in Figure 10.6. The combined field of a 1.6 T dipole plus a 50.6 T/m quadrupole is seen. The slight left-right asymmetry of the winding cross section is a result of an effort to produce left-right symmetric cylindrical multipoles in a curved magnet. The field along the length of the bends is seen in Figure 10.7. In this figure the fields generated by the dipole and AG-CCT layers are compared to those of the desired SCOFF model. The CCT fields are seen approaching the sharp edge model in the integrated sense. The ability of an AG-CCT section to produce a "flat top" straight-section field is based on the length and bore size of the section. The smaller bore of the 75 degree bend allows for the production of flat-top sections over a much smaller angle. This resulted in a better agreement between the SCOFF and CCT fields when compared to the 90 degree bend.

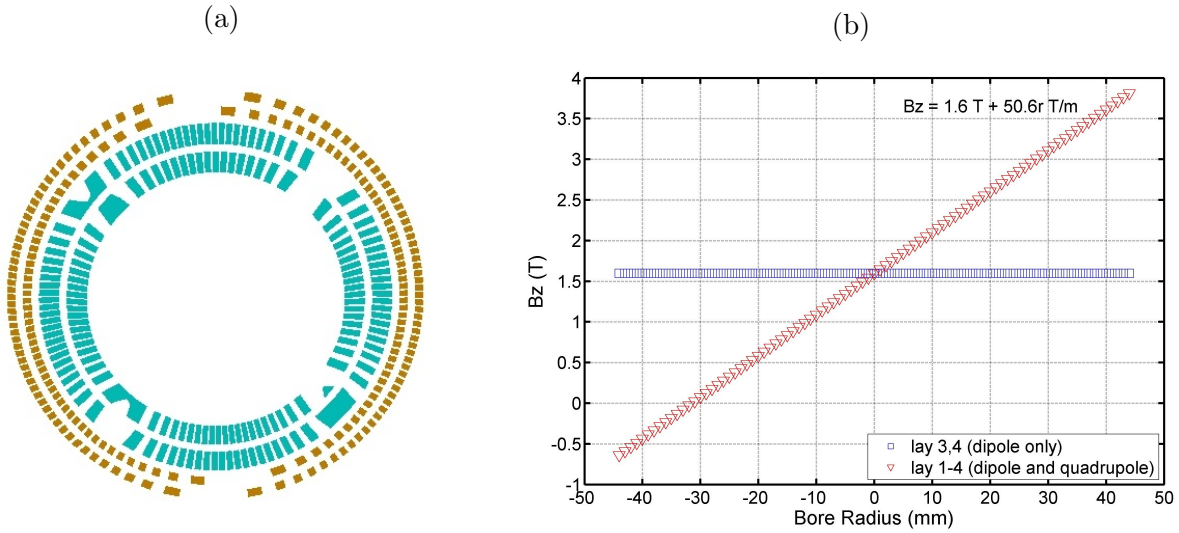

Figure 10.6: (a) A slice of the coils for the 75 degree bend. The inner two layers were designed to produce a quadrupole field and the outer two a dipole field. (b) The vertical field on the midplane produced by the windings.

Short-sample

An Opera3D model of the dipole and AG-CCT conductor layers for both bends was generated using the method described in Section 3.2. This model corresponded to optimized coil after the beam tracking (Table 10.3) and contained the detail of the transitions (short reverse bends). The field at the conductor of each layer was calculated with the current set at the maximum operating point. Similar to the previous gantry magnet study, SSC inner NbTi strand was considered as a baseline for the conductor (Table 9.5). This is a well characterized

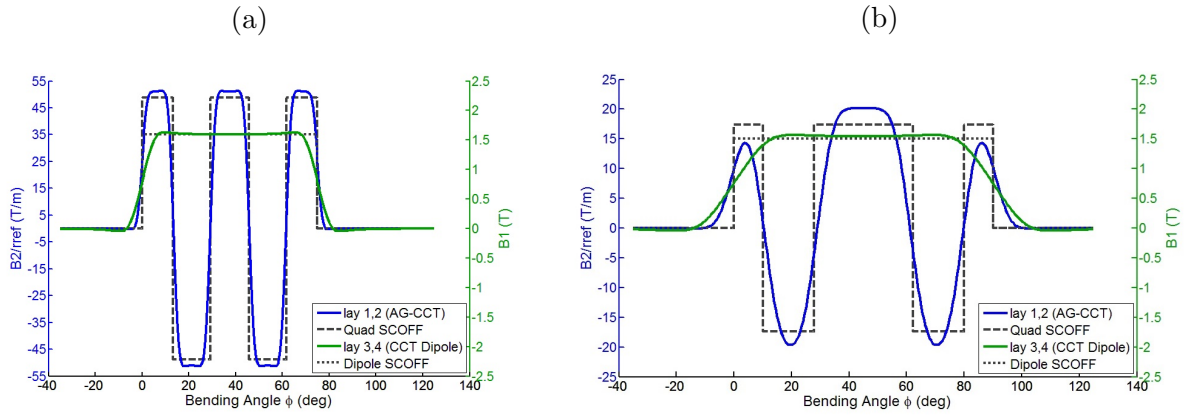

Figure 10.7: The dipole and alternating quadrupole contributions from the CCT dipole and AG-CCT layers are shown as a function of bending angle for the 75 degree bend (a) and 90 degree bend (b).

NbTi strand that is readily available. It also has the advantage of using a small filament diameter which reduces AC losses in the strand during field ramping.

The number of strands used in each layer was chosen to provide a current margin of at least 20% and keep the current per strand less than 500 A. Here the current is limited to maintain compatibility with a "dry" cryogenics system. In this case the strands are assumed to be in series and electrically isolated from one another so that the operating current is that of a single strand. An efficient method for isolating the strands and creating the many connections needed between layers is an area of future research, during which an alternate conductor or approach may be chosen.

Table 10.4 shows the maximum field at the conductor, the chosen number of strands, the current per strand, and the resulting margin using SSC inner NbTi for each layer. It is seen that 20% margin can be obtained with a reasonable number of strands. The maximum required channel depth (sized to 37 strands) is approximately 16 mm. If necessary, additional margin can be gained by increasing the number of strands. Figures 10.8 and 10.9 show the operating point of 75 and 90 degree bends. In this case it is important to note the "load lines" in the figures are coupled because changing the current in the dipole layers changes the maximum field at the AG-CCT layers and vice versa.

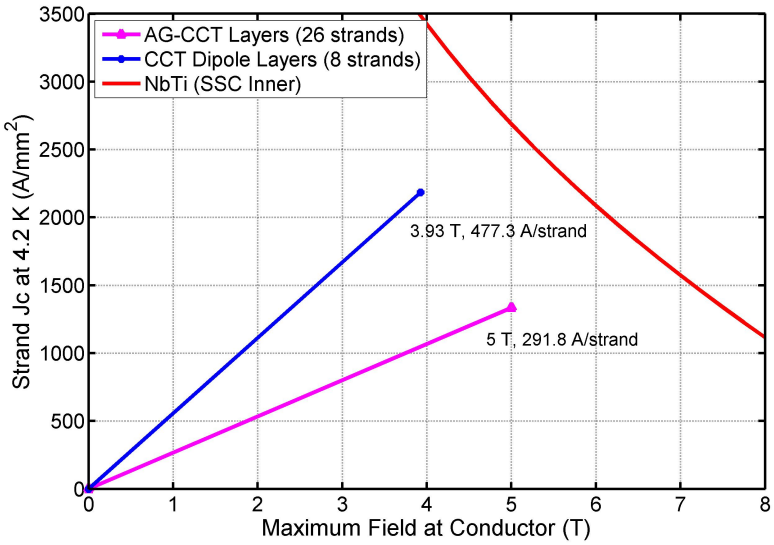

Figure 10.8: The short-sample in the superconductor is shown for both the AG-CCT and CCT dipole layers of the 75 degree bend (B1,B2).

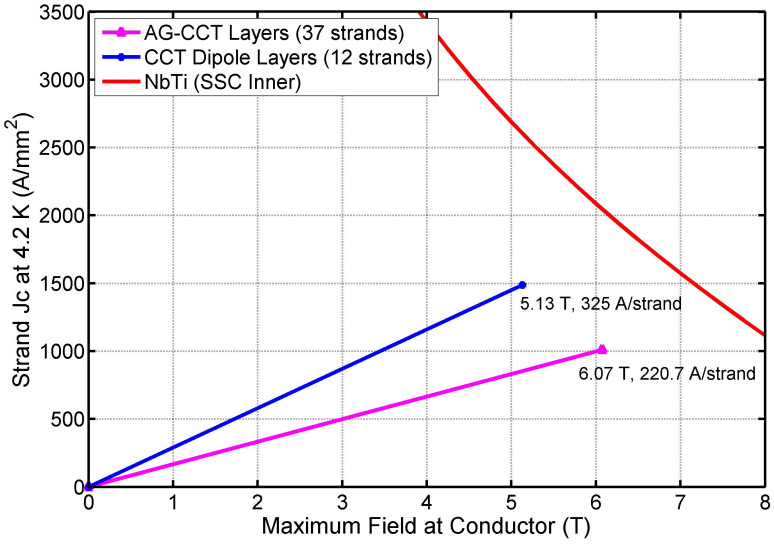

Figure 10.9: The short-sample in the superconductor is shown for both the AG-CCT and CCT dipole layers of the 90 degree bend (B3).

Table 10.4: Short Sample at the Maximum Operating Point

		75 degree (B1,B2)				90 degree bore (B3)			
Lay	Type	I/str. (A)	B_{max}(T)	str.	mrg.	I/str.(A)	B_{max}(T)	str.	mrg.
1	AG-CCT	291.8	5.0	26	24%	220.7	6.03	37	21%
2	AG-CCT	291.8	5.0	26	24%	220.7	6.07	37	21%
3	CCT dipole	477.3	3.93	8	26%	325	5.13	12	26%
4	CCT dipole	477.3	2.86	8	48%	325	4.03	12	45%

10.4 Conclusion and alternative applications

The AG-CCT concept was shown to be an efficient method for producing alternating quadrupole fields along the bend of a torus. This concept appears to be a practical design for producing the fields desired by achromatic gantries. The large energy acceptance of these gantries show promise to greatly reduce the need for fast field ramping, potentially eliminating a key risk to the introduction of superconducting technology in this area. A preliminary design study of an AG-CCT magnet system for a proton therapy gantry was presented, showing the feasibility of the magnetic design.

While this application is focused on alternating quadrupole fields, the concept applies more generally to any alternating harmonic (dipole, quadrupole, sextupole, etc.) in the curved or straight geometry. In the general sense this concept is called a Left-Right CCT magnet (LR-CCT). A compact and efficient method for generating alternating harmonics should be desired in fields outside of ion beam cancer therapy. One application that appears promising is the use of a LR-CCT magnet to generate an alternating dipole field for a "wavelength shifter". These devices are applied to charged particle beams (typically electrons) to produce intense, high photon-energy synchrotron radiation without any net steering or displacement of the beam.

Part III

Conclusion

Chapter 11

Summary and Future Work

The performance of the Canted-Cosine-Theta (CCT) design for high energy physics and ion beam cancer therapy will ultimately be determined by a series of magnet tests. Two programs at Lawrence Berkeley National Laboratory have been established to achieve this. The first is within the high field base program of the Superconducting Magnet Group of the Accelerator Technology and Applied Physics Division. A series of staged tests are planned for the Nb_3Sn CCT dipole magnet design CCT2 presented in this thesis. This magnet will be tested in configurations increasing from 10 to 16 T over the next several years, with the goal of determining the performance of the CCT at the field level desired for a future hadron collider.

The application to ion beam cancer therapy will be actively pursued using a recent grant from DOE's Accelerator R&D Stewardship Program. This newly established program seeks to promote the application of accelerator technology developed for high energy physics to the needs of the general community. In this case, superconducting CCT magnets (in particular the AG-CCT) have been identified as a way to reduce the weight and cost of ion beam cancer therapy gantries, and potentially open the door to treatment for more patients who can benefit from this therapy. This three year grant will be used to build and test a superconducting AG-CCT magnet system for a proton therapy gantry. The research will be performed by a collaboration of Lawrence Berkeley National Laboratory, the Paul Scherrer Institute, and Varian Particle Therapy.

It is my hope the developments of this thesis will contribute to the success of both projects. In this thesis an analytic approach to the CCT was presented that can be used for design and optimization in both the straight and curved geometry. New finite element methods were given with a focus on structural modeling. The design of two dipole magnets for high energy physics was presented (CCT1 and CCT2). The fabrication and successful test of the 2.5 T NbTi dipole CCT1 was completed, serving as a proof-of-principle step towards a high field Nb_3Sn magnet. Initial steps were taken in the fabrication of the 16 T Nb_3Sn dipole CCT2 which will be tested as part of LBNL's high field base program.

Two design studies were performed for ion beam therapy. The first focused on a curved superconducting CCT to reduce the weight of a final bending magnet in a proton therapy

gantry with upstream active scanning. This study showed the feasibility of the magnetic and structural design, which can be adapted to a future study of the cryogenics for a specific gantry. The second study makes use of a new magnet concept (the AG-CCT) to reduce the weight and improve the functionality of a proton gantry. This concept produces alternating high gradient fields desired for achromatic (high energy acceptance) beam optics. A preliminary design study of an AG-CCT magnet system for a proton therapy gantry was performed, showing the feasibility of the magnetic concept. This study lays the groundwork for the AG-CCT design that will be built and tested as part of the stewardship program.

Bibliography

[1] A. Tollestrup and E. Todesco. "The Development of Superconducting Magnets for Use in Particle Accelerators: From the Tevatron to the LHC". In: *Reviews of Accelerator Science and Technology* 1 (2008).

[2] L. Rossi and L. Bottura. "Superconducting Magnets for Particle Accelerators". In: *Reviews of Accelerator Science and Technology* 5 (2012), pp. 51–89.

[3] G. Ambrosio. "Nb3Sn High Field Magnets for the High Luminosity LHC Upgrade Project". In: *IEEE Trans. Appl. Supercond.* 25.3 (2015), p. 4002107.

[4] L. Boturra. *Technology challenges in high field magnets for LHC upgrades and future accelerators, Beam Dynamics Meets Magnets II, Bad Zurzach, Switzerland, December 3.* 2014. URL: https://indico.psi.ch/contributionDisplay.py?contribId=17&sessionId=8&confId=3033.

[5] *US LHC Accelerator Research Program.* URL: http://www.uslarp.org/.

[6] *High Luminosity Upgrade for the LHC.* URL: http://hilumilhc.web.cern.ch/.

[7] *Future Circular Collider Study.* URL: https://espace2013.cern.ch/fcc/Pages/default.aspx.

[8] F. Zimmermann. *Challenges for Future Circular Colliders, Beam Dynamics Meets Magnets II, Bad Zurzach, Switzerland, December 1.* 2014. URL: https://indico.psi.ch/contributionDisplay.py?contribId=2&sessionId=2&confId=3033.

[9] W. Barletta et al. "Future hadron colliders: From physics perspectives to technology R&D". In: *Nuclear Instruments and Methods in Physics Research Section A: Accelerators, Spectrometers, Detectors and Associated Equipment* 764 (2014), 352368.

[10] L. Boturra. *Status of Magnet R&D for the FCC, Preparation Meeting for the FCC International Collaboration Board, September 9th.* 2014. URL: http://indico.cern.ch/event/333236/contribution/10/material/slides/1.pdf.

[11] P. Ferracin, S. Caspi, and A.F. Lietzke. "Towards Computing Ratcheting and Training in Superconducting Magnets". In: *IEEE Trans. Appl. Supercond.* 17.2 (2007), p. 2373.

[12] P. Ferracin et al. "Electro-magnetic forces and stresses in superconducting accelerator magnets". In: *USPAS 2012 Lecture: Austin, Texas* (2012).

[13] K. Koepke. "Fermilab doubler magnet design and fabrication techniques". In: *IEEE Trans. Magn.* 17.1 (1979).

[14] P. Schmuser. "Superconducting magnets for particle accelerators". In: *Rep. Prog. Phys.* 54 (1991), p. 683.

[15] A. Devred. "About the mechanics of SSC dipole magnet prototypes". In: *AIP Conf. Proc.* 249.2 (1992), pp. 1309–1372.

[16] T. Ogitsu. "Mechanical performance of 5-cm aperture, 15-m long SSC dipole magnet prototypes". In: *IEEE Trans. Appl. Supercond.* 3.1 (1993), pp. 686–691.

[17] A. Greene et al. "The Magnet System of the Relativistic Heavy Ion Collider (RHIC)". In: *IEEE Trans. Magn.* 32.4 (1996), p. 2041.

[18] "LHC design report v.1: the main LHC ring". In: *CERN-2004-003-v-1* 1 (2004).

[19] S. Caspi et al. "The use of pressurized bladders for stress control of superconducting magnets". In: *IEEE Trans. Appl. Supercond.* 11.1 (2001), pp. 2272–2275.

[20] L. Rossi. "Manufactoring and Testing of Accelerator Superconducting Magnets". In: *arXiv:1501.07164* (2015).

[21] E. Barzi, T. Wokas, and A.V. Zlobin. "Sensitivity of Nb3Sn Rutherford-Type Cables to Transverse Pressure". In: *IEEE Trans. Appl. Supercond.* 15.2 (2005), p. 1541.

[22] E. Barzi, D. Turrioni, and A.V. Zlobin. "Effect of Transverse Pressure on Brittle Superconductors". In: *IEEE Trans. Appl. Supercond.* 18.2 (2008), p. 980.

[23] B. Bordini et al. "Critical Current Measurements of High-Jc Nb3Sn Rutherford Cables Under Transverse Compression". In: *IEEE Trans. Appl. Supercond.* 24.3 (2014), p. 9501005.

[24] H. Felice et al. "Test results of TQS03: a LARP shell-based Nb3Sn quadrupole using 108/127 conductor". In: *J. Phys.: Conf. Ser.* 234 (2010), p. 032010.

[25] P. Ferracin et al. "Magnet Design of the 150 mm Aperture Low- Quadrupoles for the High Luminosity LHC". In: *IEEE Trans. Appl. Supercond.* 24.3 (2014), p. 4002306.

[26] A.V. Zlobin et al. "Design and Fabrication of a Single-Aperture 11 T Dipole Model for LHC Upgrades". In: *IEEE Trans. Appl. Supercond.* 22.3 (2012), p. 4001705.

[27] A. Milanese et al. "Design of the EuCARD High Field Model Dipole Magnet FRESCA2". In: *IEEE Trans. Appl. Supercond.* 22.3 (2012), p. 4002604.

[28] P. Ferracin et al. "Development of the 15 T Nb3Sn Dipole HD2". In: *IEEE Trans. Appl. Supercond.* 18.2 (2008), p. 277.

[29] P. Ferracin et al. "Mechanical Design of HD2, a 15 T Nb3Sn Dipole Magnet with a 35 mm Bore". In: *IEEE Trans. Appl. Supercond.* 16.2 (2006), p. 378.

[30] D.I. Meyer and R. Flasck. "A new configuration for a dipole magnet for use in high energy physics applications". In: *Nuclear Instruments and Methods in Physics Research Section A: Accelerators, Spectrometers, Detectors and Associated Equipment* 80.2 (1970), pp. 339–341.

[31] C.L. Goodzeit, M.J. Ball, and R.B. Meinke. "The Double-Helix Dipole - a Novel Approach to Accelerator Magnet Design". In: *IEEE Trans. Appl. Supercond.* 13.2 (2003), pp. 1365–1378.

[32] R. Meinke, C.L. Goodzeit, and M.J. Ball. "Modulated Double-Helix Quadrupole Magnets". In: *IEEE Trans. Appl. Supercond.* 13.2 (2003), pp. 1369–1372.

[33] A. V. Gavrilin et al. "New concepts in transverse field magnet design". In: *IEEE Trans. Appl. Supercond.* 13.2 (2003), pp. 1213–1216.

[34] C. Goodzeit, R. Meinke, and M. Ball. "Combined function magnets using double-helix coils". In: *Proceedings of IPAC2007*. 2007, pp. 560–562.

[35] S. Caspi et al. "Design, Fabrication, and Test of a Superconducting Dipole Magnet Based on Tilted Solenoids". In: *IEEE Trans. Appl. Supercond.* 17.2 (2007), pp. 2266–2269.

[36] J. H. Rochford, D. E. Baynham, and A. Devred. "An Evaluation of the Helical Winding Method Applied to the Next European Dipole Project". In: *IEEE Trans. Appl. Supercond.* 18.2 (2008), pp. 1541–1544.

[37] S. Caspi et al. "Test of a NbTi Superconducting Quadrupole Magnet Based on Alternating Helical Windings". In: *IEEE Trans. Appl. Supercond.* 19.3 (2009), pp. 1195–1198.

[38] H. Witte et al. "The Advantages and Challenges of Helical Coils for Small Accelerators - A Case Study". In: *IEEE Trans. Appl. Supercond.* 22.2 (2012), p. 4100110.

[39] S. Farinon and P. Fabbricatore. "Refined modeling of superconducting double helical coils using finite element analyses". In: *Supercond. Sci. Technol.* 25.6 (2012), p. 065006.

[40] F. Bosi et al. "Compact Superconducting High Gradient Quadrupole Magnets for the Interaction Regions of High Luminosity Colliders". In: *IEEE Trans. Appl. Supercond.* 23.3 (2013), p. 4001004.

[41] S. Russenschuck. "ROXIE - A Computer Code for the Integrated Design of Accelerator Magnets". In: *LHC Project Report* 276 (1999).

[42] Martin Wilson. *Superconducting Magnets*. Oxford University Press, 1983. ISBN: 0198548052.

[43] Cobham. *Opera3D 15R2*.

[44] R. Meuser. "Magnetic Field for a Thick Cos(nt) Winding". In: *LBNL Engineering Note* M5254 (1978).

[45] L. Brouwer and S. Caspi. "Comparison of 3D Lamination Boundary Conditions to 2D Plane Strain and Plane Stress for Finite Element Modeling of CCT Magnets". In: *LBNL Engineering Note* SU1210-10875A (2013).

[46] ANSYS. *Mechanical APDL, Release 14.0*.

[47] L. Brouwer et al. "Structural Design and Analysis of Canted-Cosine-Theta Dipoles". In: *IEEE Trans. Appl. Supercond.* 24.3 (2014), p. 4001506.

[48] Helene Felice et al. "Magnetic and Mechanical Analysis of the HQ Model Quadrupole Designs for LARP". In: *IEEE Trans. Appl. Supercond.* 18.2 (2008), pp. 281–284.

[49] Kitware. *Paraview 4.2*.

[50] S. Caspi. *Prospects for a 16T CCT Magnet, 2015 FCC Workshop, Washington, DC, USA, March 23-27*. 2015. URL: `http://indico.cern.ch/event/340703/`.

[51] S. Caspi and P. Ferracin. "Limits of Nb3Sn Accelerator Magnets". In: *Proceedings of IPAC2005*. 2005, pp. 107–111.

[52] A. Godeke et al. "Characterization of High Current RRP Wires as a Function of Magnetic Field, Temperature, and Strain". In: *IEEE Trans. Appl. Supercond.* 19.3 (2009), pp. 2610–2614.

[53] D. Dietderich. Private Communication.

[54] S. Caspi et al. "The Canted-Cosine-Theta Magnet (CCT) - a Concept for High Field Accelerator Magnets". In: *IEEE Trans. Appl. Supercond.* 24.3 (2014), p. 4001804.

[55] A. Hafalia et al. "The Structural Design for a Canted-Cosine-Theta Superconducting Dipole Coil and Magnet Structure-CCT1". In: *IEEE Trans. Appl. Supercond.* 24.3 (2014), p. 4001904.

[56] S. Caspi et al. "Test Results of CCT1 - A 2.4T Canted-Cosine-Theta Dipole Magnet". In: *IEEE Trans. Appl. Supercond.* 25.3 (2015), p. 4002304.

[57] J. Laslett, S. Caspi, and M. Helm. "Configuration of Coil Ends for Multipole Magnets". In: *Particle Accelerators* 22 (1987), pp. 1–14.

[58] L. Bottura. "A Practical Pit for the Critical SurEace of NbTi". In: *IEEE Trans. Appl. Supercond.* 10.1 (2000), pp. 1054–1057.

[59] R. Meuser. "Stresses in a Thick Cosine(nt) Coil Winding". In: *LBNL Engineering Note* M5256 (1978).

[60] S. Caspi et al. "Design of an 18T Canted-Cosine-Theta Superconducting Dipole Magnet". In: *IEEE Trans. Appl. Supercond.* 25.3 (2015), p. 4000205.

[61] L. Brouwer, S. Caspi, and S. Prestemon. "Structural Analysis of an 18 T Hybrid Canted-Cosine-Theta Superconducting Dipole". In: *IEEE Trans. Appl. Supercond.* 25.3 (2015), p. 4000404.

[62] A. Godeke et al. "Bi-2212 Canted-Cosine-Theta Coils for High-Field Accelerator Magnets". In: *IEEE Trans. Appl. Supercond.* 25.3 (2015), p. 4002404.

[63] A. Godeke. Private Communication.

[64] R.R. Wilson. "Radiological use of fast protons". In: *Radiology* 19.3 (2009), pp. 487–491.

[65] A.M. Sessler. *Introduction to Ion Beam Cancer Therapy, Lawrence Berkeley National Laboratory, Berkeley, CA, Sept. 10th.* 2010.

[66] J.M. Slater et al. "The proton treatment center at Loma Linda University Medical Center: Rationale and description of its development". In: *Int. J. Radiat. Oncol. Biol. Phys.* 22 (1992), p. 383.

[67] T. Kamada et al. "Carbon ion radiotherapy in Japan: an assessment of 20 years of clinical experience". In: *Lancet Oncol.* 16.2 (2015), pp. 93–100.

[68] *PTCOG: Facilities in Operation.* URL: `http://www.ptcog.ch/index.php/facilities-in-operation`.

[69] Francesca Albertini. "Planning and Optimizing Treatment Plans for Actively Scanned Proton Therapy: evaluation and estimating the effect of uncertainties". In: *Dissertation, ETH Zurich, Switzerland* (2011).

[70] A.M. Koehler, R.J. Schneider, and J. M. Sisterson. "Range Modulators for Protons and Heavy Ions". In: *Nuclear Instruments and Methods* 131 (1975), pp. 437–440.

[71] T. Kanai et al. "Spot scanning system for proton radiotherapy". In: *Med. Phys.* 7.4 (1975), 365369.

[72] T. Haberer et al. "Magnetic scanning system for heavy ion therapy". In: *Nucl. Instrum. Methods Phys. Res. A* 330 (1993), 296305.

[73] E. Pedroni et al. "The 200-MeV proton therapy project at the Paul Scherrer Institute: conceptual design and practical realization". In: *Med. Phys.* 22.1 (1995), 3753.

[74] Gerhard Kraft. *History of the Heavy Ion Therapy at GSI, GSI, Darmstadt, Germany.* 2013.

[75] M.Pavlovic, E.Griesmayer, and R.Seemann. "Beam-transport study of an isocentric rotating ion gantry with minimum number of quadrupoles". In: *Nucl. Instrum. Methods Phys. Res. A* 545 (2005), pp. 412–426.

[76] Ute Linz. *Ion Beam Therapy: Fundamentals, Technology, Clinical Applications.* Springer, 2011. ISBN: 978-3-642-21413-4.

[77] *Workshop on Ion Beam: Summary Report.* URL: `http://science.energy.gov/~/media/hep/pdf/accelerator-rd-stewardship/Workshop_on_Ion_Beam_Therapy_Report_Final_R1.pdf`.

[78] "D. Trbojevic et al. ""Carbon/proton therapy: A novel gantry design"". In: *Physical Review Special Topics - Accelerators and Beams* 10 (2007), p. 053503.

[79] A. Gerbershagen et al. "Beam optics simulation studies for a proton therapy gantry design with curved superconducting magnets". PTCOG 53, Scientific Meeting, June 12 - June 14. 2014.

[80] W. Wan et al. "Alternating Gradient CCT (AG-CCT) Superconducting Magnets for a Compact Large Momentum Acceptance Proton Gantry Design". Submitted for publication. 2015.

[81] A. Gerbershagen et al. "Design of a superconducting gantry with local dispersion suppression". Submitted for publication. 2015.

[82] Harald Paganetti. *Proton Therapy Physics*. CRC Press, 2011. ISBN: 1439836442.

[83] Charlie Ma and Tony Lomax. *Proton and Carbon Ion Therapy*. CRC Press, 2012. ISBN: 1439816077.

[84] Hirohiko Tsujii et al. *Carbon-Ion Radiotherapy: Principles, Practices, and Treatment Planning*. Springer, 2014. ISBN: 978-4-431-54456-2.

[85] P. Fabbricatore. *Challenges to design and test fast ramped superconducting dipole magnet, Beam Dynamics Meets Magnets II, Bad Zurzach, Switzerland, December 3*. 2014. URL: https://indico.psi.ch/contributionDisplay.py?contribId=15&sessionId=3&confId=3033.

[86] D.S. Robin et al. "Superconducting toroidal combined-function magnet for a compact ion beam cancer therapy gantry". In: *Nuclear Instruments and Methods in Physics Research Section A: Accelerators, Spectrometers, Detectors and Associated Equipment* 659.1 (2011), pp. 484 –493.

[87] S. Caspi et al. "Conceptual Design of a 260 mm Bore 5T Superconducting Curved Dipole Magnet for a Carbon Beam Therapy Gantry". In: *IEEE Trans. Appl. Supercond.* 22.3 (2012), p. 4401204.

[88] L. Brouwer and S. Caspi. *Magnets meet beams in gantries for medical application, Beam Dynamics Meets Magnets II, Bad Zurzach, Switzerland, December 3*. 2014. URL: https://indico.psi.ch/contributionDisplay.py?contribId=10&sessionId=3&confId=3033.

[89] S. Caspi et al. "A superconducting magnet mandrel with minimum symmetry laminations for proton therapy". In: *Nuclear Instruments and Methods in Physics Research Section A: Accelerators, Spectrometers, Detectors and Associated Equipment* 719.0 (2013), pp. 44 –49.

[90] C. Priano et al. "A Superconducting Magnet for a Beam Delivery System for Carbon Ion Cancer Therapy". In: *IEEE Trans. Appl. Supercond.* 12.1 (2002), pp. 988–992.

[91] M. Schaer et al. *A Design of a Gantry with Superconducting Magnets for 350 MeV Protons, Presentation at ECPM, May 12*. 2012. URL: http://indico.hep.manchester.ac.uk/getFile.py/access?contribId=19&resId=1&materialId=slides&confId=4226.

[92] M. Bajard and F. Kircher. "Rotative Gantry for Dose Distribution in Hadron Therapy". In: *Proceedings of EPAC2008*. 2008, TUPP110.

[93] D.J. Holder, A.F. Green, and H.L. Owen. "A Compact Superconducting 330 MeV Proton Gantry for Radiotherapy and Computed Tomography". In: *Proceedings of IPAC2014*. 2014, WEPRO101.

[94] *The MEVION S250*. URL: `http://www.mevion.com/the-system`.

[95] Y. Iwata et al. "Design of a superconducting rotating gantry for heavy-ion therapy". In: *Physical Review Special Topics - Accelerators and Beams* 15.4 (2012), p. 044701.

[96] Y. Iwata et al. "Development of a superconducting rotating-gantry for heavy-ion therapy". In: *Nuclear Instruments and Methods in Physics Research Section B: Beam Interactions with Materials and Atoms* 317 (2013), 793797.

[97] Y. Iwata et al. "Development of Curved Combined-Function Superconducting Magnets for a Heavy-Ion Rotating-Gantry". In: *IEEE Trans. Appl. Supercond.* 23.3 (2014), p. 4400505.

[98] T. Antaya. *Superconducting Magnet Needs for Cutting Edge Medical and Security Applications, Lawrence Berkeley National Laboratory, October, 2*. 2012.

[99] V. Derenchuk. *The ProNova SC360 Gantry, Presentation at the Modern Hadron Therapy Gantry Developments, Cockcroft Institute, January, 2014*. 2014. URL: `http://indico.hep.manchester.ac.uk/getFile.py/accesscontribId=27&resId=0&materialId=slides&confId=4226`.

[100] Y. Iwata. *Development of a superconducting rotating-gantry for heavy-ion therapy, Presentation at the Modern Hadron Therapy Gantry Developments, Cockcroft Institute, January, 2014*. 2014. URL: `http://indico.hep.manchester.ac.uk/getFile.py/access?contribId=10&resId=0&materialId=slides&confId=4226`.

[101] P. Fabbricatore and et al. "Development of a Curved Fast Ramped Dipole for FAIR SIS300". In: *IEEE Trans. Appl. Supercond.* 18.2 (2008), pp. 4232–235.

[102] Egbert Fischer et al. "Fast Ramped Superconducting Magnets for FAIR - Production Status and First Test Results". In: *IEEE Trans. Appl. Supercond.* 25.3 (2015), p. 4003805.

[103] A Kovalenko et al. "Design of a Twin-Aperture 4 T Curved Dipole Based on High Current Hollow Superconducting Cables for the NICA Collider at JINR". In: *J. Phys.: Conf.* 234.3 (2010), p. 032033.

[104] P. Schnizer et al. "Plane elliptic or toroidal multipole expansions for static fields: Applications within the gap of straight and curved accelerator magnet". In: *The International Journal for Computation and Mathematics in Electrical Engineering (COMPEL)* 28.4 (2009), pp. 1044–1058.

[105] P. Schnizer and et al. "SIS100 Dipole Magnet Optimization and Local Toroidal Multipoles". In: *IEEE Trans. Appl. Supercond.* 22.3 (2012), p. 4001505.

[106] P. Moon and D.E. Spencer. "The Meaning of the Vector Laplacian". In: *Journal of the Franklin Institute* 256.6 (1953), pp. 551–558.

[107] M. Abramowitz and I.A. Stegun. *Handbook of Mathematical Functions*. 9th ed. New York, NY: Dover, 1972.

[108] J. Segura and A.Gil. "Evaluation of Toroidal Harmonics". In: *Computer Physics Communications* 124 (2000), pp. 104–122.

[109] S.Y. Lee. *Accelerator Physics*. World Scientific, 1999. ISBN: 9810237103.

[110] Helmut Wiedemann. *Particle Accelerator Physics*. Spring-Verlag, 1993. ISBN: 9783540646716.

[111] S. Caspi, M. Helm, and L.J. Laslett. "3D Field Harmonics". In: *SC-MAG* 328.30313 (1991).

Appendix A

Magnetic Field Representation in Accelerator Magnets

A.1 Straight-section harmonics

It is typical to express the transverse magnetic field in the center or "straight-section" of a magnet in terms of harmonics. This straight-section is far from the ends of the magnet in the region where the current density is independent of axial position (Fig. A.1). Field harmonics are chosen due to being the standard representation for accelerator physics [109], serving as a common language between beam dynamics and magnet design. This representation corresponds to a 2D solution of Laplace's equation for the magnetic vector potential in a region of no current, $\nabla \times \vec{B} = \nabla \times (\nabla \times \vec{A}) = -\nabla^2 \vec{A} = 0$, with the choice of Coulomb gauge. This solution is conveniently expressed in the complex plane as

$$B_y(x,y) + iB_x(x,y) = \sum_{n=1}^{\infty} (B_n + iA_n) \left(\frac{x+iy}{R_0} \right)^{n-1}, \tag{A.1}$$

where B_n and A_n give the magnitude of the harmonics, and R_0 is a reference radius typically chosen to be 2/3 of the magnet's aperture.

It is common to normalize this expression to the harmonic the magnet is designed to produce,

$$B_y(x,y) + iB_x(x,y) = 10^{-4} B_{main} \sum_{n=1}^{\infty} (b_n + ia_n) \left(\frac{x+iy}{R_0} \right)^{n-1}, \tag{A.2}$$

such that B_{main} is B_1 for a dipole, B_2 for a quadrupole, B_3 for a sextupole, and so on. B_{main} corresponds to the magnitude of the field from the design harmonic on the midplane ($y = 0$) at the reference radius R_0. The 10^{-4} is chosen as a convenient normalization for field errors. Here the normal and skew coefficients b_n and a_n represent 100 ppm of the desired harmonic,

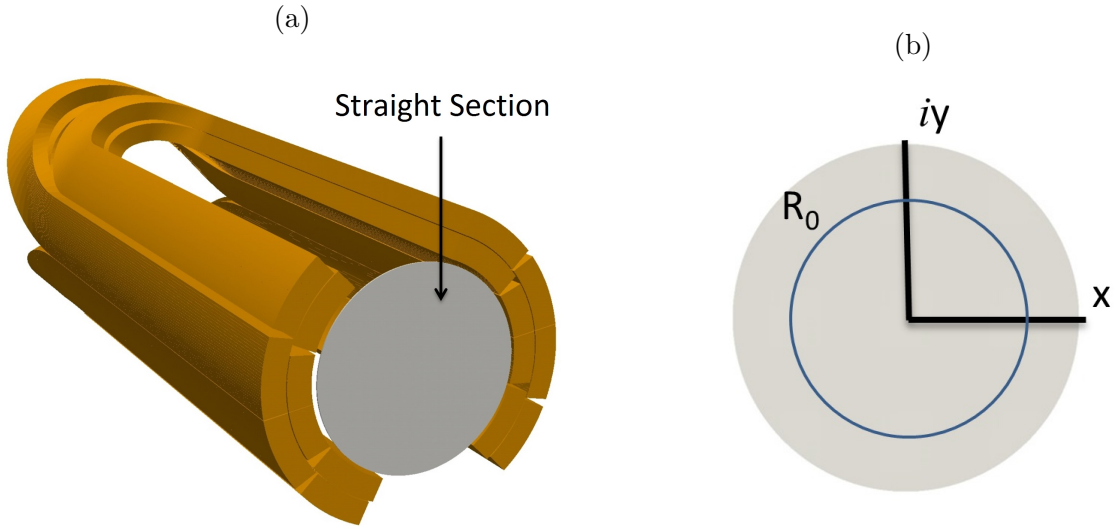

Figure A.1: (a) A coil configuration is shown cut through the center of the straight-section (away from the ends). (b) The complex plane used for the harmonic expression of the transverse fields.

and are referred to as field "units". This scales the coefficients to the order of magnitude of allowed field error. A typical specification for the field quality of an accelerator magnet is the bore field should contain less than a few units of the non-desired harmonics.

A.2 Integrated harmonics

The ends of the magnet break the 2D symmetry assumed in Section A.1 for the straight-section harmonics. This leads to variation of the field along the length of the magnet, a full treatment of which requires the use of 3D harmonics [111]. It is typical to describe the harmonics along the length in terms of integrated values. For typical accelerator magnets it is desirable to maximize the integral of the main harmonic and minimize the integral of the undesired harmonics (referred to as integrated field errors).

Figure A.2 shows the typical form of the dipole field along the length of a CCT magnet with the location of the straight-section dipole B_1^{SS} indicated. If z represents the length along the axial direction, the integrated dipole field is

$$B_{1,int} = \int B_1(z)dz. \tag{A.3}$$

It is typical to represent the integrated dipole field with a step function of value B_1^{SS} and width

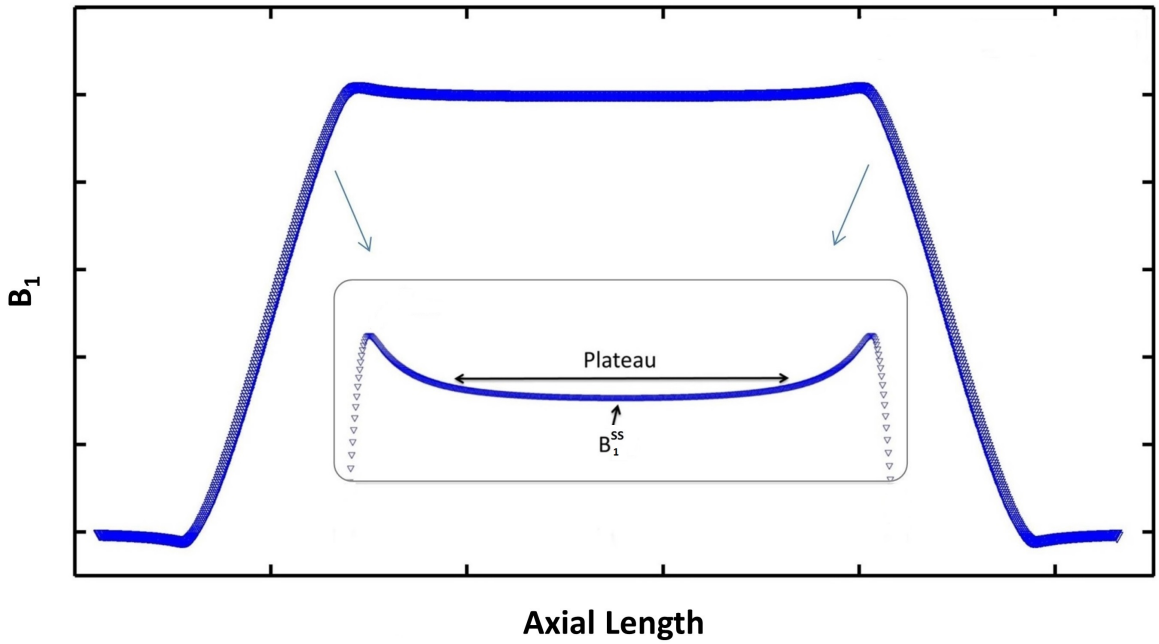

Figure A.2: The typical form of the dipole harmonic B_1 along the length of a CCT magnet is shown with the location straight-section dipole field B_1^{SS} indicated.

$$L_m = \frac{B_{1,int}}{B_1^{SS}} = \frac{\int B_1(z)dz}{B_1^{SS}}, \tag{A.4}$$

which is referred to as the magnetic length of the magnet. This representation can be seen in Figure A.3.

The higher order harmonics also vary along the length of the magnet. Examples of this variation can be seen for CCT1 in Figure 5.6 and CCT2 in Figure 6.5. To describe the higher order field error through the ends of a dipole magnet, normalized integrated harmonics are defined

$$\bar{b}_n = \frac{\int B_n(z)dz}{B_1^{SS} L_m}, \tag{A.5}$$

where B_1^{SS} is the dipole harmonic in the straight-section and L_m is the magnetic length. For a dipole magnet it is desirable to minimize these integrated field errors.

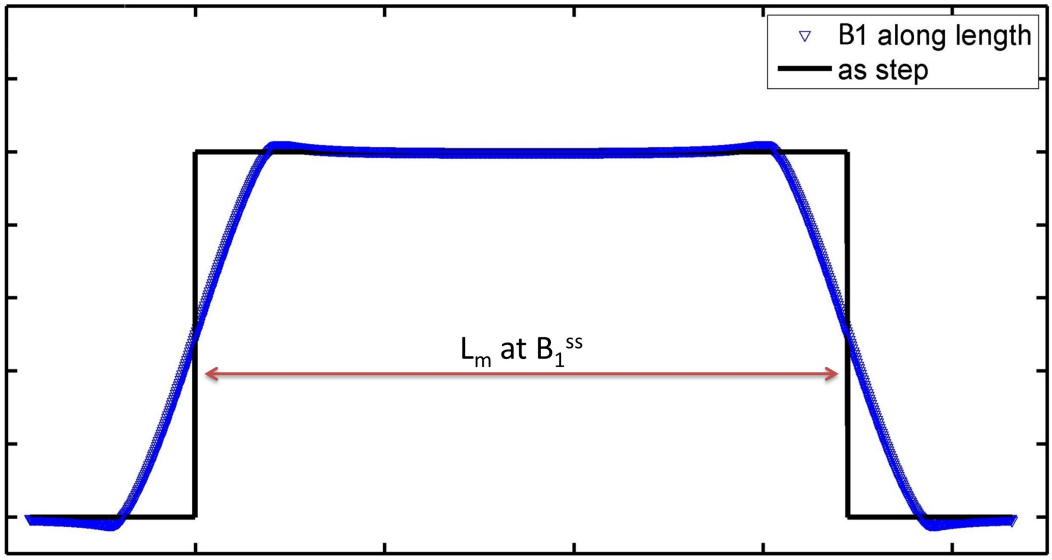

Figure A.3: The integrated dipole field is represented as a step function of height B_1^{SS} and magnetic length L_m.

Appendix B

Current Sheet Vector Potentials

B.1 The vector potential from integration

The magnetic vector potential resulting from a current distribution can be directly determined by integration. If primed coordinates are used to represent the location of source current, the static vector potential $\vec{A}$ is given by

$$\vec{A}(\vec{r}) = \frac{\mu_0}{4\pi} \int \frac{\vec{J}(\vec{r}')}{|\vec{r} - \vec{r}'|} d^3\vec{r}'. \tag{B.1}$$

For a current sheet located at a fixed radius of $r' = a$, the integration in cylindrical coordinates becomes

$$\vec{A}(r, \theta, z) = \frac{a\mu_0}{4\pi} \int \int \frac{\vec{j}(\theta', z')}{|\vec{r} - \vec{r}'|} d\theta' dz', \tag{B.2}$$

where $\vec{j}$ is the linear current density of the sheet. The integration variables $t \equiv \theta - \theta'$ and $s \equiv z - z'$ are introduced, such that

$$|\vec{r} - \vec{r}'| = \sqrt{a^2 + r^2 + s^2 - 2ar\cos t}. \tag{B.3}$$

B.2 Integration for a current sheet with no axial variation

For a current sheet with no axial variation located at fixed radius a, the axial integration is given by

$$\vec{A} = \frac{a\mu_0}{4\pi} \int_0^{2\pi} \vec{j}(t) dt \int_{-\infty}^{\infty} \frac{1}{\sqrt{a^2 + r^2 + s^2 - 2ar\cos t}} ds, \tag{B.4}$$

where the length of the sheet is assumed to be infinite. The axial integration over s can be performed with $C^* \equiv a^2 + r^2 - 2ar\cos t$ so that

$$\int_{-\infty}^{\infty} \frac{1}{\sqrt{C^* + s^2}} ds = 2\int_0^{\infty} \frac{1}{\sqrt{C^* + s^2}} ds = 2\log(s + \sqrt{C^* + s^2})\Big|_0^{\infty} = -2\log(\sqrt{C^*}), \quad \text{(B.5)}$$

where the constant terms are discarded. The identity

$$\sum_{k=1}^{\infty} \frac{z^k \cos kx}{k} = \log\left(\frac{1}{\sqrt{z^2 - 2z\cos x + 1}}\right) \qquad |x| < 1 \quad \text{(B.6)}$$

is considered to show that within the bore

$$\int_{-\infty}^{\infty} \frac{1}{\sqrt{a^2 + r^2 + s^2 - 2ar\cos t}} ds = -2\log(a) + 2\sum_{k=1}^{\infty} \left(\frac{r}{a}\right)^k \frac{\cos kt}{k} \qquad r < a, \quad \text{(B.7)}$$

and outside the bore

$$\int_{-\infty}^{\infty} \frac{1}{\sqrt{a^2 + r^2 + s^2 - 2ar\cos t}} ds = -2\log(r) + 2\sum_{k=1}^{\infty} \left(\frac{a}{r}\right)^k \frac{\cos kt}{k} \qquad r > a. \quad \text{(B.8)}$$

B.3 Potential for a solenoidal current sheet

A constant azimuthal current $\vec{j}(\theta', z') = j_{0\theta}\hat{\theta}'$ can be written in the integration coordinates as

$$\vec{j}(t) = j_{0\theta}\hat{\theta}' = j_{0\theta}\left[\sin t\hat{r} + \cos t\hat{\theta}\right]. \quad \text{(B.9)}$$

The vector potential for this current can then be found using Equations B.4, B.7, and B.8 such that

$$\vec{A} = \frac{a\mu_0}{4\pi}\int_0^{2\pi} j_{0\theta}\left[\sin t\hat{r} + \cos t\hat{\theta}\right]\left[-2\log(a) + 2\sum_{k=1}^{\infty}\left(\frac{r}{a}\right)^k \frac{\cos kt}{k}\right] dt \qquad r < a \quad \text{(B.10)}$$

inside the bore, and

$$\vec{A} = \frac{a\mu_0}{4\pi}\int_0^{2\pi} j_{0\theta}\left[\sin t\hat{r} + \cos t\hat{\theta}\right]\left[-2\log(r) + 2\sum_{k=1}^{\infty}\left(\frac{a}{r}\right)^k \frac{\cos kt}{k}\right] dt \qquad r > a \quad \text{(B.11)}$$

outside the bore. The integration picks out the $k = 1$ component so that

$$\boxed{\vec{A}(r) = \begin{cases} \frac{\mu_0 j_{0\theta}}{2} r\hat{\theta}, & r < a \\ \frac{\mu_0 j_{0\theta} a^2}{2r}\hat{\theta}, & r > a \end{cases}}. \tag{B.12}$$

It is seen that the potential is continuous at $r = a$, and the magnetic field (as a check) is the expected

$$\vec{B} = \nabla \times \vec{A} = \frac{1}{r}\left(\frac{\partial(rA_\theta)}{\partial r}\right)\hat{z} = \begin{cases} \mu_0 j_{0\theta}\hat{z}, & r < a \\ 0, & r > a \end{cases}. \tag{B.13}$$

B.4 Potential for a cos(nθ) current sheet

An axial current varying azimuthally as $\vec{j}(\theta', z') = j_{0zn}\cos(n\theta')\hat{z}'$ can be written in the integration coordinates as

$$\vec{j}(t) = j_{0zn}\cos(n\theta')\hat{z}' = j_{0zn}\left[\cos n\theta\cos nt - \sin n\theta\sin nt\right]\hat{z}. \tag{B.14}$$

The vector potential for this current can then be found using Equations B.4, B.7, and B.8 such that

$$\vec{A} = \frac{a\mu_0}{4\pi}\int_0^{2\pi} j_{0zn}\left[\cos n\theta\cos nt - \sin n\theta\sin nt\right]\left[-2\log(a) + 2\sum_{k=1}^{\infty}\left(\frac{r}{a}\right)^k\frac{\cos kt}{k}\right]\hat{z}dt \qquad r < a \tag{B.15}$$

inside the bore, and

$$\vec{A} = \frac{a\mu_0}{4\pi}\int_0^{2\pi} j_{0zn}\left[\cos n\theta\cos nt - \sin n\theta\sin nt\right]\left[-2\log(r) + 2\sum_{k=1}^{\infty}\left(\frac{a}{r}\right)^k\frac{\cos kt}{k}\right]\hat{z}dt \qquad r > a \tag{B.16}$$

outside the bore. The integration picks out the $k = n$ component so that

$$\boxed{\vec{A}(r,\theta) = \begin{cases} \frac{\mu_0 j_{0nz}}{2n} a\left(\frac{r}{a}\right)^n\cos n\theta\hat{z}, & r < a \\ \frac{\mu_0 j_{0nz}}{2n} a\left(\frac{r}{a}\right)^{-n}\cos n\theta\hat{z}, & r > a \end{cases}}. \tag{B.17}$$

It is seen that the potential is continuous at $r = a$, and the magnetic field (as a check) is the expected

$$\vec{B} = \nabla \times \vec{A} = \frac{1}{r}\frac{\partial A_z}{\partial\theta}\hat{r} - \frac{\partial A_z}{\partial r}\hat{\theta} \tag{B.18}$$

$$\vec{B}(r,\theta) = \begin{cases} -\frac{\mu_0 j_{0nz}}{2}\left(\frac{r}{a}\right)^{n-1}\left[\sin n\theta\hat{r} + \cos n\theta\hat{\theta}\right], & r < a \\ -\frac{\mu_0 j_{0nz}}{2}\left(\frac{r}{a}\right)^{-n-1}\left[\sin n\theta\hat{r} - \cos n\theta\hat{\theta}\right], & r > a \end{cases}. \tag{B.19}$$

B.5 Potential for a constant axial current

A constant axial current $\vec{j}(\theta', z') = j_{0z}\hat{z}'$ can be written in the integration coordinates as $\vec{j} = j_{0z}\hat{z}$. The vector potential for this current can then be found using Equations B.4, B.7, and B.8 such that

$$\vec{A} = \frac{a\mu_0}{4\pi} j_{0z}\hat{z}\int_0^{2\pi}\left[-2\log(a) + 2\sum_{k=1}^{\infty}\left(\frac{r}{a}\right)^k \frac{\cos kt}{k}\right]dt \qquad r < a \tag{B.20}$$

inside the bore, and

$$\vec{A} = \frac{a\mu_0}{4\pi} j_{0z}\hat{z}\int_0^{2\pi}\left[-2\log(r) + 2\sum_{k=1}^{\infty}\left(\frac{a}{r}\right)^k \frac{\cos kt}{k}\right]dt \qquad r > a \tag{B.21}$$

outside the bore. The vector potential is then

$$\boxed{\vec{A}(r) = \begin{cases} -\mu_0 j_{0z} a\log(a), & r < a \\ -\mu_0 j_{0z} a\log(r), & r > a \end{cases}}. \tag{B.22}$$

It is seen that the potential is continuous at $r = a$, and the magnetic field (as a check) is the expected

$$\vec{B} = \nabla \times \vec{A} = \frac{1}{r}\frac{\partial A_z}{\partial \theta}\hat{r} - \frac{\partial A_z}{\partial r}\hat{\theta} \tag{B.23}$$

$$\vec{B}(r) = \begin{cases} 0, & r < a \\ \mu_0 j_{0z}\frac{a}{r}\hat{\theta}, & r > a \end{cases}. \tag{B.24}$$

Substitution of the enclosed current $I_0 = 2\pi a j_{0z}$ leads to the familiar variation of fields outside of a line current of

$$\vec{B} = \frac{\mu_0 I_0}{2\pi r}\hat{\theta}. \tag{B.25}$$

Appendix C

Cost Study Design Data

C.1 A two layer 11.3 T CCT dipole

Table C.1: Load Line Calculation for Two Layers

Layer	Ungraded		Graded	
	n_s	Bcond	n_s	Bcond
1	22	13.89	22	13.90
2	22	12.57	18	12.79
Results at I_0=22.38 kA				

(a) (b)

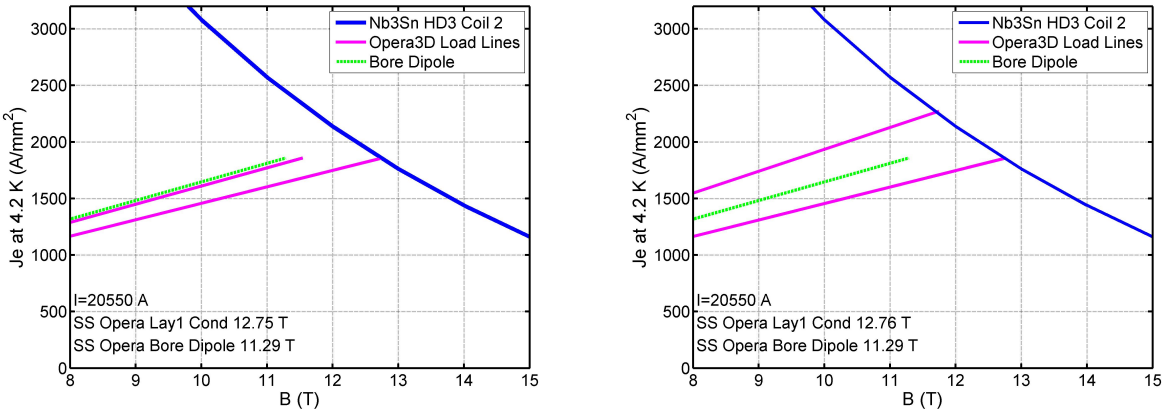

Figure C.1: The load lines for each layer of the 2 layer magnet are shown for the ungraded case (a) and the graded case (b).

Table C.2: Two Layer Conductor Use: Ungraded

	Ungraded					
Layer	n_s	r_{cond}	L_{turn}	L_{cable}/L_m	L_{strand}/L_m	\$/m of L_m
1	22	58.525	973.508	112.937	2484.61	21988.8
2	22	71.575	1190.57	138.119	3038.62	26891.8
Tot				251.056	5523.23	48880.6

Table C.3: Two Layer Conductor Use: Graded

	Graded					
Layer	n_s	r_{cond}	L_{turn}	L_{cable}/L_m	L_{strand}/L_m	\$/m of L_m
1	22	58.525	973.508	112.937	2484.61	21988.8
2	18	70.775	1177.27	136.575	2458.35	21756.4
Tot				249.512	4942.97	43745.3

Table C.4: Two Layer Conductor Cost Summary

Ungraded			Graded		
L_{cable}/L_m	L_{strand}/L_m	\$/m of L_m	L_{cable}/L_m	L_{strand}/L_m	\$/m of L_m
251	5520	48.9 k\$/m	250	4940	43.7 k\$/m

Table C.5: Two Layer Short-Sample Fields

Bore Dipole	Cond. Field	Current
11.29 T	12.75 T	20.55 kA

C.2 A four layer 14.3 T CCT dipole

Table C.6: Load Line Calculation for Four Layers

Layer	Ungraded		Graded	
	n_s	Bcond	n_s	Bcond
1	22	15.60	22	15.62
2	22	14.67	19	14.77
3	22	13.16	15	13.56
4	22	11.53	12	12.25
Results at I_0=13.5 kA				

(a) (b)

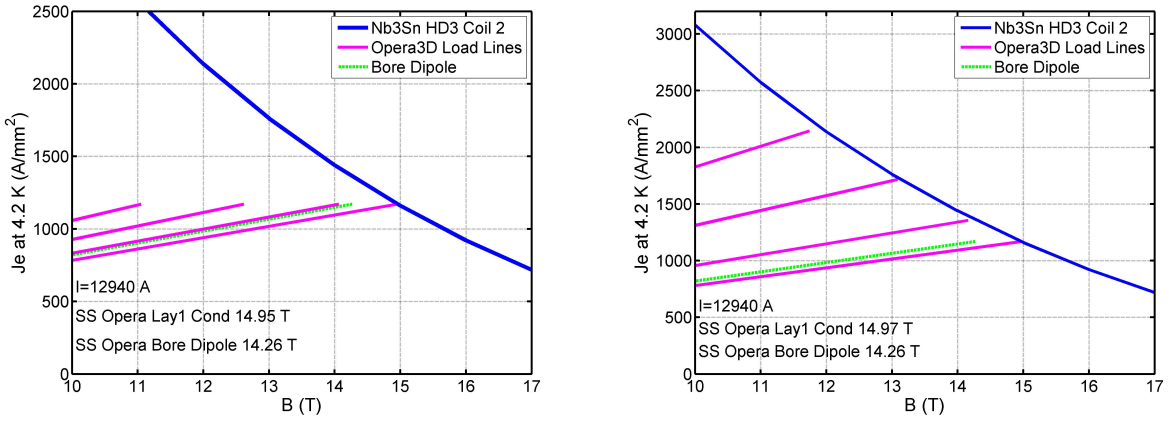

Figure C.2: The load lines for each layer of the 4 layer magnet are shown for the ungraded case (a) and the graded case (b).

Table C.7: Four Layer Conductor Use: Ungraded

	Ungraded					
Layer	n_s	r_{cond}	L_{turn}	L_{cable}/L_m	L_{strand}/L_m	\$/m of L_m
1	22	58.525	973.508	112.937	2484.61	21988.8
2	22	71.575	1190.57	138.119	3038.62	26891.8
3	22	84.625	1407.64	163.301	3592.62	31794.7
4	22	97.675	1624.71	188.483	4146.63	36697.7
Tot				602.84	13262.5	117373

Table C.8: Four Layer Conductor Use: Graded

	Graded					
Layer	n_s	r_{cond}	L_{turn}	L_{cable}/L_m	L_{strand}/L_m	\$/m of L_m
1	22	58.525	973.508	112.937	2484.61	21988.8
2	19	70.975	1180.59	136.961	2602.26	23030
3	15	82.025	1364.4	158.284	2374.26	21012.2
4	12	91.675	1524.91	176.905	2122.86	18787.3
Tot				585.087	9584	84818.4

Table C.9: Four Layer Conductor Cost Summary

Ungraded			Graded		
L_{cable}/L_m	L_{strand}/L_m	\$/m of L_m	L_{cable}/L_m	L_{strand}/L_m	\$/m of L_m
603	13.26 k	117.4 k\$/m	585	9.58 k	84.8 k\$/m

Table C.10: Four Layer Short-Sample Fields

Bore Dipole	Cond. Field	Current
14.25 T	14.95 T	12.94 kA

C.3 A six layer 15.8 T CCT dipole

Table C.11: Load Line Calculation for Six Layers

lay	Ungraded		Graded	
	n_s	Bcond	n_s	Bcond
1	22	16.74	22	16.74
2	22	16.01	19	16.07
3	22	14.82	15	15.08
4	22	13.57	13	14.05
5	22	12.11	11	13.05
6	22	10.66	9	12.00
Results at I_0=9.8 kA				

(a) (b)

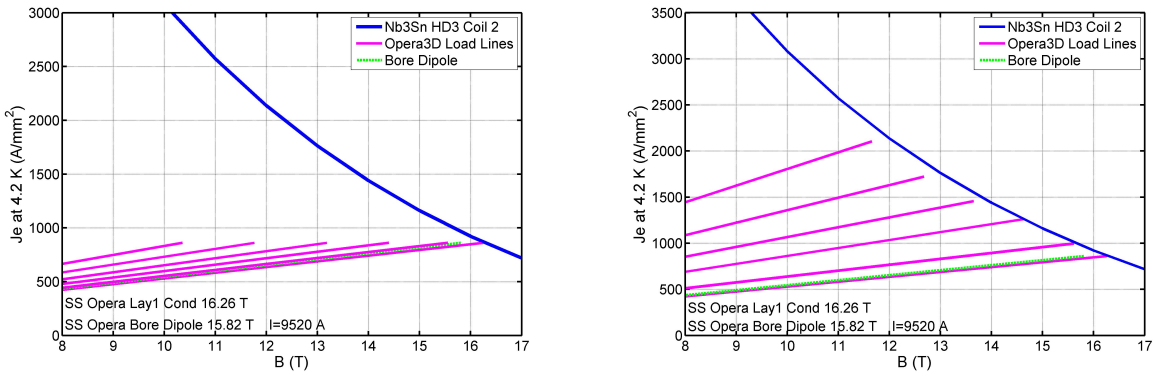

Figure C.3: The load lines for each layer of the 6 layer magnet are shown for the ungraded case (a) and the graded case (b).

Table C.12: Six Layer Conductor Use: Ungraded

	Ungraded					
Layer	n_s	r_{cond}	L_{turn}	L_{cable}/L_m	L_{strand}/L_m	\$/m of L_m
1	22	58.525	973.508	112.937	2484.61	21988.8
2	22	71.575	1190.57	138.119	3038.62	26891.8
3	22	84.625	1407.64	163.301	3592.62	31794.7
4	22	97.675	1624.71	188.483	4146.63	36697.7
5	22	110.725	1841.78	213.666	4700.64	41600.7
6	22	123.775	2058.85	238.848	5254.65	46503.7
Tot				1055.35	23217.8	205477

Table C.13: Six Layer Conductor Use: Graded

	Graded					
Layer	n_s	r_{cond}	L_{turn}	L_{cable}/L_m	L_{strand}/L_m	\$/m of L_m
1	22	58.525	973.508	112.937	2484.61	21988.8
2	19	70.975	1180.59	136.961	2602.26	23030
3	15	82.025	1364.4	158.284	2374.26	21012.2
4	13	91.875	1528.24	177.291	2304.79	20397.4
5	11	100.925	1678.77	194.755	2142.3	18959.4
6	9	109.175	1816	210.675	1896.07	16780.2
Tot				990.902	13804.3	122168

Table C.14: Six Layer Conductor Cost Summary

Ungraded			Graded		
L_{cable}/L_m	L_{strand}/L_m	\$/m of L_m	L_{cable}/L_m	L_{strand}/L_m	\$/m of L_m
1055	23.2 k	205.5 k\$/m	991	13.8 k	122.1 k\$/m

Table C.15: Six Layer Short-Sample Fields

Bore Dipole	Cond. Field	Current
15.82 T	16.26 T	9.52 kA

C.4 A eight layer 16.8 T CCT dipole

Table C.16: Load Line Calculation for Eight Layers

Layer	Ungraded		Graded	
	n_s	Bcond	n_s	Bcond
1	22	17.46	22	17.44
2	22	16.87	19	16.89
3	22	15.96	16	16.07
4	22	14.94	13	15.24
5	22	13.71	11	14.37
6	22	12.57	10	13.46
7	22	11.36	8	12.70
8	22	10.10	7	11.82
Results at I_0=7.7 kA				

(a) (b)

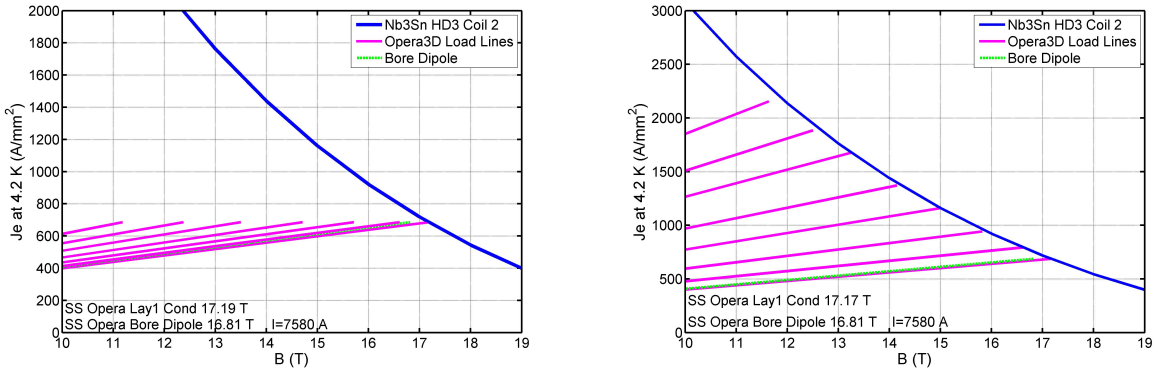

Figure C.4: The load lines for each layer of the 8 layer magnet are shown for the ungraded case (a) and the graded case (b).

Table C.17: Eight Layer Conductor Use: Ungraded

	Ungraded					
Layer	n_s	r_{cond}	L_{turn}	L_{cable}/L_m	L_{strand}/L_m	\$/m of L_m
1	22	58.525	973.508	112.937	2484.61	21988.8
2	22	71.575	1190.57	138.119	3038.62	26891.8
3	22	84.625	1407.64	163.301	3592.62	31794.7
4	22	97.675	1624.71	188.483	4146.63	36697.7
5	22	110.725	1841.78	213.666	4700.64	41600.7
6	22	123.775	2058.85	238.848	5254.65	46503.7
7	22	136.825	2275.92	264.03	5808.66	51406.7
8	22	149.875	2492.99	289.212	6362.67	56309.7
Tot				1608.6	35389.1	313194

Table C.18: Eight Layer Conductor Use: Graded

	Graded					
Layer	n_s	r_{cond}	L_{turn}	L_{cable}/L_m	L_{strand}/L_m	\$/m of L_m
1	22	58.525	973.508	112.937	2484.61	21988.8
2	19	70.975	1180.59	136.961	2602.26	23030
3	16	82.225	1367.72	158.67	2538.72	22467.7
4	13	92.275	1534.89	178.063	2314.82	20486.2
5	11	101.325	1685.42	195.527	2150.79	19034.5
6	10	109.775	1825.98	211.832	2118.32	18747.2
7	8	117.625	1956.55	226.98	1815.84	16070.2
8	7	124.875	2077.15	240.97	1686.79	14928.1
Tot				1461.94	17712.2	156753

Table C.19: Eight Layer Conductor Cost Summary

Ungraded			Graded		
L_{cable}/L_m	L_{strand}/L_m	\$/m of L_m	L_{cable}/L_m	L_{strand}/L_m	\$/m of L_m
1609	35.39 k	313.2 k\$/m	1462	17.7 k	156.8 k\$/m

Table C.20: Eight Layer Short-Sample Fields

Bore Dipole	Cond. Field	Current
16.81 T	17.19 T	7.58 kA